Petrogenesis and age of the Peltetec Ophiolitic belt and the Tampanchi ultramafic-mafic complex, Cordillera Real (Ecuador): Geodynamic implications for the evolution of the Andean active margin

Fabián Marcelo Villares Jibaja

DOCTORAL THESIS

March, 2021

UNIVERSIDAD DE GRANADA

Departamento de Mineralogía y Petrología

Programa Doctorado Ciencias de la Tierra

UNIVERSIDAD DE GRANADA

FACULTAD DE CIENCIAS

DEPARTAMENTO DE MINERALOGÍA Y PETROLOGÍA

PROGRAMA DE DOCTORADO EN CIENCIAS DE LA TIERRA

TESIS DOCTORAL

Petrogenesis and age of the Peltetec Ophiolitic belt and the Tampanchi ultramafic-mafic complex, Cordillera Real (Ecuador): Geodynamic implications for the evolution of the Andean active margin

Tesis que presenta FABIÁN MARCELO VILLARES JIBAJA para optar al grado de Doctor por la Universidad de Granada.

Fdo. Fabián Marcelo Villares Jibaja

VºBº del Director

GARCIA CASCO ANTONIO - 08804875S

Firmado digitalmente por GARCIA CASCO ANTONIO - 08804875S
Fecha: 2021.02.22 13:52:32 +01'00'

Dr. Antonio García Casco

VºBº del Director

IDAEL FRANCISCO| BLANCO| QUINTERO

Digitally signed by IDAEL FRANCISCO| BLANCO|QUINTERO
DN: cn=IDAEL FRANCISCO|BLANCO| QUINTERO, serialNumber=X7864247H, givenName=IDAEL FRANCISCO, sn=BLANCO QUINTERO, ou=CIUDADANOS, o=ACCV, c=ES
Date: 2021.02.22 13:40:51 +01'00'

Dr. Idael Francisco Blanco Quintero

Granada, 19 de marzo de 2021

Editor: Universidad de Granada. Tesis Doctorales
Autor: Fabián Marcelo Villares Jibaja
ISBN: 978-84-1306-816-9
URI: http://hdl.handle.net/10481/67843

Esta tesis doctoral ha sido financiada por el proyecto de investigación junior del Vicerrectorado de Investigación y Proyección Social de la Escuela Politécnica Nacional (PIJ-16-04), así como por la Licencia con Remuneración otorgada por la Escuela Politécnica Nacional a favor del doctorando. El trabajo de investigación se ha llevado a cabo en el Departamento de Mineralogía y Petrología de la Universidad de Granada y las técnicas analíticas se desarrollaron en el Centro de Instrumentación Científica (CIC) de la Universidad de Granada.

Agradecimientos

Este trabajo se ha desarrollado gracias al apoyo de muchas personas e instituciones que han facilitado las cosas para que llegue a un feliz término. Por ello, expreso mi agradecimiento a todos quienes contribuyeron de forma directa o indirecta en esta investigación.

En primer lugar deseo expresar mi agradecimiento a mis directores Antonio García Casco e Idael Blanco Quintero, por aceptarme para realizar esta tesis doctoral bajo su dirección, por todo el apoyo ofrecido durante el desarrollo de la investigación, además por todo el tiempo dedicado, compartir su conocimiento y sus exhaustivas revisiones y discusiones. Gracias por la confianza, apoyo y seguimiento brindado desde que se planteó la idea de desarrollar esta investigación, hasta ahora que se culmina esta etapa. Sus enseñanzas y recomendaciones han sido un aporte invaluable en mi formación como investigador y más aún en lo personal.

También expreso mi agradecimiento a Camilo Montes, por el tiempo dedicado, apoyo y conocimiento compartido durante mi estancia en Barranquilla-Colombia. De la misma forma a Agustín Cardona y a todo su grupo de investigación, por las interesantes discusiones sobre la geología de los Andes del Norte y recorridos en el campo en Colombia. Al igual que a Joaquín Proenza, por sus valiosas revisiones y recomendaciones, y por su colaboración para obtener los datos analíticos en la etapa inicial de la investigación.

Mi agradecimiento al Departamento de Mineralogía y Petrología de la Universidad de Granada, a Nicolás Velilla Sánchez y Concepción Lázaro Calisalvo directores del departamento durante el desarrollo de esta tesis doctoral. De la misma forma a todos los profesores, técnicos y personal de administración. Mi especial agradecimiento a Fernando Bea, Pilar González Montero, Fernando Gervilla, Antonio Sánchez Navas, José Francisco Molina, J.M. Fernández Soler, Concepción Lázaro, José María González y Aitor Cambeses, por su orientación y atención a mis consultas, su predisposición a resolver toda duda y brindar su apoyo.

También quiero agradecer a todo el personal administrativo y técnico del Departamento de Mineralogía y Petrología, en especial a Jesús Montes, y del Centro de Instrumentación Científica (CIC) en donde se realizaron los análisis de laboratorio, en especial a Fernando Bea, Pilar González Montero, Delia Ortega e Isabel Nieto por el apoyo durante la datación de circones, también a Miguel Ángel Hidalgo (EPM), Olga Cazalla (ICP-MS), María José

Delgado y Lorena Quintanilla (TIMS) e Isabel Moreno (XRF) por el apoyo y soporte durante todos los análisis de laboratorio.

Agradezco a la Escuela Politécnica Nacional, por haber financiado gran parte de los análisis de laboratorio y mi estadía en Granada durante el desarrollo de la tesis. Así mismo a Pedro Reyes y Vanesa Escobar por la gestión administrativa del proyecto PIJ-16-04 que permitió el financiamiento.

Muchas gracias a todos quienes colaboraron en el trabajo de campo y muestreo por los Andes ecuatorianos, además a quienes proporcionaron información cartográfica y analítica: Pedro Reyes, Ernesto Yánez, Daniel Salguero, Darío Fuentes, Ricardo Cartagena, Asdrúbal Arteaga y Diego Narváez.

Mi especial agradecimiento a mis compañeros de la sala 5 de doctorandos Irene Morales, Jesús Muñoz, María Repczynska, Júlia Farré de Pablo, Núria Pujol, Poliana Toledo, Paola Silva, quienes fueron un soporte durante mi estadía en Granada e hicieron que mi estancia sea muy amena.

También quiero agradecer a Carla Flores por todas las conversaciones y apoyo brindado durante estos años.

Un agradecimiento especial a toda mi familia, quienes a pesar de la distancia siempre me apoyaron.

A todos, muchas gracias, sin su apoyo, colaboración e inspiración habría sido imposible llevar a cabo este trabajo.

Contenido

Abstract

Resumen

Abstract

The aim of this PhD Thesis is to address the geodynamic evolution of the active Andean continental margin during the Mesozoic, centered in the Northern Andean branch of the chain, by means of a petrological approach. Initially, two mafic - ultramafic complexes of nominally Cretaceous age were selected. One related to an oceanic environment (oceanic lithosphere) obducted onto the continental margin termed the Peltetec ophiolitic belt (Peltetec Unit) and a continental volcanic arc intrusion termed the Tampamchi ultramafic – mafic complex, both located in the Cordillera Real of Ecuador. However, the Triassic U-Pb zircon age obtained in this work allow discarding the previous published Ar-Ar plagioclase (albite) Cretaceous age of the Peltetec ophiolite, which must be considered an overprinting age. This unexpected result prevents considering the potential geodynamic relationship of the selected complexes.

New field data, deformation studies, petrographic observations, whole-rock major- and trace-element and Nd and Sr isotopic data, U-Pb SHRIMP zircon ages, mineral composition and P-T determinations of the Peltetec metaophiolite and related rocks allow the characterization of the igneous and sedimentary protoliths, the metamorphic characteristics and the evaluation of the geodynamic evolution of the active western margin of Gondwana during the Mesozoic (Triassic). The Peltetec ophiolitic belt, exposed along the western margin of the Cordillera Real (Ecuador) comprises slices of metamorphosed (greenschist facies) and variably deformed metaperidotites (serpentinites), gabbros (locally cumulate), basaltic lavas and dykes, hydrothermal breccias and sedimentary rocks. The geochemical characteristics show tholeiitic basaltic rocks with a Sr-Nd isotopic systematics indicative of a depleted mantle source in a supra-subduction environment, and variable imprint of subduction zone-derived fluids and/or continental crust-derived (assimilated) components, as indicated by enrichment in Th, negative anomaly of Nb and relative depletion in high field strength elements (HFSE). Geochemical diversity allows defining different groups of noncumulate basaltic igneous rocks with oceanic island arc and back-arc (normal mid-ocean ridge basalt-like) affinities. U-Pb zircon ages from a metabasite dyke yielded 228.1 ± 1.7 Ma, interpreted as the crystallization age of the magma. These data allow proposing the generation of the Peltetec ophiolite in a back-arc setting as a consequence of late Triassic extension of the western continental margin of Gondwana. Granites located at the western margin of the Peltetec Unit with S-type affinity and the same Triassic age (U-Pb age of 228.2 ± 0.8 Ma) document coeval anatexis of the continental crust as a consequence of heating associated with the extensional event that originated the back-arc basin and the

ophiolite. Geologic correlation with ophiolitic units in Colombia allows proposing such tectonic scenario for the whole Northern Andean margin during the Triassic.

The Peltetec ophiolite underwent two metamorphic events: (i) ocean-floor metamorphism during oceanic lithopshere formation at the back-arc spreading center under low pressure amphibolite facies conditions and (ii) prograde metamorphism up to the greenschist facies along an intermediate (barrovian) P/T gradient. The first metamorphic event occurred under near-static stress conditions and rocks did not suffer significant deformation. During this event pyroxenes were replaced by hornblende while plagioclase recrystallized. The second event produced strongly recrystallized and foliated greenschist rocks with a peak assemblage of actinolite + chlorite + albite + epidote + titanite ± phengite that developed during the closure of the back-arc basin and emplacement onto the continental margin in the late Triassic. Igneous minerals were generally not preserved. The Jurassic-Cretaceous Guamote sedimentary sequence, that limit the Peltetec Unit, also shows a penetrative cleavage that affects the stratification, and a weak diagenetic cleavage. Similar deformation is also observed in the unmetamorphosed Cretaceous Maguazo Unit, suggesting a common event of deformation for the Maguazo and Guamote units associated with the closure of Cretaceous sedimentary basins. Later processes are related to the regional mostly strike-slip Peltetec fault/shear zone that produced displacement and mixing of blocks, as indicated by cataclastic/mylonitic foliation and shear zones present in most of the slivers, but without differentiable metamorphic recrystallization overprint.

On the other hand, the Tampanchi Ultramafic-Mafic Complex (TUMC), located in the central segment of the Cordillera Real (Ecuador), is an oval-shaped intrusive body (6 km x 3 km) emplaced within a metavolcanic and metavolcano-sedimentary sequence of Cretaceous age (Alao arc). New field data, mineral and whole-rock elemental and Nd and Sr isotopic composition and zircon SHRIMP U-Th-Pb ages allowed constraining the nature of the parental magma, physical conditions of emplacement and crystallization, tectonic setting of formation and crystallization age of the TUMC. The main lithologies consist of wehrlite and olivine-hornblende clinopyroxenite crosscut by hornblende gabbros and minor dykes/veins of diorite and granite. Hornblendites formed mainly at the contact between olivine-hornblende clinopyroxenite and intrusive hornblende gabbros. At the local scale, transitions from olivine-hornblende clinopyroxenite through hornblendite to hornblende gabbros document a reaction-replacement process of olivine and pyroxene by amphibole in pyroxenites that produced hornblendites during intrusion of hornblende gabbros. Geochemical data of both wehrlites and pyroxenites define a cumulate trend with dominantly olivine and clinopyroxene fractionation, while a second trend is formed by

hornblende gabbros which differentiated to leucocratic rocks (acid residual melts) with amphibole as the dominant crystallized mafic phase. The main minerals are olivine (Fo= 75-91), clinopyroxene (diopside, Mg# = 0.84-0.97), amphibole (pargasite, magnesio-hastingsite, magnesio-ferri-hornblende and magnesio-hornblende), plagioclase (dominated by bytownite with normal zoning towards andesine and oligoclase), and minor chromium spinel, alkali-feldspar, mica, quartz and Fe-Ti oxides. All lithologies show enrichment in light rare earth elements (LREE) relative to heavy rare earth elements (HREE) compared to chondrite. The trace elements show enrichment in large ion lithophile elements (LILE), depletion in high field strength elements (Nb, Zr, Ti) and P, and enrichment in Pb, Sr and Ba relative to primitive mantle, indicating subduction-related parental hydrous basaltic liquids. Thermobarometric estimations suggest emplacement and crystallization at intermediate to shallow continental crust levels (2.2-5 kbar; ~3.6 kbar) under oxygen fugacity conditions above the NNO buffer (ΔNNO = 0-2) that point to a relatively oxidized magma. The Nd and Sr isotopic composition suggests a uniform mantle source metasomatized by crustal components evolved from the subduction zone. Zircon SHRIMP U-Th-Pb age data constrain crystallization at 75.1 ± 0.2 - 76.0 ± 0.4 Ma. The internal structure, the calc-alkaline affinity and the lack of widespread dunite/wehrlite prevent classifying TUMC as a typical Alaskan-type complex, but is regarded as a magmatic chamber reservoir of subduction zone-related volcanoes. These results confirm magmatic arc activity in the continental margin of South America during the late Cretaceous as a result of an E-dipping subduction zone prior to the accretion of the Ecuadorian-Colombian-Caribbean oceanic plateau (ECCOP), and support simultaneous double subduction in the northwest margin of South America during the Cretaceous.

The Peltetec and Tampanchi ultramafic-mafic complexes evidence a long history of subduction in the western margin of the Northern Andes, and variations in the tectonic regime with extensional and compressive periods. The Peltetec ophiolite shows the opening of a retro-arc basin in the late Triassic, initially underwent ocean floor metamorphism and then a second event related to a compressive regime associated with its emplacement onto the continental margin. The Tampanchi complex confirms that the East-directed subduction system and related magmatism in the Cordillera Real remained active to at least up to 75 Ma, shortly before the accretion of the ECCOP to the margin.

Resumen

El objetivo de esta tesis doctoral es abordar la evolución geodinámica del margen continental occidental de los Andes del Norte durante el Mesozoico mediante una aproximación petrológica. Para esto se seleccionaron dos complejos máficos-ultramáficos de edad nominalmente Cretácica, uno relacionado a un ambiente oceánico correspondiente a litósfera oceánica obductada sobre el margen continental, llamado Cinturón ofiolítico Peltetec (Unidad Peltetec), y el otro una intrusión de arco continental llamado Complejo ultramáfico-máfico Tampanchi, ambos localizados en la Cordillera Real de Ecuador. Sin embargo, la edad U-Pb en circón Triásica obtenida en este estudio descarta la edad Cretácica (Ar-Ar en plagioclasa/albita) previamente interpretada como edad de formación de la ofiolita Peltetec, la cual debe considerarse como una edad sobreimpuesta. Este resultado impide considerar la potencial relación geodinámica entre los complejos seleccionados.

Nuevos datos de campo, estudios de deformación, observaciones petrográficas, análisis geoquímicos de roca total de elementos mayores, traza y relaciones isotópicas de Nd y Sr, dataciones U-Pb en circones, composición mineral y determinaciones de presión-temperatura (P-T) de la metaofiolita Peltetec y rocas relacionadas, permitieron caracterizar los protolitos ígneos y sedimentarios, determinar las características metamórficas y la evaluación de la evolución geodinámica del margen occidental de Gondwana durante el Triásico tardío. El Cinturón ofiolítico Peltetec, expuesto a lo largo del margen occidental de la Cordillera Real, está constituido por escamas tectónicas metamorfizadas (facies de esquisto verde) y variablemente deformadas de metaperidotitas (serpentinitas), gabros (localmente acumulados), lavas basálticas, diques, brechas hidrotermales y rocas sedimentarias. Las características geoquímicas de las rocas basálticas muestran una afinidad toleítica con relaciones isotópicas de Sr y Nd que indican una fuente mantélica empobrecida asociada a un ambiente de supra-subducción. Estas rocas además presentan enriquecimiento en Th, anomalía negativa de Nb y empobrecimiento relativo de HFSE, indicativo de una firma variable de fluidos derivados de la zona de subducción y/o componentes derivados (asimilados) de la corteza continental. Se han identificado tres grupos de rocas basálticas no cumuláticas, uno con afinidades de arco de islas y dos grupos con afinidad de retro-arco (similar a basalto normal de dorsal mediooceánica). Se obtuvo una edad U-Pb en circones de 228.1 ± 1.7 Ma en una metadiabasa, interpretada como la edad de cristalización magmática. La ofiolita Peltetec se formó en un ambiente de retro-arco como consecuencia de la extensión del margen continental occidental de Gondwana en el Triásico tardío. La correlación geoquímica y geocronológica con otras

unidades oceánicas de Colombia permiten proponer dicho escenario tectónico en el margen de los Andes del Norte durante el Triásico. Los granitos localizados en el margen occidental de la Unidad Peltetec tienen afinidad peraluminosa y son clasificados como granitos Tipo-S, con una edad U-Pb de 228.2 ± 0.8 Ma. Estos granitos se interpretan por tanto como el resultado de anatexis de la corteza continental debido a flujo de calor asociado al mismo evento extensional que originó la cuenca de retro-arco y la ofiolita.

La ofiolita Peltetec sufrió dos eventos metamórficos: (i) metamorfismo de fondo oceánico durante la formación de la corteza oceánica en una cuenca de retro-arco, en condiciones de facies de anfibolita a baja presión; (ii) metamorfismo prógrado alcanzando facies de esquisto verde con un gradiente P/T intermedio (barroviano). El primer evento metamórfico ocurrió en condiciones de deformación estática, sin mostrar deformación significativa. Durante este evento, la plagioclasa recristalizó y los piroxenos fueron reemplazados por hornblenda. El segundo evento metamórfico produjo esquistos verdes foliados, con una asociación mineral de actinolita + clorita + albita + epidota + titanita ± fengita representativa de las condiciones del pico metamórfico, el cual se desarrolló durante el cierre de la cuenca de retro-arco y emplazamiento de la unidad sobre el margen continental en el Triásico tardío. La secuencia sedimentaria Guamote de edad Jurásico-Cretácico limita con la Unidad Peltetec al occidente y localmente al este, tiene un clivaje penetrativo que deforma la estratificación y una débil foliación diagenética. La deformación es similar en la Unidad Maguazo localizada al este de la Unidad Peltetec, lo que sugiere un evento común de deformación para las unidades Maguazo y Guamote, relacionado con el cierre de cuencas marginales en el Cretácico. Eventos tardíos asociados a la actividad esencialmente transcurrente de la zona de falla/cizalla Peltetec produjeron el desplazamiento y mezcla de bloques, caracterizados por una estructura cataclástica/milonítica sin recristalización diferenciable.

Por otro lado, el Complejo Ultramáfico-Máfico Tampanchi (TUMC por sus siglas en inglés), localizado en la parte central de la Cordillera Real es un cuerpo intrusivo de forma ovalada (6 km x 3 km) emplazado en rocas metavolcánicas y secuencias metavolcano-sedimentarias de edad Cretácica (Alao). Nuevos datos de campo, geoquímica de roca total de elementos mayores, traza y relaciones isotópicas de Nd y Sr, química mineral y dataciones U-Th-Pb en circones han permitido determinar la naturaleza del magma parental, las condiciones físicas de emplazamiento y cristalización y el ambiente tectónico y edad de formación del TUMC. El cuerpo intrusivo está conformado por wehrlita y clinopiroxenita con olivino y hornblenda, las cuales están cortadas por gabros hornbléndicos y diques/venas de leucodiorita y granito. Las hornblenditas se formaron

principalmente en el contacto entre clinopiroxenita con olivino y hornblenda y los gabros hornbléndicos. A escala local la transición de clinopiroxenita con olivino y hornblenda, hornblendita y gabro hornbléndico evidencian un proceso de reacción-reemplazamiento de olivino y piroxeno por anfíbol en las piroxenitas, la que produce hornblenditas durante la intrusión del gabro hornbléndico. Los datos geoquímicos de la wehrlita y piroxenita definen un patrón de acumulación con fraccionamiento dominante de olivino y clinopiroxeno, mientras que un segundo patrón está definido por los gabros hornbléndicos, los cuales se diferencian a rocas leucocráticas (leucodiorita y granito; líquido residual) con anfíbol como la fase dominante cristalizada. Los minerales principales son olivino (Fo= 75-91), clinopiroxeno (diópsido, Mg# = 0.84-0.97), anfíbol (pargasita, magnesio-hastingsita, magnesio-ferri-hornblenda y magnesio-hornblenda), plagioclasa (principalmente bytownita con zonación normal a andesina y oligoclasa), y en menor proporción espinela crómica, feldespato alcalino, mica, cuarzo y óxidos de Fe-Ti. Comparadas con la composición del condrito, todas las litologías muestran enriquecimiento de las tierras raras ligeras (LREE) con respecto a las tierras raras pesadas (HREE), enriquecimiento en (LILE), anomalía negativa de los HFSE (Nb, Zr, Ti) y P, y enriquecimiento en Pb, Sr, y Ba, con respecto al manto primitivo, indicando líquidos parentales relacionados a una zona de subducción. Las estimaciones termobarométricas en base a la composición mineral sugieren un emplazamiento y cristalización a niveles intermedios a superficiales de la corteza continental (2.2-5 kbar; ~3.6 kbar), con condiciones de fugacidad de oxígeno sobre el tampón NNO (ΔNNO = 0-2), indicando un magma relativamente oxidado. La composición isotópica sugiere una fuente mantélica uniforme metasomatizada por componentes corticales en la zona de subducción. Las edades U-Th-Pb en circones indican que la cristalización ocurrió entre 75.1 ± 0.2 y 76.0 ± 0.4 Ma. La estructura interna, la afinidad calco-alcalina y la ausencia de dunita y escasez de wehrlita impiden clasificar a TUMC como un típico complejo tipo Alaska, siendo considerado como una cámara magmática relacionada con vulcanismo de la zona de subducción. Estos resultados confirman la actividad magmática en el margen continental de Sudamérica durante el Cretácico tardío, resultado de una zona de subducción inclinada hacia el este, previa a la acreción del plateau oceánico Ecuatoriano-Colombiano-Caribeño (POECC).

Los Complejos de Peltetec y Tampanchi evidencian una larga historia de subducción en la margen occidental de los Andes del Norte, y variaciones en el régimen tectónico con períodos extensionales y compresivos. La ofiolita Peltetec muestra la apertura de una cuenca de retro-arco en el Triásico tardío, con metamorfismo de fondo oceánico y un segundo evento relacionado a un régimen compresivo, asociado a su emplazamiento sobre

el margen continental. El complejo Tampanchi confirma que el sistema de subducción oceánica inclinada al este y magmatismo asociado en la Cordillera Real permaneció activo hasta, al menos, 75 Ma, previo a la acreción del POECC.

Resumen

Capítulo 1

Introducción

1 Introducción

El origen de la Cordillera de los Andes está relacionado con un sistema de subducción Mesozoico-Cenozoico desde el Océano Pacífico debajo del margen occidental de Sudamérica. La geodinámica actual de los Andes del Norte está controlada por la subducción de las placas Nazca, Cocos y Caribe (litosferas oceánicas) debajo de la placa Sudamericana (litosfera continental). Los mayores rasgos morfológicos corresponden a cordilleras subparalelas separadas por depresiones topográficas. En el territorio de Ecuador se encuentran las Cordilleras Occidental y Real (Oriental), separadas por el Valle Interandino, mientras que en Colombia corresponden a las Cordilleras Occidental, Central y Oriental separadas por los valles Cauca-Patía y Magdalena, respectivamente. Hacia el este de las cordilleras se encuentra la cuenca de antepaís y al oeste una planicie costera (Figura 1.1).

Además de la subducción actual en los Andes del Norte, se registran en el margen múltiples fases de extensión y compresión con subducción y magmatismo asociados al menos desde el Triásico tardío (Litherland et al., 1994; Ramos, 1999; Restrepo et al., 1991; Spikings et al., 2015). En esta región, además del magmatismo, se registran procesos de adelgazamiento cortical, colisión, levantamiento, erosión y sedimentación, por lo que la misma constituye un excelente laboratorio natural para el estudio de los procesos tectónicos y geodinámicos relacionados con la evolución del margen Noroccidental de Gondwana (Sudamérica a partir del Cretácico Inferior, cuando se desgajó de Gondwana al abrirse el Atlático Sur) y con los márgenes activos de tipo andino en general.

La presente investigación aborda el estudio de dos complejos caracterizados por rocas máficas – ultramáficas, con variable grado de deformación y metamorfismo. Por un lado, el Cinturón ofiolítico Peltetec, formado en un ambiente oceánico (generación de litosfera oceánica) y por otro el Complejo ultrámáfico-máfico Tampanchi, que representa una intrusión de magmas básicos relacionados con la zona de subducción en la corteza continental. Están ubicados al occidente y centro de la Cordillera Real, respectivamente (Figura 1.1). Ambos complejos presentan características distintivas asociados a diferentes procesos de generación y emplazamiento, por lo que su estudio permite no solo su caracterización, sino también discernir la evolución tectónica del margen.

1.1 Ofiolitas

Los restos de litosfera oceánica que se han emplazado tectónicamente en la corteza continental o en arcos volcánicos en el contexto de márgenes de placa activos son llamados ofiolitas. Estos complejos geológicos constituyen un indicador importante no solo

para los procesos geodinámicos de formación de litosfera oceánica, sino también para los relacionados con subducción y obducción, marcando los eventos de colisión y suturas entre terrenos acrecionados. Su estudio a partir de observaciones de campo, características petrográficas, geoquímicas y de edad contribuye a establecer la naturaleza y las condiciones de su emplazamiento, permitiendo entender la evolución geodinámica de una zona particular y su correlación a nivel regional.

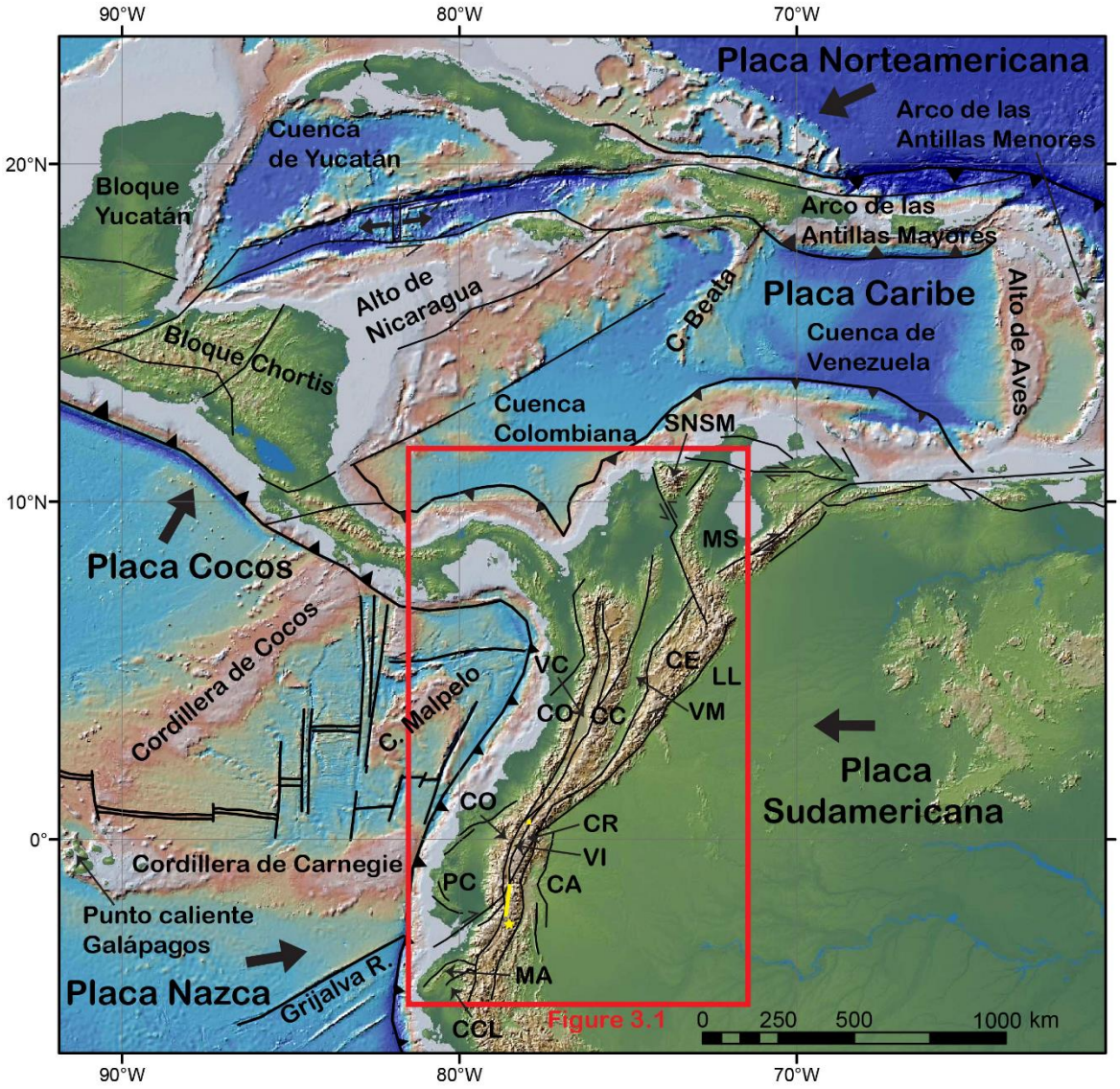

Figura 1.1. Marco geodinámico del Noroeste de Sudamérica y el Caribe. Se muestra los límites de placa, las fallas principales, cordilleras y zonas geomorfológicas. Mapa base modificado de Global Multi-Resolution Topography Data Synthesis (www.gmrt.org). CA: Cuenca de antepaís Oriente; CC: Cordillera Central; CCL: Cuenca Celica-Lancones; CE: Cordillera del Este (Oriental); CO: Cordillera Occidental; LL: Cuenca de antepaís Llanos Orientales; MA: Macizo Amotape (Complejo metamórfico El Oro); MS: Macizo de Santander; PC: Planicie de la Costa; SNSM: Sierra Nevada de Santa Marta; VC: Valle de Cauca-Patía; VI: Valle Interandino; VM: Valle de Magdalena; (Modificado de Luzieux et al., 2006). Se muestra en amarillo la ubicación de los complejos objeto de estudio.

La secuencia seudoestratigráfica tradicional generalizada de una ofiolita tipo “Penrose” consiste de base a techo de tectonitas (peridotita del manto superior), gabros estratificados a isotrópicos, complejo de diques paralelos, lavas almohadilladas y una fina cobertura de sedimentos pelágicos (Anonymous, 1972). El modelo original de su formación asociado a dorsales mediooceánicas fue cuestionado luego de observar características geoquímicas similares entre lavas de Troodos y rocas volcánicas del arco de Izu-Bonin al sur de Japón (Miyashiro, 1973), a partir de lo cual se identificaron estructuras de corteza oceánica con composición geoquímica que indica influencia de zonas de subducción, proponiéndose por tanto la existencia de centros de expansión con formación de ofiolitas ubicados en posición de tras-arco, intra arco o ante-arco (p.e. Pearce, 2003). Futuras contribuciones han identificado y asociado repetidamente a zonas de suprasubducción como sitios comunes para la formación de ofiolitas (p.e. Dilek and Furnes, 2014 y sus referencias). Las ofiolitas de suprasubducción indican un enriquecimiento metasomático del manto por componentes derivados de la placa subducida, lo que les confiere características geoquímicas particulares a los magmas derivados. En cambio, las ofiolitas no relacionadas con zonas de subducción corresponden al desarrollo de litosfera oceánica influenciada por una pluma, o se caracterizan por fusión parcial de un manto litosférico empobrecido en un ambiente “normal” mediooceánico o en un margen continental (p.e. Dilek and Furnes, 2014; Pearce, 2014).

1.2 Complejos ultramáficos-máficos

Los complejos ultramáfico-máficos no asociados a centros de expansión litosférica pueden ocurrir como cuerpos volcánicos o plutónicos en cinturones de rocas verdes Arcaicos y Proterozoicos (p.e. afinidad komatiitica, afinidad toleítica y anortositas), intrusiones intra-cratónicas (p.e. intrusiones máficas estratificadas) o cuerpos orogénicos relacionados con zonas de subducción (p.e. arco de islas o continental, complejos zonados tipo Urales-Alaska, cumulados en cámaras magmáticas).

Las grandes intrusiones máficas estratificadas comúnmente expuestas en cratones constituyen grandes cámaras magmáticas y han sido correlacionadas con plumas mantélicas. Un aspecto importante de su estudio viene dado por su interés para la exploración de cromititas, elementos del grupo del platino (EGP), Ni, Fe, Cu, Ti y V (p.e. Li et al., 2003; Naldrett, 1999, 2005; Song et al., 2011; Wang et al., 2011). En cambio, los complejos tipo Urales-Alaska son considerados un tipo particular de intrusiones debido a su entorno tectónico (margen de placa convergente), tamaño (intrusiones pequeñas), composición mineralógica (olivino, clinopiroxeno, anfíbol, magnetita), estructura interna concéntrica zonada (dunita-wehrlita, clinopiroxenita olivínica, clinopiroxenita,

clinopiroxenita hornbléndica, hornblendita, y gabros) y mineralización asociada (Ti-V magnetita, EGP) (Himmelberg and Loney, 1995). Su origen se ha relacionado con cumulados fraccionados a partir de magmas basálticos sub-alcalinos hidratados asociados a zonas de subducción, con reservorios a niveles medios de la corteza o en las raíces de los arcos volcánicos (Murray, 1972; De Bari and Coleman, 1986; Himmelberg and Loney, 1995). Por otro lado, repetidamente se han identificado pequeñas intrusiones con asociaciones ultramáficas-máficas de origen cumulático relacionadas con la evolución del magmatismo en entornos de arco, no necesariamente zonados y/o sin zonación concéntrica, y potencialmente asociadas con los reservorios y conductos del volcanismo (p.e. Morris et al., 2019; Xu et al., 2019; Wang et al., 2019), lo cual permite entender la evolución del magmatismo y construcción de los arcos volcánicos.

Capítulo 2

Objetivos y estructura de la tesis

2 Objetivos y estructura de la tesis

Esta tesis doctoral se titula "*Petrogenesis and age of the Peltetec Ophiolitic belt and the Tampanchi ultramafic-mafic complex, Cordillera Real (Ecuador): Geodynamic implications for the evolution of the Andean active margin*". El objetivo principal se enfoca en dilucidar la geodinámica de un segmento del margen activo en los Andes del Norte a través del estudio de la naturaleza geológica, contexto geodinámico de formación y emplazamiento de las rocas máficas – ultramáficas aflorantes en las zonas de Peltetec y Tampanchi mediante un estudio petrogenético. Para cumplir con este propósito este trabajo aporta nuevos datos de relaciones de campo, características estructurales, texturales y asociaciones mineralógicas y geoquímica de roca total, presentando por primera vez datos de química mineral, estimaciones termobarométricas, geoquímica isotópica de roca total y geocronología U-Th-Pb en circones de los complejos estudiados.

El manuscrito incluye un Resumen (en español e inglés), Introducción y Geología de los Andes del Norte (español), Muestreo y métodos analíticos (inglés), tres capítulos (Capítulo 5, Capítulo 6, Capítulo 7) que presentan los principales resultados obtenidos en la investigación (inglés), Discusión General y Conclusiones (español). Debido a que los capítulos tratan los mismos complejos, un cierto grado de repetición fue inevitable, especialmente en las descripciones geológicas. De los resultados de la tesis, el Capítulo 5 ha sido publicado en *International Geology Review*, y los Capítulos 6 y 7 serán sometidos para su publicación próximamente en revistas de impacto.

El Capítulo 5, "*The Peltetec ophiolitic belt (Ecuador): A window to the tectonic evolution of the Triassic margin of western Gondwana*" presenta las relaciones de campo, descripción petrográfica, geoquímica elemental e isotópica de roca total y geocronología U-Th-Pb en circones de la Unidad Peltetec. Se presenta un modelo petrogenético para esta unidad y para las litologías asociadas. Los datos se correlacionan con otras unidades en los Andes del Norte para ofrecer una visión geodinámica regional integrada.

El Capítulo 6, "*Metamorphism and deformation of the Peltetec belt*" presenta la caracterización de la deformación y metamorfismo a través de nuevos datos de campo, descripciones microscópicas, geoquímica de roca total de elementos mayores y química mineral. A partir de estos resultados se determinan las condiciones metamórficas de las rocas mediante el método "average P-T" con el programa THERMOCAL 3.33 (Holland and Powel, 1998; utilizando la base de datos termodinámica internamente consistente tc-ds55 de noviembre 2003) y proyecciones P-T isoquímicas utilizando el programa PERPLE_X

(Connolly, 1990, 2005; version 6.9.0). Los resultados permiten proponer un modelo tectónico en el que se contextualiza los eventos metamórficos sufridos por este complejo.

El Capítulo 7, "*The Tampanchi ultramafic-mafic complex (Ecuador): Origin, magmatic differentiation and age*" presenta nuevos datos de campo, caracterización textural y petrográfica, química mineral, geoquímica de roca total de elementos mayores, trazas e isótopos de Sr y Nd, y geocronología U-Th-Pb en circones del complejo ultramáfico-máfico Tampanchi. Se presentan estimaciones termobarométricas, modelo petrogenético y su implicación en la geodinámica regional en los Andes del Norte.

El Capítulo 8 presenta una discusión y conclusiones generales, abordando por separado cada complejo.

Capítulo 3

Geología de los Andes del Norte

3 Geología de los Andes del Norte

El margen occidental de Gondwana (preapertura del Atlántico Sur en el Cretácico Inferior) o Sudamérica (post-Cretácico Inferior) presenta una continua y prolongada historia de subducción y magmatismo desde el Paleozoico hasta la actualidad (e.g. Ramos et a., 2009; Spikings et al., 2015; Pepper et al., 2016). El sistema orogénico localizado al norte del paralelo 5°S se conoce como los Andes del Norte, una región en la que se exponen litologías formadas en diferentes ambientes y edades. La variación en el régimen subductivo ha provocado períodos extensionales y compresionales en el margen activo, con la apertura y cierre de cuencas marginales (Blanco-Quintero et al., 2014; Cochrane et al., 2014a; Spikings et al., 2015; Zapata et a., 2019; Cardona et al., 2020), además de eventos caracterizados por la colisión/acreción de terrenos (Eguez, 1986; Litherland et al., 1994; Luzieux et al., 2006; Vallejo et al., 2009; Montes et al., 2012).

Las rocas más antiguas expuestas en los Andes del Norte corresponden al basamento cristalino Meso- Neoproterozoico, que se reconoce en los Andes de Colombia conformado por rocas metamórficas de la parte alta de la facies de anfibolita a granulita (Kroonemberg, 1982). Incluye los macizos de Garzón y Santander en la Cordillera Oriental de Colombia, los macizos Las Minas y San Lucas en la Cordillera Central y los macizos de Santa Marta y la Guajira en el Norte (Figura 3.1, e.g. Kroonemberg, 1982; Cardona et al., 2010; Ibañez-Mejía, 2020). En Ecuador se ha asignado al Neoproterozoico a gabros localizados la zona de falla Peltetec (Spikings et al., 2021) y varios techos colgantes (“roof pendant”) entre batolitos jurásicos del sur de Ecuador, aunque éstos últimos no se han confirmado (Eguez et al., 2017).

Rocas cristalinas paleozoicas se han reportado en el margen Occidental de la Cordillera Central y en el Macizo de Santander, las cuales corresponden a cuerpos dispersos de gneises de edad Ordovícico (e.g., Vinasco et al., 2006; Martens et al., 2014; Villagómez et al., 2011; Mantilla-Figueroa et al., 2012). En cambio, gran parte del núcleo de las Cordilleras Central y Real y del Complejo Metamórfico el Oro (Macizo Amotape, Ecuador) y el Macizo de Santander (Colombia) están conformados por rocas metasedimentarias paleozoicas, las cuales corresponden a secuencias semipelíticas de cuarcitas y filitas, metalimolitas, esquistos grafíticos y raramente metagrauvacas, que en Ecuador se les asigna una edad de Devónico-Carbonifero y han sido interpretadas como una cuenca intra-cratónica, margen pasivo o una cuenca de tras-arco (Litherland et al., 1994; Chew et al., 2007; Spikings et al., 2021). Este grupo de rocas son intruíadas por plutones datados desde el Pérmico al Paleógeno y albergan también para- y orto- gneises y migmatitas del Triásico (Figura 3.1).

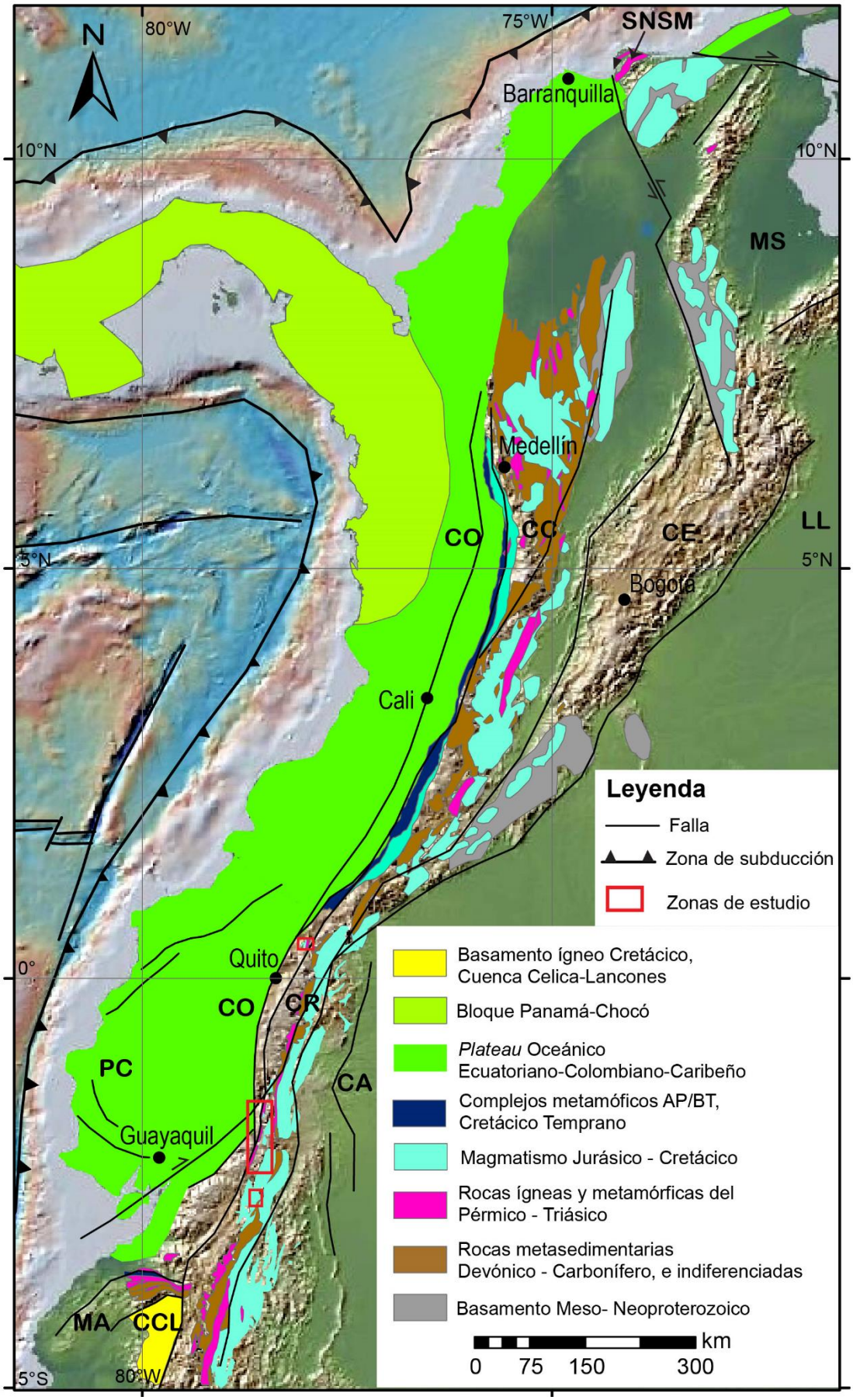
N
80°W
75°W
SNSM
Barranquilla
10°N
10°N
MS
Medellín
CO
CC
CE
LL
5°N
5°N
Bogotá
Cali
Quito
0°
CO
CR
PC
CA
Guayaquil
MA
CCL
5°S
80°W
Leyenda
Falla
Zona de subducción
Zonas de estudio
Basamento ígneo Cretácico, Cuenca Celica-Lancones
Bloque Panamá-Chocó
Plateau Oceánico Ecuatoriano-Colombiano-Caribeño
Complejos metamóficos AP/BT, Cretácico Temprano
Magmatismo Jurásico - Cretácico
Rocas ígneas y metamórficas del Pérmico - Triásico
Rocas metasedimentarias Devónico - Carbonífero, e indiferenciadas
Basamento Meso- Neoproterozoico
km
0 75 150 300

Figura 3.1. (Página anterior). Representación esquemática de los principales grupos litológicos del basamento de los Andes del Norte. Se muestran las fallas regionales y principales estructuras geomorfológicas. Mapa base modificado de Global Multi-Resolution Topography Data Synthesis (www.gmrt.org). AP/BT: metamorfismo de alta presión y baja temperatura; CA: Cuenca de antepaís Oriente; CC: Cordillera Central; CCL: Cuenca Celica-Lancones; CE: Cordillera del Este (Oriental); CO: Cordillera Occidental; LL: Cuenca de antepaís Llanos Orientales; MA: Macizo Amotape (Complejo Metamórfico El Oro); MS: Macizo de Santander; PC: Planicie de la Costa; SNSM: Sierra Nevada de Santa Marta. Se muestra en rojo la ubicación de las zonas de estudio. (según John et al., 2010; Riel et al., 2013; Spikings et al., 2015; Bustamante et al., 2016; Eguez et al., 2017; Zapata et al., 2019; Vallejo et al., 2019; Cardona et al., 2020; Ibañez-Mejía, 2020; Spikings et al., 2019; Rodriguez-García et al., 2019, 2020; Spikings et al., 2021).

Las litologías de edad Pérmica son rocas intrusivas variablemente deformadas y metamorfizadas. Han sido reconocidas en Colombia a lo largo de la Cordillera Central, en la Península de la Guajira y en la Sierra Nevada de Santa Marta. Son dominantemente de composición ácida, tienen afinidad cálcica a alcalino-cálcica con variación entre metaluminosas y peraluminosas, y han sido interpretadas como intrusiones de arco continental (e.g. Ordoñez-Carmona and Pimentel, 2002; Cardona et al., 2010; Villagomez et al., 2011; Cochrane et al., 2014a; Piraquive, 2017; Spikings et al., 2019; Rodriguez-García et al., 2019). En Ecuador solamente se ha reportado una edad Pérmica en un leucosoma de una migamatita cartografiada previamente como Triásico tardío (Paul et al., 2018).

Durante el Triásico se formaron litologías de diferente composición y entorno tectónico. Las rocas Triásicas como granitoides, para- y orto- gneises y migmatitas (~250 Ma a ~ 210 Ma) son dominantemente del Triásico tardío. En Colombia se identifican en la Cordillera Central incluidas en el Complejo Cajamarca y en la Sierra Nevada de Santa Marta (Cardona et al., 2010; Montes et al., 2010; Weber et al., 2010; Villagomez et al., 2011; Restrepo et al., 2011; Cochrane et al., 2014a; Martens et al., 2014; Bustamante et al., 2017, Piraquive, 2017). En Ecuador aparecen como un cinturón semi continuo de dirección NNE – SSW a lo largo de toda la Cordillera Real conocidas como Unidades Tres Lagunas y Sabanilla y en el Complejo Metamórfico El Oro como Complejo Moromoro (Aspden et al., 1995; Litherland et al., 1994; Noble et al., 1997; Cochrane et al., 2014a; Riel et al., 2013; Paul et al., 2018). Los granitodides tienen una afinidad peralumiosa de tipo-S con un origen asociado con anatexis en un ambiente extensional (e.g. Litherland et al., 1994; Riel et al., 2013; Cochrane et al., 2014a; Spikings et al., 2015).

Así mismo, son identificados varios complejos máficos de edad Triásico tardío (~240 Ma a ~216 Ma) y afinidad oceánica, los cuales presentan variable grado de deformación y

metamorfismo. En Colombia corresponden al Complejo Aburrá (ofiolita Aburrá; Correa-Martinez, 2007; Restrepo, 2008; García-Casco et al., 2020; Ibañez-Mejia et al., 2020) y el stock de Chinchina (Cochrane et al., 2014a) en la Cordillera Central, y en Ecuador a las anfibolitas de la Unidad Monte Olivo en la Cordillera Real y de la Unidad Piedras en el Complejo Metamórfico El Oro (e.g. Cochrane et al., 2014a). Las características geoquímicas indican una afinidad oceánica en un ambiente de tras-arco o ante-arco (Apsden et al., 1995; Correa-Martinez, 2007; Restrepo, 2008; Riel et al., 2013; Cochrane et al., 2014a; Ibañez-Mejía et al., 2020), mientras que esquistos azules de la Unidad Arenillas-Panupali (Complejo Metamórfico El Oro), con una afinidad de basaltos de dorsal medio oceánica (MORB, por sus siglas en ingles), presentan una edad de enfriamiento ($^{40}Ar/^{39}Ar$ en hornblenda) de 226 Ma, interpretada como la edad de emplazamiento tectónico (Gabriele, 2002). En el suroriente ecuatoriano se ha identificado una secuencia no deformada de lavas basálticas a dacíticas y volcanosedimentos continentales/marinos (Unidades Piuntza y Pachicutza) que están cortados y skarnificados por intrusiones del Jurásico (e.g. Litherland et al., 1994; PRODEMINCA, 2000; Villares et al., 2014), siendo asignados potencialmente una edad Triásico superior (Noriense; Litherland et al., 1994).

El magmatismo de arco Jurásico - Cretácico temprano (~200 Ma a ~129 Ma) se extiende ampliamente a lo largo de los Andes de Norte (Figura 3.1), tanto en la Cordillera Central (Bustamante et al., 2010, Villagomez et al., 2011; Bustamante et al., 2016; Rodriguez-García et al., 2020), Sierra Nevada de Santa Marta (Leal-Mejía, 2011), Macizo de Santander (Mantilla-Figueroa et al., 2013; Van der Lelij et al., 2016), Cordillera Real y zona sub-Andina de Ecuador (Lihterland et al., 1994; Romeuf et al. 1995; PRODEMINCA, 2000; Spikings et al. 2001; Chiaradia et al., 2009; Drobe et al., 2013; Cochrane et al., 2014b; Spikings et al., 2015). Se caracterizan por intrusiones de compoción diorítica a granítica y por volcanismo dominantemente andesítico a riolítico. Geoquímicamente tienen carácter metaluminoso, con intrusiones cordilleranas cálcicas a alcalino-cálcicas de tipo-I y volcanismo calco-alcalino, en ambos casos asociados a un arco continental (e.g. Aspden et al., 1992; Litherland et al., 1994; Spikings et al., 2015; Bustamente et al., 2016), mientras que hacia la cuenca de antepaís se conservan los productos volcano-sedimentarios no metamorfizados (e.g. Tschopp, 1953; Aspden and Litherland, 1992; Litherland et al., 1994). Las características geoquímicas de las rocas magmáticas muestran un cambio progresivo con el tiempo, siendo las rocas más recientes isotópicamente más juveniles y geoquímicamente más empobrecidas en elementos incompatibles que las más antiguas (Cochrane et al., 2014b; Spikings et al., 2015; Bustamante et al., 2016), aunque sin una clara distribución latitudinal o longitudinal (e.g. Bustamante et al., 2016). Al occidente del cinturón Jurásico principal existen intrusiones granodioríticas a graníticas del Jurásico

tardío al Cretácico, además de depósitos volcánicos principalmente basálticos y andesíticos y volcanosedimentarios de cuenca marginal. Tienen variable grado de deformación y metamorfismo alcanzando hasta facies de anfibolita (Litherland et al., 1994; Noble et al., 1997; Blanco-Quintero et al., 2014; Cochrane et al., 2014b; Bustamante et al., 2016), aunque también se ha sugerido condiciones de alta presión (Massone and Toulkeridis, 2012).

Durante el Cretácico temprano las rocas volcánicas, plutónicas y sedimentarias localizadas en la parte central y occidental de la Cordillera Central y Real documentan una fase extensional, caracterizada por el relleno de cuencas y magmatismo activo con características geoquímicas compatibles con una corteza continental adelgazada (e.g. Cochrane et al., 2014b; Spikings et al., 2015; Zapata et al., 2019; Cardona et al., 2020), con el posterior cierre de las cuencas en el Cretácico tardío (Spikings et al., 2015; Zapata et al., 2019; Cardona et al., 2020). Las litologías son asignadas en Colombia a la Formación Abejorral y el Complejo Quebradagrande (e.g. Jaramillo et al., 2017; Zapata et al., 2019; Cochrane et al., 2014b; Villagomez et al., 2011), y en Ecuador la secuencia sedimentaria Guamote y el arco Alao (Unidades Maguazo, Alao Paute y El Pan) (Litehrland et al., 1994; Cochrane et al., 2014b; Spikings et al., 2015). La Formación Abejorral y la secuencia sedimentaria Guamote corresponden a secuencias siliciclásticas depositadas sobre el basamento continental. Se ha asignado un rango de depósito de 150 - 100 Ma para la Formación Abejorral (e.g. Zapata et al., 2019) mientras que para la secuencia metasedimentaria Guamote se ha estimado una edad deposicional máxima de 163.7 ± 1.6 Ma (Cochrane et al., 2014b). El Complejo Quebradagrande incluye litologías volcánicas y sedimentarias asignadas al Cretácico tardío (Zapata et al., 2019; Cardona et al., 2020). En cambio, la Unidad Alao–Paute está constituida por rocas metavolcánicas con afinidades toleíticas y calco-alcalinas y rocas metavolcanoclásticas (Litherland et al., 1994; Cochrane et a., 2014b; Yanez et al., 2017) de las cuales no se han obtenido edades precisas (edades K/Ar (hornblenda) de 115 ±12 Ma y 142 ± 36 Ma; Litherland et al., 1994). Por otro lado, las Unidades El Pan y Maguazo corresponden a secuencias volcanosedimentarias sin metamorfismo (Unidad Maguazo) o débilmente metamórficas (facies de esquistos verdes, Unidad El Pan). El magmatismo en el Cretácico tardío está representado además por una serie de intrusiones distribuidas en la Cordilleras Central y Real con composiciones desde básica a ácida y con edades de 100 a 75 Ma (e.g. Kennerley, 1980, Litherland et al., 1994; Ibañez-Mejía et al., 2007; Villagomez et al., 2011; Cochrane, 2013; Jaramillo et al., 2017; Zapata et al., 2019; Cardona et al., 2020; este estudio). Entre estas destaca el Complejo ultramáfico–máfico Tampanchi, el cual intruye a la Unidad Alao-Paute y ha sido

caracterizado nominalmente como un cuerpo intrusivo calco-alcalino tipo Urales-Alaska (Pozo, 1990; Litherland et al., 1994).

En el borde occidental de la Cordillera Central a lo largo del sistema de fallas Romeral, y en el Complejo Metamórfico El Oro se localizan los complejos metamórficos de alta presión y baja temperatura de Arquía y Raspas, respectivamente (Figura 3.1). El Complejo Arquía tienen afinidad NMORB (Villagomez et al., 2011; Bustamante et al., 2012; Ruiz-Jimenez et al., 2012), mientras que en el Complejo Raspas los protolitos corresponden a litosfera oceánica de afinidad NMORB y montes submarinos (John et al., 2010). Las edades de metamorfismo tienen un rango entre 130 a 120 Ma (e.g. Feininger, 1980; Bosch et al., 2002; John et al., 2010; García-Ramírez et al., 2017). En cambio, en la Cordillera Real, en similar posición estructural en la sección central y norte de Ecuador y a lo largo de la zona de falla Peltetec, se ubica la Unidad Peltetec. Está constituida por rocas ultramáficas, máficas y sedimentarias recristalizadas en condiciones de facies de esquistos verdes, y ha sido interpretada como una mélange de rocas de una secuencia ofiolítica desmembrada (Aspden y Litherland, 1992; Litherland et al., 1994). Nominalmente, la edad Cretácica de ~134 Ma ($^{40}Ar/^{39}Ar$ en plagioclasa) se ha interpretado como edad de enfriamiento magmático (Spikings et al., 2015).

Por otro lado, el basamento de la Cordillera Occidental y de la planice de la Costa del Pácifico es conocido en los Andes del Norte como bloques Calima y Panamá-Chocó en Colombia y Piñón-Pallatanga en Ecuador. Estos bloques corresponden a material alóctono constituido principalmente por rocas máficas con afinidades de plateau oceánico, tienen edades que varían entre ~140 a 87 Ma y se ha propuesto su acreción en el Mezosoico tardío (Figura 3.1; e.g. Kerr et al., 2002; Hoernle et al., 2004; Vallejo et al., 2009). También incluyen rocas con afinidad de arco y con edades que varían entre 99-79 Ma (e.g. Vallejo et al., 2006; Whattam and Stern, 2015; Macías-Mosquera and Rojas-Agramonte, 2019), las cuales son interpretadas como resultado de subducción bajo el plateau oceánico previo a su acreción (Vallejo et al., 2009). En Colombia el límite de este plateau acrecionado con el paleo-margen continental es a través del Sistema de Fallas Romeral (Chicangana, 2005), mientras que en Ecuador es a través del Sistema de Fallas Calacalí-Pujilí (Hughes and Pilatasig, 2002).

Otra ocurrencia con afinidad oceánica corresponden a parte del basamento de la Cuenca Cretácica Celica-Lancones en el Suroeste de Ecuador, la cual está cubierta por secuencias volcanosedimentarias (Jaillard et al., 1996; Winter et al., 2010).

Capítulo 4

Sample and analytical methods

4 Sample and analytical methods

For the study of the Peltetec and adjacent units, fieldwork and sampling were carried out along several W-E transects perpendicular to the trend of the Peltetec Unit from the Ambuquí sector in the North to the Zula River in the South (Figures 5.1). The geological sections from north to south correspond to the sectors: Ambuqui, Patate, Penipe, Quimiag, Chambo, Alao valley, Guarguallá valley, Cebadas and Zula River. A total of 100 samples were collected for petrographic inspection, of which 70 correspond to the Peltetec Unit, 5 to the Tres Lagunas Unit, 7 to the Alao-Paute Unit, 10 to the Guamote sedimentary sequence and 8 to the Maguazo Unit. Mineral assemblages and textures were studied in 35 polished thin sections by transmitted light optical and electron microscopy.

A total of 90 samples were collected in the Tampanchi ultramafic-mafic complex (TUMC) and adjacent units, 60 correspond to TUMC and 30 to the country rocks (13 samples from the Alao–Paute Unit and 17 from El Pan Unit). The petrographic/mineralogical study was carried out on 30 polished thin sections by transmitted and reflected light optical and electron microscopy.

4.1 Sample preparation

The samples were prepared in the laboratory of the Department of Mineralogy and Petrology of the University of Granada using a diamond disc cutter to remove the weathered surfaces and secondary veins. Fragments were crushed to powder using a tungsten carbide mill.

All elemental and isotopic analyses were carried out in the IBERSIMS Laboratory and the Centre for Scientific Instrumentation of the University of Granada (CIC-UGR, Spain).

4.2 Electron Micro Probe Analysis (EMPA)

Major element mineral analyses were obtained using a CAMECA SX-100 electron microprobe operated at 20 kV acceleration voltage and 20 nA beam current with a beam diameter of 5 µm. Amphibole composition was normalized to 23 oxygens (Fe^{3+} and cation distribution follow the method of Schumacher, in Hawthorne et al., 2012), H_2O was calculated by stoichiometry and the classification follows the scheme of Hawthorne et al. (2012). Pyroxene, titanite, olivine, spinel, pumpellyite, magnetite and ilmenite were normalized to 6, 5, 4, 4, 24.5, 4 and 3 oxygens, respectively, and Fe^{3+} was estimated by stoichiometry. Epidote, feldspar and rutile were normalized to 12.5, 8 and 2 oxygens respectively assuming Fe(total) = Fe^{3+}. Mica, chlorite and serpentine were normalized to 11, 28 and 7 oxygens respectively assuming Fe(total) = Fe^{2+}. The ratio Mg/(Mg+Fe^{2+}) is

abbreviated Mg#. Atoms per formula unit is abbreviated as apfu. The mineral and end-members abbreviations are from Whitney and Evans (2010) completed with the abbreviations of Hawthorne et al. (2012) for amphiboles.

Elemental X-ray maps (Si, Al, Ti, Fe, Mn, Mg, Ca, Na, K, P) were obtained in the same machine operated at 20 kv and 300 nA, with a beam diameter of 4 µm, a step size (pixel) of 6 µm, and counting time of 0.03 s/pixel. The X-ray maps, which consist of the X-ray signals of the elements or element ratios (color-coded; expressed in counts/nA/s), were processed with software DWImager (Torres-Roldán and Garcia Casco, unpublished). The images were clipped to show the mineral of interest and overlaid onto a gray-scale "Z" image calculated by the sum of the products of the counts by atomic number (Si, Ti, Al, Fe, Mn, Mg, Ca, Na, K, P), which contains the basic textural information of the scanned areas (see Garcia-Casco, 2007). The spot analyses were performed on points selected using the X-ray maps and in other representative areas and samples.

4.3 X-ray Fluorescence (XRF)

Thirty-one samples, including serpentinite (2 samples), metagabbroic rocks (4 samples), metadiabase dykes (4 samples), metabasaltic rocks (19 samples), and metasedimentary rocks (2 samples) were selected from the Peltetec Unit and 3 acid rocks from the Tres Lagunas Unit for whole-rock geochemical analyses. While, 25 samples were selected from the Tampanchi ultramafic-mafic complex, including wehrlite (1 sample), olivine-hornblende clinopyroxenite (7 samples), hornblendite (3 samples), fine-grained hornblende gabbro (4 samples), coarse-grained hornblende gabbro (6 samples), pegmatitic hornblende gabbro (2 samples) and leucocratic rocks (1 leucodiorite and 1 granite).

Major element oxides were determined with a Philips Magix Pro (Pw-2440) X-ray fluorescence (XRF) equipment after melting the sample in a solution with tetra lithium borate. The characteristic precision as determined from standards AN-G and BE-N, was better than ± 1,5 % (relative error) for an analyte concentration of 10 wt.% (see Table 4.1). The iron content is expressed as FeO* total. The molar ratio MgO/(MgO+FeO*) is abbreviated Mg#. Loss on Ignition (LOI) was determined by weight difference before and after ignition of samples in a furnace. In the diagrams, oxide concentrations are reported in an anhydrous (volatile free) basis.

Zirconium was determined in the same machine using the same glass beads with a precision better than ± 0.2% for a reference 5 ppm concentration of zirconium.

Table 4.1. XRF analyses of standards analyzed along with unknowns and quantitation limits (LoQ). Measured concentrations, actual concentrations and absolute errors are given for each standard.

id	Limit of Quantitation (LoQ) (wt.%)	AN-G			BE-N		
		Anal. Result	Real value	±	Anal. Result	Real value	±
SiO_2	0.2	46.78	46.3	0.48	38.68	38.2	0.48
Al_2O_3	0.06	30.32	29.8	0.52	10.07	10.07	0
Fe_2O_3	0.03	3.34	3.36	0.02	13.08	12.84	0.24
MnO	0.002	0.04	0.04	0	0.2	0.2	0
MgO	0.03	1.81	1.8	0.01	13.13	13.15	0.02
CaO	0.01	15.95	15.9	0.05	14.09	13.87	0.22
Na_2O	0.04	1.78	1.63	0.15	3.71	3.18	0.53
K_2O	0.01	0.12	0.13	0.01	1.49	1.39	0.1
TiO_2	0.01	0.2	0.22	0.02	2.58	2.61	0.03
P_2O_5	0.02	0.02	0.01	0.01	1.09	1.05	0.04
Zr (ppm)	5				260	249	11

4.4 Inductively Coupled Plasma Mass Spectrometry (ICP-MS)

Trace elements, except Zr, of the same samples analyzed by X-ray Fluorescence were analyzed by Inductively Coupled Plasma-Mass Spectrometry (ICP-MS) after HNO3 + HF digestion of 0.1000 g of sample powder in a Teflon- lined vessel at 180 °C and 200 psi for 30 min, evaporation to dryness and subsequent dissolution in 100 ml of 4 vol.% HNO3. The precision, as determined from standards PMS, WSE, UBN, BEN, BR and AGV run as unknowns, was better than ± 2% for analyte concentrations of 50 ppm and ± 5 % for analyte concentrations of 5 ppm (see Table 4.2).

4.5 Trace element modelling

For the Tampanchi ultramafic-mafic complex, the Rare Earth Elements (REE) modeling follows the fractional crystallization process (FC, Rayleigh fractionation). Mineral-liquid Kd values for amphibole are from Nandedkar et al. (2016); plagioclase, magnetite, and apatite from Paster et al. (1974); biotite from the compilation of Ersoy and Helvaci (2010); titanite from Tiepolo et al. (2002) and zircon from Fujimaki (1986).

Table 4.2. ICP-MS (Perkin Elmer NexION 300Q) analysis of standards analyzed along with unknowns and detection limits.

id	Detection limits (ppt)	PMS measured	PMS certified	WSE measured	WSE certified	UBN measured	UBN certified
Li	0.1-1	7.48	7.3	13.5	13.6	27	27
Rb	0.1-1	0.91	1	25	25	3.29	4
Cs	<0.1	0.52	0.35	0.59	0.5	10.1	10
Be	0.1-1	0.23	0.5	0.95	1.14	0.13	0.2
Sr	<0.1	271	280	405	410	7.34	9
Ba	0.1-1	142	148	330	338	25	27
Sc	1-10	34	34	27	28	13.3	13
V	0.1-1	192	192	335	340	65	75
Cr	1-10	320	314	108	99	2267	2300
Co	0.1-1	49	49	44	44	100	100
Ni	0.1-1	122	115	56	55	1983	2000
Cu	0.1-1	61	59	69	65	25	28
Zn	1-10	69	60	129	117	81	85
Ga	0.1-1	15.7	16	22	23	2.28	3
Y	<0.1	10.8	11	31	30.4	2.56	2.5
Nb	<0.1	2.07	2.6	15.9	18	0.15	0.14
Ta	<0.1	0.25	0.18	1.31	1.16	0.07	0.02
Mo	0.1-1	1.86	1.9	3.74	3.7	0.25	0.55
Sn	0.1-1	2.97	3	17.9	18	0.30	
Tl	<0.1	0.04	0.04	0.13	0.16	0.03	0.06
Pb	0.1-1	2.06	2.5	13.5	13.8	12.5	13
U	<0.1	0.01	0.03	0.63	0.65	0.07	0.07
Th	0.1-1	0.04	0.05	3.04	3	0.10	0.07
La	<0.1	2.74	2.8	26.2	27	0.37	0.35
Ce	<0.1	6.70	6.8	59.4	61	0.82	0.8
Pr	<0.1	1.03	1.08	7.67	7.8	0.12	0.12
Nd	0.1-1	5.34	5.5	32	33	0.61	0.6
Sm	0.1-1	1.75	1.75	8.46	8.8	0.19	0.2
Eu	<0.1	1.02	1.07	2.11	2.25	0.07	0.08
Gd	0.1-1	2.05	2	7.06	7.2	0.33	0.3
Tb	<0.1	0.34	0.36	1.10	1.1	0.07	0.06
Dy	0.1-1	1.93	2	5.92	6	0.39	0.38
Ho	<0.1	0.41	0.42	1.19	1.2	0.09	0.09
Er	0.1-1	1.09	1.1	2.87	3	0.27	0.28
Tm	<0.1	0.17	0.17	0.41	0.43	0.04	0.045
Yb	0.1-1	0.93	1	2.44	2.5	0.28	0.28
Lu	<0.1	0.15	0.15	0.36	0.37	0.04	0.045

Table 4.2. (Continued). ICP-MS (Perkin Elmer NexION 300Q) analysis of standards analyzed along with unknowns and detection limits.

id	Detection limits (ppt)	BEN measured	BEN certified	BR measured	BR certified	AGV measured	AGV certified
Li	0.1-1	12.4	13	14.2	13	11.0	12
Rb	0.1-1	47	47	47	47	68	67.3
Cs	<0.1	0.81	0.8	0.74	0.8	1.28	1.28
Be	0.1-1	1.90	1.9	1.61	1.5	2.20	2.1
Sr	<0.1	1370	1370	1323	1320	671	662
Ba	0.1-1	1001	1025	1054	1050	1213	1226
Sc	1-10	22	22	22	25	12.0	12.2
V	0.1-1	235	235	239	235	125	121
Cr	1-10	365	360	369	380	27	10.1
Co	0.1-1	61	60	58	52	15.4	15.3
Ni	0.1-1	264	267	260	260	17.4	16
Cu	0.1-1	73	72	72	72	58	60
Zn	1-10	133	133	171	160	95	88
Ga	0.1-1	18.2	17	17.9	19	21	20
Y	<0.1	28	30	28	30	19.1	20
Nb	<0.1	103	105	103	98	13.0	15
Ta	<0.1	5.68	6.2	6.12	6.2	0.88	0.9
Mo	0.1-1	2.78	2.8	2.45	2.4	2.29	2.7
Sn	0.1-1	1.89	2	2.27	2	4.31	4.2
Tl	<0.1	0.02	0.04	0.05	0.05	0.29	0.34
Pb	0.1-1	4.00	4	4.67	5	37	36
U	<0.1	2.37	2.4	2.44	2.5	1.96	1.92
Th	0.1-1	10.9	10.4	11.0	11	6.79	6.5
La	<0.1	81	82	81	82	39	38
Ce	<0.1	149	152	149	151	68	67
Pr	<0.1	16.8	17.5	17.1	17	8.31	7.6
Nd	0.1-1	64	67	66	65	33	33
Sm	0.1-1	12.0	12.2	12.1	12.2	6.00	5.9
Eu	<0.1	3.66	3.6	3.67	3.7	1.65	1.64
Gd	0.1-1	9.75	9.7	9.83	9.5	4.76	5
Tb	<0.1	1.40	1.3	1.40	1.25	0.74	0.7
Dy	0.1-1	6.14	6.4	6.03	6.4	3.54	3.6
Ho	<0.1	1.08	1.1	1.08	1.1	0.71	0.67
Er	0.1-1	2.28	2.5	2.42	2.5	1.72	1.7
Tm	<0.1	0.30	0.34	0.32	0.34	0.24	0.34
Yb	0.1-1	1.72	1.8	1.72	1.8	1.57	1.72
Lu	<0.1	0.23	0.24	0.24	0.25	0.25	0.27

4.6 U-Th-Pb zircon SHRIMP dating

For U-Th-Pb dating of the Peltetec Unit, zircon grains were obtained only from one sample of metadiabase (P-23), in addition to from the Tres Lagunas granite located at the western margin of the Peltetec ophiolite (sample P-26). For the Tampanchi ultramafic-mafic complex, zircons were separated from four samples including olivine-hornblende clinopyroxenite, fine-grained hornblende gabbro, leucodiorite and granite.

Zircon grains were separated using conventional density and magnetic techniques and handpicked under binocular lens. Once mounted and polished, zircon grains were studied by cathodoluminescence imaging and analyzed for U-Pb using a SHRIMP IIe/mc ion microprobe. The analytical method follows that of Williams and Claesson (1987); as described in www.ugr.es/~ibersims. The U/Pb ratios were calibrated using the TEMORA-1 reference zircon (416.75 ± 0.24 Ma; Black et al., 2003) which was measured every 4 unknowns. Point-to-point errors, calculated on replicates of the TEMORA standard during the session were 0.32 % for $^{206}Pb/^{238}U$ and 0.37 % for $^{207}Pb/^{206}Pb$. Isotopic ratios used for age determination are concordant and were not corrected for common lead. Errors are at one sigma level. Data processing was performed using ISOPLOTR software (Vermeesch, 2018). For a single zircon age around and greater than 1000 Ma, the $^{207}Pb/^{206}Pb$ ratio was considered more reliable for determining the apparent age because of the large amount of radiogenic Pb. In contrast, ages less than 1000 Ma have a more reliable $^{206}Pb/^{238}U$ ratio.

4.7 Thermal Ionization Mass Spectrometry

Neodymium and strontium isotopic analyses were measured for a total of 9 whole-rock aliquots from the Peltetec Unit, including 2 metagabbros and 7 metabasalts, and 7 whole-rock powders from the Tampanchi ultramafic-mafic complex, including 1 sample of each relevant lithology (olivine-hornblende clinopyroxenite, hornblendite, plagioclase-bearing hornblendite, fine-grained hornblende gabbro, coarse-grained hornblende gabbro, leucodiorite and granite).

The analyses were carried by Thermal Ionization Mass Spectrometry (TIMS) with a Finnigan MAT 262 spectrometer after digestion of 100 mg of powdered rock samples by HNO3 + HF in Teflon-lined vessels at 200 psi, using ultra-clean reagents and chromatographic separation with ion-exchange resins. Normalization values were $^{146}Nd/^{144}Nd = 0.7219$ and $^{86}Sr/^{88}Sr = 0.1194$. Blanks were 0.09 ng and 0.6 ng for Nd and Sr respectively. The external precision (2σ) estimated by analyzing 10 replicates of the standard WS-E (Govindaraju, 1994) was better than ± 0.0015 % for $^{143}Nd/^{144}Nd$ and ± 0.003 % for $^{87}Sr/^{86}Sr$. $^{147}Sm/^{144}Nd$ and $^{87}Rb/^{86}Sr$ were directly determined by ICP-MS following the

method developed by Montero and Bea (1998), with a precision better than ± 0.9 % and ± 1.2 % (2σ) for $^{147}Sm/^{144}Nd$ and $^{87}Rb/^{86}Sr$ respectively. The $\varepsilon Nd_{(t)}$ values were calculated using present-day values of $^{147}Sm/^{144}Nd = 0.1960 \pm 4$ and $^{143}Nd/^{144}Nd = 0.512630 \pm 11$ for CHUR (Bouvier et al., 2008). The εSr values were calculated using present-day values of $^{87}Rb/^{86}Sr = 0.0827$ and $^{87}Sr/^{86}Sr = 0.7045$ for Actual Bulk Earth (De Paolo, 1988).

4.8 Chemographic diagrams

The composition diagrams (triangular and tetrahedral) were constructed after the projection of chemical composition from phases and exchange vectors using software CSpace (Torres-Roldán et al., 2000). CSpace software uses the algebraic method "Singular Value Decomposition" (SVD; Fisher, 1989; 1993) which allow projection and condensation of the composition space to 3- or 4-component system in a triangular or tetrahedron diagram, respectively. Fe is treated as Fe^{2+}_{total}.

4.9 Pseudosection modelling and thermo barometric estimations

The system KNCFMASTHO (K_2O-Na_2O-CaO-FeO-MgO-Al_2O_3-SiO_2-TiO_2-H_2O-O_2) was considered in the isochemical thermodynamic modeling (pseudosection) performed using the computer program package Perplex_X (Connolly, 1990, 2005; version 6.9.0). A fluid phase, assumed to be pure H_2O, was considered in excess. The oxygen content for partial transformation of ferrous to ferric iron was chosen at 5% Fe^{3+} of the total iron. This value reproduces the observed mineral assemblage within the P-T window of interest. The solid-solution models used for amphibole, pyroxene, epidote, ilmenite, spinel, plagioclase, garnet, mica and chlorite are those of Diener et al. (2007), Green et al. (2007), Holland and Powell (2011), White et al. (2000), White et al. (2002), Fuhrman and Lindsley (1988), Holland and Powell (1998), White et al. (2014) and White et al. (2014), respectively.

P-T conditions also were calculated using the software THERMOCALC 3.33 with the "average P-T" method and the thermodynamic dataset tc-ds55 (Holland and Powel, 1998, updated in 2003; Powell and Holland, 1994). A H_2O-fluid was included in all assemblages. The activities and activity uncertainties of each end-member considered in the calculations were obtained with software AX2 (2014). To reduce the error, phase components with low activities were excluded from the calculations (cf. Powell and Holland, 1994).

For the Tampanchi ultramafic-mafic complex the temperature, oxygen fugacity (fO_2) and melt H_2O content were calculated using the calibrations of Ridolfi et al. (2010) for amphibole in calc-alkaline magmas, using a chemical formula calculated on the basis of 13 cations excluding Ca, Na and K (13-CNK). The temperature of clinopyroxene crystallization was

estimated using equation 32d of Putirka (2008). Pressure was estimated according to the calibrated temperature-dependent plagioclase/amphibole Al-Si partitioning of Molina et al. (2015) with amphibole normalized to 13-CNK.

Capítulo 5

The Peltetec ophiolitic belt: A window to the tectonic evolution of the Triassic margin of western Gondwana

5 The Peltetec ophiolitic belt: A window to the tectonic evolution of the Triassic margin of western Gondwana

5.1 Introduction

The tectonic evolution of the Northern Andes is characterized by a continuous long-term subduction system with alternated (trans)compressional a (trans)extensional phases (e.g. Ramos, 1999; Spikings et al., 2015; Zapata et al., 2019; Cardona et al., 2020) and episodic amalgamation of exotic and para-autochthonous terranes (Restrepo and Toussaint, 1988; Litherland et al., 1994; Kerr et al., 1996; Villagómez and Spikings, 2013; Cochrane et al., 2014b; Spikings et al., 2015). However, the age of the protoliths of accreted rock bodies, their tectonic setting of formation and the age of tectonic emplacement are still a matter of debate, including numerous ophiolitic complexes that document recurrent emplacement of oceanic lithosphere onto the (Paleo)Pacific margin of Gondwana and South America.

Ophiolitic complexes are particularly important because they mark sutures between colliding lithospheric blocks, thereby recording the geodynamic processes of formation and emplacement (onto continental margins or volcanic arcs) of oceanic lithosphere. Since Miyashiro (1973) found strong geochemical similarities between the Troodos lavas and the volcanic rocks of the Izu-Bonin arc south of Japan, suprasubduction zone (SSZ) environments have been repeatedly identified as common loci of ophiolite formation (Dilek and Furnes, 2014 and references therein), implying the existence of magmatic accretion centers at back-, intra- and fore-arc positions above subduction zones (Pearce, 2003). In the Northern Andes, variable tectonic settings have been proposed to explain the formation of ophiolites and terranes of oceanic affinity. For example, the Triassic mafic units along the Northern Andes in Colombia and Ecuador have been considered formed in back-arc basins, in fore-arc position or in mid-ocean-ridges emplaced by tectonic underplating (Figure 5.1a; Apsden et al., 1995; Bosch et al., 2002; Gabriele, 2002, Correa-Martinez, 2007; Restrepo, 2008; Riel et al., 2013, Cochrane et al., 2014a). In contrast, some of the protoliths from the early-mid Cretaceous high-pressure (HP) complexes are classified as basalts of mid-ocean ridge and seamount affinities (Figure 5.1a; Gabriele, 2002; Bosh et al., 2002; John et al., 2010; Villagomez et al., 2011; Bustamante et al., 2012; Ruiz-Jimenez et al., 2012; García-Ramirez et al., 2017). The Peltetec Ophiolitic Belt in the Cordillera Real of Ecuador is in an apparent equivalent structural position of these HP complexes and Triassic mafic complexes (Figure 5.1a). This belt is constituted by basaltic rocks with NMORB and EMORB affinities (Litherland et al., 1994; Cochrane et al., 2014b; Spikings et al., 2015) and, based on two plagioclase $^{40}Ar/^{39}Ar$ ages, it is interpreted as the result of early Cretaceous rifting that detached continental slivers from the continental margin (Spikings et al., 2015).

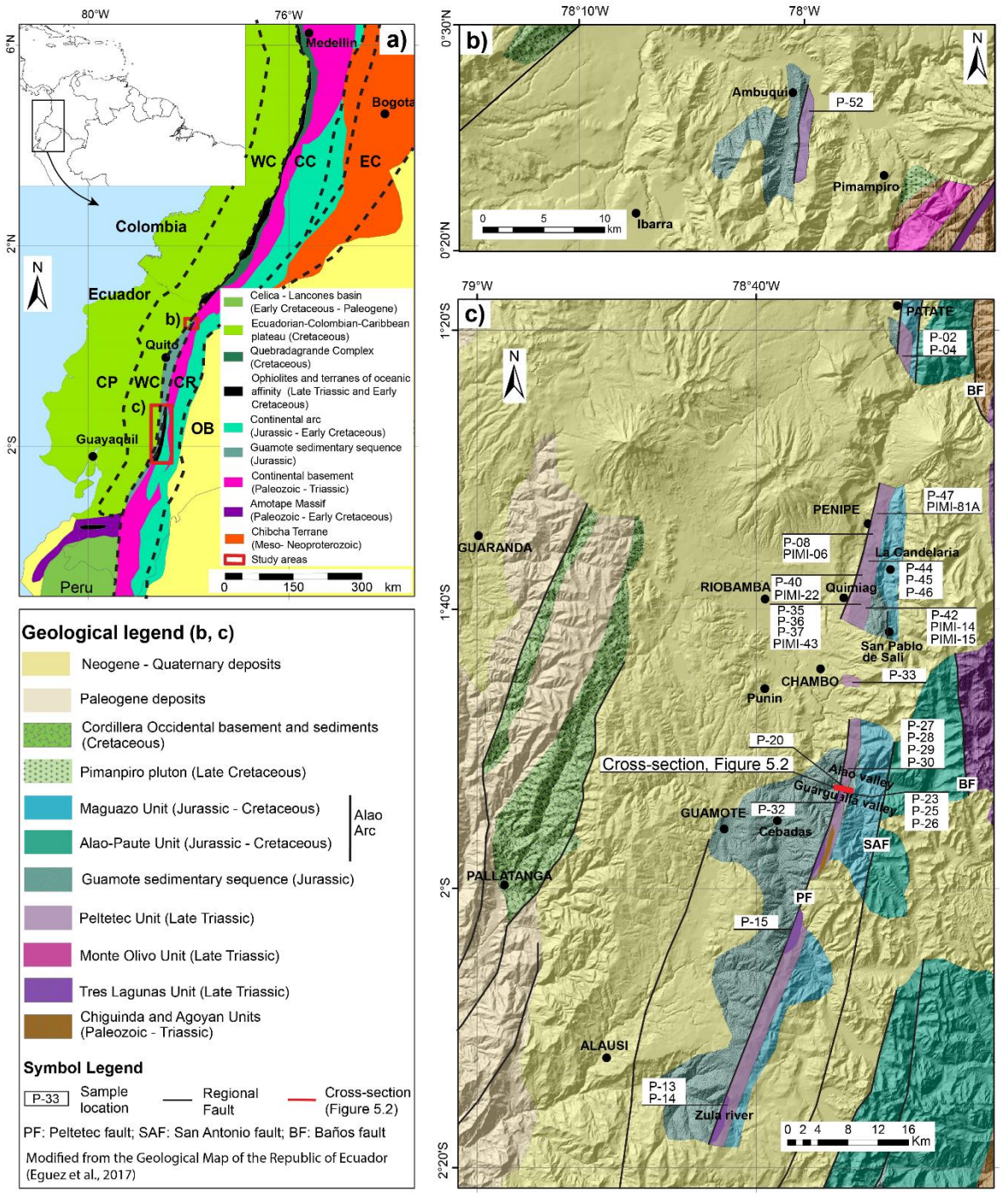

Figure 5.1. a) Schematic representation of tectonic complexes in the Northern Andes and location of the study area. Ophiolites and terranes of oceanic affinity are represented in black, including the late Triassic amphibolitized Piedras metagabbro and high-pressure (HP) Arenillas-Panupali Unit and the early Cretaceous HP Raspas complex (Amotape Massif, El Oro metamorphic complex, Southwestern Ecuador), the Peltetec Unit (central Ecuador) and the early Cretaceous Arquía complex (Colombia); dashed line represents the morphological boundary of the Cordilleras, WC: Western Cordillera, CC: Central Cordillera, CP: Coastal plain, CR: Cordillera Real, EC: Eastern Cordillera, OB: Oriente Basin (retroarc foreland basin). b) and c) Geological maps of the studied area; b) Ambuqui zone and c) the zone between Patate – Zula river with the location of analyzed samples (simplified after Egüez et al., 2017).

The aim of this study is the precise characterization of the petrological-geochemical nature, tectonic environment and age of formation of the Peltetec Ophiolitic Belt, as well as to establish correlations with other units in the Northern Andes in order to better understand the tectonic evolution of the northwestern margin of Gondwana. We provide new field and petrological observations, elemental and isotopic ($^{87}Sr/^{86}Sr$ and $^{143}Nd/^{144}Nd$) whole-rock data and U-Pb SHRIMP zircon ages of the ophiolitic and related rocks that bear important implications for the tectonic evolution of the northwestern margin of Gondwana. Our results reveal a complex geochemical-tectonic evolution that can be traced back to Triassic times, rather than the Cretaceous, requiring a revision of the tectonic arrangement of a part of the Ecuadorian Cordillera Real.

5.2 Geological setting

Despite the complex strike-slip faulting, a significant part of the basement units of the Cordillera Real, the easternmost elevation of the Ecuadorian Andes, can be correlated to the North with complexes of the Central Cordillera of Colombia (Figure 3.1, Figure 5.1a; e.g. Cochrane et al., 2014a; Spikings et al., 2015). Both are formed by variably metamorphosed and deformed continental and oceanic rock units intruded by plutons of varied geochemical affinity and of Paleozoic and Meso- to Cenozoic ages, and both record a long-lasting history of subduction and amalgamation of blocks along the northwestern continental margin of Gondwana and South America during pre- and post- mid Cretaceous times, respectively. The rock units are strongly sheared by right-lateral strike-slip faults, separating major crustal blocks (commonly, terranes) recognized in the northwestern Andes (Figure 5.1). In Ecuador, this fact allowed Aspden and Litherland (1992) and Litherland et al. (1994) to group rock units in informal major lithotectonic divisions that range from late Paleozoic to early Cretaceous age and have been variably affected by late Triassic and early Cretaceous tectono-thermal and collision or accretion events (Litherland et al., 1994; Chew et al., 2007; Spikings et al., 2015; Paul et al., 2018). The allochthonous vs. autochthonous origin of these terranes is still matter of debate, as well as their boundaries and nature of the contacts. Most recent studies, however, propose parautochthonous blocks detached from the continental margin during extensional episodes as well as a single subduction system with westward arc migration (Pratt et al., 2005; Cochrane et al., 2014b; and Spikings et al., 2015).

Much of the basement of the Cordillera Real is made of Paleozoic metasediments (Chiguinda Unit), late Triassic migmatites (Sabanilla Unit), late Triassic metamafic dykes (Monte Olivo Unit), and late Triassic S-type granites (Tres Lagunas Unit) (Litherland et al., 1994; Noble et al., 1997; Chew et al., 2007; Cochrane et al., 2014a; Spikings et al., 2015;

Paul et al., 2018; Spikings et al., 2021). These rocks can be considered equivalent to those exposed in some segments of the Permian-Triassic Cajamarca Complex in the Central Cordillera of Colombia (Maya and González, 1995; Vinasco et al., 2006) and with the Paleozoic-late Triassic Tahuin Group and late Triassic units of oceanic affinity (Piedras and Arenillas-Panupali Units) of the El Oro Metamorphic Complex (Amotape Massif) in southwestern Ecuador (Figure 5.1a) (e.g. Feininger, 1978; Litherland et al., 1994; Apsden et al., 1995; Gabriele, 2002; Riel et al., 2013; Suhr et al., 2019).

Jurassic to early Cretaceous arc-related rocks of the Misahuallí and Alao arcs occur to the East and West of Paleozoic-Triassic units in the Cordillera Real (Lihterland et al., 1994; Chiaradia et al., 2009; Drobe et al., 2013; Cochrane et al., 2014b; Figure 5.1a). The Alao arc (Maguazo, Alao–Paute and El Pan Units, Litherland et al., 1994) has been correlated with the Quebradagrande Complex in Colombia (Cochrane et al., 2014b; Spikings et al., 2015), that records volcanism from ~150 Ma to 80 Ma (Villagomez et al., 2011; Cochrane et al., 2014b; Zapata et al., 2019). The Maguazo and El Pan Units include variably deformed and metamorphosed volcano-sedimentary sequences with a suggested middle Jurassic-early Cretaceous age (Riding, 1989), while the Alao–Paute Unit is formed by tholeiitic to calc-alkaline andesitic–basaltic rocks with variable metamorphic overprint reaching the greenschist facies and minor occurrences of pelitic schists, graphitic schists, quartzites and marbles (Figure 5.1c) (Litherland et al., 1994; Cochrane et al., 2014b). The age of formation of these units is not well constrained; hornblende K/Ar ages of 115 ± 12 Ma and 142 ± 36 Ma were interpreted by Litherland et al. (1994) as the result of a Cretaceous tectono-thermal overprint of Jurassic rocks, while U-Pb ages of rims of detrital zircons from a quartzite of the Alao–Paute Unit yielded a maximum depositional age of 163.7 ± 1.6 Ma (Cochrane et al., 2014b). West of the Alao arc, Litherland et al. (1994) described the Guamote metasedimentary sequence (Figure 5.1) as a set of intercalated quartzites and slates with late Jurassic maximum depositional age (Cochrane et al., 2014b). They are equivalent to volcano-sedimentary units related to the Alao arc (Pratt et al., 2005; Spikings et al., 2015).

Oceanic units are represented in the Cordillera Real by the nominally Cretaceous Peltetec ophiolitic belt (Peltetec Unit; Litherland et al., 1994; Figure 5.1b-c) with MORB and EMORB affinities (Litherland et al., 1994; Spikings et al., 2015). This belt is bounded by the Guamote sequence to the West and the Alao-related rocks to the East. The ophiolitic rocks show greenschist facies metamorphic overprint, with the development of chlorite, epidote and albite, and relicts of altered clinopyroxene and (saussuritized) plagioclase. An early Cretaceous age of the basaltic protoliths has been inferred based on plagioclase $^{40}Ar/^{39}Ar$ data yielding 134.7 ± 0.9 and 134 ± 13 Ma (Spikings et al., 2015). However, the chemical

composition and extent of alteration of the dated plagioclase was not reported. The Peltetec ophiolitic belt is best described as a tectonic mélange (Litherland et al., 1994), with most of the deformation related to a penetrative shear zone that affects both the matrix and the dismembered slices of the ophiolitic sequence. Oceanic rocks also occur in the Cretaceous Celica-Lancones basin of Southwestern Ecuador, which are overlain by volcano-sedimentary sequences (Jaillard et al., 1996; Winter et al., 2010) and in the Raspas Complex (Figure 5.1a), the latter including metaperidotites and metamafic rocks, including eclogites and blueschists of NMORB and seamount affinities, respectively (John et al., 2010), with peak HP metamorphism at ca. 130 Ma (Gabriele, 2002; John et al., 2010). Unrelated oceanic rocks of the Cretaceous Ecuadorian-Colombian-Caribbean plateau accreted against the continental margin of South America during the late Cretaceous-Paleocene in the Western Cordilleras of Ecuador and Colombia (e.g. Reynaud et al., 1999; Kerr et al., 2003; Vallejo et al., 2009).

5.3 Field relations

The Peltetec Unit is largely covered by Neogene-Quaternary volcanic deposits, being discontinuously exposed along a N-S to NNE-SSW trend through the western margin of the Cordillera Real, from the Ambuquí sector in the North near the Colombian border to the Zula River in the South (Figure 5.1). The best-exposed occurrences are around and to the South of the Penipe locality (Figure 5.1c).

The Unit is tectonically bounded by the Jurassic Guamote sequence to the West and the Maguazo Unit of the Alao arc to the East (Figure 5.1, Figure 5.2, Figure 5.3a; Litherland et al., 1994). However, we could not confirm such configuration during our fieldwork. At the western boundary in the South of the Unit, we identified small slivers of variably deformed granitic rocks of the Tres Lagunas Unit and of graphitic phyllites and quartzites of the Paleozoic Chiguinda Unit. On the other hand, slivers of black slates and quartzites of the Guamote sequence were identified in the eastern limit (Figure 5.1c, Figure 5.2) together with the Maguazo Unit, which is very low-grade to not metamorphosed and preserves primary sedimentary structures with faint or no penetrative cleavage. The rocks at the eastern fault-contact are intensely sheared showing a high-angle cleavage dipping to the East, while to the West of Peltetec the foliation is flatter. Occasionally, undated discordant non-deformed andesitic dykes occur to the East of the unit (Figure 5.2). To the South of the Guarguallá Valley, small outcrops of the Peltetec Unit appear below Pliocene-Quaternary volcanic cover; however, the lineament of the belt and isolated outcrops are identified further South in the region of the Zula River.

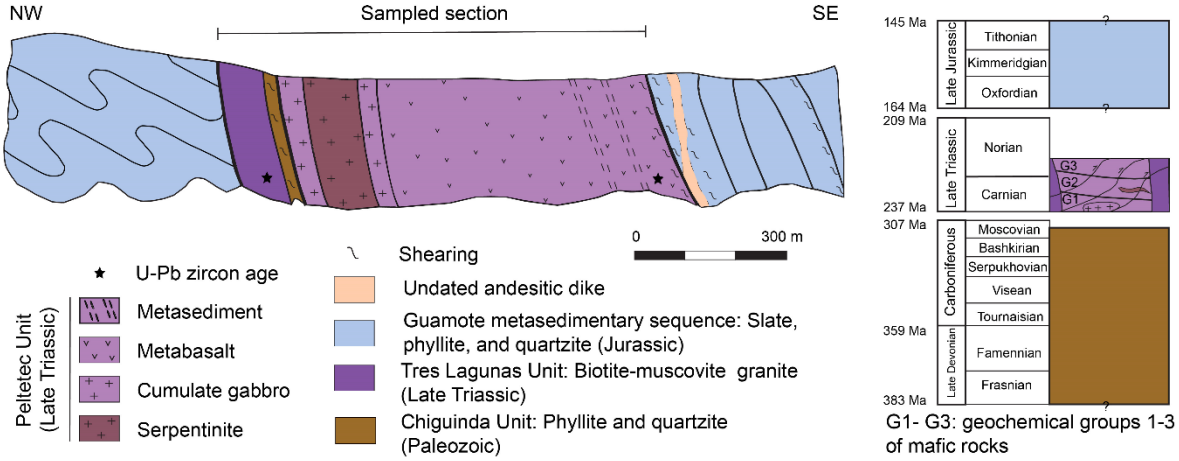

Figure 5.2. Schematic cross-section along the Guarguallá Valley showing the lithologies and field relationships of the Peltetec Unit, and a suggested stratigraphic column based on Litherland et al. (1994), Noble et al. (1997), Chew et al. (2007), Cochrane et al. (2014a), Spikings et al. (2015) and Spikings et al., 2021 and the geochemical and geochronological data of the Peltetec and Tres Lagunas units (this study).

5.4 Rock types and mineral assemblages

A wide variety of rock types have been described in the Peltetec Unit (Litherland et al., 1994; Fortey, 1990; Reyes, 2006), including slivers of serpentinite and metasedimentary rocks and a variety of metamorphosed and slightly to intensely deformed mafic magmatic rocks (gabbro, olivine gabbro and basalt) that are locally affected by hydrothermal alteration and brecciated. In addition, metamorphosed mafic dykes with relict phaneritic to aphanitic texture crosscut the igneous lithologies. These dykes share the same deformation and metamorphic characteristics as the country rock, providing evidence for sharing a common origin. Serpentinites were identified locally in the center and in the South of the complex (Figure 5.2, Figure 5.3b). They are mainly composed of serpentine group minerals, with minor chlorite, magnetite, chromian spinel and carbonates; intense shearing defines foliation planes dipping towards the East.

The textural and mineralogical characteristics of these lithotypes are described below.

5.4.1 Metagabbro

Scattered outcrops of metagabbro are distributed from Patate in the North to the Guarguallá Valley in the South (Figure 5.1c, Figure 5.2). The thickness of each occurrence is difficult to estimate due to Quaternary volcanic, soil and vegetation covers. The rocks are greenish-gray and intensely foliated although non-foliated gabbros locally occur. Microscopically, this type of rock shows intense metamorphic transformation, with mm-sized elongated clots of

chlorite corresponding to pseudomorphs after former mafic minerals and sericite/saussurite (altered plagioclase) surrounded by a fine light gray groundmass. Fine-grained anhedral opaque minerals are ubiquitous. The foliated gabbros are sheared and fractured and show a marked foliation with N-S to NNE-SSW trending dipping to the East (Figure 5.3c). Non-foliated gabbros occur in the Guarguallá and Alao valleys and south of Penipe; they show cumulate poikilitic texture (plagioclase included in pyroxene) (Figure 5.4a). This variety is constituted by relict igneous clinopyroxene, plagioclase, opaque minerals and rare olivine (Figure 5.4a) overprinted by actinolitic amphibole, albite, chlorite, epidote, serpentine, sericite and calcite. Plagioclase is strongly altered but it locally shows fresh relicts, while olivine is systematically replaced by serpentine. Micro-fractures are filled by chlorite or albite.

5.4.2 Metabasalts

This is the most abundant lithology of the Peltetec Unit. Metabasalts are greenish-grey rocks with dominant fine-grained fabric and variable extent metamorphic transformation. The best outcrops were identified between the Penipe sector and Guarguallá Valley (Figure 5.1c). The greatest thickness (2000 meters) can be observed in Quimiag, while towards the north of Penipe the thickness decreases progressively until the body disappears below Neogene-Quaternary volcanic cover (Figure 5.1c). Slices of greenschist show a well-developed foliation with local crenulation cleavage (Figure 5.3d). The rocks are very fine- to fine-grained and composed of clinozoisite-epidote, chlorite, actinolitic amphibole, albite, titanite and locally muscovite (Figure 5.4b-c). Other varieties show local relict porphyritic texture (pyroxene and altered plagioclase porphyroclasts) and variably deformed and altered zones with abundant chlorite (Figure 5.4d-e). The foliation has a dominant NNE to NE direction with a predominant dip to the east (Figure 5.3e). Crenulation cleavage is locally present in fine-grained varieties (Figure 5.4e). Deformed micro-veinlets of calcite and quartz crosscut the rocks. The porphyritic rocks show mylonitic fabric with rotated clinopyroxenes, locally broken and replaced by amphibole (Figure 5.4f). Small elongated amygdules are filled by chlorite and epidote. Non-foliated rocks (Figure 5.4d) have the same primary and secondary mineralogical associations as deformed varieties.

Brecciated rocks (Figure 5.4g) contain fragments of aphanitic and porphyritic basaltic rocks with scarce microliths of plagioclase, pyroxene and opaque minerals. They are slightly foliated with oriented fine-grained chlorite and epidote. Fractures are filled with clinozoisite, chlorite, albite or quartz.

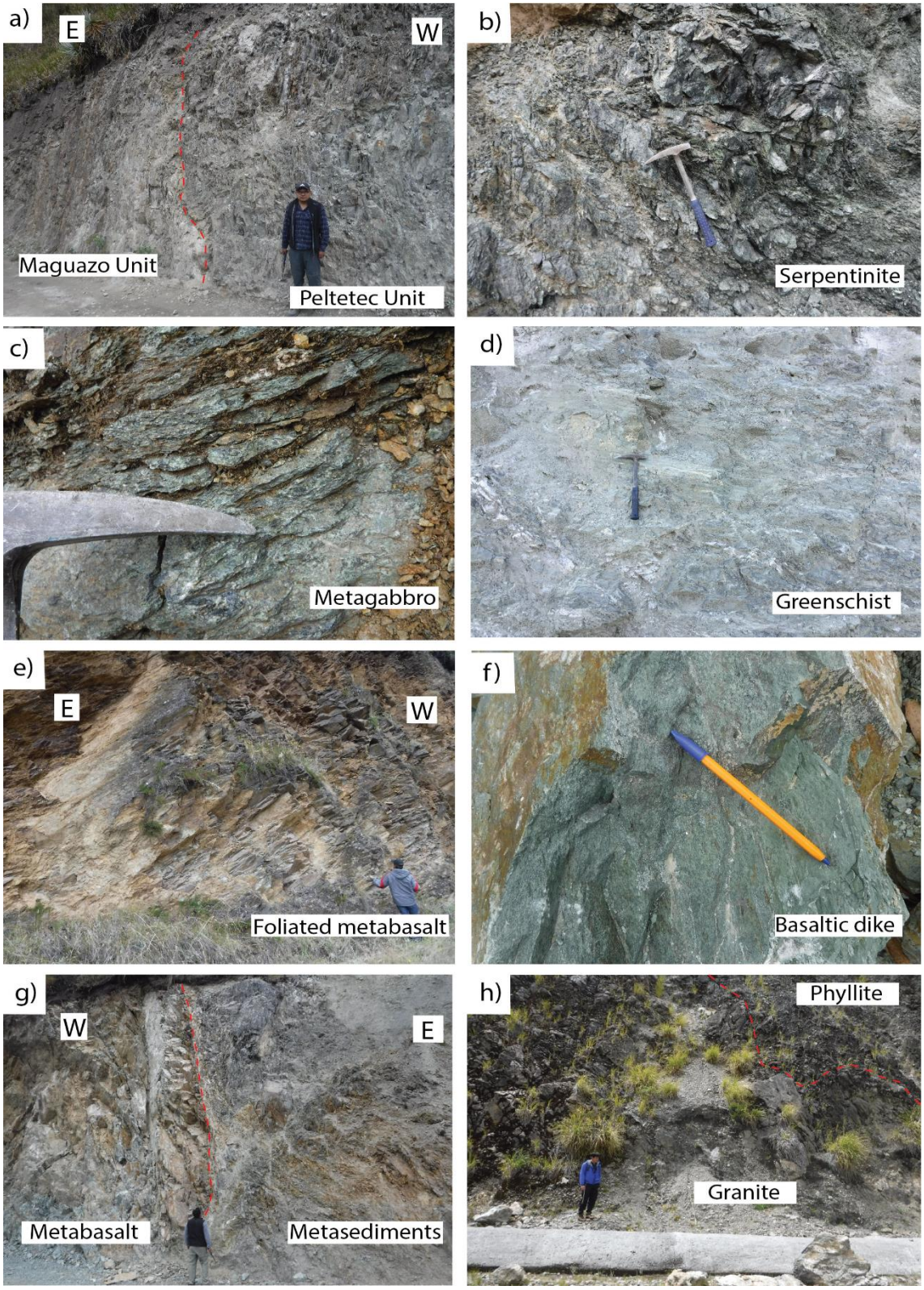

Figure 5.3. Field relations of the Peltetec Unit. a) Upright tectonic contact between the Maguazo Unit to the East and the Peltetec Unit to the West. b) Sheared brittle serpentinite. c) Foliated metagabbro. d) Greenschist. e) Foliated metabasalts dipping to the East. f) Basaltic dyke crosscutting metabasalts. g) Contact between metabasalt and metasedimentary rocks. h) Contact between granite of the Tres Lagunas Unit and phyllite of the Chiguinda Unit.

5.4.1 Metabasic dykes

Dykes less than 2 meters in thickness crosscut the metabasalts (Figure 5.3f). They show the same deformation and metamorphic features than the metabasaltic host rocks, with a predominant relict micro-phaneritic and porphyritic texture and scarce relicts of clinopyroxene and plagioclase overprinted by actinolitic amphibole, albite, epidote and chlorite (Figure 5.4h). Amphibole is fine-grained anhedral to subhedral, shows internal deformation and is locally broken.

5.4.2 Metasediments

These rocks crop out discontinuously all along the Peltetec Unit intercalated between metabasaltic rocks and as tectonic slivers (Figure 5.3g), being more abundant close to the eastern boundary of the unit (Figure 5.2). In all sectors, they show a penetrative foliation that is locally crenulated. Mostly they are fine-grained greenish and purple phyllites with a silky appearance due to the presence of abundant sericite, but minor intercalations (~5 meters thick) of dark gray to ocher phyllites appear in-between the metabasalts. Along the Zula River, a ca. 100 m thick sliver of greenish to yellowish metagreywacke and quartz-breccia shows a poorly developed foliation and preserved clastic textures. The rocks are composed of quartz, plagioclase and scarce pyroxene in a clay groundmass.

Figure 5.4. (Next page). Optical microphotographs showing the mineralogy and textural details of studied rocks: a) Metagabbro with phaneritic cumulate texture; plagioclase, locally included in clinopyroxene, is altered, olivine shows pseudomorphic texture and fresh clinopyroxene is the cumulus mineral. b) Foliated metabasalt with relicts of pyroxene, altered groundmass and broken metamorphic amphibole. c) Greenschist. d) Massive microcrystalline basaltic rock with microliths of plagioclase and pyroxene in a glassy altered groundmass. e) Deformed aphanitic basaltic rock with crenulation cleavage. f) Basaltic porphyritic foliated rock; the groundmass is cryptocrystalline and pyroxene phenocrysts are rotated and partially replaced by calcic amphibole forming a pressure shadow tail. g) Altered breccia; note fracturation of basaltic rock and strongly altered regions (lighter shade). h) Basaltic dyke; fresh minerals are surrounded by an altered plagioclase groundmass. Mineral abbreviations: Ol-olivine, Cpx-clinopyroxene, Pl-plagioclase, Px-pyroxene, Amp-amphibole, Ep-epidote, Ttn-titanite, Czo-clinozoisite, Srp-serpentine, Chl-chlorite, Cal-calcite, Ab-albite (Whitney and Evans, 2010).

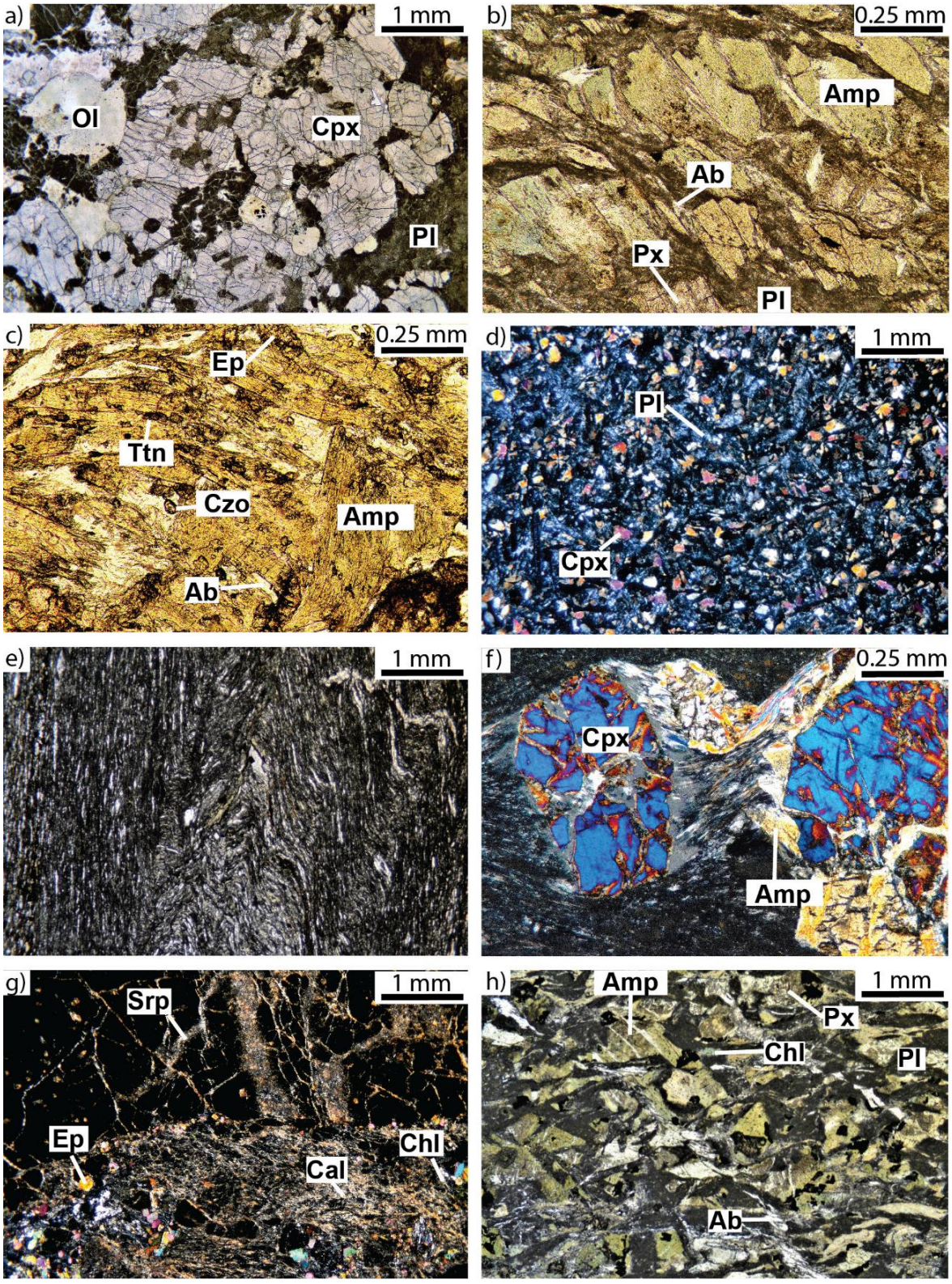
a)
1 mm
Ol
Cpx
Pl
b)
0.25 mm
Amp
Ab
Px
Pl
c)
0.25 mm
Ep
Ttn
Czo
Amp
Ab
d)
1 mm
Pl
Cpx
e)
1 mm
f)
0.25 mm
Cpx
Amp
g)
1 mm
Srp
Ep
Chl
Cal
h)
Amp
1 mm
Px
Chl
Pl
Ab

5.4.1 Tres Lagunas Unit

Discontinuous slivers of leucocratic granite were identified along the western margin of the Peltetec Unit from the Guarguallá valley in the North to the Zula River in the South (Figure 5.1c, Figure 5.2, Figure 5.3h). These rocks generally have a massive coarse-grained phaneritic igneous texture, though they occasionally show mylonitic fabric. They are composed of quartz, K-feldspar, plagioclase, biotite, muscovite and traces of monazite, rutile, zircon and apatite.

5.5 Geochemistry

5.5.1 Evaluation of element mobility

Element mobility is a complex process affected by different factors, such as the composition and stability of the mineral phases in unaltered protoliths and in the alteration products, and the composition, temperature and volume of fluid phases flowing through the rock volume. Metamorphism and alteration of the Peltetec Unit, with hydration and formation of amphibole, clinozoisite-epidote, chlorite, albite and calcite ± serpentine group minerals and sericite, prevents the use of fluid-mobile elements for characterizing the primary igneous and sedimentary composition of the rocks. The metabasalts have an Ishikawa alteration index (AI; Ishikawa et al., 1976) of 22-40 and a chlorite-carbonate-pyrite index (CCPI; Large et al., 2001) of 66-91 (Table 5.1). Since AI varies from 20 to 60 in unaltered rocks and between 50 and 100 in hydrothermally altered rocks, and the CCPI ranges from 70 to 90 in unaltered basalts (Large et al., 2001), we conclude that the analyzed samples are fresh to slightly altered. However, we have further analyzed individual element mobility according to the isocon analysis (Gresens, 1967; Grant, 1986, 2005), which allows the quantitative evaluation of chemical gain and losses (in mass, volume or concentrations) in mass-transfer processes through a linear relationship of the concentration of a component in the altered rock and that in the original (least altered) (Grant, 1986).

Because of their predominance in the Peltetec Unit and their more important petrogenetic significance, we have restricted the isocon analysis to metabasalts (Group 3, see below). The reference sample selected for the isocon analysis is sample PIMI-43 (Table 5.1). For this selection, the petrographic characteristics of the samples and their AI and CCPI values (39 and 84, respectively, in sample PIMI-43) were considered. The results of the analysis (Appendix 5.1 and Figure 5.5) show that REE and HFSE behave immobile, while the transition metals Cr, Ni and Co behave variably, perhaps because of both element mobility and the natural variations of the rocks. On the other hand, LILE and the transition metals

Cu and Zn show stronger mobility. Specifically, the elements that show the strongest evidence for mobility and, hence, will not be considered in the geochemical description and petrogenetic interpretation of the rocks, are: Rb, Cs, Ba, Pb and Li, which generally show gains, Cu, Zn and Mo, that show losses and K, P and Sr, that show variable gains/losses. These results are consistent with general views that consider Rb, Ba, Cs, U, K, Sr, P and Pb as mobile elements and Ti, Al, V, Y, Zr, Nb, REE (particularly HREE) and Th as immobile (e.g., Scott and Hajash, 1976; Staudigel and Hart, 1983; Seyfried et al., 1988; Hofmann and Wilson, 2007; Dilek et al., 2008; Pearce, 2014, Furnes and Dilek, 2017).

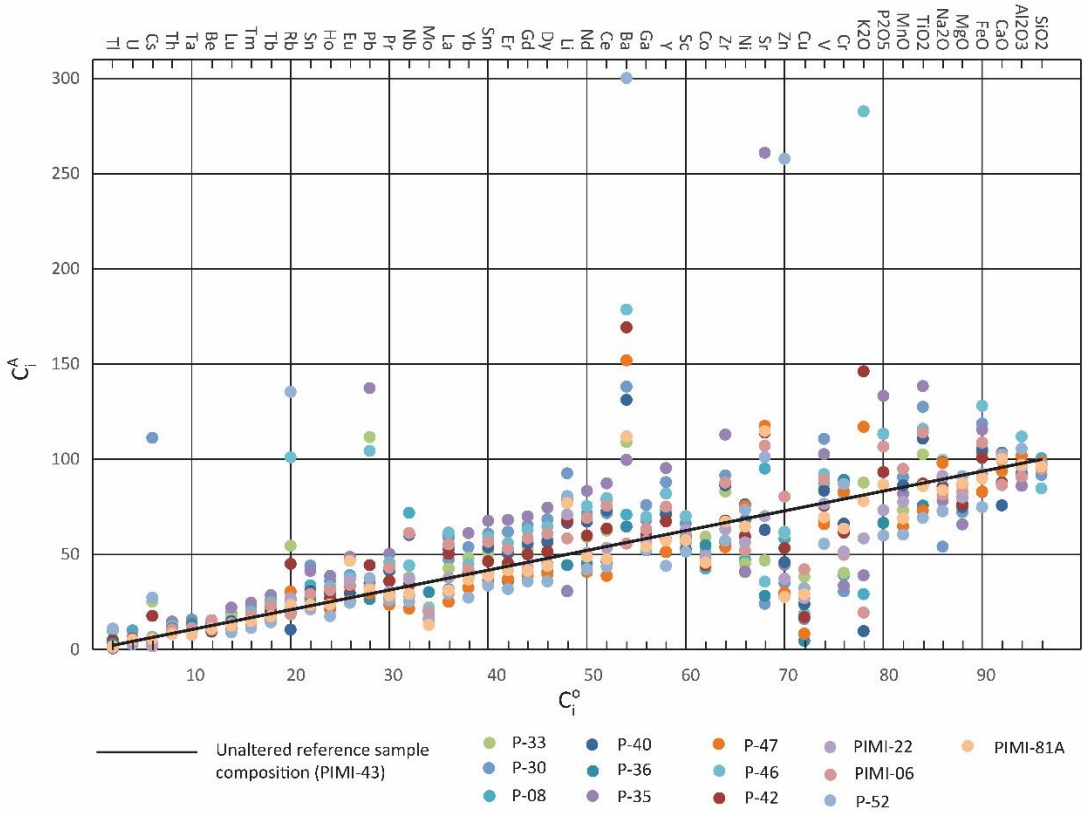

Figure 5.5. Isocon diagram for Group 3 samples. C_i^o: scaled unaltered (reference) composition; C_i^A: scaled altered composition. The elements are arranged according to their abundance (wt.% and ppm) in the reference sample and are assigned the value 2 for the least abundant element and increasing 2 units for each element in increasing order of concentration reaching 96 for SiO_2. These values correspond to C_i^o of each sample and represent the X-axis of the diagram. The scale factor of each element was obtained by the relation C_i^o / C_i^o(wt.% and ppm) of the reference sample. C_i^A in the Y axis is the result of the product of the scale factor of the element and the composition of each element from each altered sample. The data portrayed are offered in Appendix 5.1. Sample P-52 has a K_2O value of 516 that exceeded the y-axis limit value selected for the diagram.

5.5.2 Whole-rock major and trace elements

A general basaltic composition of metamafic rocks is observed in the immobile element-based TAS proxy diagram of Figure 5.6a (from Pearce 1996, after Floyd and Winchester, 1978), where the ratio Zr/Ti is used as a differentiation index. The concentration of major elements suggests a tholeiitic affinity (Irvine and Baragar, 1971) (Figure 5.6b; see below) for the basaltic rocks, while the cumulate gabbros (samples P-25, P-29 and P-45; Table 5.1) trend towards higher MgO content, and have high values for both Sc (42-65 ppm) and Ni (121-263 ppm), pointing to cumulate clinopyroxene and olivine (cf. Pearce, 1996).

In addition to cumulate gabbros, we have identified three different geochemical groups of metabasalts based on TiO_2 and Cr (immobile element proxy for MgO; Pearce, 2014) contents (Figure 5.6c) and chondrite- and NMORB-normalized (Sun and McDonough, 1989) trace element patterns (Figure 5.7). Group 1 includes one noncumulate gabbro sample and two metabasalts from the Patate sector and from the South of Penipe town. Group 2 includes three metadiabase and four metabasalts located in the Guarguallá and Alao valleys and in Quimiag close to the eastern contact with Guamote-related rocks. Group 3 includes one metadiabase and 13 metabasalts from the Ambuquí, Penipe, Quimiag and Chambo sectors and the Alao valley close the eastern contact with Guamote-related rocks. The geochemical data and the geographical coordinates are presented in Table 5.1 (see also Figure 5.1b-c).

5.5.3 Geochemical groups

Cumulate gabbros. These rocks have a high Cr (700-1164 ppm) and low TiO_2 contents (0.39 to 0.44 wt.%; Figure 5.6c), with Mg# ranging between 0.69 and 0.78. Two samples show flat chondrite-normalized REE patterns ($(La/Yb)_n$ = 0.97-1.02, $(La/Sm)_n$ = 0.93-0.96, $(Sm/Yb)_n$ = 1.05-1.06; Figure 5.7a) while a third one shows depletion in LREE with respect to MREE ($(La/Sm)_n$ = 0.47) and has a flat slope from MREE to HREE ($(Sm/Yb)_n$ = 0.87). All samples show positive Eu anomalies (Eu/Eu* = 1.16-1.83) indicating plagioclase fractionation. Immobile elements are depleted relative to MORB (Figure 5.7a), except Th that is enriched ($(Th/La)_{NMORB}$ = 7.14-7.37), while Nb and Zr show slight negative anomalies. The $(Th/Nb)_{NMORB}$ relations range between 9.22 and 11.67.

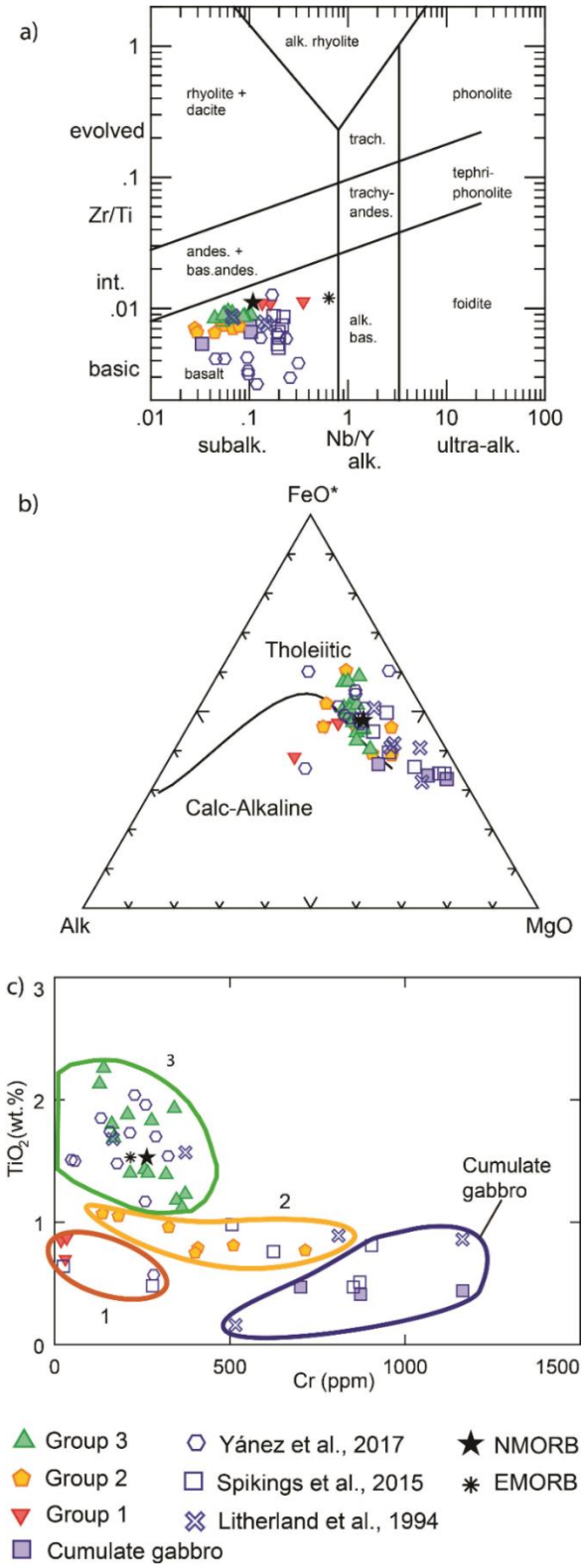

Figure 5.6. Classification of studied rocks. a) TAS proxy diagram (Pearce 1996, Floyd and Winchester, 1978). b) AFM diagram of Irvine and Baragar (1971) showing the boundary between tholeiitic and calc-alkaline fields. c) TiO2 (wt.%) vs Cr (ppm) diagram showing the non-cumulate mafic groups 1, 2 and 3 defined in this study and cumulate gabbros. NMORB and EMORB compositions are from Gale et al. (2013). Also plotted are published geochemical data of mafic rocks (blue symbols) of the Peltetec Unit.

Table 5.1. Major (wt.%) and trace (ppm) element composition of the studied samples of the Peltetec and Tres Lagunas Units.

Sample	P-25	P-29	P-45	Group 1 P-02	Group 1 P-04	Group 1 P-44	Group 2 P-20	Group 2 P-23
Lithology	Cumulate metagabbro	Cumulate metagabbro	Cumulate metagabbro	Metabasalt	Metagabbro	Metabasalt	Metabasalt	Metadiabase
Longitude	770924	771394	775154	779276	779276	775719	771336	771349
Latitude	9791781	9794374	9822066	9849012	9849012	9822085	9791694	9791388
SiO2	48.2	46.7	48.4	58.7	52.3	50.0	47.0	48.0
TiO2	0.39	0.42	0.44	0.67	0.80	0.82	1.01	0.75
Al2O3	11.0	9.83	15.4	17.0	18.9	18.1	16.5	15.2
FeO*	7.19	7.37	6.45	5.93	7.62	8.75	11.8	7.91
MnO	0.14	0.15	0.14	0.08	0.07	0.10	0.21	0.13
MgO	12.6	14.3	8.24	4.21	4.93	6.06	6.23	8.86
CaO	14.5	15.6	11.8	3.56	5.68	6.48	6.64	9.96
Na2O	1.50	0.80	2.92	4.53	3.55	3.26	3.92	3.33
K2O	0.07	0.02	0.04	0.77	0.33	0.54	0.73	0.05
P2O5	0.03	0.04	0.02	0.09	0.06	0.07	0.14	0.07
LOI	2.86	3.31	5.10	3.06	4.24	4.33	3.95	4.29
Total	98.5	98.6	98.9	98.5	98.4	98.5	98.1	98.6
Li	13.4	10.6	10.3	12.8	25.4	19.6	22	20
Rb	1.74	0.68	2.28	13.0	4.61	15.2	15.6	2.17
Cs	0.71	0.95	0.06	0.53	0.39	0.60	0.67	1.71
Be	0.08	0.09	0.18	0.39	0.52	0.59	0.33	0.13
Sr	73	27	42	251	205	87	245	38
Ba	21	13.4	12.6	131	165	202	93	19.0
Sc	58	65	42	25	28	35	51	42
V	202	224	194	182	269	291	300	253
Cr	873	1164	702	30	18.22	34	136	409
Co	59	65	42	33	35	25	44	41
Ni	223	263	121	15	7.08	6.82	66	113
Cu	111	54	79	68	25	20	77	10.3
Zn	45	45	46	65	52	77	108	37
Ga	9.14	8.90	12.5	14.2	18.7	19.1	15.8	13.4
Y	8.98	9.55	12.1	15.6	14.6	14.1	30	25
Nb	0.91	0.99	0.40	5.51	2.38	1.90	1.72	0.69
Ta	0.30	0.32	0.20	0.60	0.40	0.27	0.35	0.30
Zr	17.9	17.4	15.1	47	56	57	47	33
Mo	2.60	2.25	1.61	2.38	2.11	0.95	1.14	1.28
Sn	0.69	0.70	0.64	1.49	1.48	0.97	1.20	1.81
Tl	0.02	0.01	0.01	0.11	0.09	0.08	0.12	0.01
Pb	1.24	1.23	1.65	3.88	3.67	5.44	2.63	1.28
U	0.03	0.03	0.08	0.39	0.50	0.50	0.21	0.13
Th	0.47	0.47	0.24	15.29	1.82	0.80	1.56	0.61
La	1.33	1.35	0.70	3.77	5.10	3.95	2.08	1.09
Ce	3.22	3.42	2.03	9.56	11.9	10.2	4.87	3.65
Pr	0.49	0.52	0.36	1.30	1.66	1.51	1.07	0.68
Nd	2.68	2.78	2.22	6.41	7.96	7.30	6.18	4.33
Sm	0.89	0.94	0.97	1.88	2.31	2.14	2.42	1.75
Eu	0.43	0.43	0.72	0.71	0.86	1.26	1.98	0.77
Gd	1.31	1.35	1.51	2.26	2.61	2.27	3.44	2.59
Tb	0.23	0.25	0.28	0.40	0.43	0.39	0.64	0.49
Dy	1.47	1.56	1.94	2.51	2.76	2.49	4.60	3.81
Ho	0.33	0.37	0.44	0.55	0.56	0.50	1.06	0.88
Er	0.91	0.94	1.22	1.51	1.59	1.37	2.82	2.44
Tm	0.15	0.16	0.20	0.24	0.24	0.24	0.46	0.40
Yb	0.94	1.00	1.24	1.48	1.51	1.47	2.81	2.51
Lu	0.13	0.14	0.18	0.22	0.22	0.22	0.43	0.39
Mg#	0.76	0.78	0.69	0.56	0.54	0.55	0.49	0.67
ASI	0.38	0.33	0.59	1.15	1.14	1.02	0.86	0.64
AI	44.2	46.6	36.1	38.1	36.3	40.4	39.7	40.1
CCPI	92.6	96.4	83.2	65.7	76.4	79.6	79.5	83.2
$(Th/Nb)_{NMORB}$	9.96	9.22	11.7	53.91	14.81	8.12	17.6	17.2

Table 5.1. (Continued). Major (wt.%) and trace (ppm) element composition of the studied samples of the Peltetec and Tres Lagunas Units.

Sample	Group 2 P-27	Group 2 P-28	Group 2 P-32	Group 2 P-37	Group 2 PIMI-15	Group 3 P-08	Group 3 P-30	Group 3 P-33
Lithology	Metabasalt	Metabasalt	Metabasalt	Metadiabase	Metadiabase	Metabasalt	Metabasalt	Metabasalt
Longitude	771081	771245	770982	774978	774969	774650	772132	773360
Latitude	9794813	9794298	9790574	9815538	9815513	9824566	9794060	9805719
SiO2	49.8	44.4	45.0	48.7	48.1	50.7	46.2	47.9
TiO2	0.76	0.90	0.69	1.00	0.73	1.73	1.99	1.60
Al2O3	16.8	15.6	15.8	14.8	15.0	12.9	13.9	13.5
FeO*	9.68	9.22	9.27	9.65	7.09	11.1	12.4	10.8
MnO	0.16	0.15	0.18	0.17	0.14	0.21	0.21	0.17
MgO	6.27	9.01	4.24	7.83	8.86	6.97	6.61	7.27
CaO	4.91	12.8	15.1	9.20	12.9	8.96	9.77	9.68
Na2O	4.98	1.85	1.42	3.54	2.30	3.14	2.03	3.74
K2O	0.10	0.01	0.42	0.02	0.04	0.03	0.06	0.09
P2O5	0.07	0.07	0.11	0.09	0.06	0.17	0.17	0.14
LOI	5.36	4.29	6.39	3.39	3.65	2.46	4.54	3.29
Total	99.0	98.3	98.6	98.4	98.9	98.2	97.9	98.1
Li	19.7	25	21	9.78	9.89	4.29	12.9	9.52
Rb	5.38	0.86	9.86	1.31	2.35	1.06	1.30	2.70
Cs	0.45	0.32	0.71	0.09	0.05	0.05	1.95	0.44
Be	0.27	0.16	0.19	0.45	0.23	0.53	0.48	0.44
Sr	39	29	55	52	17.1	122	31	60
Ba	61	33	75	12.4	13.0	11.8	23.0	18.1
Sc	48	43	43	43	46	41	48	44
V	228	285	232	280	242	366	464	355
Cr	510	325	401	182	715	163	128	169
Co	52	51	61	50	42	39	48	55
Ni	88	102	97	87	114	61	53	59
Cu	94	59	610	85	64	64	43	102
Zn	98	55	67	65	51	110	67	116
Ga	14.6	17.3	17.9	16.3	13.5	16.5	21.3	16.9
Y	21	25	25	27	19.1	39	47	39
Nb	1.41	0.75	1.09	1.38	1.51	4.11	2.52	2.18
Ta	0.28	0.30	0.31	0.28	0.29	0.51	0.34	0.41
Zr	34	38	29	52	34	95	101	91
Mo	1.24	1.30	2.85	2.19	2.21	1.63	1.31	1.85
Sn	0.96	0.93	0.87	1.04	0.81	1.71	2.23	1.47
Tl	0.05	0.01	0.07	0.01	0.02	0.01	0.02	0.02
Pb	1.57	4.45	2.38	1.56	1.36	1.54	1.29	5.01
U	0.10	0.03	0.14	0.02	0.02	0.13	0.05	0.07
Th	1.92	0.58	0.39	0.25	0.30	0.85	0.37	0.34
La	3.13	0.94	1.51	2.37	1.60	4.76	3.84	3.45
Ce	4.41	3.24	3.67	6.36	4.45	13.1	12.0	10.4
Pr	0.98	0.66	0.71	1.13	0.77	2.13	2.07	1.78
Nd	5.37	4.49	4.10	6.68	4.37	11.7	12.1	9.99
Sm	1.85	1.95	1.74	2.46	1.68	3.94	4.56	3.79
Eu	1.01	1.40	1.76	1.01	0.61	1.76	1.67	2.13
Gd	2.63	2.95	2.46	3.24	2.35	5.03	5.90	4.77
Tb	0.47	0.56	0.49	0.60	0.44	0.92	1.07	0.88
Dy	3.36	4.03	3.54	4.33	3.13	6.42	7.62	6.29
Ho	0.75	0.93	0.84	0.95	0.70	1.44	1.72	1.43
Er	2.01	2.52	2.31	2.60	1.87	3.75	4.47	3.84
Tm	0.33	0.41	0.38	0.39	0.30	0.58	0.70	0.60
Yb	1.93	2.40	2.35	2.41	1.77	3.32	4.20	3.75
Lu	0.29	0.37	0.35	0.37	0.26	0.48	0.64	0.59
Mg#	0.54	0.64	0.45	0.59	0.69	0.53	0.49	0.55
ASI	0.98	0.59	0.52	0.66	0.55	0.60	0.66	0.57
AI	39.2	38.2	22.0	38.1	37.0	36.6	36.1	35.4
CCPI	75.8	90.7	88.0	83.1	87.2	85.1	90.1	82.5
$(Th/Nb)_{NMORB}$	26.4	14.9	6.98	3.50	3.86	4.01	2.86	3.01

Table 5.1. (Continued). Major (wt.%) and trace (ppm) element composition of the studied samples of the Peltetec and Tres Lagunas Units.

Sample	Group 3 P-35	Group 3 P-36	Group 3 P-40	Group 3 P-42	Group 3 P-46	Group 3 P-47	Group 3 P-52	Group 3 PIMI-6
Lithology	Metabasalt	Metabasalt	Metabasalt	Metabasalt	Metadiabase	Metabasalt	Metabasalt	Metabasalt
Longitude	774339	774717	774935	772948	774345	775671	166223	774863
Latitude	9815797	9815714	9818622	9816433	9821938	9827733	10098714	9825434
SiO2	48.6	42.7	49.1	48.9	49.7	49.7	49.0	47.8
TiO2	2.16	1.81	1.73	1.36	1.18	1.14	1.08	1.78
Al2O3	12.8	16.7	13.7	14.6	14.5	15.2	15.7	13.6
FeO*	12.1	13.4	10.9	10.6	8.66	8.68	7.84	11.37
MnO	0.19	0.18	0.20	0.15	0.16	0.15	0.14	0.22
MgO	6.02	6.87	6.85	6.98	7.34	7.94	8.34	7.58
CaO	10.3	8.96	7.85	9.11	10.7	9.77	10.5	8.99
Na2O	2.93	2.73	3.69	3.21	3.39	3.67	2.72	3.05
K2O	0.04	0.29	0.01	0.15	0.02	0.12	0.53	0.02
P2O5	0.20	0.17	0.16	0.14	0.10	0.09	0.09	0.16
LOI	2.75	3.94	3.88	3.66	2.64	2.22	2.61	3.65
Total	98.1	97.7	98.2	98.8	98.4	98.7	98.5	98.2
Li	4.25	11.2	9.25	9.41	6.17	10.9	11.1	8.12
Rb	1.10	4.99	0.52	2.23	0.97	1.51	6.70	0.92
Cs	0.06	0.12	0.06	0.31	0.06	0.11	0.48	0.03
Be	0.52	0.46	0.47	0.32	0.47	0.38	0.36	0.52
Sr	334	46	80	146	36	150	129	137
Ba	16.6	30	22	28	10.7	25	50	9.26
Sc	43	50	38	43	43	42	37	44
V	430	386	350	317	284	276	233	374
Cr	140	342	277	257	373	347	364	208
Co	46	48	44	41	51	42	43	45
Ni	53	78	99	77	88	98	95	67
Cu	86	50	64	46	12.3	23	86	112
Zn	85	117	87	101	56	57	489	152
Ga	19.2	19.6	16.2	16.8	14.6	15.9	14.7	17.8
Y	51	44	38	36	28	28	24	40
Nb	3.44	2.53	3.45	1.95	1.64	1.23	1.44	3.50
Ta	0.48	0.35	0.37	0.29	0.44	0.25	0.28	0.37
Zr	124	95	95	75	62	59	63	97
Mo	1.74	1.68	1.67	1.37	2.51	1.36	1.77	1.55
Sn	2.09	1.59	1.57	1.39	1.35	1.08	1.07	1.47
Tl	0.03	0.06	0.00	0.03	0.02	0.01	0.06	0.01
Pb	6.17	4.69	1.57	2.00	1.20	1.33	1.69	1.47
U	0.08	0.05	0.06	0.07	0.04	0.05	0.04	0.06
Th	0.39	0.32	0.29	0.27	0.23	0.22	0.22	0.28
La	4.90	4.98	4.30	4.08	2.57	2.03	2.39	4.48
Ce	14.6	13.3	12.2	10.6	7.71	6.47	7.27	12.6
Pr	2.47	2.25	2.03	1.77	1.32	1.16	1.27	2.11
Nd	14.1	12.7	11.4	10.1	7.65	6.89	7.15	11.7
Sm	5.06	4.43	4.02	3.47	2.72	2.58	2.51	4.24
Eu	2.19	1.71	1.33	1.50	1.12	1.15	1.10	1.53
Gd	6.32	5.67	5.03	4.53	3.67	3.50	3.24	5.28
Tb	1.16	1.01	0.91	0.81	0.66	0.64	0.58	0.94
Dy	8.32	7.21	6.29	5.74	4.55	4.43	3.99	6.79
Ho	1.84	1.57	1.40	1.29	1.01	1.00	0.84	1.48
Er	4.93	4.06	3.65	3.29	2.60	2.68	2.30	3.83
Tm	0.77	0.63	0.56	0.51	0.42	0.42	0.36	0.56
Yb	4.77	3.50	3.25	3.03	2.54	2.53	2.13	3.30
Lu	0.74	0.50	0.50	0.46	0.37	0.38	0.31	0.45
Mg#	0.47	0.48	0.53	0.54	0.60	0.62	0.65	0.54
ASI	0.54	0.79	0.68	0.67	0.58	0.63	0.65	0.64
AI	31.4	38.0	37.3	36.7	34.3	37.5	40.2	38.7
CCPI	85.9	87.0	82.8	83.9	82.4	81.4	83.3	86.1
$(Th/Nb)_{NMORB}$	2.17	2.49	1.63	2.67	2.72	3.50	2.90	1.55

Table 5.1. (Continued). Major (wt.%) and trace (ppm) element composition of the studied samples of the Peltetec and Tres Lagunas Units.

Sample	Group 3 PIMI-22	Group 3 PIMI-43	Group 3 PIMI-81A	Msed P-13	Msed PIMI-14	T. Lagunas P-14	T. Lagunas P-15	T. Lagunas P-26
Lithology	Metabasalt	Metabasalt	Metabasalt	Phyllite	Phyllite	Granite	Granite	Granite
Longitude	773791	771814	775685	755082	774342	755111	764979	770804
Latitude	9817910	9818192	9827810	9748892	9815825	9748972	9774019	9794719
SiO2	48.6	48.3	48.4	75.4	45.2	72.3	70.5	69.5
TiO2	1.34	1.31	1.34	0.64	3.18	0.55	0.64	0.48
Al2O3	14.3	14.0	14.5	11.8	17.6	13.9	13.2	13.5
FeO*	9.66	9.41	9.39	3.81	11.47	2.58	4.13	3.19
MnO	0.18	0.19	0.16	0.03	0.15	0.04	0.12	0.07
MgO	7.32	8.05	7.99	1.10	4.92	1.12	1.73	0.73
CaO	10.6	9.53	10.4	0.19	4.64	0.65	0.74	2.17
Na2O	3.42	3.22	3.14	2.03	2.59	3.38	2.97	4.63
K2O	0.06	0.08	0.08	2.12	3.82	2.25	3.04	1.71
P2O5	0.11	0.12	0.13	0.13	0.54	0.16	0.16	0.15
LOI	2.86	3.87	2.80	2.09	3.95	1.99	1.59	3.03
Total	98.5	98.1	98.3	99.3	98.0	99.0	98.9	99.2
Li	9.86	6.66	10.7	14.9	14.0	12.8	21	7.89
Rb	1.34	0.99	1.17	95	88	86	108	83
Cs	0.05	0.11	0.10	2.93	1.98	3.58	4.41	4.69
Be	0.39	0.41	0.37	1.28	1.80	1.70	2.05	1.90
Sr	90	87	147	24	150	78	204	73
Ba	18.6	8.97	18.6	157	365	173	766	282
Sc	45	43	41	8.56	26	6.91	10.8	9.15
V	321	310	291	79	252	51	70	48
Cr	215	318	266	44	160	53	70	46
Co	46	58	43	18.2	53	28	43	24
Ni	73	85	84	10.2	132	10.7	17.0	10.8
Cu	72	192	77	39	54	15.0	13.2	10.3
Zn	71	133	53	80	141	46	87	54
Ga	16.1	15.7	15.2	13.5	23	17.6	18.0	16.3
Y	31	31	31	18.1	28	17.9	25	21
Nb	2.13	1.83	1.68	10.0	41	11.3	11.8	10.7
Ta	0.29	0.33	0.25	0.89	2.82	1.16	1.27	1.04
Zr	70	70	74	277	233	216	241	216
Mo	1.37	2.81	1.07	3.56	0.83	5.36	6.13	4.52
Sn	1.11	1.11	1.19	2.37	2.42	4.92	3.00	4.05
Tl	0.01	0.01	0.01	0.56	0.35	0.53	0.80	0.63
Pb	1.48	1.26	1.42	13.2	4.82	23.5	12.2	38
U	0.04	0.05	0.07	2.54	0.56	1.07	1.68	1.44
Th	0.23	0.21	0.22	9.74	2.69	8.15	11.6	9.58
La	3.07	2.92	2.52	29.8	34.0	24.3	32.2	59
Ce	8.92	8.67	7.95	56	73	57	68	98
Pr	1.49	1.47	1.40	6.18	8.60	5.94	7.61	9.93
Nd	8.58	8.44	8.26	23	35	23	29	37
Sm	2.95	2.99	2.90	4.63	7.72	4.79	6.03	7.10
Eu	1.66	1.17	2.09	1.56	5.68	0.73	1.13	2.16
Gd	3.92	3.97	3.74	4.18	7.35	4.20	5.68	6.57
Tb	0.71	0.73	0.71	0.55	1.00	0.56	0.79	0.78
Dy	5.02	5.12	4.89	3.14	5.54	3.12	4.49	3.76
Ho	1.13	1.14	1.13	0.63	1.07	0.63	0.87	0.69
Er	3.02	3.03	3.01	1.76	2.56	1.69	2.17	1.68
Tm	0.49	0.50	0.47	0.29	0.37	0.26	0.33	0.26
Yb	2.91	2.96	2.87	1.81	2.13	1.61	1.92	1.65
Lu	0.46	0.47	0.42	0.28	0.34	0.22	0.26	0.23
Mg#	0.57	0.60	0.60	0.34	0.43	0.44	0.43	0.29
ASI	0.57	0.62	0.60	1.97	1.05	1.52	1.39	1.01
AI	34.4	38.9	37.4					
CCPI	83.0	84.1	84.4					
$(Th/Nb)_{NMORB}$	2.06	2.22	2.50	18.8	1.28	14.0	19.06	17.3

Table 5.1. (Continued).

FeO*: Total iron content

Mg#: molar ratio MgO/(MgO+FeO*)

ASI: aluminium saturation index; ASI = molar Al2O3/(CaO + Na2O + K2O)

AI: Ishikawa alteration index (Ishikawa et al., 1976); AI=100*(K2O+MgO)/(K2O+MgO+Na2O+CaO)

CCPI: chlorite-carbonate-pyrite index (Large et al., 2001); CCPI=100*(MgO+FeO)/(MgO+FeO+Na2O+K2O)

(Th/Nb)NMORB : ratio normalized to NMORB (Sun and McDonough, 1989)

Latitude and longitude in the coordinate system WGS84 UTM zone 17S

Group 1 mafic rocks. This group is defined by the lowest TiO_2 content (0.67 to 0.82 wt.%; Figure 5.6c) of non-cumulate mafic rocks, together with low Cr content (18-34 ppm) and Mg# ranging between 0.54 and 0.56. Their chondrite-normalized REE patterns show enrichment in LREE with respect to MREE and HREE ($(La/Yb)_n$ = 1.83-2.43, $(La/Sm)_n$ = 1.19-1.42, $(Sm/Yb)_n$ = 1.41-1.71), similar to EMORB and oceanic arc basalts (Figure 5.7b). One sample has a positive Eu anomaly (Eu/Eu* = 1.75) suggesting local plagioclase fractionation. In the multi-element diagram normalized to NMORB (Figure 5.7b) the most incompatible immobile elements (Th, La, Ce) are enriched, Th shows a moderate to highly positive anomaly ($(Th/La)_{NMORB}$ = 4.20-84.40) and some samples have slightly negative Nb ($(Nb/La)_{NMORB}$ = 0.50-0.52) and Zr anomalies. The Nb/Yb ratio is high (average 2.2). In general, the compatible elements are depleted relative to NMORB. The degree of influence of subduction derived components or of continental crust assimilation is moderate to high, as indicated by $(Th/Nb)_{NMORB}$ = 8.12-53.91 (Figure 5.7b; Pearce, 2014).

Group 2 mafic rocks. This group is defined by intermediate TiO_2 (0.69-1.01 wt.%) and intermediate to high Cr (136-716 ppm) contents (Figure 5.6c). The Mg# in metabasalts ranges between 0.45 and 0.64, while it is slightly higher in metadiabases (0.59-0.69). The chondrite-normalized REE patterns are similar to NMORB ($(La/Yb)_n$ = 0.28-1.16, $(La/Sm)_n$ = 0.31-1.09, $(Sm/Yb)_n$ = 0.78-1.14) with occasional mild enrichment in La (Figure 5.7c). Metabasalts show a positive Eu anomaly (Eu/Eu* = 1.4-2.60) that is absent in metadiabases, indicating a more primitive nature of the latter. In the multi-element NMORB-normalized diagram (Figure 5.7c), the samples show flat patterns except for Th that shows positive anomalies ($(Th/La)_{NMORB}$ = 2.19-15.59). It is notorious the negative anomaly of Nb ($(Nb/La)_{NMORB}$ = 0.49-1.00), the slightly negative anomaly of Zr and the low Nb/Yb ratio (mean 0.55). The NMORB-normalized patterns (Figure 5.7c) show a slight depletion of incompatible elements. The $(Th/Nb)_{NMORB}$ ratio is moderate to high (3.5-26.42).

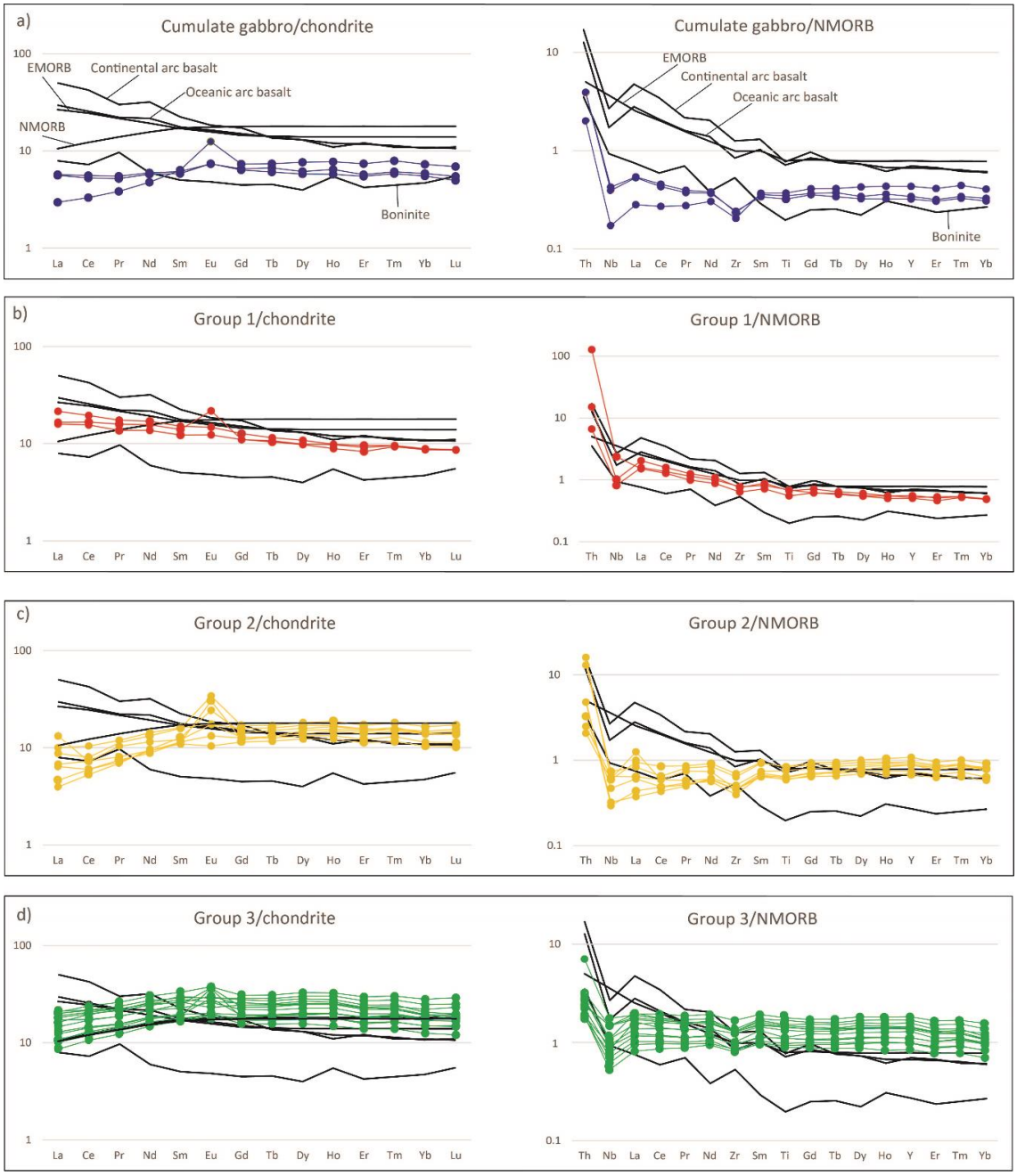

Figure 5.7. Chondrite-normalized REE and NMORB-normalized immobile multi-element diagrams (Sun and McDonough, 1989). a) cumulate grabbros, b) group 1, c) group 2, and d) group 3. The reference NMORB and EMORB are from Sun and McDonough (1989) and the continental and oceanic arc basalts and boninite are from Kelemen et al. (2014).

Group 3 mafic rocks. This group includes most of the metamafic samples and is defined by the highest TiO_2 contents (1.08-2.16 wt.%) and intermediate Cr contents (128-373 ppm) (Figure 5.6c). They correspond to evolved basaltic rocks, as indicated by Mg# ranging between 0.47-0.65. Metadiabases and metabasalts show the same geochemical features. Like group 2 rocks, chondrite-normalized REE patterns show a NMORB like signature with

$(La/Yb)_n$ = 0.58-1.03 and $(La/Sm)_n$ = 0.51-0.78 (Figure 5.7d). However, this group has higher ∑REE (35-72) than group 2 (24-35) and does not show local La enrichments (Figure 5.7c-d). Some samples have positive Eu anomalies (Eu/Eu* = 1.16-1.94). The MREE are slightly enriched (10-40 sample/chondrite values) and tend to develop flat patterns with respect to HREE ($(Sm/Yb)_n$ = 1.12-1.43). In the multi-element diagram normalized to NMORB, immobile elements have flat patterns close to 1x, with positive anomalies in Th ($(Th/La)_{NMORB}$ = 1.3-3.72) and negative anomalies in Nb ($(Nb/La)_{NMORB}$ = 0.51-0.93) and, to a much lesser extent, Zr. The Nb/Yb ratio (mean 0.7) and the $(Th/Nb)_{NMORB}$ ratio (1.55-4.01; Figure 5.7d) are low.

Metasedimentary rocks. Major element contents are varied, but the samples show a similar composition in terms of REE. According to the classification of terrigenous sandstones and shales using $log(Na_2O/K_2O)$ vs $log(SiO_2/Al_2O_3)$ (Figure 5.8a; Herron, 1988) the samples corresponds to litharenite and greywacke, while using the $log(Fe_2O_3/K_2O)$ vs $log(SiO_2/Al_2O_3)$ (Figure 5.8b), one sample plots in the litharenite field and the other evidence enrichment in Fe_2O_3 and classifies as shale.

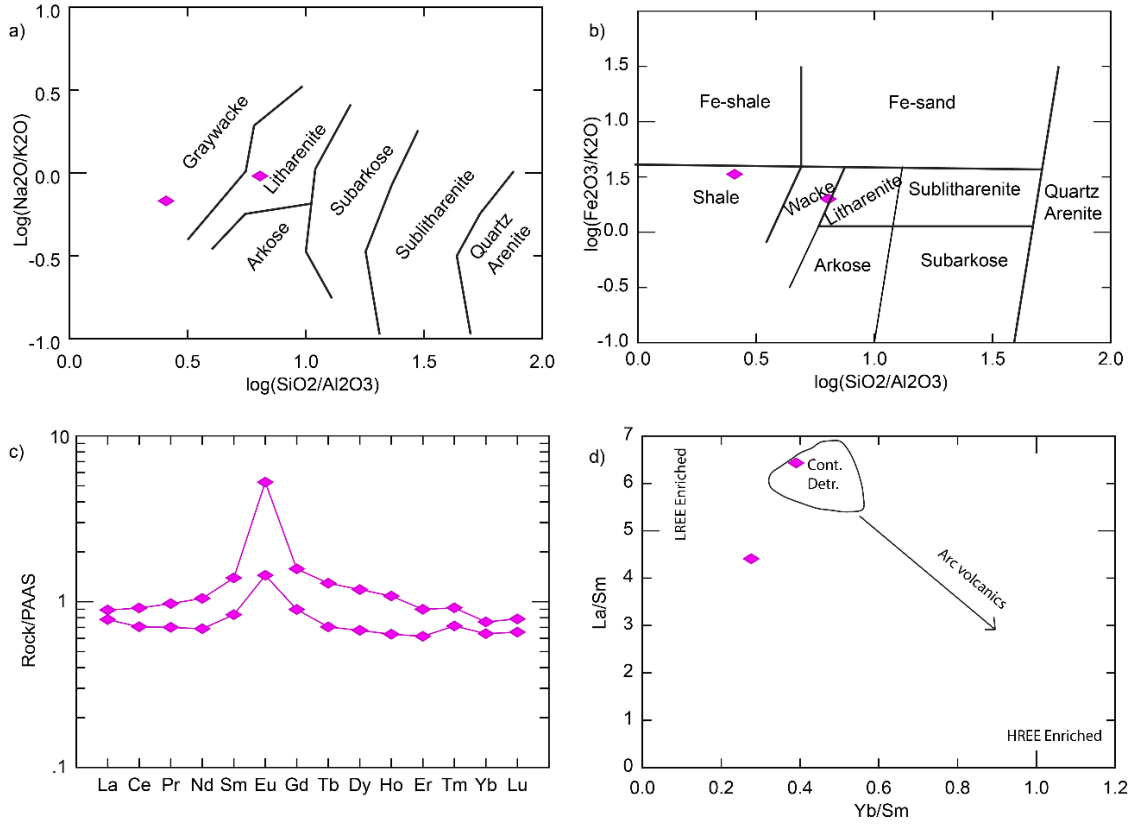

Figure 5.8. Geochemical characteristics of metasediments. a) Classification of terrigenous sandstones using $log(Na_2O/K_2O)$ vs $log(SiO_2/Al_2O_3)$ (Herron, 1988). b) Classification of terrigenous sandstones and shales using the $log(Fe_2O_3/K_2O)$ vs $log(SiO_2/Al_2O_3)$ (Herron, 1988). c) REE normalized to Post Archaean Australian Shale (PAAS) (Taylor and McLennan, 1985). d) La/Sm – Yb/Sm diagram (fields from Plank and Langmuir, 1998).

REE show flat patterns around 1x normalized to Post Archaean Australian Shale (PAAS) (Figure 5.8c, Taylor and McLennan, 1985), but show a clear positive Eu anomaly denoting the presence of detrital plagioclase. The chondrite-normalized REE show enrichment in LREE relative to MREE and HREE ($(La/Yb)_n$ = 11.46-11.82, $(La/Sm)_n$ = 2.85-4.15, $(Sm/Yb)_n$ = 2.85-4.03)) that suggests a continental source (Figure 5.8d).

Tres Lagunas Unit. Three granite samples show homogeneous geochemical characteristics with high SiO_2 wt.% content (69.5-72.3), high $Na_2O + K_2O$ wt.% (5.6-6.3) and peraluminous affinity with Alumina Saturation Index (ASI) of 1-1.5 (Table 5.1). In the multi-element diagram normalized to Primitive Mantle the most incompatible elements are enriched with respect to compatibles, Pb shows positive anomaly and Ba, Nb, Sr, P, and Ti show negative anomalies (Figure 5.9a). The chondrite-normalized REE patterns (Figure 5.9b) show enrichment in LREE relative to MREE and HREE ($(La/Yb)_n$ = 10.8-25.6, $(La/Sm)_n$ = 3.3-5.3 and $(Sm/Yb)_n$ = 3.3-4.8)). Two samples show a negative Eu anomaly (Eu/Eu* = 0.50 and 0.59). LILE, HFSE and the REE show patterns near-flat around 1x when normalized to Upper Continental Crust (UCC) (Figure 5.9c-d; Taylor and McLennan, 1985) with negative Ba, U, Nb and Sr anomalies (Figure 5.9c).

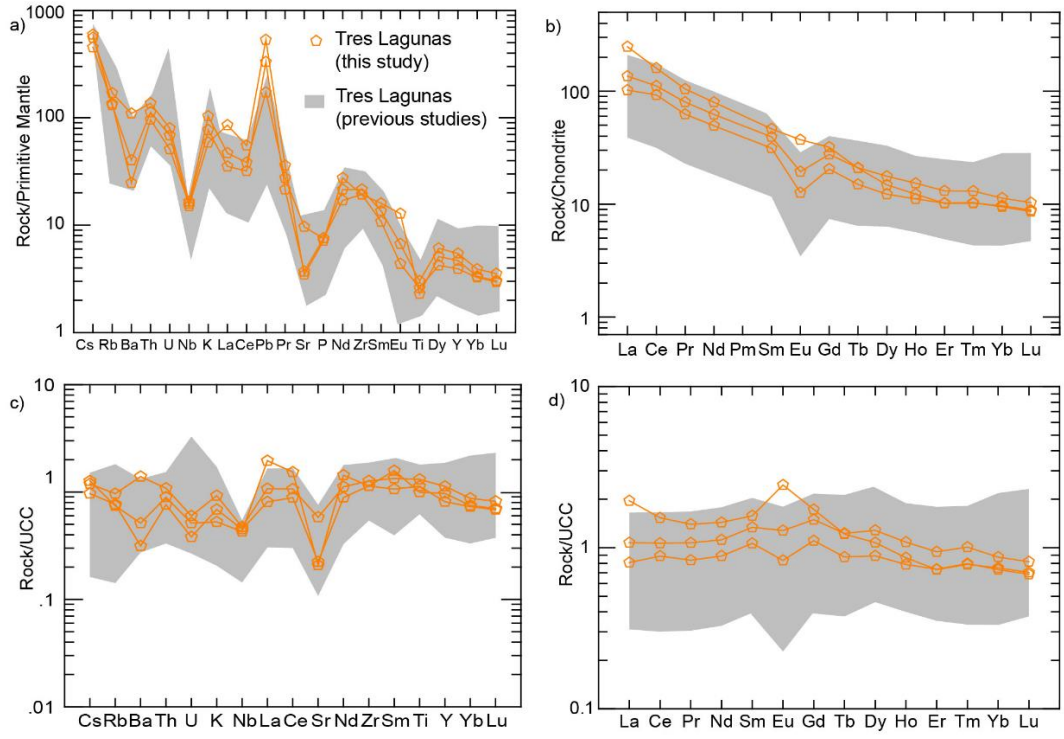

Figure 5.9. Composition of granites of the Tres Lagunas Unit to the West of the Peltetec Unit. a) Multi-element diagram normalized to Primitive Mantle (Sun and McDonough, 1989). b) REE normalized to chondrite (Sun and McDonough, 1989). c) Multi-element diagram normalized to upper continental crust (UCC; Taylor and MacLennan, 1985) d) REE normalized to UCC (Taylor and MacLennan, 1985). Also represented is the field of published data of this unit from other sectors (Cochrane et al. 2014a; Paul et al., 2018).

5.5.4 U-Pb zircon geochronology

SHRIMP U-Pb analyses of zircons from Peltetec and Tres Lagunas Units are presented in Figure 5.10 and Table 5.2. The discordant analyses (>5% discordance as defined in Table 5.2) were excluded for the weighted mean age calculations.

Zircon crystals from metadiabase sample P-23 are small (transversal section of 150 µm length and 70 µm width), most of them euhedral to subhedral in shape. Cathodoluminescence images show oscillatory zoning in most grains and some crystals have inherited cores (Figure 5.10a). Eight measurements on 8 zircons show U content ranging from 248 to 1195 ppm and Th from 35 to 595 ppm, with Th/U in the range of 0.08-0.91. Seven concordant analyses (0.9 to 2.3% discordance) yielded a weighted mean $^{206}Pb/^{238}U$ age of 228.1 ± 1.7 Ma (MSWD = 0.96) (Figure 5.10a; Table 5.2), which is considered the age of magmatic crystallization. Five measurements from inherited grains and cores show U content ranging from 143 to 587 ppm and Th from 122 to 574 ppm, with Th/U in the range of 0.57-1. The concordant analyses (0.6 to 4.6% discordance) show a $^{206}Pb/^{238}U$ apparent age of 247.7 ± 5.3 Ma and 258 ± 3.0 Ma, and a $^{207}Pb/^{206}Pb$ apparent age of 1064 ± 17 Ma. Two discordant analyses yield a $^{206}Pb/^{238}U$ apparent age of 325 ± 8 Ma and $^{207}Pb/^{206}Pb$ apparent age of 1776 ± 7 Ma (6.5 and 6.6%, discordance, respectively).

Zircon grains of granite sample P-26 from the Tres Lagunas Unit have euhedral to subhedral shapes and bipyramidal terminations. Cathodoluminescence images show well defined oscillatory zoning and inherited cores (Figure 5.10b). Eighteen measurements show a wide range of U (212-1151 ppm) and Th (33-596) concentration, with Th/U = 0.06-0.97 (Table 5.2). All analyses are concordant (-2.7 to 3.3% discordance) and yield a $^{206}Pb/^{238}U$ weighted mean age of 228.2 ± 0.8 Ma (MSWD = 2.5), which is considered the age of magmatic crystallization (Figure 5.10b). Thirteen measurements from inherited cores and grains show U content ranging from 98 to 1265 ppm and Th from 4 to 714 ppm, with Th/U in the range of 0.03-1.35. The analyses are concordant (-2.8 to 4.6% discordance) and show different ages with one $^{207}Pb/^{206}Pb$ apparent age of 919 ± 57 Ma and one of 1030 ± 69 Ma, and varied $^{206}Pb/^{238}U$ apparent ages with four ages ranging from 511 Ma to 617 Ma, one age of 465 Ma and one of 475 Ma, one determination of 345 Ma and three ages that range from 241 Ma to 249 Ma. One discordant (6% discordance) analysis yield $^{206}Pb/^{238}U$ apparent age of 580 Ma.

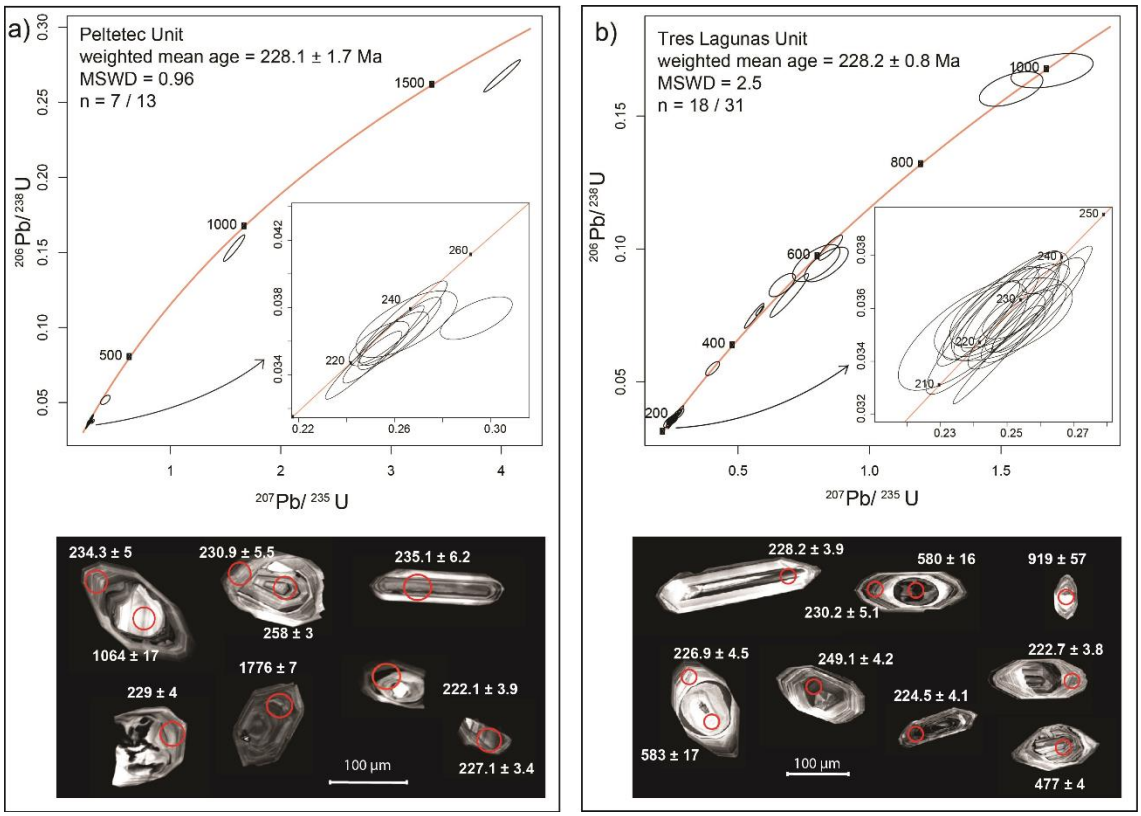

Figure 5.10. Zircon U-Pb data and representative CL images from a) metadiabase sample P-23 of the Peltetec Unit and b) granite sample P-26 of the Tres Lagunas Unit. The concordia plots include inherited grains and cores. Analytical spots and the corresponding $^{206}Pb/^{238}U$ ages are shown in the cathodoluminescence images; pre-Cambrian ages correspond to $^{207}Pb/^{206}Pb$ apparent ages. Data are uncorrected for common lead. MSWD: mean standard weighted deviation. n is the number of concordant spots considered in the weighted mean age from the total analyses (see text for details).

5.5.5 Nd-Sr isotope systematics

Rb-Sr and Sm-Nd isotope systematics of 9 mafic samples, their initial isotopic composition corrected for a magmatic crystallization age of 228.1 Ma and the $\varepsilon Nd_{(t)}$ values are presented in Table 5.3 and in Figure 5.11. Cumulate gabbros have similar values of $(^{87}Sr/^{86}Sr)_i$ (0.704827-0.704968) and $(^{143}Nd/^{144}Nd)_i$ (0.512341-0.512422) with low positive $\varepsilon Nd_{(t)}$ values (+0.07-+1.65; Figure 5.11). Group 1 mafic rocks have similar $(^{143}Nd/^{144}Nd)_i$ = 0.512427 and $\varepsilon Nd_{(t)}$= +1.75 than cumulate gabbros but slightly higher $(^{87}Sr/^{86}Sr)_i$= 0.705211 (Figure 5.11). Both types of mafic groups show relatively low Sm/Nd ratio at low $\varepsilon Nd_{(t)}$ values (Figure 5.11b), indicating a deviation to an enriched source.

Table 5.2. U–Pb zircon SHRIMP data of samples of the Peltetec and Tres Lagunas Units. Data are

Spot	U	Th	206Pb	f206_4	f206_8	Th/U	Isotope ratios						
							$^{207}Pb/^{206}Pb$	±err	$^{206}Pb/^{238}U$	±err	$^{207}Pb/^{235}U$	±err	$^{207}Pb/^{206}Pb$
Sample P-23 (n=13) Peltetec Unit													
zr 1	429	64.9	13.7	0.1	0.0	0.16	0.05194	0.00123	0.03701	0.00083	0.26489	0.00863	281.7
zr 1 core	143	122	19.0	0.1	0.7	0.87	0.07487	0.00064	0.15288	0.00363	1.57740	0.03984	1064.1
zr 2	276	153	12.4	0.0	1.0	0.57	0.05727	0.00205	0.05179	0.00125	0.40880	0.01765	501.0
zr 3	669	595	20.8	0.0	0.8	0.91	0.05127	0.00071	0.03586	0.00053	0.25343	0.00513	252.0
zr 4	330	234	10.7	0.6	2.1	0.73	0.05707	0.00091	0.03737	0.00051	0.29392	0.00615	493.2
zr 5	539	51.8	17.0	0.1	0.1	0.10	0.05215	0.00062	0.03646	0.00089	0.26203	0.00708	291.0
zr 5 core	587	574	20.7	0.0	0.0	1.00	0.05178	0.00043	0.04083	0.00050	0.29135	0.00432	274.7
zr 6	300	271	69.4	0.2	-0.9	0.93	0.10867	0.00044	0.26757	0.00438	4.00739	0.06755	1776.4
zr 7	459	48.3	14.8	-0.2	0.2	0.11	0.05142	0.00054	0.03714	0.00100	0.26317	0.00760	258.7
zr 8	248	34.8	7.6	0.1	0.2	0.14	0.05166	0.00046	0.03534	0.00114	0.25166	0.00841	269.4
zr 9	495	38.7	15.5	0.1	0.0	0.08	0.05210	0.00074	0.03616	0.00064	0.25965	0.00590	288.8
zr 10	1195	93.4	36.3	0.1	-0.1	0.08	0.05189	0.00045	0.03505	0.00063	0.25068	0.00503	279.5
zr 11	267	202	9.1	0.1	0.5	0.78	0.05195	0.00071	0.03917	0.00086	0.28045	0.00727	282.2
Sample P-26 (n=31) Tres Lagunas Unit													
zr 1	442	42.5	13.7	0.0	0.0	0.10	0.04965	0.00066	0.03582	0.00072	0.24512	0.00588	177.6
zr 1 core	157	4.35	12.9	0.2	0.2	0.03	0.06111	0.00215	0.09468	0.00285	0.79735	0.03691	642.1
zr 2 core	220	159	16.5	0.0	-0.1	0.74	0.05611	0.00126	0.08640	0.00179	0.66808	0.02044	455.7
zr 3 core	229	26.3	31.7	0.0	0.1	0.12	0.06970	0.00192	0.16015	0.00266	1.53847	0.04948	918.6
zr 4	790	66.0	24.2	0.0	0.1	0.09	0.05038	0.00069	0.03545	0.00110	0.24611	0.00837	211.5
zr 5 core	432	142	20.6	0.0	0.2	0.34	0.05323	0.00099	0.05500	0.00107	0.40347	0.01084	337.6
zr 6	406	290	13.4	0.2	0.4	0.73	0.05291	0.00085	0.03804	0.00075	0.27740	0.00707	323.9
zr 7 core	169	118	12.0	0.0	0.9	0.72	0.06113	0.00082	0.08251	0.00336	0.69517	0.02984	642.8
zr 8 core	191	45.0	27.7	0.0	0.2	0.24	0.07360	0.00251	0.16705	0.00265	1.69437	0.06375	1029.6

Table 5.2. (Continued). U–Pb zircon SHRIMP data of samples of the Peltetec and Tre

							Isotope ratios						
Spot	U	Th	206Pb	f206_4	f206_8	Th/U	$^{207}Pb/^{206}Pb$	±err	$^{206}Pb/^{238}U$	±err	$^{207}Pb/^{235}U$	±err	$^{207}Pb/^{206}Pb$
zr 9	476	78.1	14.9	0.0	0.3	0.17	0.05026	0.00059	0.03627	0.00078	0.25122	0.00613	206.0
zr 10	340	153	11.2	0.0	0.7	0.46	0.05153	0.00085	0.03820	0.00055	0.27126	0.00594	263.6
zr 11	212	103	6.5	0.0	0.6	0.50	0.05074	0.00147	0.03559	0.00064	0.24891	0.00849	228.0
zr 12 core	98.3	78.7	6.4	0.0	1.8	0.82	0.05441	0.00045	0.07484	0.00191	0.56121	0.01503	387.0
zr 13	723	61.7	22.6	0.1	0.0	0.09	0.05188	0.00064	0.03613	0.00073	0.25832	0.00612	279.1
zr 14	499	76.4	15.3	0.1	0.2	0.16	0.05223	0.00061	0.03543	0.00060	0.25502	0.00524	294.5
zr 15	891	91.3	27.7	0.0	0.0	0.11	0.05055	0.00078	0.03587	0.00075	0.24987	0.00649	219.3
zr 16	692	71.3	21.2	0.0	0.1	0.11	0.04943	0.00049	0.03544	0.00066	0.24139	0.00508	167.2
zr 17	865	69.1	25.5	0.1	0.3	0.08	0.05243	0.00022	0.03411	0.00070	0.24648	0.00519	303.2
zr 18	1151	72.3	36.1	0.0	0.0	0.06	0.05006	0.00019	0.03623	0.00057	0.24997	0.00404	196.7
zr 19	240	58.6	7.2	0.0	0.3	0.25	0.04913	0.00114	0.03496	0.00084	0.23670	0.00793	153.0
zr 20 core	404	375	26.8	0.0	0.2	0.95	0.05506	0.00029	0.07678	0.00072	0.58260	0.00626	413.7
zr 21	571	61.0	18.4	0.0	0.0	0.11	0.05115	0.00048	0.03711	0.00023	0.26164	0.00295	246.6
zr 22	570	70.1	17.6	0.1	0.1	0.13	0.05121	0.00061	0.03571	0.00035	0.25204	0.00387	249.3
zr 23	627	596	19.6	0.0	-0.2	0.97	0.05016	0.00103	0.03603	0.00062	0.24906	0.00665	201.4
zr 24	1048	82.1	33.0	-0.1	0.0	0.08	0.05199	0.00038	0.03635	0.00082	0.26047	0.00617	283.9
zr 24 core	1265	227	103.1	0.0	0.3	0.18	0.06441	0.00189	0.09416	0.00267	0.83592	0.03410	754.2
zr 25	748	714	25.5	0.0	0.5	0.98	0.05161	0.00045	0.03940	0.00067	0.28026	0.00538	267.1
zr 26	443	61.4	13.5	0.1	0.2	0.14	0.05175	0.00060	0.03520	0.00061	0.25107	0.00524	273.3
zr 27 core	188	248	16.4	0.1	0.8	1.35	0.06151	0.00067	0.10047	0.00192	0.85171	0.01873	656.2
zr 28	335	32.9	10.2	0.1	0.1	0.10	0.05225	0.00040	0.03522	0.00036	0.25361	0.00324	295.3
zr 29	650	62.3	20.3	0.0	0.0	0.10	0.05035	0.00089	0.03616	0.00081	0.25090	0.00719	210.1

Table 5.2. (Continued). U–Pb zircon SHRIMP data of samples of the Peltetec and Tres Lagunas Units.

Errors are at one sigma level. The error in $^{206}Pb/^{238}U$ averaging the standard has been already propagated.
Point-to point errors, calculated on replicates of the TEMORA standard, are: 0.32 % for $^{206}Pb/^{238}U$, and 0.37 % for $^{207}Pb/^{206}Pb$
discordance, d(%) = 100*(1-$^{206}Pb/^{238}U$ age /$^{207}Pb/^{235}U$ age)

Basaltic rocks of group 2 have higher values of $(^{143}Nd/^{144}Nd)_i$ (0.512676-0.512776) and $\varepsilon Nd_{(t)}$ (+6.61-+8.56) than gabbros and group 1 mafic rocks, while basaltic rocks of group 3 have uniform $(^{143}Nd/^{144}Nd)_i$ (0.512810-0.512874) and $\varepsilon Nd_{(t)}$ (+9.22-+10.48), indicating an origin from a depleted mantle reservoir. $(^{87}Sr/^{86}Sr)_i$ ratios of groups 2 and 3 are highly variable and range from 0.706673 to 0.708466 and from 0.703773 to 0.706110, respectively. This spread in composition implies a decoupled behavior of the Sr-Nd isotopic system that is best explained by the effect of seawater alteration, less evident in cumulate gabbros and group 1 (Figure 5.11a; e.g. McCulloch et al., 1979; Menuge et al., 1989). In terms of Nd isotopic composition, the basaltic groups 2 and 3 overlap with oceanic rocks of Triassic mafic complexes of the Northern Andes (Piedras, Aburrá, Chinchina, Monte Olivo complexes; Figure 5.11a-b).

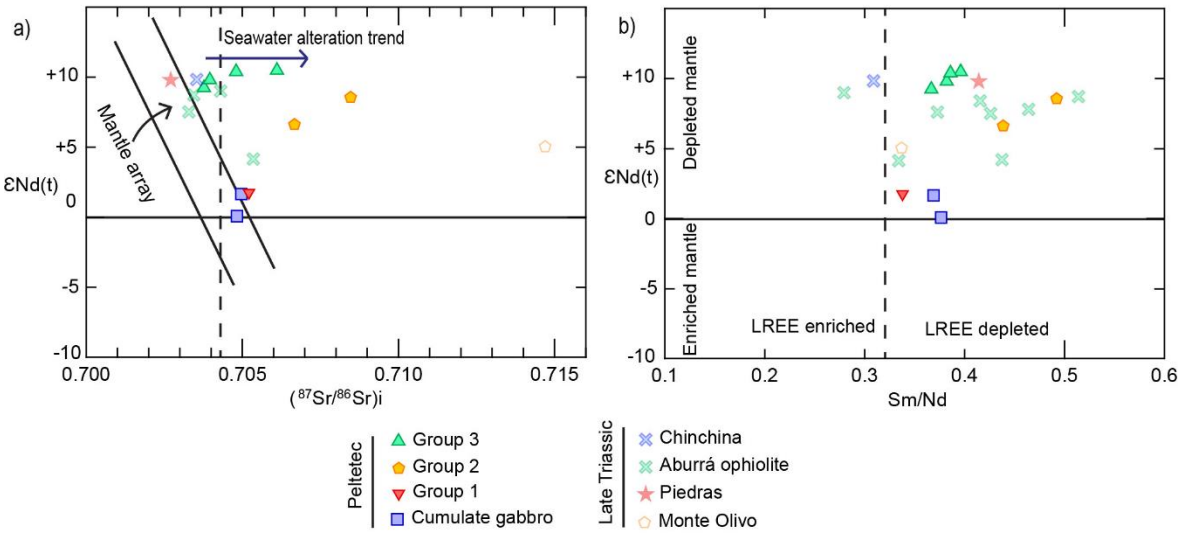

Figure 5.11. a) $\varepsilon Nd_{(t)}$ vs. $(^{87}Sr/^{86}Sr)_i$ and b) $\varepsilon Nd_{(t)}$ vs. Sm/Nd diagrams of mafic rocks of the Peltetec Unit. The $\varepsilon Nd_{(t)}$ values were calculated at 228.1 Ma using present-day CHUR values of $^{147}Sm/^{144}Nd$ = 0.1960 ± 4 and $^{143}Nd/^{144}Nd$ = 0.512630 ± 11 (Bouvier et al., 2008). Data of the Triassic Chinchina, Piedras and Monteolivo units taken from Cochrane et al. (2014a), and the Aburrá Ophiolite-related El Picacho gabbro and Triassic amphibolites from Correa-Martinez et al. (2007) and Cochrane et al. (2014a), respectively.

Table 5.3. Rb-Sr and Sm-Nd isotopic data for mafic rocks of the Peltetec

Sample	Rock type	Basalt group	Rb(ppm)	Sr(ppm)	$^{87}Rb/^{86}Sr$	$^{87}Sr/^{86}Sr$	Error Sr/Sr	$(^{87}Sr/^{86}Sr)_i$ (228.1 Ma)	Sm(ppm)	Nd(ppm)	$^{147}Sm/^{144}Nd$	^{143}N
P-25	Metagabbro		1.40	65.3	0.06185	0.705169	0.003	0.704968	1.03	2.79	0.2231	0.5
P-29	Metagabbro		0.56	25.7	0.06277	0.705031	0.004	0.704827	1.11	2.95	0.2277	0.5
P-44	Metabasalt	1	10.2	103	0.2863	0.706140	0.004	0.705211	2.44	7.23	0.2043	0.5
P-23	Metadiabase	2	1.28	35.1	0.1052	0.707014	0.003	0.706673	1.94	4.43	0.2652	0.5
P-28	Metabasalt	2	0.40	28.4	0.04057	0.708598	0.003	0.708466	2.23	4.54	0.2976	0.5
P-08	Metabasalt	3	0.71	111	0.01844	0.703833	0.003	0.703773	4.47	12.2	0.2217	0.5
P-33	Metabasalt	3	1.46	103	0.04077	0.704097	0.004	0.703965	4.07	10.7	0.2311	0.5
P-47	Metabasalt	3	1.61	131	0.03544	0.706225	0.002	0.706110	2.74	6.93	0.2395	0.5
PIMI-43	Metabasalt	3	0.84	688	0.00353	0.704812	0.002	0.704801	3.19	8.27	0.2333	0.5

Errors are instrumental measurements of $^{87}Sr/^{86}Sr$ and $^{143}Nd/^{144}Nd$ ratios, expressed as 2 sigma

5.6 Discussion

5.6.1 Age of the Peltetec Unit

Litherland et al. (1994) assigned a Jurassic-Early Cretaceous age to the Peltetec ophiolite based in its association with sedimentary slices of the Guamote sequence and Maguazo Unit included in the Peltetec shear zone. On the other hand, two plagioclase $^{40}Ar/^{39}Ar$ ages of ca. 134 Ma were interpreted as the Cretaceous age of the unit (Spikings et al., 2015). However, our weighted mean $^{206}Pb/^{238}U$ Triassic age of 228.1 ± 1.7 Ma from group 2 diabase sample P-23 indicate a much older age of crystallization. We note that magmatic plagioclase is largely altered in the metabasic rocks of the unit, and that the unaltered plagioclase grains correspond to metamorphic albite. Hence, the 134 Ma $^{40}Ar/^{39}Ar$ plagioclase age needs to be reinterpreted as the result of a Cretaceous thermal event, likely the metamorphic imprint of the unit. Similar age (ca. 130 Ma) was determined for the peak HP metamorphism in the Raspas Complex at southwestern Ecuador (Gabriele, 2002; John et al., 2010), while thermochronological studies made in Triassic granitoids and migmatites of the Cordillera Real show re-heating during Middle Jurassic to Cretaceous times associated with burial and increased heat flow during an extensional event (Paul et al., 2018). This thermal event, which may not have to do with the tectonic emplacement of the unit onto the continental margin, would have reset the $^{40}Ar/^{39}Ar$ plagioclase age reported in the Peltetec Unit.

5.6.2 Geochemical affinities and tectonic setting of formation

Immobile elements and isotopic ratios provide valuable information for interpreting the tectonic setting and origin of the igneous protoliths. The mafic rocks of the Peltetec Unit have a tholeiitic affinity, according to immobile elements La and Yb, with a few deviations potentially due to differentiation and/or alteration (Figure 5.12a; Ross and Bédard, 2009). Most of the rocks have NMORB-EMORB signature, although some samples deviate towards volcanic arc basalts (Figure 5.12b; Cabanis and Lecolle, 1989). As shown in Figure 5.12c, the samples have a relatively high Cr content, while Y is variable with the lowest content in cumulate gabbros and increasing from group 1 to 3 mafic rocks. Among the latter, group 1 shows the lowest values of Cr and Y (Figure 5.12c), compatible with arc basalts composition (Cr<34 and Y<16), while basalts groups 2 and 3 are MORB-like (Cr>128 ppm and Y>19; Figure 5.12c). This MORB-like affinity agrees with the low $(La/Sm)_n$ of groups 2 and 3, which is lower than 1 in MORB (Arevalo and McDonough, 2010).

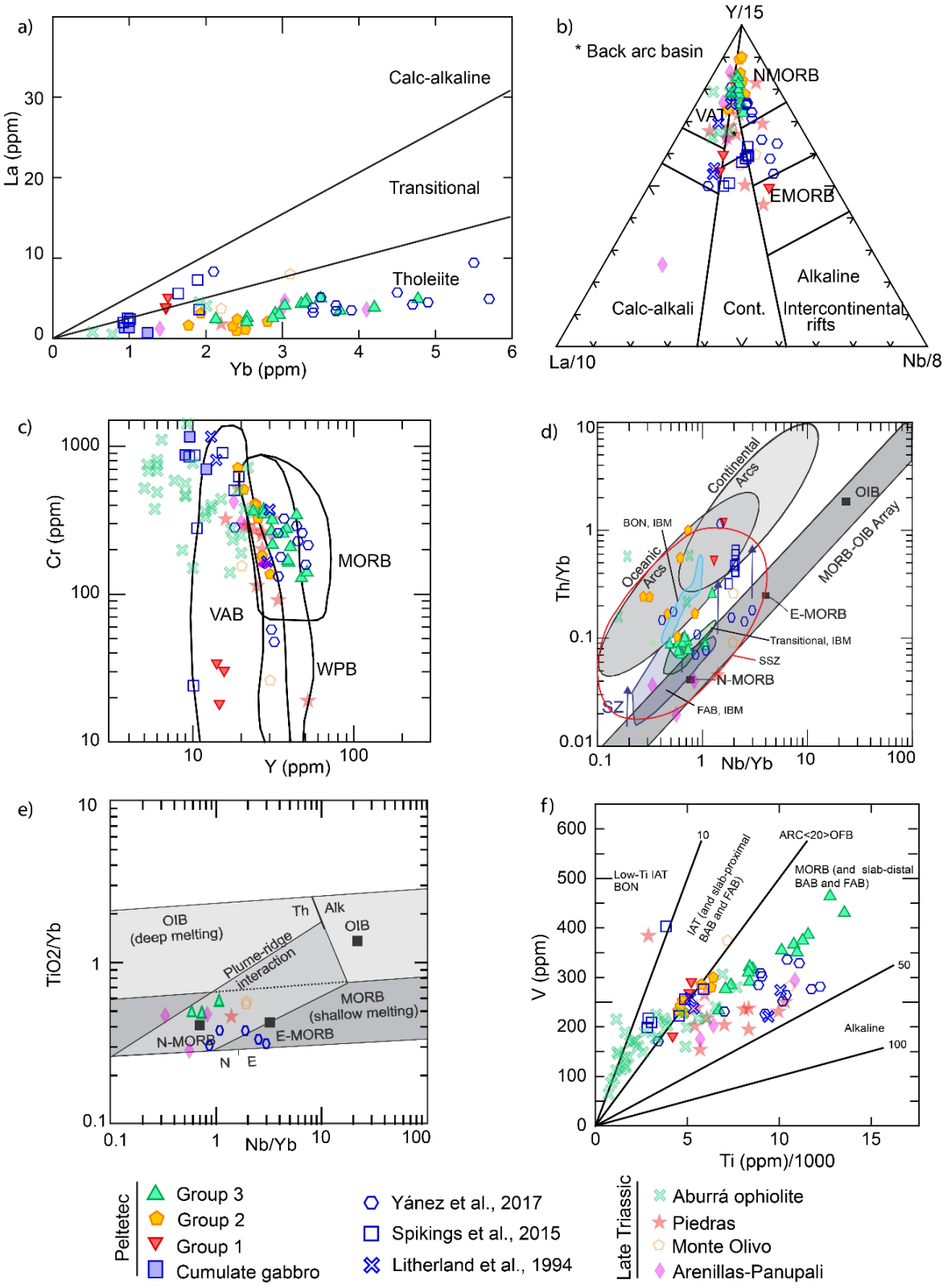
a)
Calc-alkaline
Transitional
Tholeiite
La (ppm)
Yb (ppm)
b)
* Back arc basin
Y/15
NMORB
VAT
EMORB
Alkaline
Calc-alkali
Cont.
Intercontinental rifts
La/10
Nb/8
c)
MORB
VAB
WPB
Cr (ppm)
Y (ppm)
d)
Continental Arcs
OIB
BON, IBM
Oceanic Arcs
MORB-OIB Array
E-MORB
Transitional, IBM
SSZ
N-MORB
SZ
FAB, IBM
Th/Yb
Nb/Yb
e)
OIB (deep melting)
Th
Alk
OIB
Plume-ridge interaction
MORB (shallow melting)
N-MORB
E-MORB
N
E
TiO2/Yb
Nb/Yb
f)
Low-Ti IAT BON
10
IAT (and slab-proximal BAB and FAB)
ARC<20>OFB
MORB (and slab-distal BAB and FAB)
50
Alkaline
100
V (ppm)
Ti (ppm)/1000
Peltetec
Group 3
Group 2
Group 1
Cumulate gabbro
Yánez et al., 2017
Spikings et al., 2015
Litherland et al., 1994
Late Triassic
Aburrá ophiolite
Piedras
Monte Olivo
Arenillas-Panupali

Figure 5.12. (Previous page). Magmatic series and tectonic discrimination diagrams for mafic rocks showing our data and previously published analyses of the Peltetec Unit and Triassic mafic complexes of the Northern Andes. a) La vs Yb (Ross and Bédard, 2009). b) Y-La-Nb (Cabanis and Lecolle, 1989), showing a NMORB-like affinity of back-arc magmas. c) Cr vs Y (Pearce, 1982). d) Nb/Yb vs. Th/Yb (Pearce, 2014) including the MORB-OIB array and NMORB and EMORB of Sun and McDonough (1989). Geochemical data of forearc basalts (FAB), transitional basalts and boninites from the Izu-Bonin-Mariana (IBM) arc are from Reagan et al. (2010) and Ishizuka et al. (2011). Field of supra-subduction zone magmas from data compiled by Dilek and Furnes (2011). e) TiO_2/Yb vs Nb/Yb (Pearce, 2008). f) V vs Ti/1000 (Shervais, 1982); BAB = back-arc basalt, FAB = forearc basalt, BON = boninite, OFB = ocean floor basalt. Data of Aburrá Ophiolite-related El Picacho gabbro, Espadera-Chupadero amphibolites and Triassic amphibolites from Correa-Martinez (2007), Restrepo (2008) and Cochrane et al. (2014a), respectively. Data of Arenillas-Panupali from Litherland et al. (1994) and Bosch et al. (2002), Monteolivo from Cochrane et al. (2014a) and Piedras from Litherland et al. (1994) and Cochrane et al. (2014a). Given that published geochemical data are not complete, the number of represented samples is different in each diagram.

Thorium in the studied rocks is variably enriched while niobium generally shows negative anomalies. These characteristics yield high $(Th/Nb)_{NMORB}$ ratios in all mafic groups of the Peltetec Unit ($(Th/Nb)_{NMORB} > 1$), decreasing from group 1 through group 2 to group 3 (Table 5.1), which suggests magmas influenced by subduction derived components or crustal assimilation (Pearce, 2014, and references therein). The use of a normalizing factor such as Yb eliminates the variations due to partial melting and fractional crystallization (Pearce, 1982). Following this statement, lavas from oceanic settings plot along the MORB-OIB array in the Th/Yb versus Nb/Yb plot, while lavas derived from a mantle modified by subduction-derived fluids and melts or affected by assimilation of continental crust are displaced to higher Th/Yb ratios (Figure 5.12d; Pearce, 2008; Pearce, 2014). Most samples from the Peltetec Unit are enriched in the Th/Yb ratio and displaced above the MORB-OIB array (Figure 5.12d), suggesting that subduction-derived components and/or assimilation of continental crust played a role in the genesis of the oceanic crust, while the Nb/Yb ratio point to variability in the enrichment in incompatible elements of the mantel source.

Samples less influenced by a subduction zone components or continental crust assimilation are represented in the TiO_2/Yb *vs.* Nb/Yb diagram of Figure 5.12e (Pearce, 2008). Rocks with low TiO_2/Yb and Nb/Yb, like in the Peltetec Unit, point to a shallow melting environment of a depleted to a moderately depleted source. On the other hand, the samples that show a subduction-related affinity (Figure 5.12d) were plotted in the V *vs.* Ti/1000 diagram (Figure 5.12f; Shervais, 1982). Group 3 basalts (Ti/V = 26-32) have the highest concentrations of Ti, plotting in the MORB/back-arc basalt (BAB) field. Instead, samples of groups 1 (Ti/V = 18-23) and 2 (Ti/V = 19-23) plot in the volcanic arc-ocean floor basalt transition, indicating

a greater influence of subduction zone derived components or continental crust contamination (Shervais, 1982; Pearce, 2014). These observations agree with a back-arc origin for the rocks of the Peltetec Unit.

Such inference for groups 2 and 3 is also supported by REE (NMORB-like chondrite normalized patterns), immobile trace element (flat NMORB normalized patterns) and isotope ratios (high $\varepsilon Nd_{(t)}$ values) (Figure 5.7 and Figure 5.11). Both groups 2 and 3 show a clear ocean-floor origin above a subducted slab, with a lower influence of subduction derived components or continental crust contamination for group 3 than for group 2. Besides, group 2 mafic rocks show a variable behavior in the Y-La-Nb and V vs. Ti diagrams with a tendency towards arc magmas (Figure 5.12b and f) that agree with the lower $\varepsilon Nd_{(t)}$ values relative to group 3 basalts (Figure 5.11), which we interpret as a result of an evolution in an oceanic back-arc environment. Continental crust contamination is supported by inherited zircon cores in the dated sample of group 2 mafic rocks (cf. Bea et al. 2020 and references therein), but a mantle derivation of recycled zircons cannot be excluded given the evidence for old zircons in ophiolitic and oceanic volcanic arc rocks (Rojas-Agramonte et al., 2016, Torró et al., 2018). While, the geochemical characteristics of group 1 are consistent with oceanic arc basalt affinity (marked enrichment in the most incompatible elements, low titanium content, high Th/Yb, moderate $(La/Sm)_n$ and $(La/Yb)_n$ and negative Nb anomaly and low $\varepsilon Nd_{(t)}$ values) discarding an EMORB affinity of this group.

The analyzed metasedimentary rocks have REE composition like average shale (Taylor and McLennan, 1985), except for a high Eu positive anomaly (Figure 5.8c) that correlates with significant detrital plagioclase in the protolith, in addition to quartz and pyroxene. High La/Sm and low Yb/Sm ratios are typical of continental detritus (Figure 5.8d; Plank and Langmuir, 1998). These characteristics allow considering a nearby continental source of detritus deposited on top of the oceanic crust.

On the other hand, the close spatial and age relationships of the granitic rocks identified in this study with the Peltetec Unit deserves further discussion. The Tres Lagunas Unit has been interpreted as the result of anatexis of continental crustal material genetically unrelated to the Peltetec oceanic unit (Aspden et al., 1992; Litherland et al., 1994; Spikings et al., 2015). An additional argument for anatexis of continental crust-derived sediments is the presence of inherited, old zircons in the dated sample. Its U-Pb zircon age (228.2 Ma), which is equal to the metadiabase dated here (228.1 Ma), makes a geologic relation between the Tres Lagunas and the Peltetec Units feasible. The studied granitic samples are peraluminous (ASI index > 1) and have a modified alkali–lime index (MALI = Na_2O+K_2O-CaO, wt%) ranging between 5.4 and 4.3 and a (FeO*)/(FeO* + MgO) ratio < 0.81 that,

according to their SiO_2 contents, correspond to calcic affinity and magnesian suite (Figure 5.13a-b; Frost et al., 2001). These compositional ranges are consistent with both I-type and S-type granitoids (Frost et al., 2001). But the CaO content is low for given total FeO content, compatible with S-type granitoids (Figure 5.13c; after Chappell and White, 2001). The trace elements and REE normalized to the UCC show flat patterns around 1x, excluding an oceanic origin. Hence, the dated samples indicate synchronous magmatism both in the continental margin of Gondwana and an adjacent oceanic back-arc basin, pointing to a common tectonic scenario. Besides, our geochemical and geochronologic data agree with the composition and age of the Tres Lagunas Unit (Litherland et al., 1994; Cochrane et a., 2014a; Paul et al., 2018), which western boundary was mapped several kilometers east of the Peltetec Unit and with the Alao arc-related rocks between both Peltetec and Tres Lagunas Units (e.g., Litherland et al., 1994). This observation has important geodynamic consequences, as discussed below.

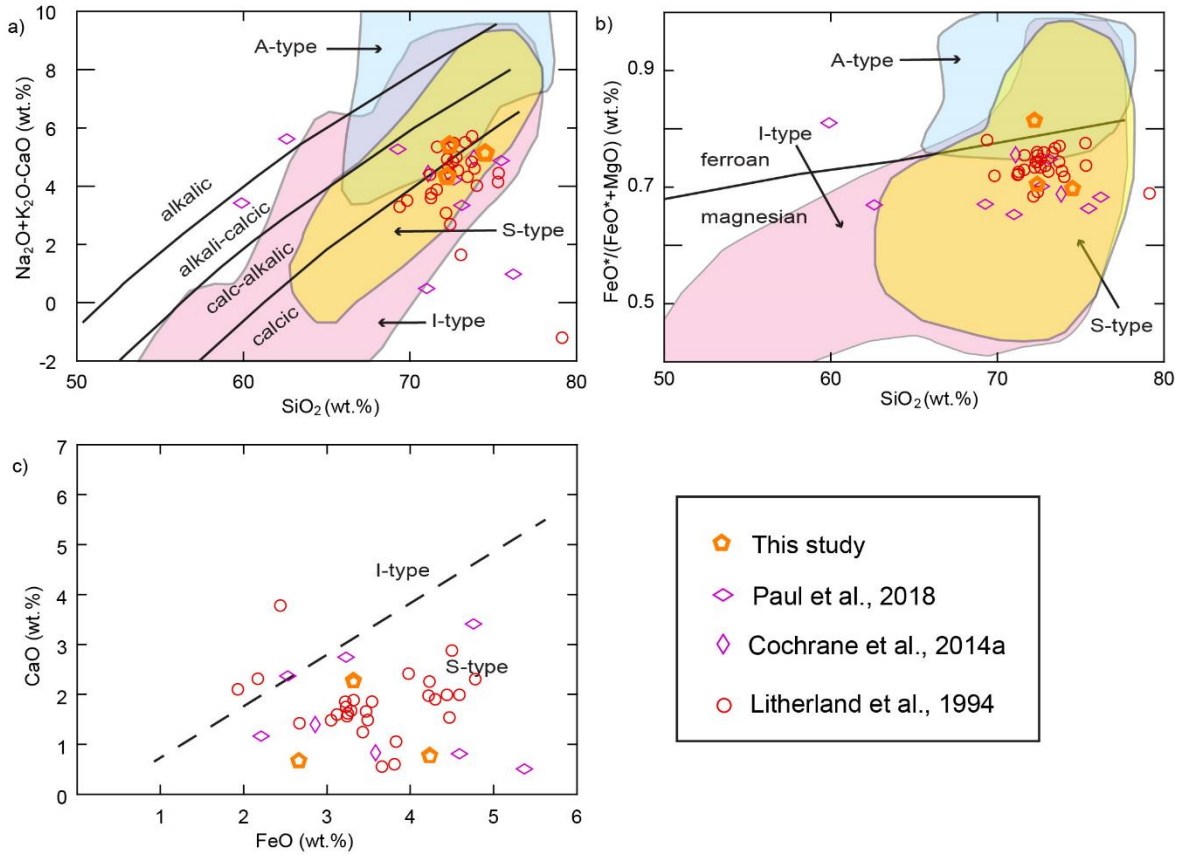

Figure 5.13. Geochemical characteristics of granites from the Tres Lagunas Unit to the West of the Peltetec Unit. a) and b) Na_2O+K_2O-CaO vs SiO_2 and FeO/(FeO*+MgO) vs SiO_2 plots (wt.%); the range of composition (I-type, S-type, A-type) is from the Lachlan Fold Belt (Frost et al., 2001). c) CaO vs FeO (wt.%) showing I-type and S-type granitoids (Chappell and White, 2001). Also represented are published data of the Tres Lagunas Unit.*

5.6.3 Pseudo-chemostratigraphic analysis of the Peltetec basaltic rocks

While an extensive volcanic cover and strong tectonic disruption hinder more comprehensive efforts to geometrically characterize the ophiolitic sequence, the geochemical character of the rock groups allows petro-tectonic analysis. To this end, we offer a pseudo-chemostratigraphic analysis based on the various geochemical groups of basaltic rocks.

As discussed above, the Peltetec ophiolite represents oceanic crust formation in a back-arc setting. Back-arc basalts include arc-like and MORB-like end-members varieties that result from variable mixtures of the end-members sources and, upon development, the influence of upwelling asthenospheric mantle on the development of the magmas as the spreading center locates further away from the arc and subducted slab (e.g., Taylor and Martinez, 2003). The geochemical characteristics of the Peltetec tholeiitic basaltic rocks indicate a DMM asthenospheric source for groups 3 and 2 basalts (Figure 5.7d and c, respectively) and a more enriched mantle source for group 1 basalts (Figure 5.7b). These relations could be interpreted as a progressive shift from an arc setting (group 1) to a NMORB-like setting (groups 2 and 3). Similar shifting is observed in the distribution of HFSEs (e.g. Ti, Y, Yb), V and $\varepsilon Nd_{(t)}$, which progressively increase from group 1 through 2 to group 3 while $(Th/Nb)_{NMORB}$ progressively decreases (Figure 5.14). In the same way, group 3 plots close to the mantle array (Th/Yb *vs*. Nb/Yb diagram, Figure 5.12d), while groups 2 and 1 plot above. Similar behavior is observed in the Cr vs. Y and V vs. Ti/1000 diagrams (Figure 5.12c and f), where group 3 plots in the MORB field while groups 2 and 1 vary from MORB to IAT/VAB. This systematic behavior allows us to suggest that group 1 basalts, with a stronger signature of subduction zone- or continental crust derived- components, could represent an initial stage of oceanic lithosphere development, while groups 2 and 3 would correspond to (diachronous) lower and upper lavas, respectively, of a suprasubduction oceanic lithosphere (cf. Whattam and Stern, 2011, for forearc settings).

The above proposal is in agreement with the evolution of a continental back-arc, where the first products would have been contaminated by the extending continental crust, while juvenile lavas would have erupted once drifting in the back-arc is established, and the influence of the subduction zone and crustal assimilation decrease (Figure 5.15). In this model, the formation of the back-arc basin started before 228 Ma (dated MORB-like sample of group 2 basaltic rocks) with the eruption of continental crust-contaminated group 1 basaltic rocks. Eruption of group 2 at 228 Ma followed, still with evidence of continental crust contamination (less juvenile εNd, Th enrichment and Nb depleted, inherited zircons of the dated sample, with ages ranging between 248 Ma to 1776 Ma), and continued with

group 3 basalts (most juvenile εNd signatures, only slight enrichment in Th and depleted in Nb). Similar conclusions based in zircon Hf isotope geochemistry have been reported in Triassic amphibolites of Ecuador and Colombia, where the oldest rocks (240-232 Ma) have evidence of crustal contamination and the youngest (225 -223 Ma) are more juvenile (Cochrane et al., 2014a; see also Riel et al., 2013; Suhr et al., 2019).

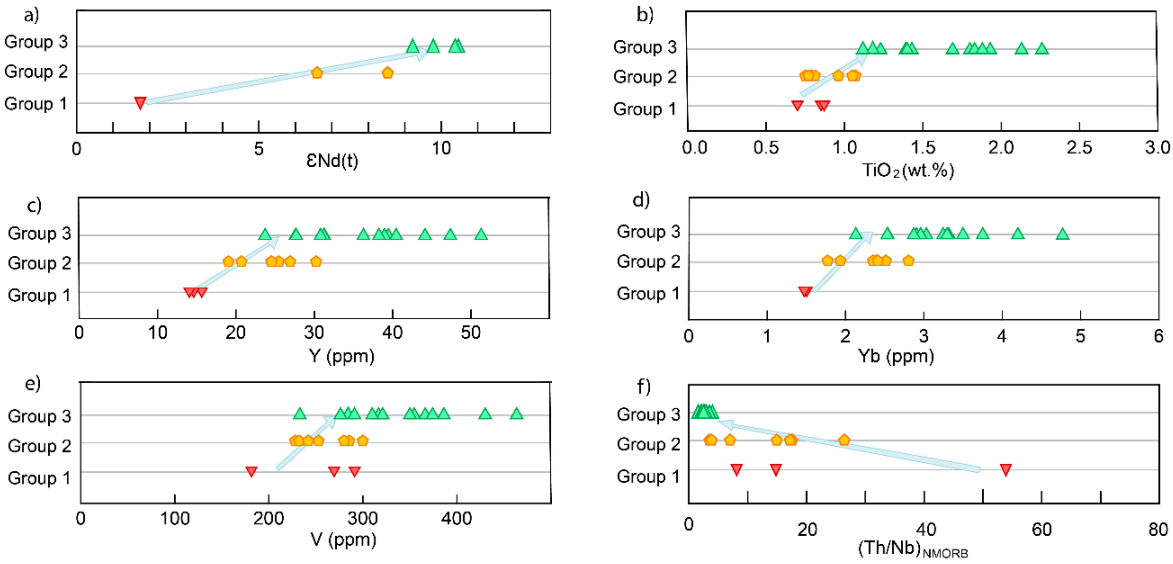

Figure 5.14. Composition ranges of group 1 to 3 metamafic rocks in terms of a) ℰNd(t), b) TiO_2 (wt.%), c) Y (ppm), d) Yb (ppm), e) V (ppm), and f) (Th/Nb)NMORB. Each geochemical group is separated in the y-axis into a single value for each group. The blue arrows indicate potential time evolution.

5.6.4 Regional correlations and tectonic implications

The Triassic age of the Peltetec Unit provided here overturn previous discussions about the Jurassic - early Cretaceous significance and correlations of the Peltetec ophiolite (Aspden and Litherland, 1992; Litherland et al., 1994; Spikings et al., 2015).

Oceanic Permian-Triassic igneous rocks along the NW margin of Gondwana have been reported from Venezuela to Peru associated with different tectonic environments (e.g. Litherland et al., 1994; Restrepo, 2008; Cardona et al., 2010, Villagómez et al., 2011; Reitsma, 2012; Van Der Lelig, 2013; Cochrane et al., 2014a). The Triassic mafic units of Piedras, Arenillas-Panupali and Monte Olivo in Ecuador, and Aburrá Ophiolite in Colombia have $^{40}Ar/^{39}Ar$ hornblende and U-Pb zircon ages ranging between 216 to 239 Ma (Gabriele, 2002; Correa-Martinez, 2007; Noble et al., 1997; Cochrane et al., 2014a; Ibañez-Mejia et al., 2020). In the geochemical comparisons offered below, only the Triassic Aburrá ophiolite-

related El Picacho gabbro, Espadera-Chupadero amphibolites (Correa-Martinez, 2007; Restrepo, 2008) and amphibolites reported by Cochrane et al. (2014a) are considered, while the nominally Triassic Santa Elena amphibolite is excluded given the recent evidence provided for a Cretaceous age (Correa-Martinez et al., 2020; Ibañez-Mejia et al., 2020). The geochemical characteristics of these Triassic Units indicate tholeiitic character and MORB-like (Arenillas-Panupali Unit), BAB (Piedras and Monte Olivo Units) and IAT to BAB (Aburrá Ophiolite) signatures (Figure 5.12), with $(La/Yb)_n$ ranging between 0.46 and 1.9 (Litherland et al., 1994; Bosh et al., 2002; Correa-Martinez, 2007; Restrepo, 2008; Cochrane et al., 2014a) and covering the same geochemical groups of mafic rocks of the Peltetec ophiolite. The Piedras Unit have variable $(Th/Nb)_{NMORB}$ ratio (0.43-19.4) (Litherland et al., 1994; Cochrane et al., 2014a), while the Arenillas-Panupali and Monte Olivo Units are more uniform with values ranging between 0.56 and 2.12 (Litherland et al., 1994; Bosh et al., 2002) and between 0.98 and 2.46 (Cochrane et al., 2014b), respectively. The Aburrá ophiolite has variable $(Th/Nb)_{NMORB}$ (6-15.23; Cochrane et al., 2014a). The $\varepsilon Nd_{(t)}$ values also show similar variation (Figure 5.11), with the Piedras and Monte Olivo Units having values of +9.79 and +5.03 respectively (Cochrane et al., 2014a), the Aburrá Ophiolite ranging between +8.9 and +4.1 (Correa-Martinez, 2007; Cochrane et al., 2014b) and the Chinchina stock +9.8 (Cochrane et al., 2014a).

All these data allow correlation of the suprasubduction Peltetec ophiolite with other oceanic units of the Northern Andes, pointing to generalized “oceanization” of the northwestern convergent continental margin of Gondwana during the Triassic (Figure 5.15).

Oceanic back-arc formation involves the complete rupture of continental lithosphere and the surface extrusion of volcanic products. Basaltic and gabbroic rocks have been described in other Triassic complexes of Ecuador, including intrusions of dykes, sills and plutons (Litherland et al., 1994; Apsden et al., 1995, Gabriele, 2002). These bodies are consistent with our interpretation of generalized Triassic extension of continental crust, magmatic accretion and a thermal anomaly that produced anatexis in the stretching continental crust (Litherland et al., 1994; Reitsma, 2012; Cochrane et al., 2014a; Riel et al., 2013; Spikings et al., 2015). Thus, the granitic rocks of the Tres Lagunas Unit likely formed by contemporaneous anatexis of the continental crust as a result of this thermal event while the back-arc basin opened (Figure 5.15). The position of this unit to the east and west of the Peltetec Unit and their similar age reinforce this view.

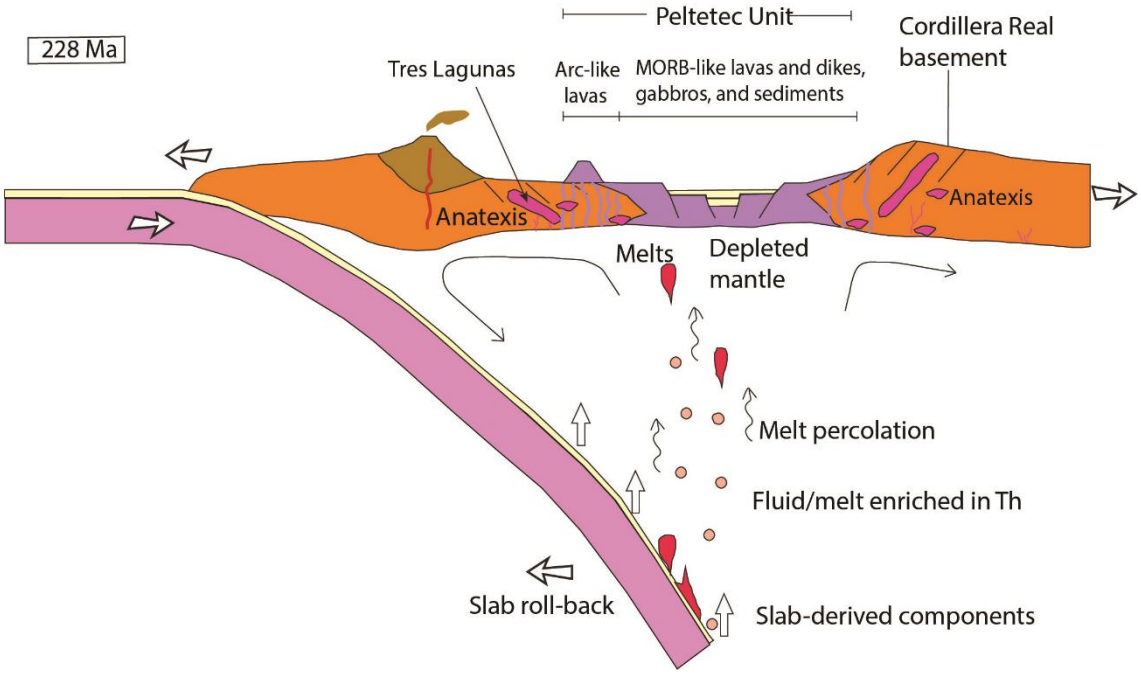

Figure 5.15. Schematic geodynamic model for the Peltetec Ophiolite. Shortly before 228 Ma, trench retreat and slab roll-back triggered extension of the continental lithosphere in a supra-subduction setting, originating the Peltetec oceanic back-arc basin with MORB-like affinity. Anatexis of stretched continental crust is indicated as a potential origin of the Tres Lagunas Unit to the East and West of the basin.

Spikings et al. (2015) have related all these geodynamic processes to the fragmentation of Pangea. However, continental crust stretching and thinning was probably triggered by slab roll-back and trench retreat, ultimately triggering oceanic lithosphere expansion in the nascent back-arc above a subduction system, shortly ensued by convergence, basin closure and ophiolite emplacement (Ibañez-Mejia et al., 2020). This scenario likely applies to (most of) all occurrences of Triassic ophiolitic rocks in the Northern Andes, attesting for the large-scale nature of this event. Indeed, the synchronous back-arc opening and crustal anatexis recorded by the basaltic crust of the Peltetec Ophiolite and the Tres Lagunas Unit suggests that sea floor spreading in the back-arc did not form a broad ocean basin by 228 Ma, Ibañez-Mejia et al (2020) have recently dated oceanic magmatism at ca. 228 Ma in the Aburrá Ophiolite and have interpreted the formation of metamorphic sole at ca. 221 Ma. To be noted, metamorphic soles mark the time of geodynamic inversion and convergence in the oceanic lithosphere that ultimately yield ophiolite obduction (see Wakabayashi and Dilek, 2003 and references therein and application for the Aburrá Ophiolite in Garcia-Casco et al., 2020 and Ibañez-Mejía et al., 2020). Though this evolution cannot be confirmed in the Peltetec ophiolite due to the lack of an associated metamorphic sole, it is chronologically consistent and it can be argued that Triassic extension in the Northern Andes was shortly

ensued by compression. The tectonomagmatic change of the margin from extension to compression is also reported in the El Oro metamorphic complex, related to the tectonic underplating of the oceanic blueschists of the Arenillas-Panupalí Unit under the gabbroic Piedras Unit rapidly cooling the complex as early as 220 Ma (Riel et al., 2014). The basin closure and the emplacement of the Peltetec and other oceanic units of the Northern Andes could be associated with this late Triassic compression regimen, implying that the thermal event that affected the Peltetec unit in the Cretaceous is not related to its emplacement onto the continental margin.

5.7 Conclusions

The Peltetec Unit is a dismembered ophiolite made of tectonic slices of metamorphosed and variably deformed lithologies including (minor) serpentinite, cumulate and non-cumulate metagabbros, metabasalts, metadiabase dykes and metasedimentary rocks. The geochemical and geochronological data (U-Pb SHRIMP zircon age of 228 Ma) suggest a suprasubduction oceanic lithospheric section generated in a back-arc setting as a consequence of extension in the active continental margin of northwestern Gondwana during the Triassic. Inherited zircons in the metamafic rocks and a continental crust affinity of the sediments reinforce its back-arc setting. One group of metabasaltic rocks document melting of a depleted mantle source influenced by subduction components or contamination of continental crust material. This type of rock may represent the initial stage of the Peltetec ophiolite formation. Another two groups of NMORB-like metabasaltic rocks formed after partial melting of a depleted mantle source and likely evolved from liquids more influenced by subduction zone components or continental crust contamination (as evidenced by Th enrichment, Nb depletion and relatively low $\varepsilon Nd_{(t)}$ values) to more depleted liquids (limited Th enrichment and Nb depletion and relatively higher $\varepsilon Nd_{(t)}$ values), documenting oceanization of the continental back-arc. Granites of the Tres Lagunas Unit, closely associated with the Peltetec ophiolite and with equal Triassic age (228 Ma) have geochemical characteristics and inherited zircons that indicate anatexis of continental crust material. Such synchronicity is likely related to heating of the continental crust triggered by the extensional event that originated the back-arc basin. The correlation of the age and geochemical characteristics of the Peltetec Unit with oceanic rocks of the Northern Andes allows confirming a generalized back-arc formation event in the active continental margin of northwestern Gondwana during the late Triassic.

Capítulo 6
Metamorphism and Deformation of the Peltetec belt

6 Metamorphism and deformation of the Peltetec belt

6.1 Introduction

The Northern Andes have been subjected to different major deformation and metamorphic events associated with regional changes in the tectonic regime, including (trans-) extensional and (trans-) compressional scenarios and accretion-collision process (e.g. Litherland et al., 1994; Kerr et al., 1996; Ramos, 1999; Riel et al., 2014; Spikings et al., 2015; Cardona et al., 2020). The Ecuadorian Andes are characterized by two subparallel mountain ranges called the Western and Eastern (Real) Cordilleras separated by the Interandean Valley, and the Oriente basin (retroarc foreland basin) and the Coast plain (forearc) to the east and west of these mountain ranges (Figure 6.1). The basement of the Cordillera Real is composed by variably metamorphosed and deformed rock bodies of continental and oceanic affinities ranging in age from the Paleozoic to the Cenozoic, which allows studying the main geological events in the northwest margin of Gondwana/South America. Using petrographic, structural, geochemical and geochronological data, Litherland et al. (1994) grouped the lithological units from the Cordillera Real in informal lithotectonic "divisions" separated by major faults systems. Recent contributions have focused on constraining the nature and tectonic setting of formation of the crystalline basement based on geochemical and geochronological data (e.g. Cochrane et al., 2014a and 2014 b; Spikings et al., 2015; Villares et al., 2020). However, few contributions have addressed the characterization of deformation and metamorphism (Pratt et al., 2005; Massonne and Toulkeridis, 2012).

Litherland et al. (1994) proposed two major tectono-metamorphic events in the Cordillera Real of Triassic and Jurassic-Cretaceous ages, termed the Tres Lagunas and Peltetec events, responsible for the main deformation and metamorphism. However, Pratt et al. (2005) considered that the main deformation of the Cordillera Real was a consequence of the late Cretaceous collision of the Ecuadorian-Colombian-Caribbean oceanic plateau (e.g. Kerr et al., 2002; Vallejo et al., 2006). On the other hand, metamorphism along the Cordillera Real is variable, with high-grade metamorphism recorded in late Triassic migmatites while other lithological groups have sub-greenschist up to lower amphibolite facies conditions (e.g. Litherland et al., 1994; Pratt et al., 2005), although relicts of high pressure (HP) metamorphism has been reported (Massonne and Toulkeridis, 2012).

The Peltetec Unit represents a dismembered ophiolitic sequence affected by the Peltetec fault zone located in the western margin of the Cordillera Real. Variably deformed and metamorphosed ophiolitic lithologies and S-type granites of Triassic age and

metasediments of Jurassic-Cretaceous age occur along this fault zone. This study offers the first characterization of deformation and metamorphism in the tectonic slices along the Peltetec fault zone focused on the Peltetec Unit by combining structural data, mineral and whole-rock geochemistry of major elements and thermobarometric estimations. Combined with published age data, the results allow constraining the geodynamic evolution of this section of the Northern Andes.

6.2 Previous studies

Litherland et al. (1994) grouped the basement of the Cordillera Real in informal lithotectonic “divisions” separated by major faults systems, namely (from east to west) the Zamora, Salado, Loja, Alao and Guamote divisions (Table 6.1). Recent data have precised the nature and age of these lithologies (e.g. Spikings et al., 2015; Cochrane et al., 2014a, b; Villares et al., 2020; Spikings et al., 2021), though deformation and metamorphism have been mainly described based on field and petrographic observations.

The Tres Lagunas tectonic-metamorphic event (late Triassic; Litherland et al., 1994) was characterized by the intrusion and deformation of the S-type Tres Lagunas granite and by high grade metamorphism in the Sabanilla migmatitic Unit (Table 6.1). According to Litherland et al. (1994), the foliation of the Tres Lagunas granite is associated with major shear zones. A steep foliation (S2) crenulates a first phase of mylonitic deformation. In the Chiguinda Unit, fold structures (D2; cleavage S2 micro crenulation) with steep axial planes refold D1 cleavage. In this unit, the metamorphic minerals are essentially syn D2. In the Agoyán Unit (Table 6.1), Litherland et al. (1994) described a steep schistosity S2 and crenulation cleavage affecting S2, while the Sabanilla migmatitic unit is characterized by a principal S2 foliation with fibrous sillimanite parallel to the S2 cleavage.

On the other hand, the Peltetec event of Litherland et al. (1994), dated late Jurassic-early Cretaceous based on K-Ar ages (interpreted as reset ages of early to medium Jurassic plutons), affected rock bodies of nominally Cretaceous and Jurassic age (Guamote, Peltetec, Alao and Salado Division/Units) and was regionally related to the uprise and erosion of the proto-Andean cordillera. Litherland et al. (1994) described a flat cleavage with local vertical folding (D3) and a first cleavage (axial-plane) of tight to isocline folds with subhorizontal axes in the Guamote metasedimentary sequence. In the Maguazo Unit, these authors described a first phase (D1; probably of isoclinal style) with a steep axial-plane cleavage (S1) dipping to the south, and a penetrative steep schistosity (S2) and higher metamorphic grade within the greenschist facies (quartz, albite, epidote, chlorite) in the Alo-Paute unit (Table 6.1) to the west while garnet and amphibole appear to the east.

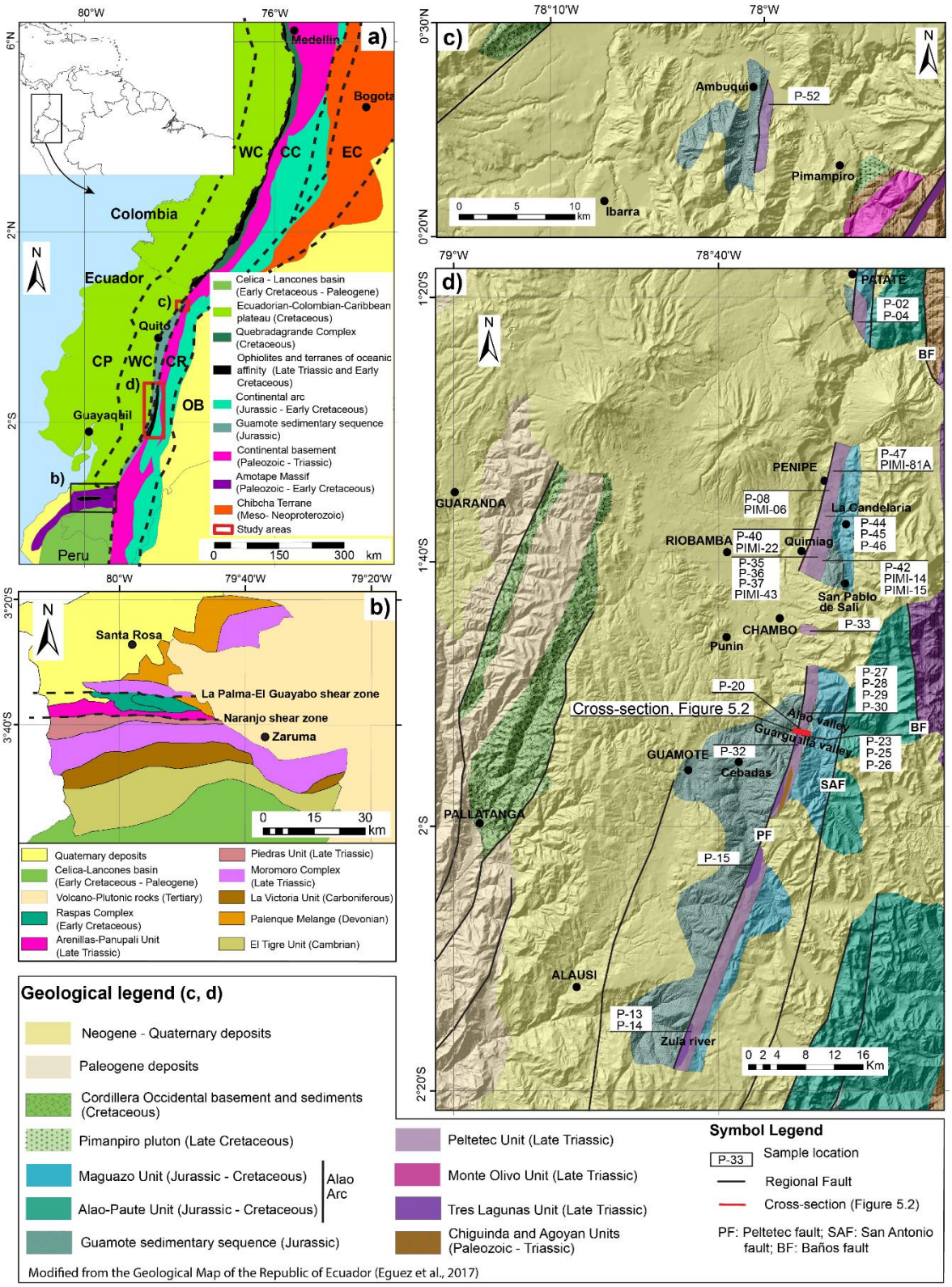
a)
Medellin
Bogota
WC
CC
EC
Colombia
Ecuador
Quito
CP
WC
CR
OB
Guayaquil
Peru
c)
d)
b)
Celica - Lancones basin (Early Cretaceous - Paleogene)
Ecuadorian-Colombian-Caribbean plateau (Cretaceous)
Quebradagrande Complex (Cretaceous)
Ophiolites and terranes of oceanic affinity (Late Triassic and Early Cretaceous)
Continental arc (Jurassic - Early Cretaceous)
Guamote sedimentary sequence (Jurassic)
Continental basement (Paleozoic - Triassic)
Amotape Massif (Paleozoic - Early Cretaceous)
Chibcha Terrane (Meso- Neoproterozoic)
Study areas
0 150 300 km
b)
Santa Rosa
La Palma-El Guayabo shear zone
Naranjo shear zone
Zaruma
0 15 30 km
Quaternary deposits
Celica-Lancones basin (Early Cretaceous - Paleogene)
Volcano-Plutonic rocks (Tertiary)
Raspas Complex (Early Cretaceous)
Arenillas-Panupali Unit (Late Triassic)
Piedras Unit (Late Triassic)
Moromoro Complex (Late Triassic)
La Victoria Unit (Carboniferous)
Palenque Melange (Devonian)
El Tigre Unit (Cambrian)
c)
Ambuqui
P-52
Pimampiro
Ibarra
0 5 10 km
d)
PATATE
P-02
P-04
BF
PENIPE
P-47
PIMI-81A
GUARANDA
P-08
PIMI-06
La Candelaria
P-44
P-45
P-46
RIOBAMBA
P-40
PIMI-22
Quimiag
P-35
P-36
P-37
PIMI-43
P-42
PIMI-14
PIMI-15
San Pablo de Sali
CHAMBO
P-33
Punin
P-20
Cross-section, Figure 5.2
P-27
P-28
P-29
P-30
Alao valley
Guarguallá valley
BF
GUAMOTE
P-32
Cebadas
P-23
P-25
P-26
SAF
PALLATANGA
PF
P-15
ALAUSI
P-13
P-14
Zula river
0 2 4 8 12 16 Km
Geological legend (c, d)
Neogene - Quaternary deposits
Paleogene deposits
Cordillera Occidental basement and sediments (Cretaceous)
Pimanpiro pluton (Late Cretaceous)
Maguazo Unit (Jurassic - Cretaceous)
Alao-Paute Unit (Jurassic - Cretaceous)
Alao Arc
Guamote sedimentary sequence (Jurassic)
Peltetec Unit (Late Triassic)
Monte Olivo Unit (Late Triassic)
Tres Lagunas Unit (Late Triassic)
Chiguinda and Agoyan Units (Paleozoic - Triassic)
Symbol Legend
P-33 Sample location
Regional Fault
Cross-section (Figure 5.2)
PF: Peltetec fault; SAF: San Antonio fault; BF: Baños fault
Modified from the Geological Map of the Republic of Ecuador (Eguez et al., 2017)

Figure 6.1. (Previous page). a) Schematic representation of tectonic complexes in the Northern Andes and location of the study area. Ophiolites and terranes of oceanic affinity are represented in black, including the late Triassic amphibolitized Piedras metagabbro and high-pressure (HP) Arenillas-Panupali Unit and the early Cretaceous HP Raspas complex (Amotape Massif, El Oro metamorphic complex, Southwestern Ecuador), the Peltetec Unit (central Ecuador) and the early Cretaceous Arquía complex (Colombia); dashed line represents the morphological boundary of the Cordilleras, WC: Western Cordillera, CC: Central Cordillera, CP, Coastal plain, CR: Cordillera Real, EC: Eastern Cordillera, OB: Oriente Basin (retroarc foreland basin). b) Simplified geological map of El Oro metamorphic complex, Southwestern Ecuador (after Aspden et al., 1995; Riel et al., 2013; Suhr et al., 2019 and Spikings et al., 2021). c) and d) Geological maps of the studied area; c) Ambuqui zone and d) the zone between Patate – Zula river with the location of analyzed samples (simplified from Egüez et al., 2017).

Litherland et al. (1994) described the Alao arc-related rocks and the Loja Division separated by the Baños fault, interpreted as a NNW-SSW directed shear zone (Figure 6.1), while to the east the Loja Division is separated from the Salado Division by the Llanganates fault. The last division is characterized by low- to medium-grade metamorphism with plutons crosscut by shear zones and development of mylonitic and gneissic fabric.

Instead, Pratt et al. (2005) identified two penetrative foliations (S1 and S2) and one no penetrative crenulation (S3) in pelitic and metavolcanic rocks along a E-W transect across the Cordillera Real. These authors considered inappropriate a terrane model and described an eastward progressive increase in the intensity of deformation and metamorphism along the transverse section across the Cordillera, from sub greenschist facies conditions and a S1 slaty cleavage to intermediate to higher greenschist conditions represented by porfidoblast growth (albite-oligoclase, garnet, chlorite, biotite) during D1 and the development of S2 denoted by oriented quartz, muscovite and biotite. Based on relict phengite composition in metapelites and metabasites, Massonne and Toulkeridis (2012) proposed a high pressure (HP) metamorphic event in rocks to the east of the Alao arc-related units. In other regions, including along the Peltetec fault zone, this event has not been noted, perhaps because the metamorphic conditions have been estimated only by means of petrographic analysis (e.g. Litherland et al., 1994).

In the El Oro Metamorphic Complex (Figure 6.1b; Table 6.2), Litherland et al. (1994) identified two major tectono-metamorphic events of late Triassic (Moromoro event) and late Jurassic-Cretaceous age (Palenque event). The Moromoro event is characterized by dextral shearing that becomes more ductile to the north as the metamorphic grade increases, reaching syntectonic/synmetamorphic granite emplacement. The Palenque event is characterized by deformation of mafic blocks in a metasedimentary matrix with evidence of dextral shearing and by high-pressure metamorphism of the Raspas complex.

Table 6.1. Main basement Units/lithologies along the Cordillera Real. Note that the Peltetec unit and the Huarguallá gabbro have been recently separated out from their original assignment to the Alao division.

Age	Divisions of Litherlant et al., 1994	Unit	Lithology	Metamorphism	Reference
Late Jurassic-early Cretaceous	Alao	Maguazo Unit	Sedimentary	No metamorphosed	Lihterland et al., 1994; Chiaradia et al., 2009; Drobe et al., 2013; Cochrane et al., 2014b; Spikings et al., 2015
		Alao-Paute Unit	Metavolcanic	Low-grade	
		El Pan Unit	Metasedimentary	Low-grade	
	Guamote	Guamote sequence	Metasedimentary	Low-grade	
	Salado	Upano Unit	Metasedimentary/ metavolcanic	Low- to medium-grade	
		e.g. Azafrán	Granitoid	Low- to medium-grade	
Early-mid Jurassic	Zamora	Misahuallí Formation	Volcanic	No metamorphosed	
		e.g. Zamora	Granitoids	No metamorphosed	
Late Triassic	Loja	Tres Lagunas Unit	S-type granite	Low- to medium-grade	Litherland et al., 1994; Noble et al., 1997; Cochrane et al., 2014a; Spikings et al., 2015; Paul et al., 2018; Villares et al., 2020
		Agoyán Unit	Metasedimentary	Low- to medium-grade	
		Sabanilla Unit	Migmatite	High grade	
		Monte Olivo Unit	Mafic dyke (amphibolitized)	Low- to medium-grade	
	Alao	Peltetec Unit	Serpentinite, metagabbro, metabasalt, metasedimentary	Low-grade	
Devonian-Carboniferous	Loja	Chiguinda and Isimanchi Units	Metasedimentary	Low-grade	Litherland et al., 1994; Chew et al., 2007, Spikings et al., 2021
Neoproterozoic	Alao	Huarguallá	Gabbro	Altered	Spikings et al., 2021

While, Riel et al. (2014) identified four major deformation events during the late Triassic to Paleocene. The first event is related to the late Triassic (ca. 230 Ma) emplacement of the Piedras Unit at the roots level of the continental crust that triggered partial melting in an extensional regimen. The deformation was heterogeneous (D1, anatectic event) and highly dependent on the P-T conditions and the proportions of leucosomes (melt above the solidus). The second event (D2; dated 226 Ma) was associated with tectonic underplating

of the blueschist of the Arenillas-Panupali Unit below the Piedras Unit, triggering fast cooling. The third event (D3; early Cretaceous) was characterized by mylonitic deformation (top of the southern tectonic contact between the Piedras Unit and the migmatitic lithologies of the Moromoro Complex), the exhumation and underplating of the high-pressure oceanic Raspas Ophiolitic Complex, and trench-parallel extension that triggered the opening of the NE-SW trending Celica-Lancones Basin in southwest Ecuador and led to the regional tilt of whole complex. The D4 compressive deformation (late Cretaceous-Paleocene) was related to the accretion of oceanic terranes both in Ecuador and Colombia, that was responsible of the regional folding of the continental units in the southern part of the massif, the deformation of the Cretaceous sediments from the north of the Celica-Lancones basin and a tectono-thermal event in the units of the northern part of the massif.

Table 6.2. Main basement Units/lithologies in El Oro Metamorphic Complex

Age	Unit	Lithology	Metamorphism	Reference
Early Cretaceous	Raspas complex	Eclogite, blueschist, serpentinite, metapelites	High pressure / low temperature	Feininger, 1980; Gabriele, 2002; Bosch et al., 2002; John et al., 2010.
Late Triassic	Moromoro complex	Granitoid, migmatite, paragneis	Low- to high-grade	Aspden et al., 1995; Noble et al., 1997; Riel et al., 2013; Suhr et al., 2019.
	Piedras Unit	Metagabbro	Low- to medium-grade	Aspden et al., 1995; Noble et al., 1997; Cochrane et al., 2014a.
	Arenillas-Panupali Unit	Blueschist	High pressure / low temperature	Gabriele, 2002.
Devonian-Carboniferous	La Victoria Unit	Metasedimentary	Low- to high-grade	Aspden et al., 1995; Suhr et al., 2019; Spikings et al., 2021
	Palenque Melange	Metasedimentary	Low- to medium-grade	
Cambrian	El Tigre Unit	Metasedimentary	No metamorphosed to low-grade	

6.3 Results

6.3.1 Field relationships

The tectonic slivers of the Peltetec Unit correspond mainly to metabasaltic and minor metaultramafic and metasedimentary rocks of late Triassic age that conform a fragmented ophiolite (Litherland et al., 1994; Villares et al., 2020). Scattered outcrops of late Triassic granites of the Tres Lagunas Unit and Paleozoic metasedimentary rocks of the Chiguinda Unit occur associated with the ophiolitic rocks (e.g. Litherland et al., 1994; Villares et al., 2020). The unit forms an NNE-SSW oriented 1–2 km wide elongate and narrow belt discontinuously exposed along the western margin of the Cordillera Real, in between the

Guamote metasedimentary sequence (west) and the Maguazo Unit (east) (Figure 1). The best exposed sections are found between Penipe town in the North and the Guamote-Macas road in the South (along ~60 km), although other sections are exposed towards Río Zula in the South, and Patate and Ambuquí in the North. The structure in the central and northern Ecuadorian Andes is dominated by the Peltetec fault (Litherland and Aspden, 1992), which continues to the North in Colombia as the Romeral fault system (e.g. Maya and Gonzalez, 1995; Vinasco, 2019; Figure 6.1) and perhaps to the Southwest in El Oro Metamorphic Complex as the Naranjo shear zone (e.g. Apsden et al., 1995; Figure 6.1b).

In its northern part, the Peltetec Unit appears between quartzites and phyllites similar to the Guamote sedimentary sequence and the Chiguinda Unit (Litherland et al., 1994; Figure 6.1c). In the Patate sector the unit is limited to the west by the Guamote sedimentary sequence and by greenschists of the Alao-Paute unit the east. In Penipe and to the south, the western limit corresponds to the Guamote sedimentary sequence with local slices of the Tres Lagunas and Chiguinda units which are most commonly found south of the Guarguallá Valley, while the eastern limit corresponds to the Maguazo Unit and slices of the Guamote metasedimentary sequence (Litherland et al., 1994; Villares et al., 2020) (Figure 6.1d). The contact zones are characterized by highly deformed and sheared rocks.

6.3.2 Whole-rock major elements composition and mineral assemblages

Villares et al. (2020) divided the metabasaltic rocks from Peltetec Unit into three groups; one with arc affinity (group 1) and two groups with NMORB affinity formed in a back-arc basin (groups 2 and 3), in addition to serpentinites, cumulate gabbros and metasediments. By means of isocon analysis, these authors evidenced changes in the original geochemical composition of the mafic rocks due to alteration and metamorphism (see Chapter 5). In this section, the descriptions are based in the following group of rocks: Serpentinites, cumulate metagabbros, group 1 metabasaltic rocks with arc affinity, groups 2 and 3 metabasaltic rocks with MORB affinity and metasediments. The geochemical data are presented in Table 5.1 and Appendix 6.1 (serpentinites).

The tectonic configuration of the Peltetec Unit does not allow establishing an eventual continuous sequence of metamorphic mineral associations, but variable associations either dominated by alteration minerals or by minerals of the prehnite-pumpellyite to greenschist facies are observed in different tectonic slices, suggesting a potential previous metamorphic zoning obliterated by strike-slip movement along the Peltetec shear zone. Metabasaltic rocks are crosscut by recrystallized and deformed veinlets of quartz and calcite, indicating that alteration (in the oceanic environment) occurred previous to the sub-greenschist and

greenschist facies deformation and metamorphic event. Hence the post-alteration chemical composition of rocks controls the developed metamorphic assemblage. To distinguish the type of alteration in the metabasaltic rocks, the whole rock composition of the samples were plotted in the triangular diagram Na_2O-CaO-MgO (Figure 6.2a; e.g. Cann, 1969; Humphris and Thompson, 1978; Widmer et al., 2000), where an enrichment in CaO suggests the development of calcium-rich phases (e.g. epidote, prehenite, pumpellyite, calcite), high MgO contents indicate chloritization, while high Na_2O contents indicate spilitization (albite growth). Metabasaltic groups 1 and 2 show a deviation towards Na_2O (spilitization), although one sample is enriched in CaO (epidotization), while group 3 is clustered and show little variation in this diagram. According to the content of Na_2O and CaO (Figure 6.2b), group 3 metabasalts cluster close to normal MORB composition, while groups 1 and 2 are scattered with some samples enriched in Na_2O and with a high Na_2O/CaO ratio, reaching the spillite field. These relations suggest mobility of Na and Ca during variably developed spilitization and epidotization of the Peltetec Unit.

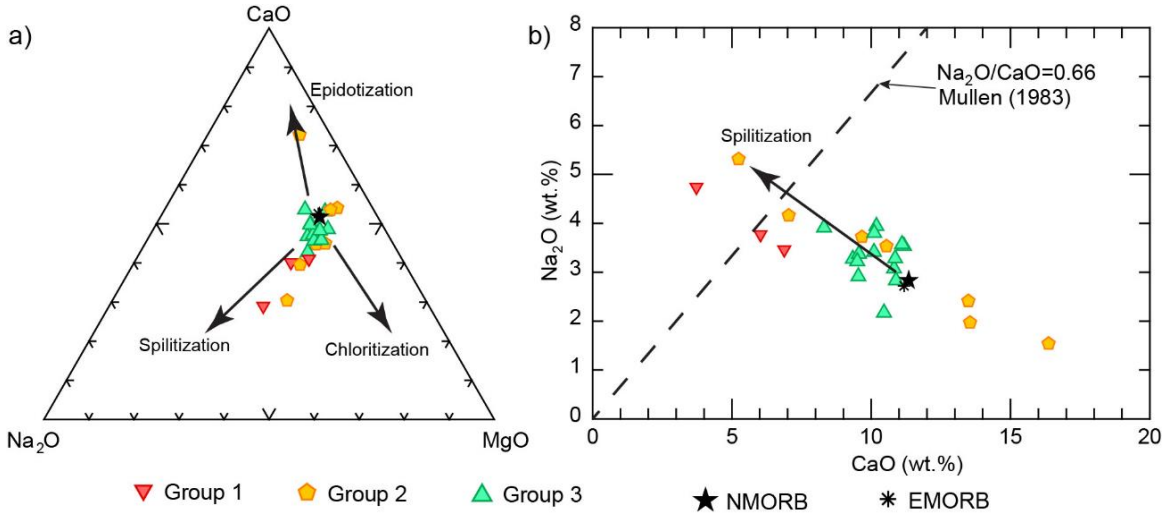

Figure 6.2. Na_2O-CaO-MgO (wt.%) diagram showing alteration trends (spilitization, epidotization and chloritization; after Starr and Pattison, 2019). b) Na_2O vs CaO (wt.%) diagram showing the spillitic field (after Mullen, 1983). NMORB and EMORB compositions are from Gale et al. (2013).

The extent of alteration was also examined using the composition of major elements projected from coexisting phases and appropriate exchange vectors which allow condensation of the composition space (ACF diagram; Figure 6.3). The group 1 of metabasaltic rocks shows a slight peraluminous composition compatible with a propylitic alteration mineral assemblage (sericite-albite-epidote-chlorite; Figure 6.3a). On the other hand, the metagabbros and groups 2 and 3 of metabasaltic rocks show a metaluminous composition compatible with a plagioclase-pyroxene-olivine mineral association typical of

basic rocks, though cumulate metagabbros deviate towards a pyroxene-olivine association, as expected. Serpentinites plot near the F vertex, denoting high Mg (and Fe) in their composition and very low Ca content, characteristic of ultrabasic rocks of harzburgite composition (Figure 6.3a), while metasediments of the Peltetec Unit and granites of the Tres Lagunas Unit show peraluminous composition (Figure 6.3a).

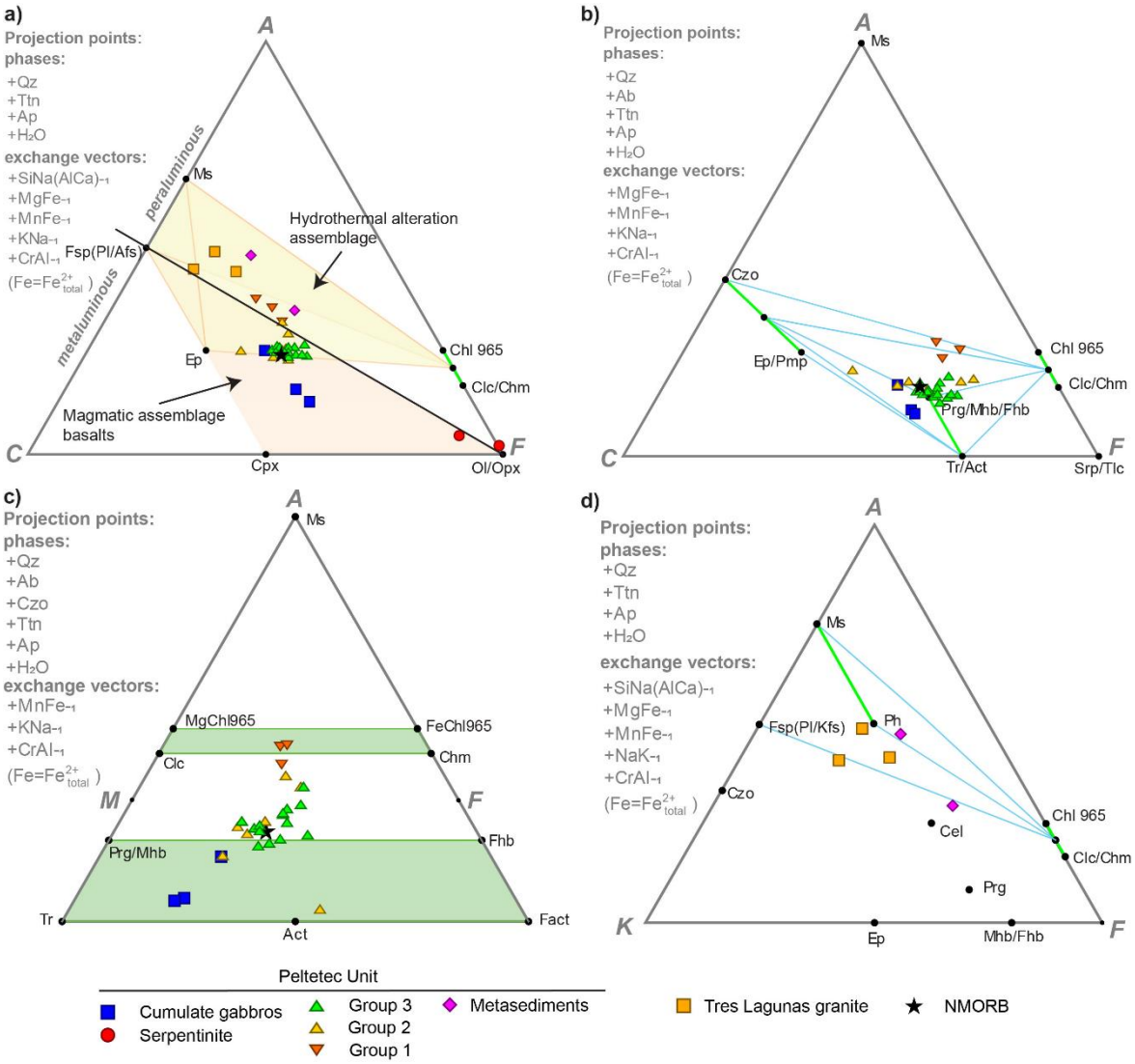

Figure 6.3. Projection of studied samples in the ACF, AMF and AKF diagrams. End-members of mineral phases are represented (black circles; Chl 965 refers to chlorite with Fe+Mg=9, Al=6 and Si=5 atoms per 10 O and 8 OH; Spear, 1993). a) ACF diagram showing the metaluminous and peraluminous fields and expected magmatic and altered compositions. b) ACF diagram for metabasic rocks after projection from albite, indicating greenschist mineral assemblage. c) AMF diagram for metabasic rocks projected from albite and clinozoisite showing that most samples should bear chlorite and amphibole in varied proportions (A-rich samples would not bear amphibole). d) AKF diagram for metasediments of the Peltetec Unit and granitoids of the Tres Lagunas Unit. The diagrams are projected from coexisting phases and appropriate exchange vectors which allow condensation of the composition space. NMORB: Normal mid-ocean ridge basalt, after Gale et al. (2013). Abbreviations are from Whitney and Evans (2010).

Serpentinite. The serpentinites (> 90 % serpentine minerals) from Guarguallá valley are composed of serpentine group minerals, chlorite and magnetite, with minor carbonates and Cr-spinel relict (Figure 6.4a-d). Orthopyroxene has been replaced by bastite and chlorite. Individual crystal of magnetite occurs as fine to coarse euhedral to anhedral grains around pseudomorphs and in veinlets indicating a late origin. Talc appears sporadically and forms very fine, dense microcrystalline aggregates, within olivine and pyroxene pseudomorphs. Chlorite occurs as small blasts between serpentine. In the Penipe sector, serpentinites are mainly massive and contain orthopyroxene and Cr-spinel relicts. Talc is more abundant than in the South, while magnetite is less abundant. The whole rock contents in MgO (26.87–33.79 wt.%), Cr (2108-2952 ppm) and Ni (1573-1837 ppm) are high, while the content in Al_2O_3 is low (1.84-3.08). The Mg# varies between 0.82 and 0.89.

Cumulate Gabbros. They are conformed by fresh cumulate pyroxenes in a matrix of altered plagioclase, albite, chlorite, serpentinized olivine and locally amphibole (Figure 4e-h). The whole-rock Mg# varies between 0.76 and 0.78, CaO (14.51-15.63 wt.%) is higher than Al_2O_3 (9.83-11.01 wt.%) and Na_2O and K_2O contents are low, less than 1.5 wt.% and 0.07 wt.%, respectively. In the ACF diagram, they show a trend from basaltic composition towards Px+Ol richer mixtures (Figure 6.3a).

Group 1 tholeiitic arc basalts. They are constituted by albite-epidote-chlorite-titanite±amphibole association. Some varieties preserve relict clinopyroxene phenocrysts partly replaced by amphibole in an altered matrix with albite-chlorite-sericite and altered plagioclase (Figure 6.5a). The whole-rock Mg# varies between 0.54 and 0.56, Al_2O_3 is high (16.95-18.86 wt.%) and CaO is low (3.56-6.48 wt.%), while Na_2O content varies between 3.26 wt.% to 4.53 wt.% and K_2O is less than 0.77 wt.%. In ACF and AMF diagrams (Figure 6.3a-c) this type of rock projects toward the highest A contents among all basic rocks, making the mineral assemblages much richer in chlorite than in amphibole.

Groups 2 and 3 NMORB basaltic rocks. They are characterized by an albite-chlorite±epidote±amphibole association (greenschist facies), though some slices show a metamorphic association of albite-pumpellyite-chlorite with relicts of hornblende (transitional to prehnite-pumpellyite facies) or actinolite-albite-epidote-chlorite-titanite with a low white mica abundance and locally pumpellyite (Figure 6.5b-k), indicating the prehnite-pumpellyite to greenschist facies transition. Some samples show cores of hornblende with actinolite rims. The samples with lower intensity of metamorphic overprint show pyroxene and altered plagioclase relics. Titanite is common in all samples; in rocks with pumpellyite it is mainly found on the rims of clinopyroxene relicts, while in rocks of greenschist facies it is mainly between amphiboles; epidote is aligned according to the schistosity.

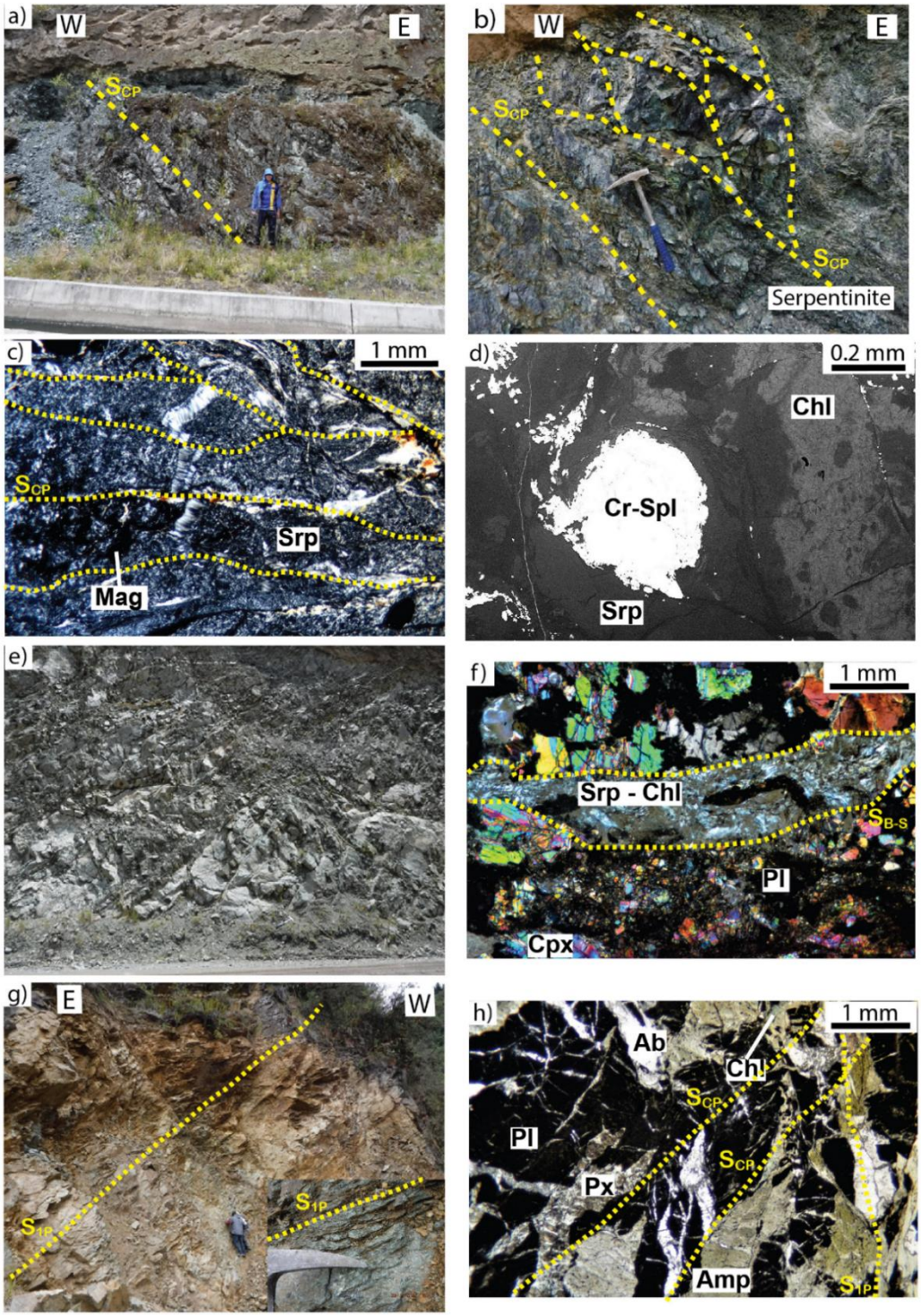

Figure 6.4. Field aspects (a, b, e and g) and microphotographs (c, d, f and h) showing the structural, textural and mineralogical details of serpentinite and metagabbro from the Peltetec Unit. a) and b) Outcrops of sheared brittle serpentinite from the Guarguallá valley; shear planes are highlighted. c) Serpentine and magnetite in serpentinite. d) BSE image of Cr-spinel surrounded by serpentine and chlorite in serpentinite. e) Fractured gabbro. f) Gabbro with broken grains of clinopyroxene showing clorite+serpentine along shear planes. g) Foliated metagabbro. h) Deformed metagabbro showing highly altered primary plagioclase and fresh secondary albite; relicts of pyroxene are preserved. S_{1P}: Slate cleavage, S_{CP}: C-type shear band cleavage. Mineral abbreviations are from Whitney and Evans (2010).

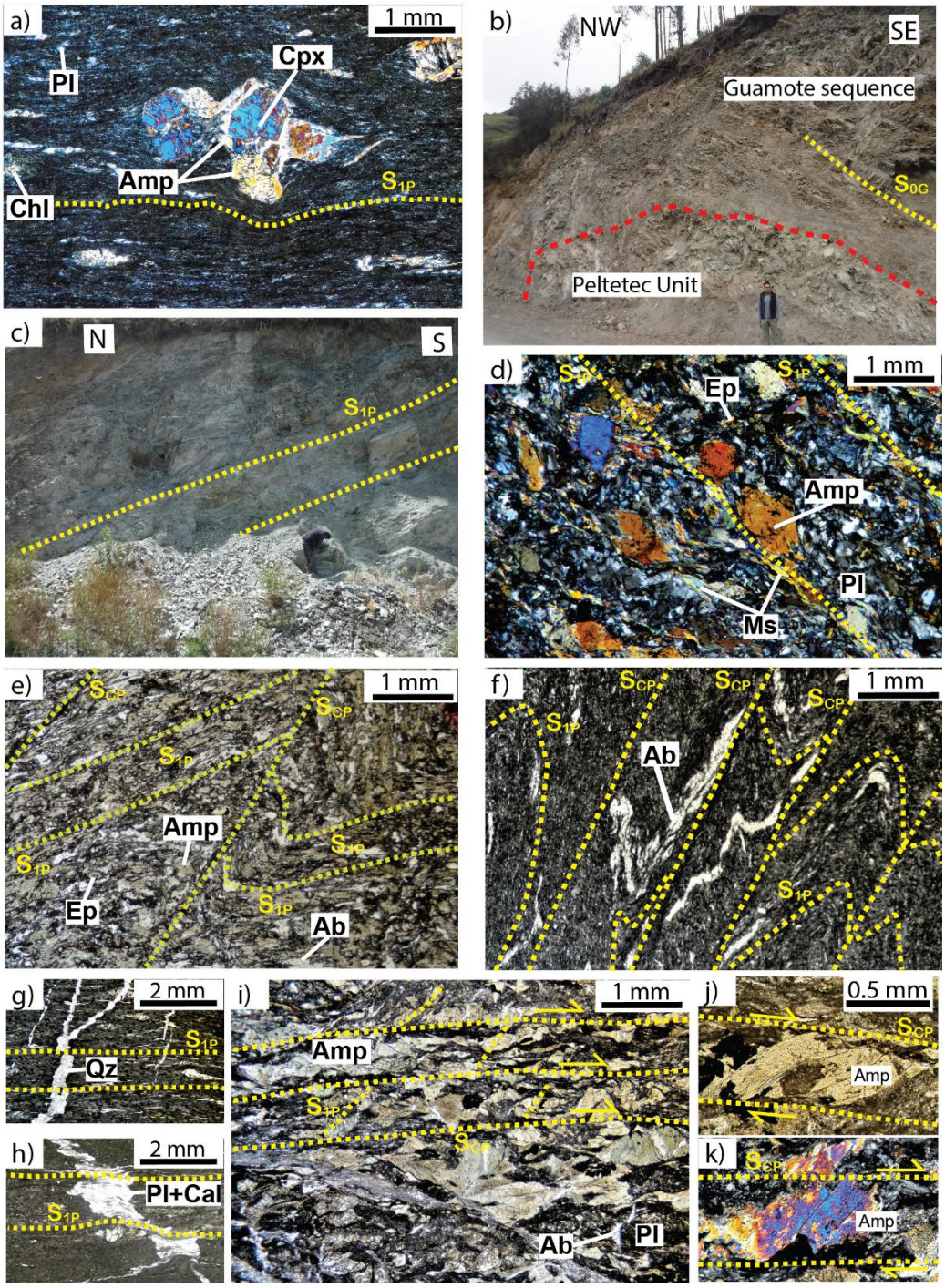

Figure 6.5. Field aspects (b and c) and microphotographs (a, d-k) showing the structural, textural and mineralogy details of metabasalts and dykes from the Peltetec Unit. a) Porphyroclastic foliated metabasalt; pyroxene porphyroclasts are rotated and partially replaced by calcic amphibole forming a pressure shadow tail. b) Metabasalts below the Guamote metasedimentary sequence. c) Foliated fine-grained metabasalt. d) Greenschist. e) Greenschist with a C-type shear band cleavage (pseudo crenulation). f) Fine-grained greenschist deformed by C-type shear band cleavage. g) and h) Deformed quartz and plagioclase+calcite veinlets. i) Mylonitized metabasalt with altered plagioclase groundmass, broken metamorphic amphibole and relicts of pyroxene. j) and k) Sheared amphibole in altered plagioclase matrix (mylonite). S_{1P}: Slate cleavage, S_{CP}: C-type shear band cleavage. Mineral abbreviations are from Whitney and Evans (2010).

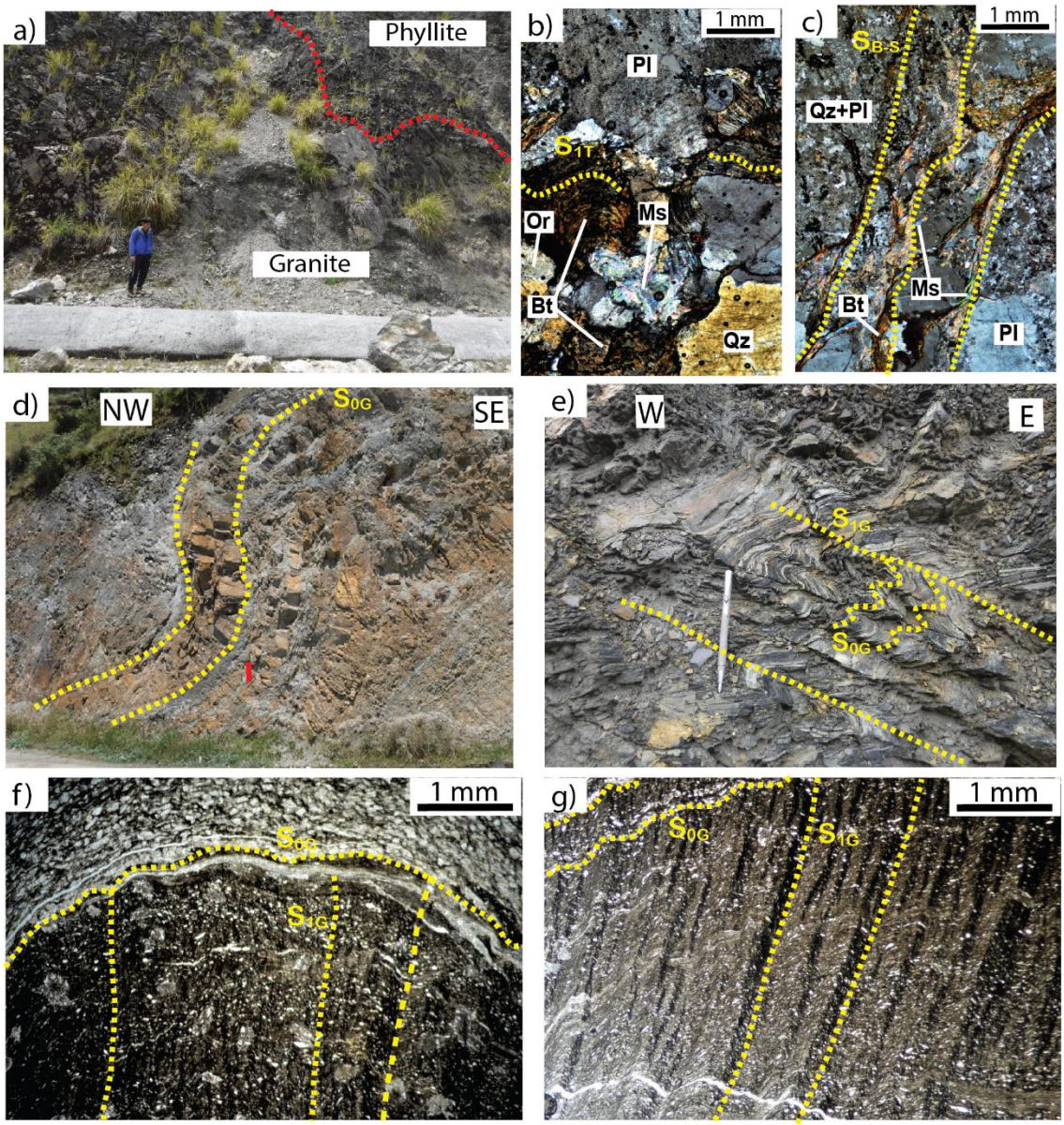

Figure 6.6. Field relations (a, d and e) and microphotographs (b, c, f and g) of the Tres Lagunas Unit and Guamote metasedimentary sequence. a) Contact between metagranite of the Tres Lagunas Unit and phyllite of the Chiguinda Unit above. b) and c) Fragile shear zone characterized by grain size reduction and sheared/broken micas between quartz and feldspar in granite from the Tres Lagunas Unit. d) Deformed stratification of the Guamote metasedimentary sequence; the red line is a reference scale corresponding to the size of a hammer. e) Deformation in the Guamote sedimentary sequence with folded bedding (S_0). f) and g) Folded bedding S_{0G} with spaced cleavage S_{1G} developed in a slate of the Guamote metasedimentary sequence. Mineral abbreviations are from Whitney and Evans (2010).

The whole-rock composition of Groups 2 and 3 NMORB basaltic rocks shows variation in Mg# between 0.45 and 0.69. The content of Al_2O_3 (12.83-16.84 wt.%) is higher than CaO (4.91-12.87 wt.%; except one sample with 15.11 CaO wt.%). Na_2O content varies between 1.42 and 4.98 wt.%, while K_2O content is low, less than 0.73 wt.%. In the ACF diagram

(Figure 6.3b) this type of rock is characterized by a trend towards higher F content, while a negative correlation between Mg# and A is appreciated in the AMF diagram (Figure 6.3c).

Metasediments. These rocks correspond to slates with quartz, albite and white mica set in a very fine-grained matrix. They show variable contents in Al_2O_3 (11.77-17.61 wt.%) and FeO_{total} (3.81-11.47 wt.%), and lower contents in CaO (0.19-4.64 wt.%), Na_2O (2.03-2.59 wt.%) and K_2O (2.12-3.82 wt.%). In the AKF diagram (Figure 6.3d), the bulk-rock compositions plot relatively close to the A-F join between feldspar (albite), muscovite and chlorite, in spite of strong variation in A.

Granites from the Tres Lagunas Unit. These rocks are constituted by plagioclase, alkali feldspar, biotite and quartz with secondary albite, muscovite and chlorite (Figure 6.6a-c). They have low contents in Mg# (0.29-0.44) and CaO (0.65-2.17 wt.%). Al_2O_3 varies between 13.24 and 13.94 wt.%, Na_2O between 2.97 and 4.63 wt.% and K_2O between 1.71 and 3.04 wt.%. In the AKF diagram, the bulk-rock compositions project in the tie-triangle defined by feldspar, muscovite and chlorite (Figure 6.3d).

6.3.3 Structural characteristics

The structural characteristics of the Peltetec and adjacent units are described independently below following the nomenclature summarized in Table 6.3.

Table 6.3. Nomenclature of tectono-metamorphic events (E) and associated metamorphism (M) and deformation (D).

Event / Unit	E_0		E_1		E_2	
	M_0	D_0	M_1	D_1	M_2	D_2
Maguazo						S_{0M}
Guamote					Ser-Chl	S_{0G}, S_{1G}
Tres Lagunas			Ms-Chl-Ab-Qz	S_{1T}	Ms-Chl	S_{B-S}
Peltetec (mafic rocks)	Amp-Andesine		Act-Ab-Ep-Chl-Ttn ±Ms	S_{1P}, S_{CP}		S_{B-S}

D: deformation event. S: planar structure, S_{B-S}: brittle-shear fabric. Mineral associations refer to peak metamorphic conditions. Ab-albite, Act-actinolite, Amp-amphibole, Chl-chlorite, Ep-epidote, Ms-muscovite, Qz-quartz, Ser = Sericite, Ttn-titanite (Whitney and Evans, 2010).

6.3.3.1 Peltetec Unit

The slices of the Peltetec Unit show variable deformation including local undeformed massive structure (Figure 6.5b-c). Slaty cleavage (S_{1P}) appears in most rocks and is variably deformed by shear planes generating micro-folding and C-type shear band cleavage (S_{CP}). The contact between different lithologies and units are tectonic, so the foliation trend changes between different slivers.

The S_{1P} foliation has a dominant N10E – N50E trend, steeply dipping to the SE (60 – 80°) in the Guarguallá and Alao valleys, while in the Penipe sector the dip is smaller than 45° (Figure 6.7a). In the Quimiag sector, the preferred trend of the S_{1P} is N-S to N60W dipping 35 - 60° NE (Figure 6.7b). Micro-folding (crenulation; S_{CP}) generated by C-type shear band cleavage is identified in the fine-grained metabasaltic and metasedimentary lithotypes. The pseudo-axial planes have variable trend and are irregularly spaced. The shear cleavage is also characterized by mylonitic fabric. The shear planes (S_{B-S}) along the contact zones between slivers have a N20E – N40E trend steeply dipping to the E.

Metamorphosed ultramafic rocks is limited to serpentinites. The outcrops were identified only at the Guarguallá valley (Figure 6.4a-b) and in the Penipe zone, occurring as meter-sized blocks. Serpentinites are fragile and quite friable, with conchoidal fractures with angular and sharp edges (Figure 6.4b). Intense shearing defines foliation planes (S_{CP}) with a steep dip towards the east (~70°). Original mantle minerals are not preserved, but pseudomorphs of olivine and pyroxene are locally present (Figure 6.4c-d). The grains of serpentine group minerals show undulate extinction with elongated shapes aligned along the shearing direction. Deformed veinlets of carbonates crosscut the rock. In the Penipe sector, serpentinites are mainly massive.

The cumulate gabbros of the Guarguallá and Alao valleys are characterized by dense fracturing (Figure 6.4e). Although the rock is massive, sectors with fragile and ductile deformation can be identified. Fragile deformation is characterized by brittle shear zones with fractured clinopyroxene mainly located in millimeter-sized bands, while ductile deformation is identified in millimeter-sized shear bands of serpentine and chlorite (horizontal in Figure 6.4f; S_{B-S}), all in a broken clinopyroxene and altered plagioclase domain.

Mylonitized gabbros occur at Quimiag, South of Penipe and Patate showing a penetrative S_{1P} foliation (diagonal in Figure 6.4g). They are constituted by amphibole, albite, chlorite, magnetite and relics of deformed clinopyroxene and altered plagioclase (Figure 6.4h). Some relict clinopyroxene grains are fractured and aligned according to the shear planes in

a dark gray matrix of altered plagioclase. Porphyroblasts (plagioclase, amphibole) and porphyroclasts (amphibole, pyroxene) show sigmoidal structures with kinematic indicators that indicate dextral shear (Figure 6.4h).

Metabasaltic rocks are the most abundant lithology of the Peltetec Unit (Figure 6.5), including massive and deformed varieties with variable grain size. Greenschist and fine-grained varieties have a penetrative S_{1P} foliation (slaty cleavage) defined by the alignment of actinolite, albite, epidote, chlorite and titanite (Figure 6.5d). S_{1P} foliation is disturbed by a mylonitic fabric characterized by C-type shear band cleavage (S_{CP}) oblique to S_{1P} that generates micro-folding (Figure 6.5e-f), locally forming small microlithons darker in color. Both S_{1P} and S_{CP} are defined by the alignment of the same minerals suggesting that they are related to the same deformation event, while late cataclastic structures cut the schistosity. Relicts of pyroxenes in porfidoclastic rocks are enclosed in a foliated fine-grained matrix. Clinopyroxenes show evidence of rotation, are partially replaced by amphibole in the rims and develop strain shadows that indicate a dextral component. The foliation is defined by the alignment of albite, epidote and chlorite (Figure 6.5a), and a mild development of a late crenulation cleavage is noted. Millimetric veins of quartz, albite and calcite are deformed (Figure 6.5g-h) evidencing formation previous to the metamorphic deformation event.

Basaltic dykes show a penetrative foliation S_{1P} similar to the host basaltic rock, and their mineral assemblage is similar as in mylonitized gabbros. Altered plagioclase constitutes the matrix with an anastomosed appearance while actinolite and albite are oriented parallel to S_{1P} and albite locally fills fractures (Figure 6.5i); some amphibole grains show internal deformation and others are broken by the shear planes (S_{CP}). S-C structures indicate dextral shear (Figure 6.5j-k).

Metasediments show the same structural characteristics as fine-grained basaltic rocks.

6.3.3.2 Tres Lagunas Unit

The tectonic slices of the Tres Lagunas Unit along the Peltetec fault zone mainly show cataclastic fabric. Sheared micas (mainly biotite) show internal ductile deformation and kink-bands indicating an older deformation event (S_{1T}). The grains of quartz, alkali feldspar and plagioclase are broken, showing grain size reduction in the shear bands and generating a local clay-micaceous matrix; quartz grains show undulose extinction (Figure 6.6a-c). Muscovite and chlorite recrystallized along the shear planes (S_{B-S}) (Figure 6.6c), which trend varies between N-S and NE-SW directions (Figure 6.6c).

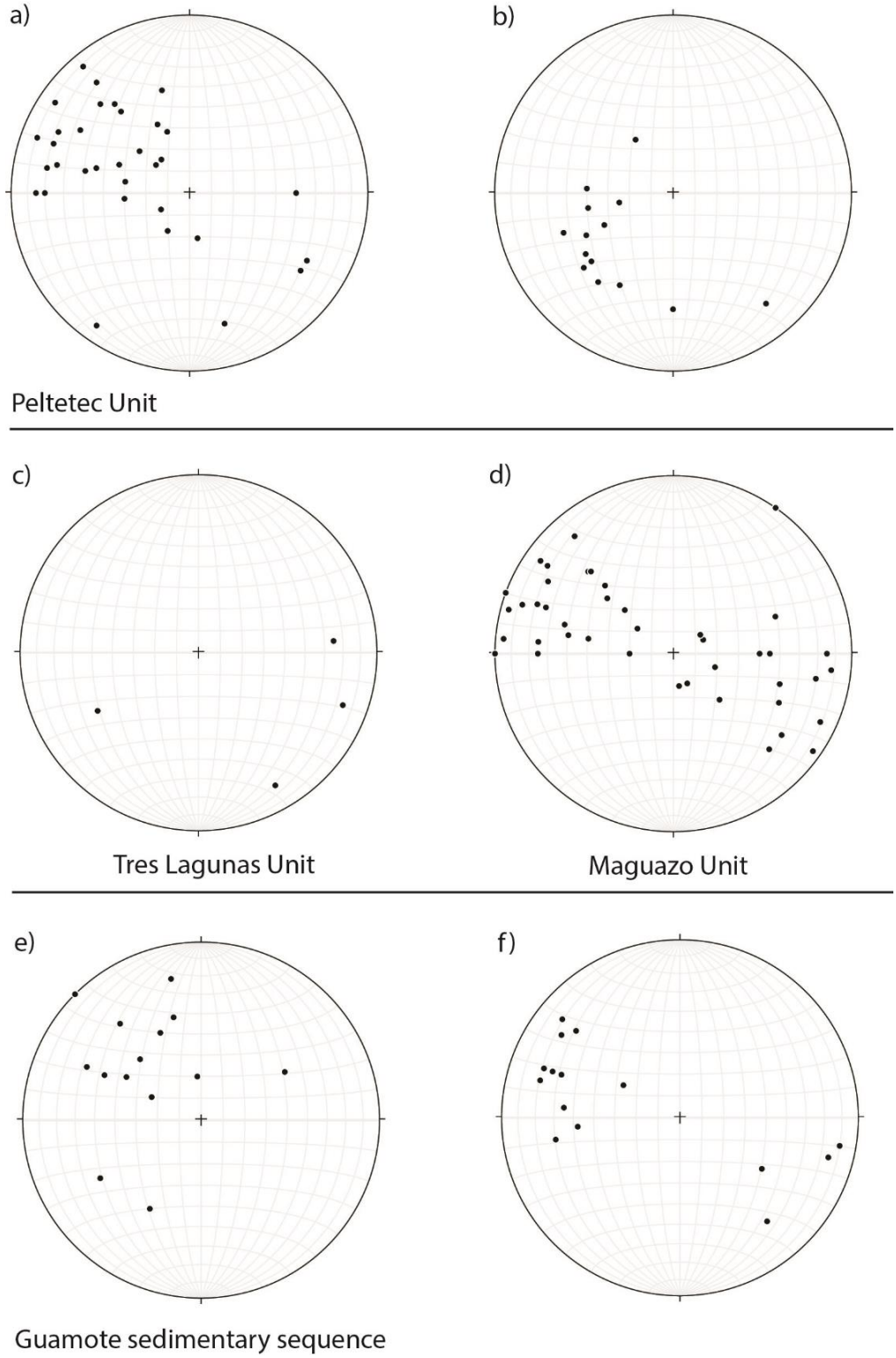

Figure 6.7. Stereonets of planar elements of the Peltetec Shear zone. The structural data were represented using the software Stereonet 10.0 (Allmendinger, et al., 2012; Cardozo and Allmendinger, 2013). a) S_{1P} foliation planes of the Peltetec Unit (excluding the Quimiag sector). b) S_{1P} foliation planes of the Peltetec Unit from the Quimiag sector. c) Shear planes from the Tres Lagunas Unit. d) Stratification planes S_{0M} of the Maguazo Unit. e) S_{0G} planes of the Guamote sedimentary sequence to the W of the Peltetec Unit. f) S_{0G} planes of the Guamote sedimentary sequence to the E of the Peltetec Unit.

6.3.3.3 Maguazo Unit

The Maguazo Unit, representing the eastern boundary of the fault zone, is constituted by clastic lithologies of varied size dominated by fine- and very fine-grained size and sporadic intercalated lavas. This unit does not generally show a penetrative cleavage except in local steeply dipping shear zones in the contact with other lithologies. The primary structures are folded, with a higher fold density close to the local shear zones. The trend of the axial planes varies between N-S to NE-SW with variable dipping to the E and W (Figure 6.7d).

6.3.3.4 Guamote metasedimentary sequence

Stratification (S_{0G}) in the Guamote metasedimentary sequence is defined by intercalations of black slate-phyllite, quartzite and metawacke (Figure 6.5b, Figure 6.6d-e). Towards the western contact with the Peltetec Unit, the planes have a preferred NE orientation with a gentle dip (25 - 45 ° SE) (Figure 6.7e). Towards the eastern contact in the Alao and Guarguallá valleys, the stratification planes have a predominant orientation range between N-S to NNE-SSW with steep W- and E-directed dip (60 - 80 °), defining folds with subhorizontal N15E – N45E trending axes (Figure 6.7f). In the Quimiag sector, the S_{0G} planes slightly dip to the E. A weak diagenetic (slaty) cleavage is developed parallel to the stratification, which is affected by a S_{1G} crenulation cleavage (Figure 6.6e-g). The crenulation cleavage has a preferential N30E orientation with sub-horizontal to low angle fold axes.

6.3.4 Mineral chemistry

About 500 point analyses of amphibole, feldspar, muscovite, epidote, chlorite, titanite, pumpellyite, serpentine, Fe-Ti oxides, chromium spinel and pyroxene were performed in representative samples of the different types of rock. Representative analyses are presented in Tables 6.4-6.13.

6.3.4.1 Amphibole

Amphiboles are present in variable abundance in all types of mafic rocks. They have a calcic composition with $Ca^B/(Ca+Na)^B$ values between 0.85 and 1.00 (Figure 6.8; classification scheme of Hawthorne et al., 2012). Amphiboles have variable contents in Si (6.59-7.91 apfu), Al_{tot} (0.14-2.08 apfu), Mg (2.62-3.88 apfu), Fe_{tot} (1.16-2.43 apfu) and Ca (1.35-2.00 apfu), and Mg# varies between 0.53 and 0.81. They have low contents in Ti (<0.08 apfu), Mn (<0.04 apfu), K (<0.1 apfu) and Cl (<0.07 apfu) (e.g. Table 6.4).

Table 6.4. Representative analysis of amphiboles from the Peltetec Unit. Prg: Pargasite, Mhb: Magnesio-hornblende, Mfhb: Magnesio-ferri-hornblende, Act: Actinolite.

Sample	P-47						P-52		
Lithology	greenschist						greenschist		
Major elements (wt.%)									
SiO_2	45.56	45.24	50.14	47.78	52.76	53.79	51.43	52.38	53.72
TiO_2	0.38	0.43	0.22	0.36	0.08	0.04	0.04	0.06	0.06
Al_2O_3	11.36	11.81	6.76	8.55	2.92	2.14	4.71	4.30	3.01
Cr_2O_3	0.43	0.01	0.31	0.11	0.06	0.06	0.05	0.19	0.20
FeOt	12.98	13.25	11.94	13.41	12.82	12.14	12.37	10.69	10.12
MnO	0.23	0.22	0.24	0.32	0.24	0.23	0.23	0.26	0.26
MgO	12.28	12.02	14.50	13.24	15.19	15.65	15.15	15.76	16.66
CaO	11.39	11.37	11.78	11.50	12.38	12.69	12.21	12.62	12.82
Na_2O	2.21	2.32	1.39	1.49	0.52	0.39	0.45	0.56	0.39
K_2O	0.29	0.23	0.17	0.20	0.10	0.06	0.14	0.14	0.09
Cl	0.00	0.00	0.01	0.01	0.01	0.00	0.00	0.01	0.00
Total	97.11	96.90	97.46	96.98	97.08	97.19	96.78	96.97	97.33
Formula based on 23 oxygens									
SiT	6.69	6.66	7.24	6.99	7.65	7.77	7.44	7.55	7.68
AlT	1.32	1.34	0.76	1.02	0.35	0.23	0.56	0.45	0.32
AlC	0.65	0.70	0.39	0.46	0.15	0.13	0.25	0.28	0.19
TiC	0.04	0.05	0.02	0.04	0.01	0.00	0.00	0.01	0.01
CrC	0.05	0.00	0.04	0.01	0.01	0.01	0.01	0.02	0.02
$Fe^{3+}C$	0.17	0.16	0.14	0.26	0.11	0.03	0.26	0.04	0.03
MgC	2.69	2.64	3.12	2.89	3.28	3.37	3.27	3.39	3.55
$Fe^{2+}C$	1.40	1.45	1.29	1.35	1.45	1.44	1.22	1.25	1.18
MnC						0.02		0.02	0.02
$Fe^{2+}B$	0.02	0.02	0.01	0.03	0.00	0.00	0.02	0.00	0.00
MnB	0.03	0.03	0.03	0.04	0.03	0.01	0.03	0.01	0.01
CaB	1.79	1.79	1.82	1.80	1.92	1.96	1.89	1.95	1.96
NaB	0.16	0.16	0.14	0.13	0.05	0.03	0.06	0.04	0.03
NaA	0.47	0.50	0.25	0.30	0.10	0.08	0.07	0.11	0.08
KA	0.05	0.04	0.03	0.04	0.02	0.01	0.03	0.03	0.02
Cl	0.00	0.00	0.00	0.00	0.00	0.00	0.00	0.00	0.00
Mg#	0.65	0.64	0.71	0.68	0.69	0.70	0.73	0.73	0.75
Subgroup	Calcic	Calcic	Calcic	Calcic	Calcic	Calcic	Calcic	Calcic	Calcic
Species	Prg	Prg	Mhb	Mhb	Act	Act	Mfhb	Act	Act

Table 6.4. (Continued). Representative analysis of amphiboles from the Peltetec Unit.

Sample	P-46				P-8		P-23			
Lithology	metadiabase				fine-grained metabasalt		metadiabase			
Major elements (wt.%)										
SiO_2	49.80	49.80	52.40	51.91	53.55	52.94	50.17	50.73	53.96	53.30
TiO_2	0.49	0.50	0.32	0.44	0.67	0.05	0.64	0.31	0.27	0.32
Al_2O_3	4.70	4.10	2.37	3.31	3.54	1.69	4.50	4.18	2.22	2.19
Cr_2O_3	0.01	0.00	0.00	0.03	0.03	0.03	0.01	0.11	0.01	0.03
FeOt	16.32	16.83	15.74	13.37	13.45	14.10	14.79	14.56	9.95	13.88
MnO	0.27	0.27	0.26	0.24	0.30	0.34	0.20	0.16	0.16	0.19
MgO	13.27	13.02	14.07	15.44	13.67	15.32	14.84	14.44	18.16	15.75
CaO	11.11	11.14	11.39	11.50	10.91	11.87	10.61	11.47	11.57	10.85
Na_2O	1.25	1.12	0.64	0.98	1.09	0.17	1.28	0.88	0.79	0.77
K_2O	0.06	0.07	0.08	0.05	0.03	0.03	0.08	0.05	0.04	0.04
Cl	0.11	0.15	0.06	0.05	0.01	0.01	0.14	0.04	0.03	0.07
Total	97.38	97.00	97.31	97.31	97.23	96.54	97.27	96.94	97.17	97.39
Formula based on 23 oxygens										
SiT	7.31	7.36	7.65	7.50	7.74	7.73	7.30	7.40	7.67	7.69
AlT	0.69	0.64	0.35	0.50	0.26	0.27	0.70	0.60	0.33	0.31
AlC	0.12	0.07	0.06	0.07	0.34	0.02	0.07	0.12	0.04	0.06
TiC	0.05	0.06	0.03	0.05	0.07	0.01	0.07	0.03	0.03	0.03
CrC	0.00	0.00	0.00	0.00	0.00	0.00	0.00	0.01	0.00	0.00
Fe3+C	0.38	0.38	0.23	0.31	0.04	0.24	0.42	0.37	0.24	0.23
MgC	2.90	2.87	3.06	3.33	2.94	3.33	3.22	3.14	3.85	3.39
Fe2+C	1.54	1.62	1.61	1.25	1.58	1.40	1.22	1.33	0.84	1.28
MnC					0.02					
Fe2+B	0.08	0.07	0.08	0.06	0.00	0.08	0.17	0.08	0.10	0.16
MnB	0.03	0.03	0.03	0.03	0.02	0.04	0.02	0.02	0.02	0.02
CaB	1.75	1.76	1.78	1.78	1.69	1.86	1.65	1.79	1.76	1.68
NaB	0.14	0.13	0.11	0.13	0.29	0.02	0.16	0.11	0.12	0.14
NaA	0.21	0.19	0.08	0.14	0.01	0.02	0.21	0.14	0.10	0.08
KA	0.01	0.01	0.01	0.01	0.01	0.01	0.01	0.01	0.01	0.01
Cl	0.03	0.04	0.01	0.01	0.00	0.00	0.03	0.01	0.01	0.02
Mg#	0.64	0.63	0.64	0.72	0.65	0.69	0.70	0.69	0.80	0.70
Subgroup	Calcic	Calcic	Calcic	Calcic	Calcic	Calcic	Calcic	Calcic	Calcic	Calcic
Species	Mfhb	Mfhb	Act	Act	Mhb	Act	Mfhb	Mfhb	Act	Act

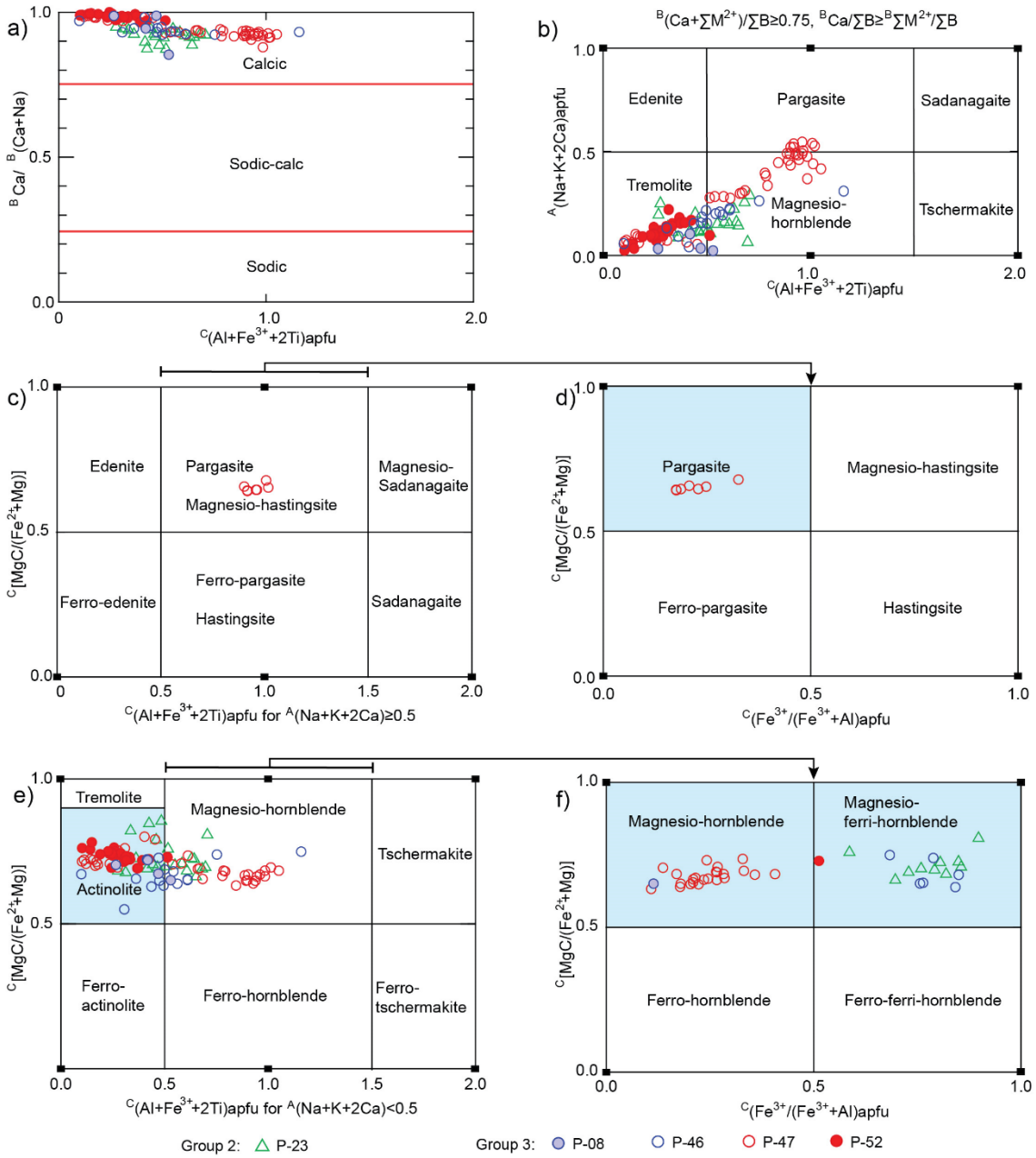

Figure 6.8. a) – f) Composition of amphiboles from the Peltetec Unit plotted according to the classification scheme of Hawthorne et al., (2012). Colors correspond to different samples.

The dominant species corresponds to actinolite, which appears as single grains or at the rims of zoned amphibole crystals (Figure 6.9a-h and Figure 6.10a-d). Zoned amphibole grains preserve cores of magnesio-hornblende, magnesio-ferri-hornblende and pargasite (Figure 6.8). Actinolite has Na contents ranging between 0.03 and 0.33 apfu, the vacancy at site A varies from 0.75 to 0.98 and the calculated Fe^{3+} is less than 0.39 apfu, while amphibole cores have a higher Na content (0.25-0.66 apfu), the vacancy at site A varies between 0.45-0.98, and calculated Fe^{3+} between 0.04-0.79 apfu. The chemical zoning is mainly given by the variation of Al and Na that trend opposed to Si and Mg (Figure 6.9).

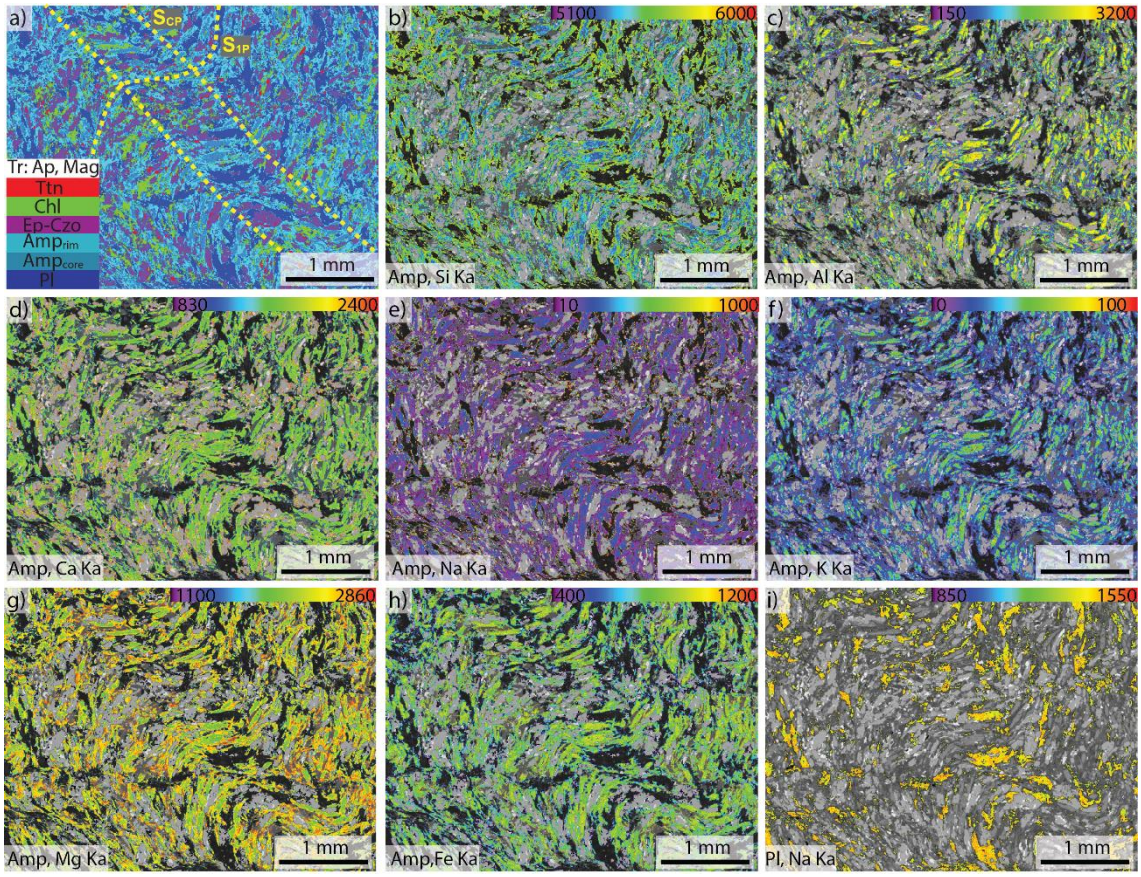

Figure 6.9. Mineral assemblage (a) and X-ray images (b-i) of an amphibole-rich domain in greenschist rock of the Peltetec Unit (sample P-47). b-h) X-ray images of Si, Al, Ca, Na, K, Mg and Fe in amphiboles; note the zoned amphibole crystals and deformation (folding). i) X-ray image of Na in plagioclase. Color scale bar represents the relative element concentration in counts/nA per second.

6.3.4.2 Feldspar

Feldspar corresponds to plagioclase, which is present in all mafic lithologies (e.g. Table 6.5). The dominant variety is albite (Ab_{90-100}), although locally oligoclase (Ab_{86}) and andesine (Ab_{53-64}) are identified in the core of the crystals (Figure 6.10d and Figure 6.11a). The orthoclase content is low, less than around Or_1. Good analyses were not obtained in altered plagioclase, which yielded relatively high FeO, MgO and CaO contents that indicate the presence of submicroscopic alteration minerals (Figure 6.4h and Figure 6.5i-k).

The plagioclase of Tres Lagunas granite corresponds to albite (Ab_{98-99}) (Figure 6.11a).

Table 6.5. Representative analysis of plagioclase from the Peltetec and Tres Lag

Sample	P-47	P-52		P-46	P-8	P-33	P-23	
Lithology	greenschist	greenschist		metadiabase	fine-grained metabasalt		metadiabase	c
Major elements (wt.%)								
SiO_2	67.63	56.28	67.89	68.04	68.15	67.84	67.74	
TiO_2	0.01	0.01	0.00	0.00	0.01	0.02	0.00	
Al_2O_3	19.63	24.84	19.49	19.25	19.14	18.81	19.41	
FeOt	0.08	0.73	0.06	0.11	0.32	0.57	0.23	
MnO	0.00	0.01	0.00	0.00	0.00	0.00	0.01	
MgO	0.00	0.23	0.00	0.00	0.00	0.17	0.06	
CaO	0.46	10.80	0.27	0.12	0.08	0.72	0.45	
Na_2O	11.73	6.85	11.91	11.92	12.12	10.87	11.86	
K_2O	0.04	0.10	0.06	0.07	0.05	0.13	0.03	
Total	99.58	99.86	99.68	99.52	99.86	99.13	99.81	
Formula based on 8 oxygens								
Si	2.96	2.52	2.97	2.98	2.97	3.00	2.96	
Ti	0.00	0.00	0.00	0.00	0.00	0.00	0.00	
Al	1.01	1.31	1.00	0.99	0.98	0.98	1.00	
Fe	0.00	0.03	0.00	0.00	0.01	0.02	0.01	
Mn	0.00	0.00	0.00	0.00	0.00	0.00	0.00	
Mg	0.00	0.02	0.00	0.00	0.00	0.01	0.00	
Ca	0.02	0.52	0.01	0.01	0.00	0.03	0.02	
Na	1.00	0.60	1.01	1.01	1.03	0.93	1.00	
K	0.00	0.01	0.00	0.00	0.00	0.01	0.00	
Or%	0.23	0.49	0.31	0.37	0.25	0.73	0.18	
Ab%	97.65	53.19	98.46	99.08	99.41	95.75	97.78	
An%	2.12	46.32	1.23	0.55	0.34	3.52	2.04	

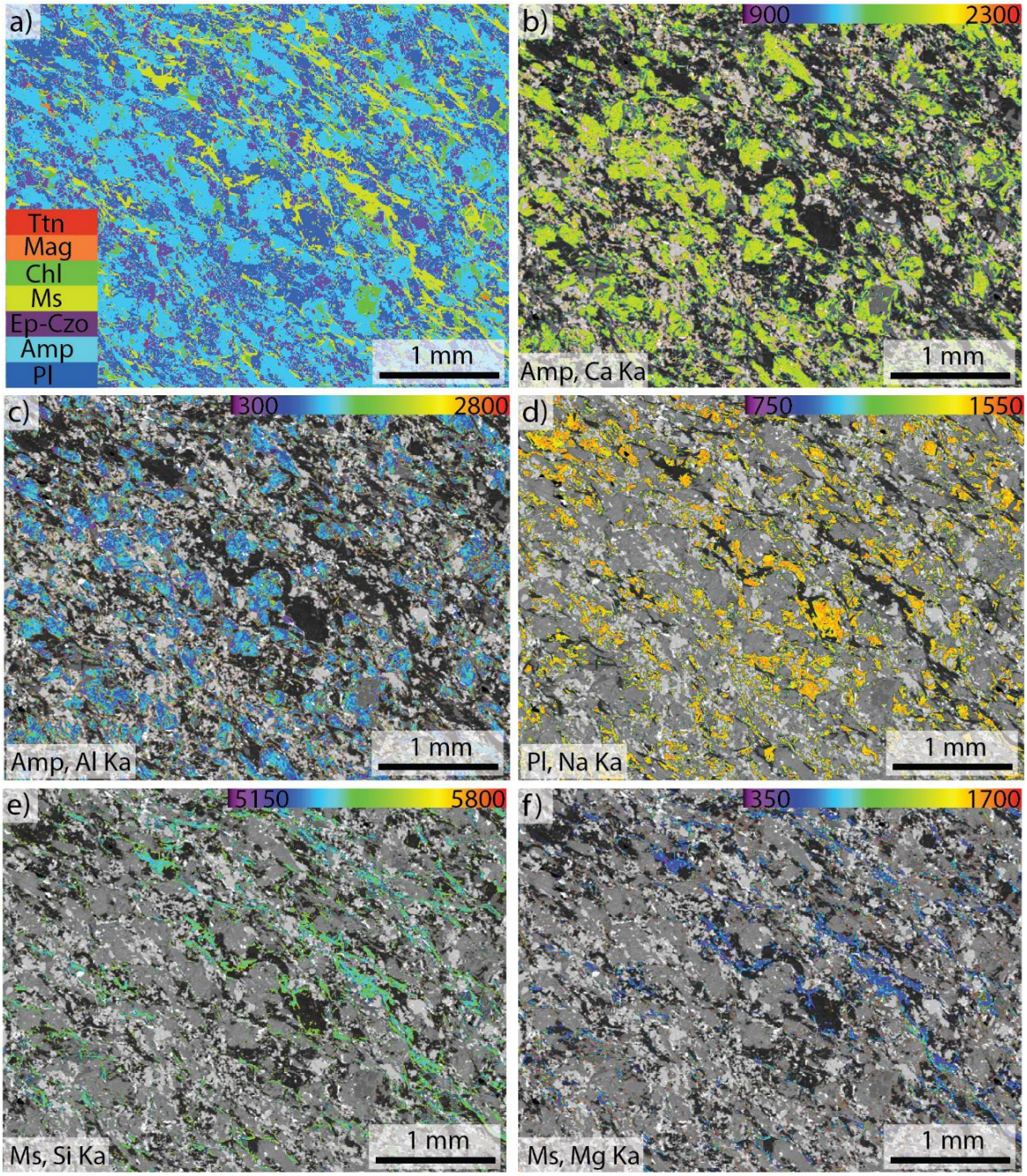

Figure 6.10. Mineral assemblage (a) and X-ray images (b-f) of greenschist sample P-52 of the Peltetec Unit. b-c) X-ray images of Ca and Al in non-zoned amphiboles. d) X-ray image of Na in plagioclase (rich-Na plagioclase). e-f) X-ray images of Si and Mg in white micas. Color scale bar represents the relative element concentration in counts/nA per second.

6.3.4.3 Mica

Sericite is a common mineral in spilitized rocks and lower grade pumpellyite-bearing rocks. However, larger white mica crystals (big enough to make reliable microprobe measurements) were analyzed in samples of the greenschist facies (Figure 6.5d and Figure 6.10e-f). The Si content varies from 3.20 to 3.36 apfu, Al_{tot} from 2.25 to 2.5 apfu, Mg from

0.22 to 0.32 apfu, Fe_{tot} from 0.09 to 0.12 apfu, and K from 0.88 to 0.95 apfu (e.g. Table 6.6). The Na content is low (0.02-0.07apfu), while the amouts of Ti and Cr are negligible. The analyses correspond to muscovite with variable composition along the muscovite-phengite join (Figure 6.11b-c). They indeed show a marked Tschermak (Si(Mg,Fe)-$^{VI}Al_{-1}{}^{IV}Al_{-1}$) exchange along the dioctahedral mica series between muscovite and celadonite end-members (Figure 6.11b-c), with variable Mg but almost constant Fe that suggests significant high $Fe^{3+}/Fe^{3+}+Fe^{2+}$).

Table 6.6. Representative analysis of muscovite from the Peltetec and Tres Lagunas Units.

Sample	P-52					P-26			
Lithology	greenschist (Peltetec Unit)					granite (Tres Lagunas Unit)			
Major elements (wt.%)									
SiO_2	48.06	48.46	47.27	48.85	48.12	46.45	49.89	48.06	49.94
TiO_2	0.33	0.25	0.14	0.25	0.33	0.06	0.17	0.07	0.14
Al_2O_3	30.44	29.85	31.53	29.53	30.71	34.27	27.18	30.60	27.10
Cr_2O_3	0.25	0.26	0.00	0.17	0.13	0.01	0.00	0.01	0.01
FeOt	1.89	1.91	1.93	1.98	1.87	1.29	4.10	2.07	4.54
MnO	0.01	0.02	0.01	0.01	0.02	0.02	0.03	0.00	0.00
MgO	2.40	2.55	2.17	2.72	2.35	0.90	2.29	1.63	2.25
CaO	0.00	0.03	0.01	0.01	0.01	0.00	0.01	0.01	0.06
BaO	0.17	0.17	0.14	0.06	0.20	0.14	0.18	0.19	0.11
Na_2O	0.50	0.31	0.44	0.32	0.51	0.41	0.04	0.20	0.08
K_2O	10.46	10.41	10.79	10.39	10.25	10.85	10.98	10.49	10.12
Cl	0.01	0.00	0.00	0.00	0.00	0.00	0.00	0.00	0.00
Total	94.51	94.22	94.43	94.30	94.51	94.40	94.87	93.34	94.35
Formula based on 11 oxygens									
SiT	3.24	3.27	3.20	3.29	3.24	3.13	3.39	3.27	3.40
AlT	0.76	0.73	0.80	0.71	0.76	0.87	0.61	0.73	0.60
AlM	1.66	1.65	1.71	1.64	1.68	1.85	1.56	1.73	1.57
TiM	0.02	0.01	0.01	0.01	0.02	0.00	0.01	0.00	0.01
CrM	0.01	0.01	0.00	0.01	0.01	0.00	0.00	0.00	0.00
$Fe^{2+}M$	0.11	0.11	0.11	0.11	0.11	0.07	0.23	0.12	0.26
MnM	0.00	0.00	0.00	0.00	0.00	0.00	0.00	0.00	0.00
MgM	0.24	0.26	0.22	0.27	0.24	0.09	0.23	0.17	0.23
CaA	0.00	0.00	0.00	0.00	0.00	0.00	0.00	0.00	0.00
BaA	0.00	0.00	0.00	0.00	0.01	0.00	0.00	0.00	0.00
NaA	0.07	0.04	0.06	0.04	0.07	0.05	0.01	0.03	0.01
KA	0.90	0.90	0.93	0.89	0.88	0.93	0.95	0.91	0.88
Cl	0.00	0.00	0.00	0.00	0.00	0.00	0.00	0.00	0.00
Mg#	0.69	0.70	0.67	0.71	0.69	0.55	0.50	0.58	0.47

Micas from the granite of the Tres Lagunas Unit have a Si content that varies from 3.05 to 3.40 apfu, Al_{tot} from 2.17 to 2.83 apfu and K from 0.88 to 0.96 apfu, with lower concentrations in Mg (0.07-0.24 apfu), Fe_{tot} (0.07-0.26 apfu) and Na (<0.06 apfu) (e.g. Table 6.6). The Ti and Cr contents are negligible. They are classified as muscovite with composition along the muscovite-phengite join and a marked Tschermak exchange along the dioctahedral mica series between muscovite and celadonite end members (Figure 6.11b-c).

6.3.4.4 Epidote

Epidote has a low Mn content (<0.01 apfu) and variable Al (M3) content (0.27-0.63 apfu) that correlates negatively with Fe^{3+}(M3) (0.31-0.71 apfu), according to the clinozoisite-epidote series (Al (M3) ←→Fe3+ (M3)). It is classified as epidote and clinozoisite (Figure 6.11d; e.g. Table 6.7).

6.3.4.5 Chlorite

The composition of chlorite in mafic rocks is variable (e.g. Table 6.8). In general, the Mg content (4.38-6.68 apfu) is higher than Fe_{tot} (2.97-4.64 apfu) and Al (4.19-5.17 apfu). In the tetrahedral site, Si ranges from 5.43 to 6.05 apfu and Al^{IV} from 1.95 to 2.58 apfu, the calculated total vacancy is lower than 0.31 (e.g. Table 6.8), indicating the local presence of submicroscopic intergrowths of micas. These data show that chlorites are trioctahedral, mainly following the clinochlore-chamosite series with certain Tschermak exchange (Figure 6.11e). They are dominantly of clinochlore composition (Mg# varies between 0.51 and 0.69), although some analyses have intermediate values between chamosite and clinochlore (Figure 6.11e).

Chlorites in serpentinite have a higher Mg (6.08-7.82 apfu) than Al (4.15-5.57 apfu), Fe (1.76-2.77 apfu) and Si (5.37-6.03 apfu) contents. Al^{IV} varies between 1.97 and 2.63, while the total vacancy is lower than 0.16. This shows that chlorites are trioctahedral. Mg# is high (0.69-0.82) and classify as clinochlore with limited Tschermak exchange (Figure 6.11e; e.g. Table 6.8).

In the granite of the Tres Lagunas Unit, chlorite has lower Mg (2.53-2.80 apfu) than Al (4.63-4.89 apfu) and Fe (6.13-6.77 apfu) contents. The tetrahedral site has a Si from 5.60 to 6.00 apfu and Al^{IV} from 2.00 to 2.41 apfu, while the total vacancy is lower than 0.27. This shows that they are trioctahedral. Mg# varies between 0.28 and 0.30 apfu, therefore they are classified as chamosite (Figure 6.11e; e.g. Table 6.8).

Table 6.7. Representative analysis of epidote from the Peltetec Unit.

Sample	P-47				P-52		
Lithology	greenschist				greenschist		
Major elements (wt.%)							
SiO_2	37.63	37.76	38.07	38.13	38.09	38.21	38.27
TiO_2	0.07	0.04	0.16	0.14	0.06	0.07	0.11
Al_2O_3	24.30	25.34	27.44	27.65	27.55	28.21	28.38
Cr_2O_3	0.06	0.05	0.01	0.03	0.11	0.00	0.26
FeOt	10.68	9.26	6.97	6.48	6.27	5.81	5.35
MnO	0.11	0.11	0.21	0.18	0.08	0.09	0.13
MgO	0.05	0.03	0.06	0.06	0.08	0.05	0.07
CaO	23.47	23.78	23.78	23.94	24.05	24.23	24.12
Na_2O	0.00	0.01	0.01	0.00	0.00	0.00	0.00
K_2O	0.02	0.01	0.02	0.02	0.03	0.01	0.01
Cl	0.01	0.01	0.00	0.00	0.02	0.00	0.00
Total	96.39	96.40	96.73	96.64	96.34	96.67	96.70
Formula base don 12.5 oxygens							
SiT	2.99	2.99	2.98	2.99	2.99	2.98	2.99
AlT	0.01	0.01	0.02	0.01	0.01	0.02	0.01
AlM1	1.00	1.00	1.00	1.00	1.00	1.00	1.00
AlM2	1.00	1.00	1.00	1.00	1.00	1.00	1.00
AlM3	0.27	0.35	0.51	0.54	0.54	0.58	0.59
$Fe^{3+}M3$	0.71	0.61	0.46	0.42	0.41	0.38	0.35
MnM3	0.01	0.01	0.01	0.01	0.01	0.01	0.01
CrM3	0.00	0.00	0.00	0.00	0.01	0.00	0.02
MgM3	0.01	0.00	0.01	0.01	0.01	0.01	0.01
TiM3	0.00	0.00	0.01	0.01	0.00	0.00	0.01
CaA1	1.00	1.00	1.00	1.00	1.00	1.00	1.00
CaA2	1.00	1.02	1.00	1.01	1.02	1.03	1.02
NaA2	0.00	0.00	0.00	0.00	0.00	0.00	0.00
KA2	0.00	0.00	0.00	0.00	0.00	0.00	0.00
Cl	0.00	0.00	0.00	0.00	0.00	0.00	0.00
Xczo	0.28	0.37	0.53	0.56	0.57	0.61	0.63
Xep	0.71	0.62	0.46	0.43	0.43	0.39	0.36
Xpmt	0.01	0.01	0.01	0.01	0.01	0.01	0.01

Table 6.8. Representative analysis of chlorite from the Peltetec and Tres Lagu

Sample	P-47		P-52		P-46	P-8	P-25
Lithology	greenschist		greenschist		metadiabase	fine-grained metabasalt	Cumulate meta
Major elements (wt.%)							
SiO_2	28.15	27.21	26.47	27.82	27.78	26.43	29.42
TiO_2	0.00	0.00	0.03	0.02	0.00	0.01	0.01
Al_2O_3	19.22	19.00	20.95	21.47	17.85	18.51	17.74
Cr_2O_3	0.02	0.03	0.10	0.00	0.00	0.04	0.03
FeOt	20.50	20.25	19.94	19.77	24.97	25.96	17.52
MnO	0.31	0.32	0.29	0.27	0.30	0.47	0.14
MgO	18.82	19.30	19.16	17.96	16.19	15.54	22.11
CaO	0.09	0.09	0.03	0.05	0.04	0.07	0.05
Na_2O	0.02	0.01	0.00	0.02	0.02	0.03	0.02
K_2O	0.03	0.03	0.04	0.04	0.07	0.02	0.04
Total	87.16	86.24	87.03	87.41	87.22	87.07	87.08
Formula based on 28 oxygens							
Si	5.80	5.68	5.46	5.68	5.87	5.65	5.97
Ti	0.00	0.00	0.01	0.00	0.00	0.00	0.00
Al	4.67	4.67	5.09	5.16	4.45	4.66	4.24
Cr	0.00	0.00	0.02	0.00	0.00	0.01	0.01
Fe^{2+}	3.53	3.53	3.44	3.37	4.41	4.64	2.97
Mn	0.05	0.06	0.05	0.05	0.05	0.08	0.02
Mg	5.78	6.00	5.89	5.46	5.10	4.95	6.68
Ca	0.02	0.02	0.01	0.01	0.01	0.02	0.01
Na	0.01	0.01	0.00	0.01	0.01	0.01	0.01
K	0.01	0.01	0.01	0.01	0.02	0.00	0.01
Fe/(Fe+Mg)	0.38	0.37	0.37	0.38	0.46	0.48	0.31

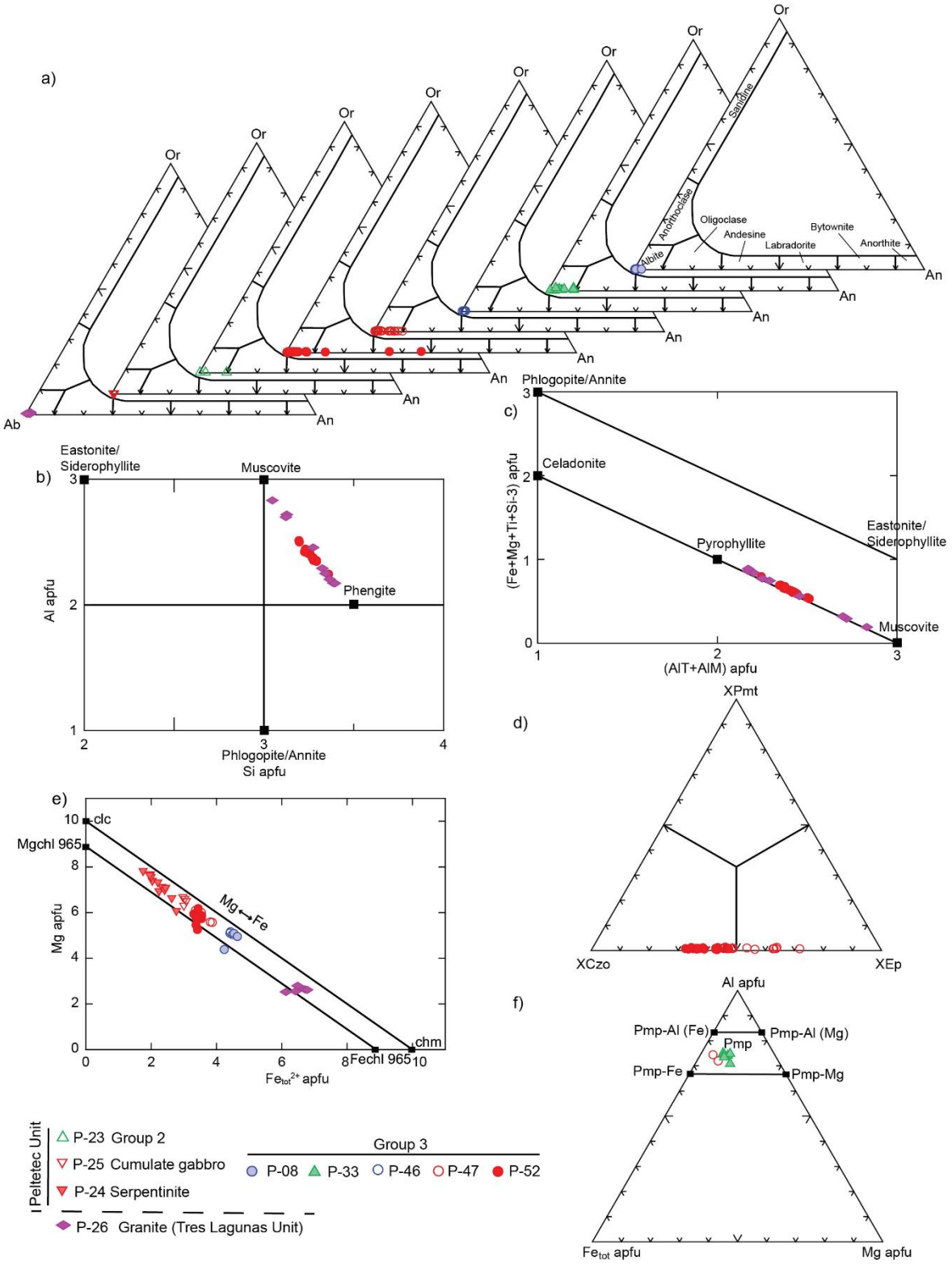

Figure 6.11. a) An-Ab-Or ternary diagram (Smith and Brown, 1988) showing the composition of plagioclase of studied samples. b) and c) Compositional variations of micas in terms of Al (apfu) vs Si (apfu) and Fe+Mg+Ti+Si-3 (apfu) vs AlT+AlM (apfu); also shown are relevant end-members. d) XCzo-XPmt-XEp ternary diagram showing the composition of epidote group minerals (after Franz and Liebscher, 2004). e) Composition of chlorite in the terms of Mg apfu vs Fe_{tot}^{2+} apfu. f) Composition of pumpellyite in the terms of Fe_{tot} apfu, Al apfu and Mg apfu; chemical formula calculated on the basis of 24.5 oxygens.

6.3.4.6 Titanite

It is a fine-grained common mineral in all samples with uniform Si contents (0.96-1.08 apfu; e.g. Table 6.9). Ti and Ca contents range 0.75-0.88 apfu and 0.82-0.97 apfu, respectively, in rocks with pumpellyite and 0.84-0.96 apfu and 0.91-1.00, respectively, in greenschist samples. This indicate a certain variable La- and/or Ce-titanite contents which is also indicated by low wt.% totals (as a consequence of the lack of La and Ce analyses, Table 6.9).

Table 6.9. Representative analysis of titanite from the Peltetec Unit.

Sample	P-47	P-52	P-46	P-8	P-33	P-25
Lithology	greenschist	greenschist	metadiabase	fine-grained metabasalt		Cumulate metagabbro
Major elements (wt.%)						
SiO_2	31.07	30.64	30.16	30.50	29.97	29.82
TiO_2	37.53	37.46	37.41	34.22	31.80	35.49
Al_2O_3	1.81	1.78	1.62	2.39	3.94	2.20
Cr_2O_3	0.08	0.09	0.04	0.00	0.00	0.12
FeOt	0.52	0.54	0.20	2.48	4.46	1.37
MnO	0.01	0.01	0.00	0.03	0.04	0.00
MgO	0.39	0.39	0.03	0.62	1.55	1.20
CaO	28.17	28.04	28.03	27.60	25.20	26.40
BaO	0.42	0.43	0.44	0.40	0.35	0.43
Na_2O	0.01	0.01	0.01	0.03	0.03	0.01
K_2O	0.06	0.06	0.02	0.01	0.03	0.02
Total	100.06	99.45	97.96	98.28	97.36	97.05
Formula based on 5 oxygens						
Si	1.00	1.00	1.00	1.00	0.98	0.99
Ti	0.91	0.92	0.93	0.84	0.78	0.88
Al	0.07	0.07	0.06	0.09	0.15	0.09
Cr	0.00	0.00	0.00	0.00	0.00	0.00
Fe	0.01	0.01	0.01	0.07	0.12	0.04
Mn	0.00	0.00	0.00	0.00	0.00	0.00
Mg	0.02	0.02	0.00	0.03	0.08	0.06
Ca	0.97	0.98	0.99	0.97	0.88	0.94
Ba	0.01	0.01	0.01	0.01	0.00	0.01
Na	0.00	0.00	0.00	0.00	0.00	0.00
K	0.00	0.00	0.00	0.00	0.00	0.00

6.3.4.7 Pumpellyite

The Fe_{tot} and Mg contents of pumpellyite vary from 0.92 to 1.27 apfu and from 0.26 to 0.75 apfu, respectively (Table 6.10), while Al and Ca vary from 4.32 to 4.53 apfu and from 3.63 to 3.95 apfu, respectively. Mg# has a range from 0.22 to 0.65. The analyses classify as pumpellyite-Fe (Figure 6.11f).

Table 6.10. Representative analysis of pumpellyite from the Peltetec Unit.

Sample	P-47		P-33	
Lithology	greenschist		fine-grained metabasalt	
Major elements (wt.%)				
SiO_2	39.10	38.43	36.69	36.73
TiO_2	0.04	0.07	0.08	0.05
Al_2O_3	23.22	23.61	22.92	22.90
Cr_2O_3	0.08	0.02	0.00	0.01
FeOt	9.43	9.51	7.12	7.57
MnO	0.10	0.10	0.11	0.13
MgO	1.88	1.09	2.35	1.81
CaO	22.41	22.85	22.26	22.35
Na_2O	0.05	0.02	0.07	0.10
K_2O	0.03	0.03	0.02	0.01
Total	96.33	95.71	91.62	91.67
Formula based on 24.5 oxygens				
Si	6.16	6.12	6.03	6.05
Ti	0.00	0.01	0.01	0.01
Al	4.31	4.43	4.44	4.45
Cr	0.01	0.00	0.00	0.00
Fe^{3+}	0.36	0.33	0.50	0.47
Fe^{2+}	0.89	0.93	0.48	0.58
Mn	0.01	0.01	0.02	0.02
Mg	0.44	0.26	0.58	0.44
Ca	3.79	3.90	3.92	3.95
Na	0.01	0.01	0.02	0.03
K	0.01	0.01	0.00	0.00

6.3.4.8 Serpentine

Serpentine in serpentinites have 2.00-2.08 Si apfu, 2.59-2.76 Mg apfu and 0.09-0.20 Fe apfu, locally with relatively low Al content (<0.08 apfu) (e.g. Table 6.11).

Table 6.11. Representative analysis of serpentine from the Peltetec Unit.

Sample	P-24			
Lithology	serpentinite			
Major elements (wt.%)				
SiO_2	44.49	43.87	44.01	43.56
TiO_2	0.00	0.01	0.01	0.01
Al_2O_3	0.47	0.67	1.14	1.20
Cr_2O_3	0.01	0.02	0.02	0.05
FeOt	4.70	2.54	4.82	4.77
MnO	0.08	0.04	0.06	0.10
MgO	37.68	39.27	37.08	37.01
NiO	0.19	0.35	0.21	0.14
CaO	0.02	0.05	0.02	0.02
Na_2O	0.00	0.01	0.01	0.00
K_2O	0.02	0.02	0.01	0.03
Cl	0.01	0.01	0.01	0.01
Total	87.69	86.86	87.40	86.90
Formula based on 7 oxygens				
Si	2.07	2.05	2.06	2.05
Ti	0.00	0.00	0.00	0.00
Al	0.03	0.04	0.06	0.07
Cr	0.00	0.00	0.00	0.00
Fe^{2+}	0.18	0.10	0.19	0.19
Mn	0.00	0.00	0.00	0.00
Mg	2.62	2.73	2.59	2.60
Ni	0.01	0.01	0.01	0.01
Ca	0.00	0.00	0.00	0.00
Na	0.00	0.00	0.00	0.00
K	0.00	0.00	0.00	0.00
Cl	0.00	0.00	0.00	0.00

6.3.4.9 Fe-Ti Oxides

Rutile was identified in the granite of the Tres Lagunas Unit, which is almost pure TiO_2 with apparent low impurities of SiO_2 (0.10-0.52 wt.%) and FeO (0.14-0.49 wt.%).

Iron oxides were analyzed in serpentinites, which correspond to magnetite (Table 6.12). Some magnetite analyses have Cr_2O_3 <8.87 wt.% and MgO <2.93 wt.%, indicating modified composition of relict Cr-spinel from the ultramafic protolith. SiO_2 contents up to <3.77 wt.% indicate submicroscopic silicates in magnetite.

6.3.4.10 Relict Minerals

Chromium spinel.

Chromium spinel in serpentinites is characterized by higher Cr (1.01-1.12 apfu) than Al (0.68-0.76 apfu), Fe_{tot} (0.62-0.77 apfu) and Mg (0.44-0.52 apfu) contents (Table 6.12). Locally it has Fe-Ni-rich mineral inclusions. The amount of Cr# [Cr=(Cr/Cr+Al)] varies from 0.59 to 0.61 apfu, Mg# from 0.45 to 0.52 and calculated Fe^{3+} content is low (<0.24 apfu). Therefore, it is classified as aluminum chromite (Figure 6.12a) with intermediate composition between spinel-chromite and magnesiochromite-hercynite end members (Figure 6.12b).

Table 6.12. Representative analysis of magnetite and chromium spinel from serpentinite of the Peltetec Unit.

Sample	P-24							
Lithology	serpentinite							
Mineral	Magnetite				Chromiun spinel			
Major elements (wt.%)								
SiO_2	0.10	1.60	0.25	0.20	0.06	0.04	0.97	0.15
TiO_2	0.13	0.06	0.06	0.01	0.12	0.12	0.13	0.13
Al_2O_3	0.82	0.00	0.00	0.00	20.20	20.16	18.17	19.73
Cr_2O_3	8.87	1.82	0.01	0.05	44.19	44.36	40.16	44.36
FeOt	82.20	89.98	93.61	92.95	23.40	23.43	28.88	23.66
MnO	1.11	0.06	0.04	0.04	0.34	0.35	0.38	0.42
MgO	0.46	1.17	0.25	0.28	11.06	11.05	10.49	10.46
NiO	0.46	0.08	0.05	0.16	0.10	0.10	0.12	0.08
CaO	0.00	0.03	0.00	0.00	0.00	0.00	0.01	0.01
K_2O	0.02	0.02	0.01	0.01	0.01	0.01	0.01	0.01
Total	94.18	94.82	94.29	93.70	99.48	99.63	99.31	99.02
Formula based on 4 oxygens								
Si	0.00	0.06	0.01	0.01	0.00	0.00	0.03	0.00
Ti	0.00	0.00	0.00	0.00	0.00	0.00	0.00	0.00
Al	0.04	0.00	0.00	0.00	0.75	0.75	0.68	0.74
Cr	0.27	0.05	0.00	0.00	1.10	1.10	1.01	1.11
Fe^{3+}	1.68	1.82	1.98	1.98	0.14	0.14	0.24	0.13
Fe^{2+}	0.93	0.99	0.99	0.98	0.47	0.47	0.52	0.50
Mn	0.04	0.00	0.00	0.00	0.01	0.01	0.01	0.01
Mg	0.03	0.07	0.01	0.02	0.52	0.52	0.50	0.50
Ni	0.01	0.00	0.00	0.00	0.00	0.00	0.00	0.00
Ca	0.00	0.00	0.00	0.00	0.00	0.00	0.00	0.00
K	0.00	0.00	0.00	0.00	0.00	0.00	0.00	0.00

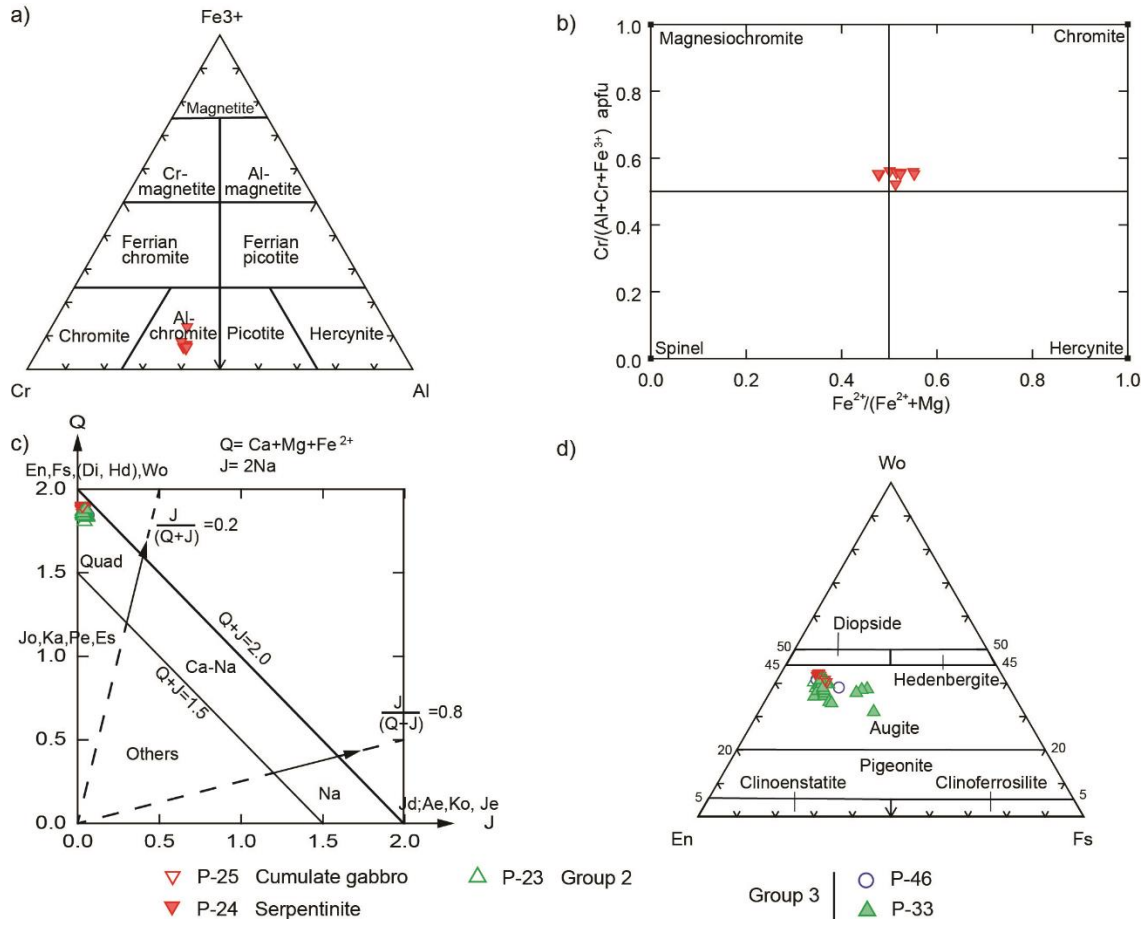

Figure 6.12. Classification of relict minerals. a) and b) Composition of chromium spinel in terms of Al-Cr-Fe^{3+} and Cr/(Al+Cr+Fe^{3+}) vs Fe^{2+}/(Fe^{2+}+Mg) (after Barnes and Roeder, 2001). c) Q–J diagram for pyroxene classification (Morimoto and Kitamura, 1983), and d) pyroxene composition in terms of En-Wo-Fs (diagrams after Morimoto et al., 1988).

Pyroxene

Pyroxene relics of cumulate gabbros, metabasalts and metadiabases with an assemblage of transitional prehnite-pumpellyite facies correspond to Ca-Mg-Fe pyroxene of augite composition (Figure 6.12c-d). The pyroxenes in cumulate metagabbro are characterized by $Wo_{40.18-42.99}$ $En_{46.54-48.16}$ $Fe_{9.60-13.20}$ (calculated as in Morimoto et al., 1988) with Mg content ranging from 0.90 to 0.95 apfu, Fe_{tot} from 0.19 to 0.26 apfu and Ca from 0.78 to 0.84 apfu, while Na is lower than 0.02 apfu and #Mg varies between 0.81 and 0.89 (Table 6.13). Instead, relicts of augite from metabasalts and metadiabase are characterized by $Wo_{31.29-41.39}$ $En_{37.09-52.01}$ $Fe_{9.89-29.86}$ with Mg content ranging from 0.72 to 1.00 apfu, Fe_{tot} from 0.19 to 0.58 apfu and Ca from 0.61 to 0.79 apfu, while Na is lower than 0.03 apfu and #Mg varies between 0.59 and 0.89 (Table 6.13).

Table 6.13. Representative analysis of pyroxene (augite) relicts from metabasalts, metadiabase and cumulate gabbro.

Sample	P-46	P-23	P-33		P-25	
Lithology	metadiabase	metadiabase	fine-grained metabasalt		cumulate metagabbro	
Major elements (wt.%)						
SiO_2	50.47	51.04	49.42	50.84	52.18	51.56
TiO_2	0.87	0.46	1.16	0.95	0.33	0.49
Al_2O_3	2.32	3.22	2.08	3.26	2.13	2.06
Cr_2O_3	0.03	0.23	0.00	0.11	0.27	0.19
FeOt	10.61	7.11	14.97	9.06	6.23	7.79
MnO	0.27	0.17	0.36	0.24	0.15	0.22
MgO	15.33	17.80	12.57	17.13	17.14	16.42
CaO	18.62	18.94	17.98	17.47	20.82	20.11
BaO	0.00	0.00	0.01	0.02	0.00	0.00
Na_2O	0.34	0.26	0.33	0.27	0.19	0.24
K_2O	0.01	0.01	0.02	0.00	0.01	0.01
Total	98.87	99.25	98.91	99.33	99.45	99.10
Formula based on 6 oxygens						
Si	1.90	1.88	1.90	1.88	1.92	1.91
Ti	0.02	0.01	0.03	0.03	0.01	0.01
Al	0.10	0.14	0.09	0.14	0.09	0.09
Cr	0.00	0.01	0.00	0.00	0.01	0.01
Fe^{3+}	0.08	0.09	0.07	0.06	0.06	0.07
Fe^{2+}	0.25	0.12	0.41	0.22	0.14	0.18
Mn	0.01	0.01	0.01	0.01	0.00	0.01
Mg	0.86	0.98	0.72	0.95	0.94	0.91
Ca	0.75	0.75	0.74	0.69	0.82	0.80
Ba	0.00	0.00	0.00	0.00	0.00	0.00
Na	0.02	0.02	0.02	0.02	0.01	0.02
K	0.00	0.00	0.00	0.00	0.00	0.00
En%	44.22	50.27	37.09	49.27	48.16	46.60
Fs%	17.17	11.27	24.78	14.62	9.81	12.40
Wo	38.61	38.46	38.13	36.11	42.03	41.00

6.4 Discussion

6.4.1 Metamorphic conditions

Litherland et al. (1994) described the alteration mineralogy of gabbros with calcite + brucite + tremolite + chlorite intergrowths and spilitized dolerite and basalts with quartz + albite + carbonate + sericite + chlorite + epidote and suggested that these assemblages resulted by reaction with heated seawater. These authors also noted hydrothermally-altered brecciated

types with epidote-quartz and carbonate-anthophyllite veins that Spikings et al. (2015) interpreted in the context of generalized greenschist facies conditions during sea-floor metamorphism. Nevertheless, mineral analysis and quantitative determinations of pressure and temperature of metamorphism have not been reported so far.

The textural characteristics and mineral composition of mafic rocks evidence local cores of magnesio-hornblende, magnesio-ferri-hornblende and pargasite in amphibole and andesine and oligoclase in plagioclase. These compositions are considered the result of a first metamorphic event referred to as M_0 (Table 6.3; Figure 6.13) developed at intermediate temperature during initial cooling (retrograde alteration) of mafic rocks in the sea-floor environment. Instead, the generalized Ab+Act+Ep+Chl+Ms+Ttn greenschist facies mineral assemblage in mafic rocks is considered the result of a second event (M_1; Figure 6.13) that developed assemblages in textural equilibrium amenable for estimation of thermobarometric conditions of crystallization and, hence, the geotectonic environment of formation. These conditions were calculated by means of isochemical P-T projections and the “average P-T” method.

Perple_X software (Connolly, 1990, 2005) was used in the calculation of the isochemical pressure-temperature (*P-T*) projections (pseudosections) for sample P-52 in the system K_2O-Na_2O-CaO-FeO-MgO-Al_2O_3-SiO_2-TiO_2-H_2O-O_2. The O_2 content of the bulk-rock composition was estimated assuming 5% Fe^{3+} of total iron (wt.%), which reproduces the observed mineral assemblage within the P-T window of interest. Sample P-52 was selected because it shows an equilibrium mineral assemblage with the largest number of mineral phases (corresponding to the lowest thermodynamic variance) and is representative of the peak conditions of the complex during M1 (Figure 6.13c). With the subprogram Werami of PERPLE_X package, contoured and smoothed *P-T* graphs were produced that include isopleths corresponding to Si in muscovite and Na in amphibole (Connolly, 2005). The calculated *P-T* pseudosection shows a general trend of increasing Na in amphibole with increasing pressure, while Si in mica decreases with increasing temperature. The stability of chlorite restricts the metamorphic conditions to <450 °C, while mica appears above ~2.5 kbar (Figure 6.14a). The absence of clinopyroxene in the assemblage is also taken into consideration for defining the P-T window of stability. In sample P-52, the highest values of Na in amphibole range between 0.1 and 0.2 apfu and cluster dominantly around 0.15, while the highest Si in muscovite ranges between 3.25 – 3.36 apfu. The corresponding Na and Si isopleths in the *P-T* pseudosection indicate a range of *P-T* conditions of 300-400 °C and <6 kbar (Figure 6.14b), that corresponds to an assemblage field consistent with the observed mineral assemblage.

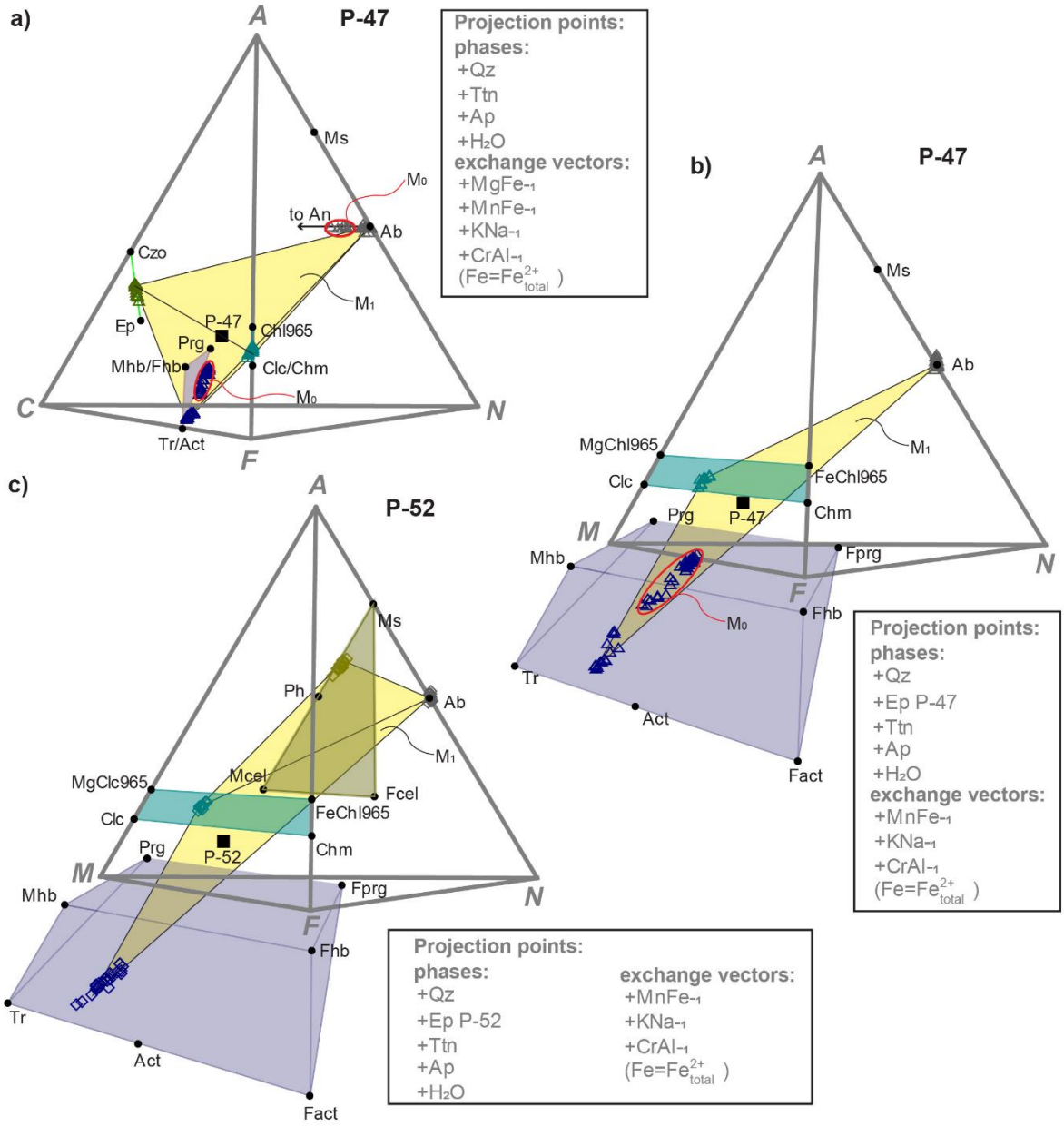

Figure 6.13. Phase relationships for greenschists in the ACFN and AFMN diagrams for samples P-47 and P-52 with indication of metamorphic stages M_0 and M_1. The minerals and bulk rock compositions are projected from the phases and exchange vectors indicated in each diagram. Ep P-47 and Ep P-52 correspond to representative compositions of epidote from the samples P-47 and P-52 respectively.

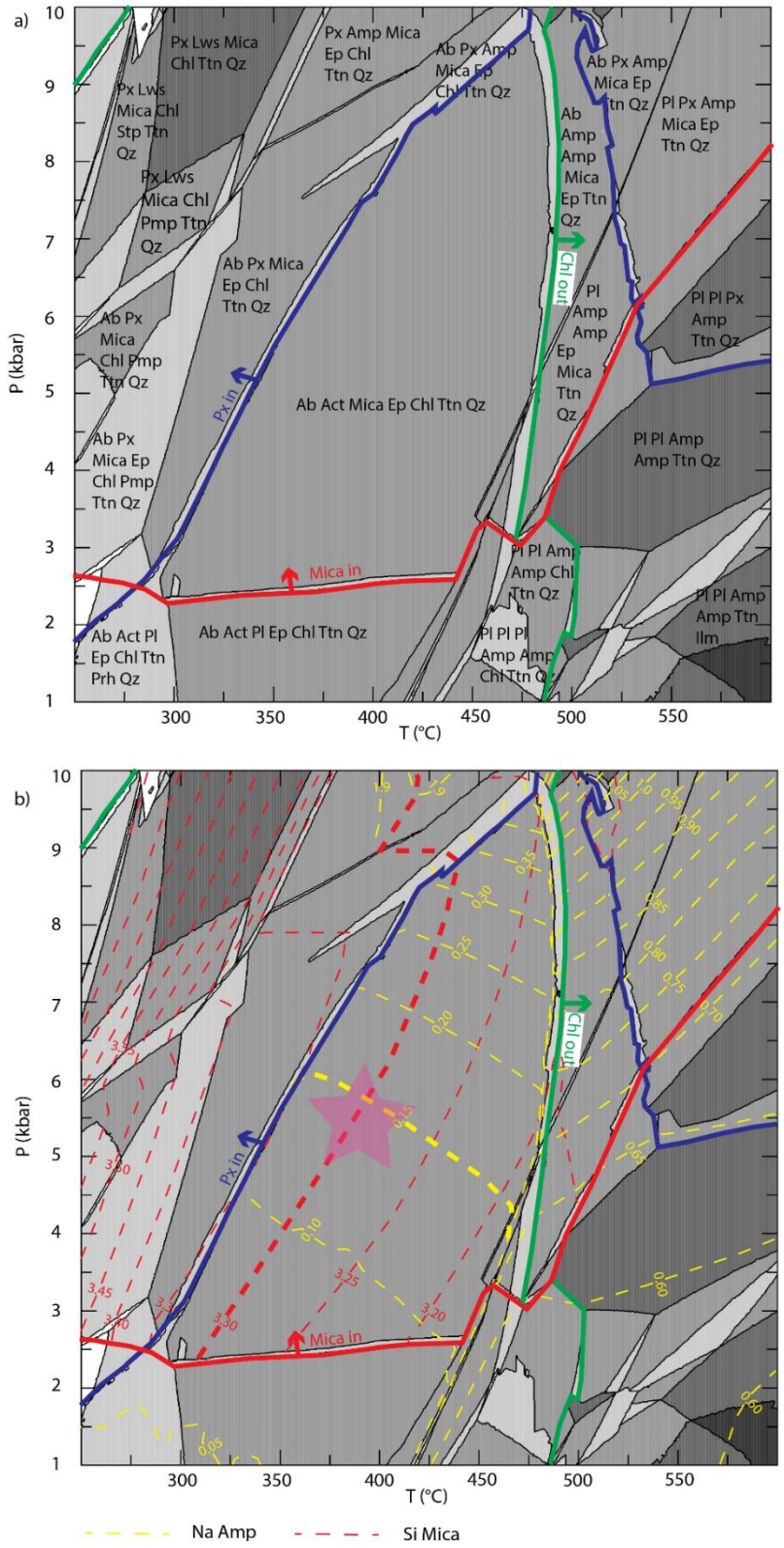

Figure 6.14. a) P-T pseudosection calculated with PERPLE_X for the composition of metabasalt P-52 [SiO_2=51.07, Al_2O_3=16.42, TiO_2= 1.13, MgO=8.7, FeO=8.17, CaO=10.92, Na_2O=2.84, K_2O=0.55, O_2=0.20 (weight percent)]. Mineral abbreviations after Whitney and Evans (2010). The color code indicates thermodynamic variance (decreasing from darker to lighter grey). b) Isopleths for Si (apfu) in muscovite (red dashed lines) and Na (apfu) in the amphibole (yellow dashed lines) are represented.

In order to precise and corroborate the results obtained with the isochemical *P-T* projection, the calculation of pressure and temperature also was performed using THERMOCALC 3.33 with the option “average P-T (AvPT)” and the thermodynamic data set tc-ds55 (Holland and Powel, 1998, updated in 2003; Powell and Holland, 1994), while the activities of the components were determined using the software AX2 (2014). The results, including the correlations, sigfit values and uncertainty ellipses are given in Table 6.14 and Figure 6.15. The calculation of average P-T was performed with the mineral association albite-amphibole-chlorite-epidote for sample P-47 and albite-amphibole-chlorite-epidote-muscovite for sample P-52 (Figure 6.13); which allowed estimating P-T conditions of 309±29 °C and 3.9±1.3 kbar and 314±26 °C and 3.7±1.1 kbar respectively (Table 6.14). These estimations indicate lower greenschist facies conditions slightly above the limit of the prehnite-pumpellyite facies (Figure 6.15) and agree with the isochemical P-T projection. These values indicate a geothermal gradient of ca. 22 °C/km, characteristic of intermediate P/T barrovian metamorphism.

Amphibole is a common mineral in metabasaltic rocks of the Peltetec Unit, either in completely recrystallized rocks or partly recrystallized rocks where it appears replacing the rims of clinopyroxene. The composition of all types of basic rocks, with relatively high CaO, FeO and Al_2O_3, moderate of MgO and Na_2O and low of K_2O contents, makes the presence of calcic amphibole favorable in the established P-T conditions (Figure 6.14 and Figure 6.15). These conditions discard, however, the crystallization of Ca-Na and Na amphiboles and, eventually, and high-Si phengite, typical of higher pressure. On the other hand, that pressure is higher than in typical of ocean floor metamorphism (i.e., ca. 1 kbar) is indicated by the local presence of pumpellyite and lack of prehnite in sub-greenschist facies rocks and transitional samples.

Table 6.14. Average P-T calculations of representative samples (P-47 and P-52)

Sample	T °C	Sd	P (kbar)	Sd	Corr	Sigfit
P-47	309	29	3.9	1.3	0.879	0.46
P52	314	26	3.7	1.1	0.865	0.23

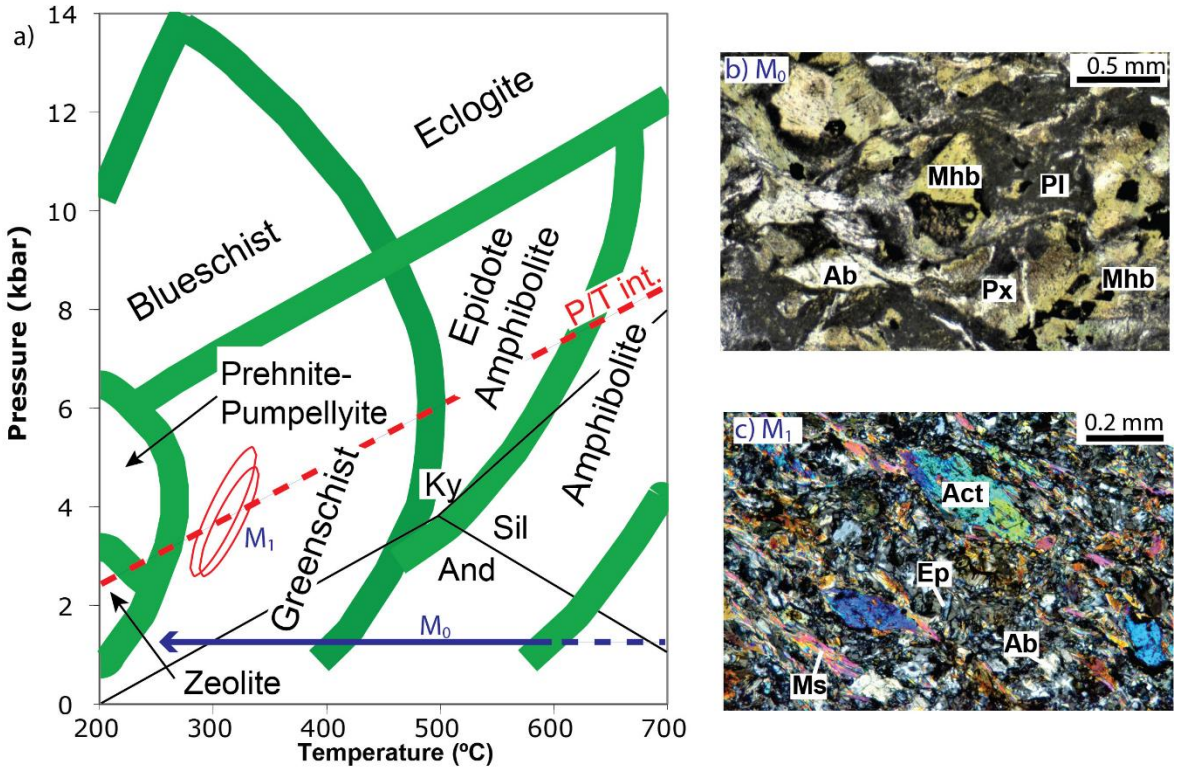

Figure 6.15. a) Pressure (P) vs temperature (T) diagram showing the metamorphic facies, the kyanite (Ky), andalusite (And) and sillimanite (Sil) phase diagram (Spear, 1993), and the P-T conditions (red ellipses) calculated using THERMOCALC 3.33 (Powell and Holland, 1994) with the option "average P-T (AvPT)" and the thermodynamic data set tc-ds55. M_0 refers to the first metamorphic event (retrogression after crystallization in the oceanic environment) and M_1 the second barrovian-type metamorphic event with intermediate geothermal gradient (P/T int, red dashed line). b-c) Photomicrographs showing b) static crystallization of magnesio-hornblende from augite during M_0 and c) peak M_1 greenschist mineral assemblage.

6.4.2 Tectonic interpretation

The composition of chromium spinel and clinopyroxene relicts in serpentinites of the Guarguallá valley and some metagabbros and metabasalts respectively, allows evaluating the tectonic setting of formation of the protoliths. The composition of chromium spinel corresponds to supra-subduction zone peridotites (Figure 6.16a-b; fields after Dick and Bullen, 1984; Ishii et al., 1992; Kamenetsky et al., 2001), while the composition of clinopyroxene shows a MORB affinity (Figure 6.16c-d; fields after Leterrrier et al., 1982; Beccaluva et al., 1979). These data support the generation of the Peltetec Unit in a supra-subduction setting with MORB-like affinity in a back-arc zone, as is also indicated by whole-rock composition (Villares et al., 2020).

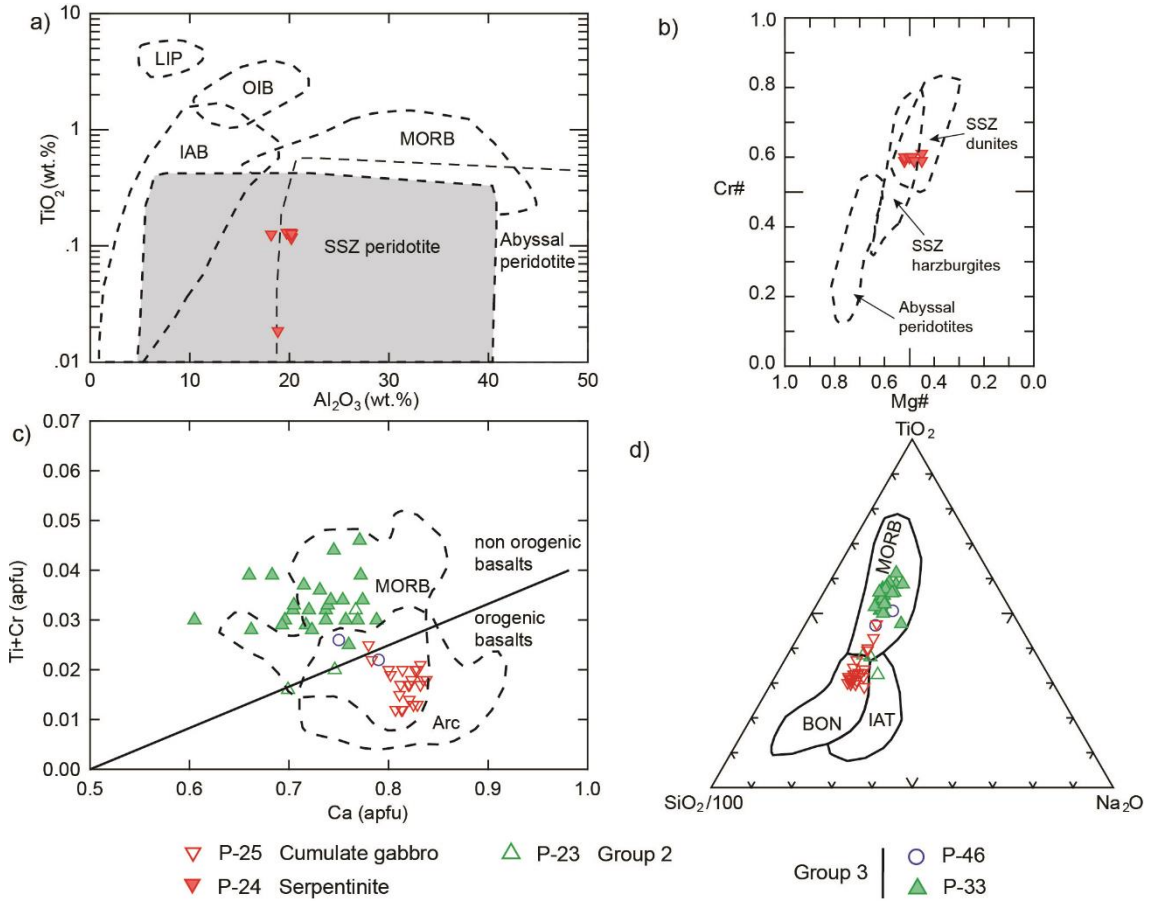

Figure 6.16. a) TiO_2 (wt%) vs Al_2O_3 (wt%) showing the fields of chromite from different geotectonic settings (after Kamenetsky et al., 2001). b) Cr# (Cr/(Cr+Al)) versus Mg# (Mg/(Mg+Fe^{2+})); data sources: abyssal peridotites (Dick and Bullen, 1984) and supra-subduction zone (SSZ) peridotites (Ishii et al., 1992). c) Ti+Cr vs Ca (apfu) diagram showing the mid-ocean ridge basalt (MORB) and arc fields of pyroxene (Leterrier et al., 1982). d) Ternary diagram in terms of SiO_2/100-TiO_2-Na_2O of pyroxene, BON: boninite, IAT: island-arc tholeiite, MORB: mid-ocean-ridge basalt (after Beccaluva et al., 1979).

The tectonic setting of metamorphism, on the other hand, was varied. The relict cores of pargasite, magnesiohornblende and magnesio-ferri-hornblende (Figure 6.8 and Figure 6.9) in samples from different sectors indicate a first retrogressive ocean-floor metamorphic event (M_0) developed in the oceanic environment upon cooling of the oceanic lithosphere in the back-arc region, as indicated by the relatively high temperature of pargasite and magnesio-hornblende in mafic rocks (> 600 °C) (e.g. Gilbert et al., 1982). This metamorphic imprint is only locally observed, as a likely consequence of episodic and local infiltration of seawater along fracture systems. This event should have taken place shortly after rock crystallization at 228 Ma (Figure 6.17, Villares et al., 2020). The absence of other minerals associated with amphibole cores rule out calculation of P-T conditions, but intermediate-

high pressure is not indicted by amphibole crystalchemistry (i.e., low Na-in-B; Figure 6.8a; Table 6.4).

On the other hand, the greenschist assemblage Act-Ab-Ep-Ttn-Chl±Ms represents a superimposed metamorphic event (M_1) with a calculated intermediate (barrovian) P-T gradient. The conditions of metamorphism estimated in greenschist samples and the presence of subgreenschist and transitional facies assemblages point to a former metamorphic zoning now obliterated by the tectonic activity of the Peltetec Fault zone, with tectonic slices corresponding to varied depth levels. The textural and structural characteristics of the rocks indicate syn-tectonic recrystallization, as evidenced by (i) the alignment of the metamorphic minerals following the schistosity planes (S_{1P}); (ii) the common “slaty” cleavage in fine-grained metabasaltic rocks and greenschists; (iii) the deformed millimeter-sized albite veinlets; (iv) the segregation of albite in folded levels; (v) common mylonitic fabric and S-C structures of actinolite. Furthermore, the P-T conditions estimated indicate burial down to ca. 15 km depth, which cannot be reached during sea-floor metamorphism of oceanic crust in an extensional regime. All these characteristics indicate instead regional metamorphism in a compressive regime that generated the dominant S_{1P} slate cleavage, the prevalent mineral assemblages and the micro-deformation in shear C-planes (S_{CP}). Such a compressional event was likely associated with the closure of the back-arc basin and the tectonic emplacement of the unit onto the continental margin. The attempt to date this metamorphic event by means of U-Pb titanite was unsuccessful due to its very fine-grained size.

The Guamote metasedimentary sequence that overlays the Peltetec Unit shows slaty cleavage and crenulation. The weak foliation parallel to S_{0G} is interpreted as a result of burial and crustal thickening, latter affected by deformation (S_{1G} crenulation cleavage). While, the unmetamorphosed Maguazo Unit is folded along a trend similar to the Guamote sequence, including steeper dip to the east of the Peltetec Unit, suggesting a single event of deformation for the Maguazo and Guamote units (Figure 6.7). According to the Jurassic – Cretaceous age of these units, deformation can be associated with the closure of marginal basins during Albian and late Cretaceous times (e.g. Spikings et al., 2015, Cardona et al., 2020) and/or the collision of the Ecuadorian-Colombian-Caribbean plateau against South America in the late Cretaceous – Paleogene (e.g. Reynaud et al., 1999; Kerr et al., 2003; Vallejo et al., 2009).

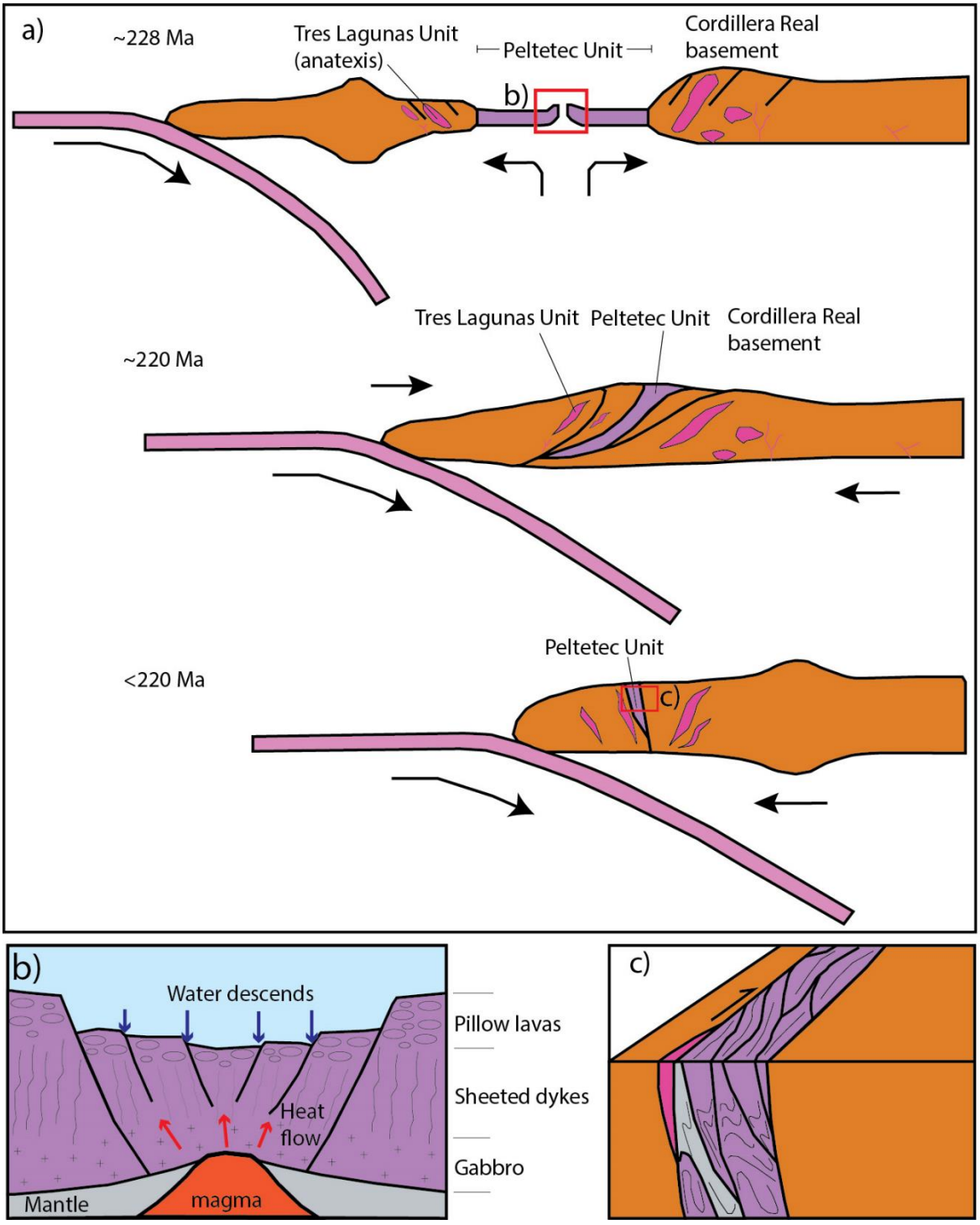

Figure 6.17. a) Schematic geodynamic model for the Peltetec Ophiolite. Shortly before 228 Ma, trench retreat and slab roll-back triggered extension of the continental lithosphere in a supra-subduction setting, originating the Peltetec oceanic back-arc basin with MORB-like affinity where seafloor metamorphism (low P/T) occurred (M_0). Anatexis of stretched continental crust is indicated as a potential origin of the Tres Lagunas Unit to the East and West of the basin. At ~220 Ma, the change in the tectonic regime from extensional to compressive generated the closure of the basin and emplacement of the Peltetec Unit onto the continental margin, triggering regional deformation and metamorphism (M_1) with intermediate (barrovian) P/T gradient. b) Schematic model for the seafloor metamorphism (M_0). c) Schematic representation of the slivers of the Peltetec Unit after emplacement.

Spikings et al. (2015) reported two $^{40}Ar/^{39}Ar$ plagioclase ages yielding 134.7 ± 0.9 and 134 ± 13 Ma in metabasaltic rocks of the Peltetec Unit, and interpreted these results as the minimum age of crystallization of the basaltic protoliths. This early Cretaceous age has been reinterpreted by Villares et al. (2020), who offered a Triassic U-Pb zircon age of 228 Ma as the timing of ophiolite formation. Besides, thermochronological data from late Triassic granitoids and migmatites from the Cordillera Real of Ecuador show re-heating during middle Jurassic to Cretaceous times related to burial and further increased heat flow during lithospheric extension (Paul et al., 2018), and a group of mid-Mesozoic K/Ar ages from the Cordillera Real was interpreted by Litherland et al. (1994) as thermally activated diffusion resetting of the isotopic system. However, because the tectonic regimen in the Northern Andes during the late Jurassic to early Cretaceous was extensional, characterized by the opening of basins and marine sedimentation, with their subsequent closure and deformation during the late Cretaceous (Spikings et al., 2015; Zapata et al., 2018, Cardona et al., 2020), the early Cretaceous $^{40}Ar/^{39}Ar$ plagioclase age cannot correspond to the timing of the M_1 event of the Peltetec Unit, which developed under a compressive regime. Therefore, this age is interpreted as a later reset age triggered by re-heating identified in this period (Paul et al., 2018), while the closure of the back-arc basin and emplacement of the Peltetc Unit onto the continental margin (M_1) is related to a change from extensional to compressive regimen in the late Triassic (Figure 6.17). A similar scenario was identified in the El Oro metamorphic complex (226 Ma, Riel et al., 2014) related to the tectonic underplating of oceanic blueschists of the Arenillas-Panupalí Unit under the gabbroic Piedras Unit, and in the north in the Aburrá Ophiolite of Colombia (ca. 221 Ma; Ibañez-Mejia et al. 2020), with metamorphic sole formation and subsequent obduction on the continental crust. This late Triassic regional compressive regimen would have triggered deformation and metamorphism in the Peltetec Unit (E_1 in Table 6.3; Figure 6.17). Later processes (E_2 in Table 6.3) that affected the Peltetec Unit correspond to cataclastic-mylonitic deformation associated with the Peltetec fault system movement. New geochronological data for the Peltetec and adjacents units are required to reconstruct a solid model since Triassic times.

6.5 Conclusions

Along the Peltetec fault zone, meter- to hundreds meter-sized tectonic slices of the late Triassic (228 Ma) Peltetec metaophiolite, composed by arc and NMORB-like lavas, cumulate gabbros, serpentinites and associated metasediments document extension of the active western margin of Gondwana and formation of an intracontinental back-arc. The chemical composition of relict chromium spinel and clinopyroxene is consistent with

formation in a back-arc basin in a supra-subduction setting, in agreement with previous interpretations of whole rock composition of metabasalts. Extension and formation of the back-arc basin was accompanied by partial melting of the extending continental curst, forming S-type granitoids of the Tres Lagunas unit associated with the ophiolite.

The tectonic slices of the different lithologies of the Peltetec Unit evidence variable deformation. Fine- to medium-grained metabasites commonly show a penetrative slaty cleavage deformed by C-type shear band cleavage, while minor medium-grained rocks show anastomosed mylonitic structures. Cumulate gabbros and granites (Tres Lagunas Unit) have a dominant cataclastic deformation with local ductile millimeter-sized shear bands. The mineral orientation evidence syn-tectonic recrystallization according to S_{1P}. The metabasites show varied metamorphic assemblages in different slices, from altered assemblages through prehnite-pumpellyite to greenschist facies, evidencing a former metamorphic zoning now obliterated by the tectonic activity of the Peltetec Fault zone and variable depth of metamorphism. Thermobarometric estimations based on the greenschist association albite+amphibole+chlorite+epidote±muscovite yielded peak metamorphic conditions of ~315 °C and ~3.9 kbar, which corresponds to a gradient of ca. 22 °C/km characteristic of intermediate P/T (barrovian) metamorphism. This event is associated with burial of the ophiolite during the closure of the back-arc basin and emplacement of the unit in Late Triassic times onto the continental margin. Cores of pargasite, magnesiohornblende and magnesio-ferri-hornblende document a previous retrograde high- to intermediate-temperature seafloor metamorphic event associated with ophiolite formation in the oceanic environment. Late processes characterized by cataclastic deformation are associated with the activity of the Peltetec fault system, when the ophiolitic slivers mingled with late Triassic S-type granitoids (Tres Lagunas Unit) and Jurassic-Cretaceous metasediments which normally bound the ophiolitic slivers.

Capítulo 7

The Tampanchi ultramafic-mafic complex (Ecuador): Origin, magmatic differentiation and age

7 The Tampanchi ultramafic-mafic complex (Ecuador): Origin, magmatic differentiation and age

7.1 Introduction

The active margin of northwestern Gondwana/South America records long-term continental-arc magmatism since, at least, the Permian, interrupted during periods when slab dip changed and/or extensional stress field and accretionary processes occurred (e.g. Burgois et al., 1987; Litherland et al., 1994; Vallejo et al., 2009; Villagómez et al., 2011; Cochrane et al., 2014b; Spikings et al., 2015; Cardona et al., 2020). In the Ecuadorian Andes, two subparallel N-S-trending mountain ranges named Western and Eastern Cordilleras (the latter also termed Cordillera Real; Figure 7.1a) record various periods of uplift (Spiking et al., 2001; Ruiz et al., 2004; Spikings and Crowhurst, 2004) that exhumed deep continental arc rocks, thereby providing a window for studying the magmatic process that control the formation and evolution of intrusive complexes. Exposed magmatic intrusions in the Cordillera Real occurred from late Triassic to, at least, Paleogene times. Late Triassic intrusions correspond to S-type granitoids and mafic dykes (Litherland et al., 1994; Cochrane et al., 2014a; Paul et al., 2018; Villares et al., in 2020), while I-type granitoid (granite-granodiorite-tonalite) plutons dominate Jurassic – early Cretaceous intrusions (e.g. Litherland et al., 1994; Chiaradia et al., 2009; Drobe et al., 2013; Cochrane et al., 2014a). Other minor intrusions of intermediate-acid composition with U-Pb and K-Ar ages ranging between ~94–30 Ma distribute throughout the Cordillera Real, including the exceptional Tampanchi Ultramafic – Mafic Complex (TUMC) (Kennerley, 1980; Litherland et al., 1994; Cochrane, 2013; Guerrero, 2020). This complex has been described as a mafic intrusion with a probable Ural-Alaskan-type complex association (Pozo, 1990; Litherland et al., 1994). In South America, only the Tertiary Alto Condoto Complex in Colombia (~20 Ma) has been classified as an Alaskan-type Complex (Tistl, 1994); however, the high concentration of platinum-group minerals (PGMs) in local alluvial deposits of the northwestern Ecuadorian Andes (Santiago River) suggests that similar mafic complexes must be exposed in this region (Weiser and Schmidt-Thomé, 1993; López-Males et al., 2020).

In this contribution we characterize the Tampanchi Ultramafic– Mafic Complex by means of lithological mapping, petrological and geochemical analysis and geochronologic dating, and evaluate the nature of the parental magma and its tectonic setting of formation in the context of the geodynamic evolution of the northwestern margin of South America.

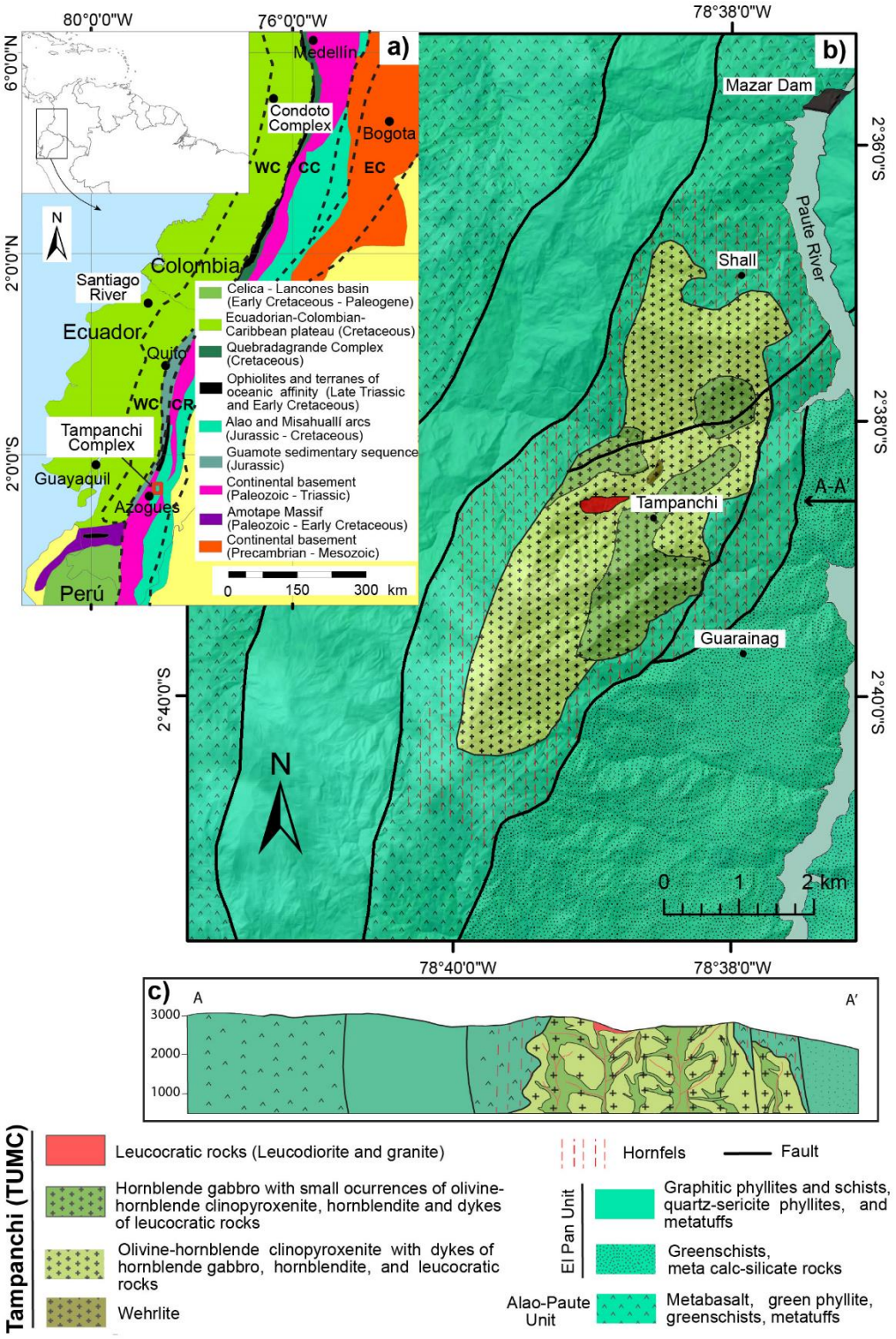

Figure 7.1. a) Schematic representation of the tectonic bocks/complexes in the Northern Andes and location of the study area; ophiolites and terranes of oceanic affinity are represented in black, including the late Triassic Peltetec ophiolitic belt, the amphibolitized Piedras metagabbro and the high-pressure (HP) Arenillas-Panupali Unit (Ecuador), and the early Cretaceous HP Raspas (Amotape Massif, Southwestern Ecuador) and Arquía (Colombia) complexes; WC: Western Cordillera, CC: Central Cordillera, CR: Cordillera Real, EC: Eastern Cordillera. b) Geological map of the study area showing the main lithological groups and faults. c) Schematic E-W cross-section (A – A' in figure b).

7.2 Geological framework

The basement of the Cordillera Real consists of variably metamorphosed and deformed continental and oceanic rock bodies intruded by plutons of varied affinity and age and covered by recent volcanic deposits (Figure 7.1a), which as whole record a long-lasting history of subduction and amalgamation of blocks along the northwestern margin of Gondwana/South America. Lithologies with older protolith age include Neo-proterozoic gabbros, late Paleozoic to Triassic metasedimentary rocks and late Triassic back-arc basalts, S-type granites, amphibolite dykes and migmatites (Litherland et al., 1994; Chew et al., 2007; Cochrane et al., 2014a; Spikings et al., 2015; Paul et al., 2018; Villares et al., 2020; Spikings et al., 2021). Jurassic to early Cretaceous lithologies include intrusive, effusive and sedimentary arc-related rocks that record no metamorphism or low- to intermediate-grade metamorphic conditions (Lihterland et al., 1994; Chiaradia et al., 2009; Drobe et al., 2013; Cochrane et al., 2014b; Spikings et al., 2015). The Tampanchi Ultramafic – Mafic Complex intrudes the Alao arc (El Pan, Alao-Paute, and Maguazo Units; Litherland et al., 1994), which has been interpreted as an allochthonous terrane of island arc affinity accreted to the continental margin during early Cretaceous times (Litherland et al., 1994) or as an autochthonous unit resulting from the continued Jurassic – Cretaceous subduction system, the progressive westward arc-axis migration and the attenuation of the upper crust (Pratt et al., 2005; Cochrane et al., 2014b; Spikings et al., 2015). The Maguazo and El Pan Units include highly deformed and variably metamorphosed sedimentary sequences of poorly constrained protolith age ranging between middle Jurassic and early Cretaceous (Riding, 1989). The Alao–Paute Unit consists of variably metamorphosed andesitic – basaltic rocks of tholeiitic and calc-alkaline affinity with subordinate pelitic schists, graphitic schists, quartzites and marbles (Litherland et al., 1994; Cochrane et al., 2014b). The age of the Alao-Paute Unit is not well defined, yielding K/Ar (igneous hornblende) ages of 115 ± 12 Ma and 142 ± 36 Ma (Rundle, 1988) interpreted as reset ages related to a tectono-thermal event (Litherland et al., 1994), while U-Pb zircons ages of a quartzite yielded a maximum depositional age of 163.7 ± 1.6 Ma (Cochrane et al., 2014b). The Alao arc-related rocks are considered equivalent to the Colombian Quebradagrande complex, which records active volcanism from ~150 Ma to 80 Ma (Villagomez et al., 2011; Cochrane et al., 2014b; Spikings et al., 2015; Zapata et al., 2019). On the other hand, west of the Maguazo Unit, the metasedimentary Guamote sequence of probable Jurassic age (Litherland et al., 1994; Cochrane et al., 2014b) occurs in contact with associated rocks to the allochthonous oceanic Ecuadorian-Colombian-Caribbean plateau (~140 to 87 Ma; e.g. Hoernle et al., 2004; Vallejo et al., 2009), which also includes arc-related rocks (99-79 Ma; e.g. Vallejo et al., 2006; Whattam and Stern, 2014; Macías-Mosquera and Rojas Agramonte, 2019)

interpreted as a result of west-dipping subduction beneath the oceanic plateau (Vallejo et al., 2009). The plateau accreted to the northwestern margin of South America during late Cretaceous-Paleocene times forming the basement of the Western Cordilleras of Ecuador and Colombia (Figure 7.1a; e.g. Reynaud et al., 1999; Kerr et al, 2003; Vallejo et al., 2009; Vallejo et al., 2019).

The Tampanchi Ultramafic – Mafic Complex is hosted in a tectonic slice of the Alao-Paute Unit, the latter composed of metabasalts, green phyllites, metavolcaniclastic rocks and local greenschists (Figure 7.1b-c). This slice is tectonically limited to the West and East by the El Pan Unit, with graphitic phyllites, graphitic schists, quartz-sericite phyllites and volcaniclastic beds to the West and clinozoisite-tremolite schists, actinolite-chlorite schists, metamorphosed calc-silicate rocks and meta-volcaniclastic beds to the East (Figure 7.1b-c). Deformation increases toward the shear-zone contacts between these units, where the rocks show schistose fabrics and crenulation cleavages. The TUMC exhibits an oval shape about 6 km long and 3 km wide that follows a NNE-SSW trend (Figure 7.1b). It was initially described as amphibolites (Bristow et al., 1975), later interpreted as an undeformed and unmetamorphosed concentric intrusion composed of serpentinite, peridotite and olivine pyroxenite in the core surrounded by concentric zones of clinopyroxenite, hornblendite, and gabbro, and with the development of contact-metamorphic hornfels in the host rock (Pozo, 1990; Litherland et al., 1994). Due to the wide lithological diversity, the apparent concentric pattern and the lack of orthopyroxene, the TUMC was associated to an Alaskan-type intrusion (Pozo, 1990; Litherland et al., 1994). Previously reported geochemical data are scarce but suggest a calc-alkaline affinity while K-Ar (hornblende) ages yield 60 to 65 Ma (Litherland et al., 1994).

7.3 Petrographic and textural characteristics

The TUMC is an intrusive body constituted by different lithologies from ultramafic to felsic composition. The field relations allow establishing a chronological sequence of intrusions at the scale of the whole complex which, from older to younger, correspond to: 1) wehrlite and olivine-hornblende clinopyroxenite, 2) hornblendite, fine-grained hornblende gabbro, coarse-grained hornblende gabbro and pegmatite hornblende gabbro and 3) leucodiorite and granite. Hornfels were produced by amphibolite facies thermal contact metamorphism of the low-grade metamorphic country rock of the Alao-Paute Unit, which also occur locally as roof pendants within the TUMC (Figure 7.1 and Figure 7.2a).

The field relationships of the different lithologies in the TUMC do not confirm a concentric zoning pattern, as previously reported (Pozo, 1990). Few locations record homogeneous

rock bodies of a single lithology, and most of the body is characterized by complex distribution of magmatic rocks, crosscutting mafic-felsic dykes and abundant cm- to m-sized enclaves of pyroxenite and hornblendite. The contact relations between all types of rock varies from transitional to sharp. For mapping purposes, the lithologies were grouped according to the dominant lithotype (Figure 7.1b-c).

7.3.1 Wehrlite

Wehrlite corresponds to the earliest cumulate lithology in the TUMC. It outcrops mostly in the center of the complex forming bodies of tens of meters in size surrounded by olivine-hornblende clinopyroxenite (Figure 7.1b). The rocks are dark brown and reddish in color, have orthocumulate texture constituted by euhedral-subhedral olivine (<80%), interstitial anhedral-subhedral clinopyroxene (<30%), minor chromium spinel included in olivine grains and disseminated magnetite (Figure 7.3a-b). Veins of serpentine group minerals crosscut olivine crystals and some grains are transformed to iddingsite at their rims while locally secondary tremolite partially replaces clinopyroxene.

7.3.2 Clinopyroxenites

This is the dominant lithology of the TUMC distributed throughout the complex (Figure 7.1). It represents the second earliest lithology, being intruded by all other groups of rocks (Figure 7.2b-e). It locally crosscuts the host Alao-Paute Unit along veins. According to the content of amphibole and olivine in the samples, mineral names are added to the nomenclature of clinopyroxenite (i.e., clinopyroxenite, olivine clinopyroxenite, olivine-hornblende clinopyroxenite, hornblende clinopyroxenite; c.f., Le Maitre et al., 2002). The term olivine-hornblende clinopyroxenite, the most abundant type of clinopyroxenite, is used through this paper to group all types of clinopyroxenite.

These rocks show a greenish coloration, have massive structure and adcumulate texture, but locally show granoblastic texture adjacent to intruding hornblende gabbros. The crystals are mainly medium-grained and have anhedral to subhedral shapes (Figure 7.3c-e). The primary mineralogy is constituted by clinopyroxene (50-90%), olivine (0-20%), hornblende (0-30 %) and magnetite (<2%). Amphibole lamellae and patches with anhedral shapes, locally with zoned amphiboles, occur within and at the rims of individual clinopyroxene grains and in between grains (Figure 7.3c-e respectively), yielding pseudopoikilitic texture in the more recrystallized rocks that points to replacement process for their origin. The abundance of amphibole is variable, increasing toward the contact with hornblende gabbros as a consequence of clinopiroxenite-gabbroic magma interactions (Figure 7.2b). Locally,

pods/veins rich in plagioclase occur adjacent to hornblende (Figure 7.2f). Secondary minerals (<5 %) are iddingsite and serpentine developed after olivine and magnetite, chlorite and epidote.

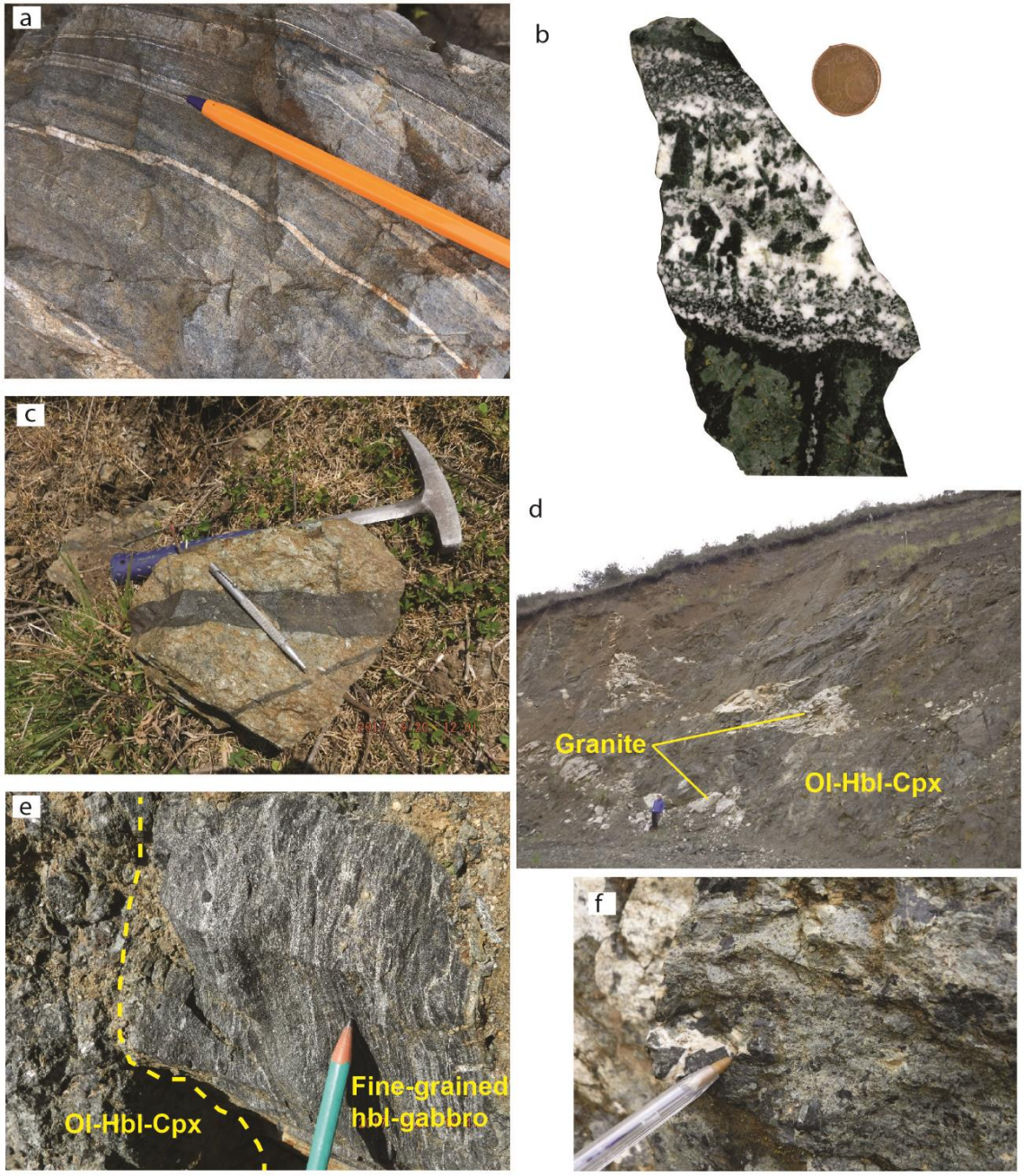

Figure 7.2. Field relations of the TUMC. a) Amphibolite hornfels with veins of plagioclase-rich rock in the Alao-Paute Unit. b) Olivine-hornblende clinopyroxenite crosscut by a vein of pegmatitic hornblende gabbro; hornblendite is generated in the contact by reaction replacement of clinopyroxene by hornblende. Note increase in grain size from the border to the center of the vein of hornblende gabbro. c) Olivine-hornblende clinopyroxenite crosscut by a vein of hornblendite. d) Olivine-hornblende clinopyroxenite crosscut by granite bodies. e) Fine-grained hornblende gabbro crosscutting olivine-hornblende clinopyroxenite. f) Clinopyroxenite partially replaced by amphibole; plagioclase is interstitial between amphibole grains.

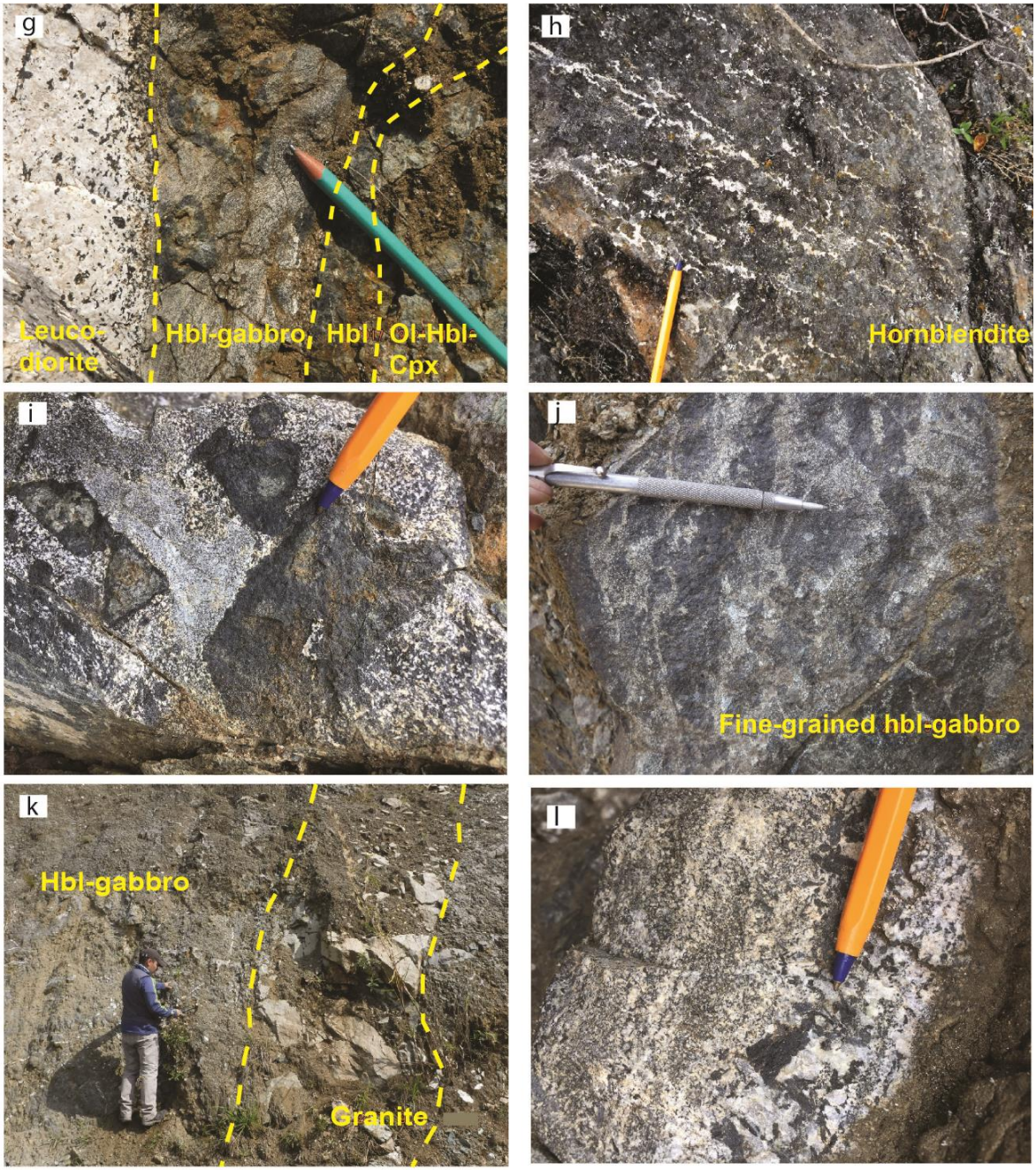

Figure 7.2. (Continued). g) Dyke of Pl-rich leucodiorite crosscutting fine-grained hornblende gabbro; note the transition from olivine-hornblende clinopyroxenite through hornblendite and fine-grained hornblende gabbro to leucodiorite. h) Coarse-grained hornblendite generated by replacement of clinopyroxenite with interstitial plagioclase. i) Enclaves of olivine-hornblende clinopyroxenite with hornblendite rims with coarse-grained hornblende gabbro. j) Stockwork-like structure with fine-grained hornblende gabbro and hornblendite. k) Granite dyke crosscutting hornblende gabbro. l) Coarse-grained hornblende gabbro with a pegmatoid band. Abbreviations: Ol-Hbl-Cpx (olivine-hornblende clinopyroxenite), Hbl-gabbro (hornblende gabbro), Hbl (hornblendite).

7.3.3 Hornblendite

This lithology is mainly located in the contact between olivine-hornblende clinopyroxenite and hornblende gabbros showing variable thickness from a few millimeters to a few meters (Figure 7.2b-h). In addition, other occurrences correspond to veins/dykes within olivine-hornblende clinopyroxenite (Figure 7.2c), enclaves in hornblende gabbros (Figure 7.2i) and cumulated pods. The contact with hornblende gabbros is sharp while with clinopyroxenite is sharp or transitional, increasing gradually the amphibole content towards the hornblende gabbro while the clinopyroxene content decreases.

This type of rock is strongly melanocratic, shows partially oriented granoblastic texture (locally orthocumulate) with average grain size ranging from 2 to 5 mm but locally reaching cm-sized crystals. It is made of amphibole (>80%), clinopyroxene (<10%), plagioclase (<10%), magnetite (<3%), biotite (<2%) and traces of titanite and ilmenite (Figure 7.3f-h). Plagioclase appears in interstitial position between coarse amphibole grains (Figure 7.2h and Figure 7.3h) and is partially replaced by late (subsolidus) white mica (<5%). Clinopyroxene is fine-grained and appears replaced and surrounded by amphibole (pseudopoikilitic texture; Figure 7.3g) or interstitial between amphiboles. Late epidote and chlorite (<5%) occur in between amphibole grains but locally within the rims of amphibole, denoting subsolidus growth.

7.3.4 Hornblende gabbros

7.3.4.1 Fine-grained hornblende gabbro

This type of rock occurs with about a few cm to a few tens of meters in size at the margins of coarse-grained hornblende gabbro in contact with olivine-hornblende clinopyroxenite (Figure 7.2b), or as veins/dykes that crosscut olivine-hornblende clinopyroxenite (Figure 7.2e, g). The contact with hornblendite is sharp, suggesting a late-stage magmatic phase. The structure is banded with millimetric to centimetric bands of plagioclase and amphibole (Figure 7.2e). Locally, it shows stockwork-like structure with hornblende gabbro surrounding hornblendite (Figure 7.2j) and enclaves of hornblendite included in gabbro.

The color is gray to dark, showing a fine- (to medium-) grained phaneritic texture constituted by amphibole (60–80%), plagioclase (20–40%), clinopyroxene (<1%) and traces of magnetite, titanite, apatite and zircon (Figure 7.3i). Plagioclase is locally transformed to subsolidus white mica while secondary chlorite overprints amphibole.

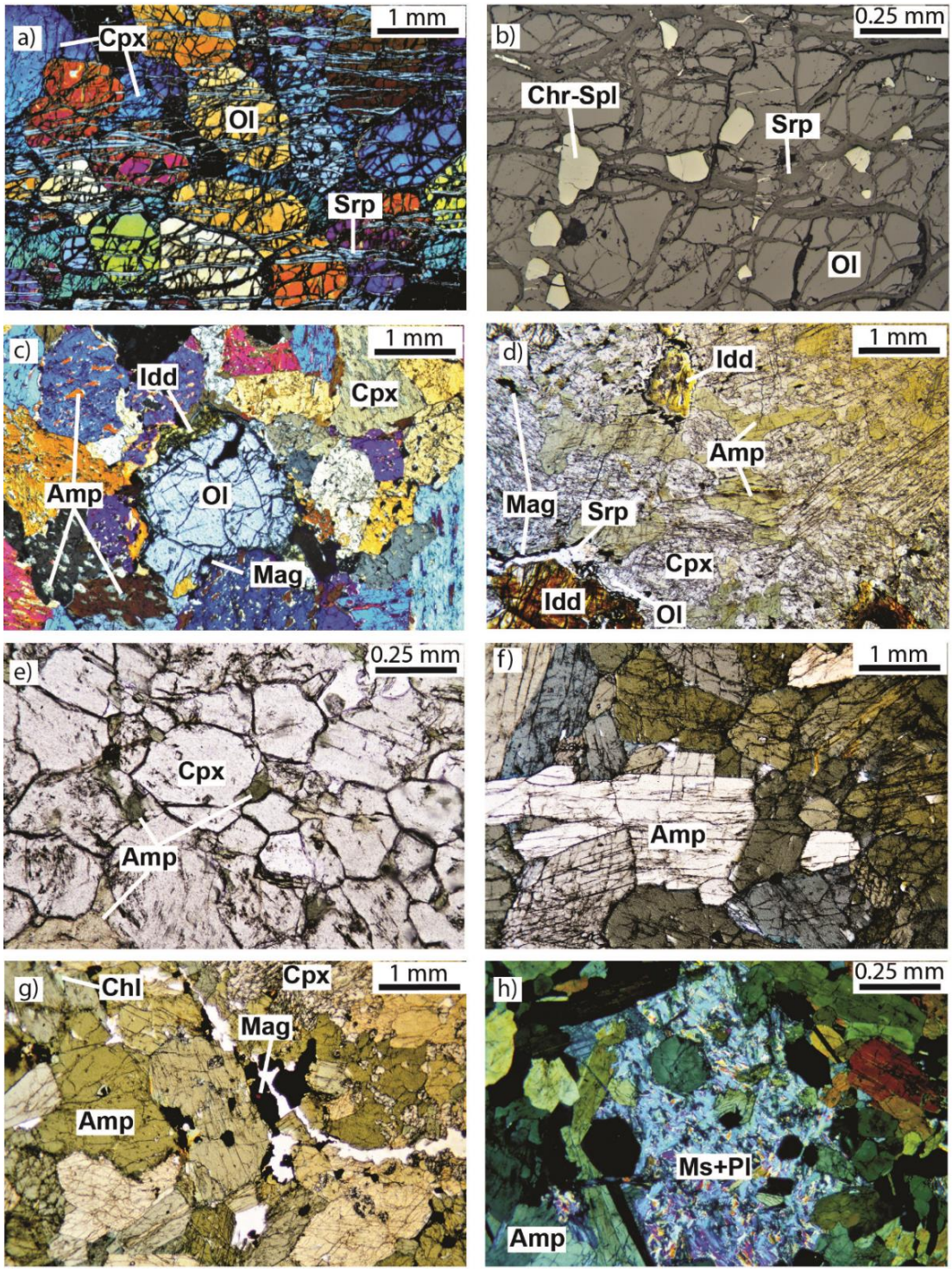

Figure 7.3. Optical microphotographs showing mineralogical and textural details of studied rocks: a) Cumulate olivine with interstitial clinopyroxene in wehrlite; veinlets of serpentine crosscut olivine. b) Reflected light view of wehrlite with chromium spinel and olivine crystals crosscut by veinlets of serpentine. c) Olivine-hornblende clinopyroxenite with cumulate texture and lamellae of amphibole in pyroxene. d) Olivine-hornblende clinopyroxenite with pyroxene replaced by amphibole; olivine is transformed to iddingsite. e) Adcumulate texture in hornblende clinopyroxenite with amphibole in interstitial position. f) Hornblendite with granoblastic texture generated by reaction-replacement of pyroxene by amphibole. g) Hornblendite; note pseudopoikilitic texture with pyroxene partially included in, and replaced by, amphibole. h) Late poikilitic plagioclase replaced by muscovite in hornblendite.

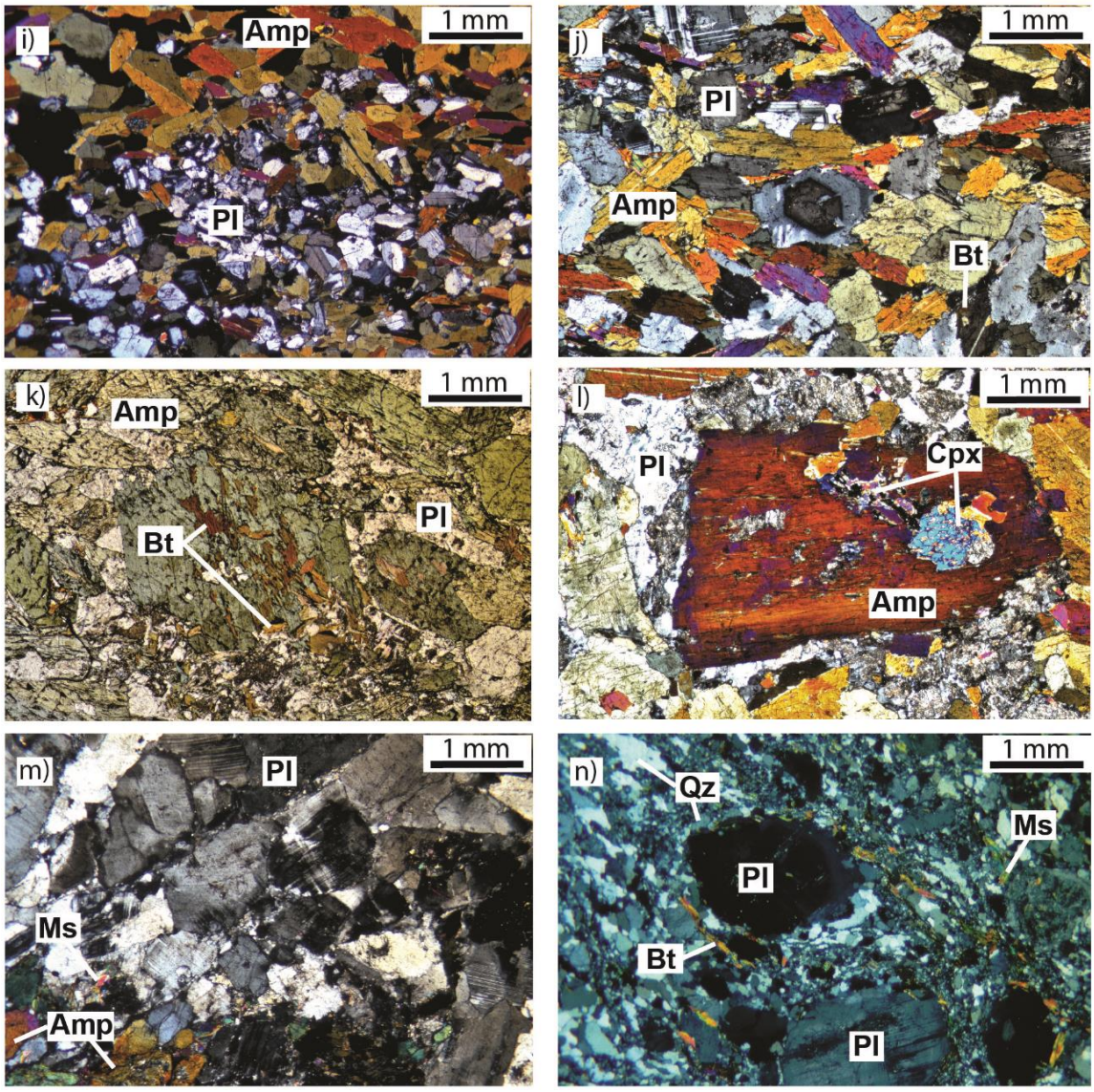

Figure 7.3. (Continued). Fine-grained hornblende gabbro with partially-oriented mineral grains. j) Zoned plagioclase and amphibole in coarse-grained hornblende gabbro. k) Coarse-grained hornblende gabbro with interstitial plagioclase in between amphibole; biotite replaces amphibole. l) Coarse-grained hornblende gabbro with poikilitic amphibole including clinopyroxene. m) Leucodiorite with zoned plagioclase. n) Mylonitized granite; quartz, biotite and muscovite affected by grain size reduction define a foliation, while feldspars are mainly porphyroclasts. Mineral abbreviations are from Whitney and Evans (2010).

7.3.4.2 Coarse-grained hornblende gabbro

Coarse-grained hornblende gabbro occurs as intrusions of variable size reaching 1 km across section. They crosscut olivine-hornblende clinopyroxenite and fine-grained hornblende gabbro, or transitionally change from coarse-grained hornblende gabbro in the core of the intrusions towards fine-grained hornblende gabbro in the rims (Figure 7.2b, k, l). Pegmatitic lithologies appear as dykes or toward the center of the gabbroic intrusions.

The rocks are light gray in color, have phaneritic locally cumulate texture, coarse- to medium-grained crystal size and generally shows mineral orientation but banding is not developed. They contain centimetric aggregates of hornblende and enclaves of clinopyroxenite and hornblendite (Figure 7.2i). The rocks are constituted by amphibole (40–65%), plagioclase (25–50%), clinopyroxene (<1%), titanite (<1%), biotite (<1%), magnetite (<1%) and traces of apatite and zircon (Figure 7.3j-k). Locally clinopyroxene is included in amphibole (poikilitic texture; Figure 7.3l). Plagioclase and amphibole grains develop strong zoning (Figure 7.3j). Biotite replaces amphibole (Figure 7.3k) and plagioclase is locally transformed to late white mica. The pegmatitic varieties show cumulate texture with phenocrysts of amphibole and/or plagioclase in a groundmass of clinopyroxene, hornblende and plagioclase, and traces of titanite, olivine and magnetite. Additional secondary minerals are epidote and chlorite.

7.3.5 Leucocratic rocks

7.3.5.1 Leucodiorite

These rocks appear in the margins of granites or as veins/dykes less than 2 meters in thickness that crosscut olivine-hornblende clinopyroxenite, hornblendite and hornblende gabbros (Figure 7.2g). They are white in color and show medium- to coarse-grained phaneritic cumulate texture and massive structure (Figure 7.3m). The constituent minerals are plagioclase (70-90%) and amphibole (<15%), with minor amount of quartz and traces apatite, magnetite, zircon and titanite (Figure 7.3m). The amphiboles are zoned and show slightly corroded rims. Late muscovite replaces plagioclase.

Some plagioclase-rich spots or centimetric plagioclase veinlets occur in hornblendites and crosscut olivine-hornblende clinopyroxenite and are related to the formation of hornblendite (Figure 7.2f and Figure 7.2h).

7.3.5.2 Granite

Granite commonly occurs as dykes of 1 to 5 meters in thickness or as individual intrusions not larger than 200 meters (Figure 7.2d and Figure 7.2k). It intrudes all other lithologies described so far and does not crop out in the wall-rock of the TUMC, pointing to a cogenetic relation with the TUMC. Generally, it shows massive structure but is locally affected by shearing, showing foliated mylonitic fabric and porphyroclastic texture (Figure 7.3n). The larger dykes show transitions towards leucodiorite in the outer parts of the bodies. The rock has light gray to white color and is constituted by quartz (30–50 %), plagioclase (30–60%), alkali feldspar (<10%), biotite (<6%), muscovite (<2%) and traces of zircon and apatite. The plagioclase crystals are zoned and, locally, fragmented.

7.4 Mineral composition

About 620 point analyses of chromium spinel, olivine, clinopyroxene, amphibole, feldspar, biotite, muscovite, Fe-Ti oxides, titanite, serpentine, epidote, iddingsite and chlorite from the all types of rock were made and representative analyses are presented in Tables 7.1-7.12.

7.4.1 Olivine

Olivine from wehrlite and olivine-hornblende clinopyroxenite is characterized by Fo (100*Mg/(Mg+Fe^{2+})) contents ranging between 87 to 91 and between 75 to 88, respectively. It has traces of Ca, Mn and Ni, with larger Ni in wehrlite (Figure 7.4a; Table 7.1).

Table 7.1. Representative electron probe analyses of olivine from the Tampanchi ultramafic-mafic Complex.

Sample	AR-65			AR-14			AR-31B		
Lithology	Wehrlite			Ol-Hbl pyroxenite			Ol-Hbl pyroxenite		
Major elements (wt.%)									
SiO_2	39.80	39.58	39.45	39.20	38.11	39.28	38.71	38.46	38.44
TiO_2	0.00	0.00	0.01	0.00	0.00	0.00	0.01	0.00	0.00
Al_2O_3	0.00	0.00	0.00	0.00	0.00	0.00	0.00	0.00	0.00
Cr_2O_3	0.00	0.01	0.10	0.01	0.01	0.00	0.00	0.00	0.00
FeO_t	13.06	12.85	11.68	16.42	17.34	16.83	19.61	21.46	21.54
MnO	0.25	0.25	0.28	0.32	0.44	0.32	0.54	0.47	0.48
MgO	46.65	46.92	48.35	44.02	43.55	43.61	41.02	39.72	38.59
NiO	0.13	0.14	0.13	0.07	0.08	0.08	0.06	0.07	0.07
CaO	0.02	0.02	0.02	0.03	0.02	0.01	0.02	0.03	0.04
Na_2O	0.01	0.01	0.00	0.00	0.01	0.00	0.02	0.00	0.01
K_2O	0.01	0.02	0.02	0.00	0.01	0.00	0.01	0.01	0.02
Total	99.95	99.80	100.03	100.06	99.57	100.14	99.99	100.23	99.19
Formula based on 4 oxygens									
Si	0.99	0.98	0.97	0.99	0.97	0.99	0.99	0.99	1.01
Ti	0.00	0.00	0.00	0.00	0.00	0.00	0.00	0.00	0.00
Al	0.00	0.00	0.00	0.00	0.00	0.00	0.00	0.00	0.00
Cr	0.00	0.00	0.00	0.00	0.00	0.00	0.00	0.00	0.00
Fe^{3+}	0.02	0.03	0.05	0.02	0.06	0.01	0.01	0.01	0.00
Fe^{2+}	0.25	0.23	0.19	0.32	0.31	0.34	0.41	0.45	0.47
Mn	0.01	0.01	0.01	0.01	0.01	0.01	0.01	0.01	0.01
Mg	1.73	1.74	1.78	1.66	1.65	1.64	1.57	1.53	1.50
Ni	0.00	0.00	0.00	0.00	0.00	0.00	0.00	0.00	0.00
Ca	0.00	0.00	0.00	0.00	0.00	0.00	0.00	0.00	0.00
Na	0.00	0.00	0.00	0.00	0.00	0.00	0.00	0.00	0.00
K	0.00	0.00	0.00	0.00	0.00	0.00	0.00	0.00	0.00
Fo%	87.38	88.11	90.49	83.62	84.37	82.82	79.38	77.26	76.16

7.4.2 Chromium spinel

Spinel in wehrlite is enriched in Cr (0.80-0.94 apfu) and Fe_{tot} (1.93-1.33 apfu) contents and depleted in Mg (<0.21 apfu) and Ti (0.02 apfu) contents, with variable Al (<0.48 apfu), and classifies as chromian magnetite and ferrian chromite (Figure 7.4b-c; Table 7.2).

Table 7.2. Representative electron probe analyses of chromium spinel from the Tampanchi ultramafic-mafic Complex.

Sample	AR-65				
Lithology	Wehrlite				
Major elements (wt.%)					
SiO_2	0.03	0.02	0.02	0.02	0.03
TiO_2	0.50	0.90	0.55	0.72	0.70
Al_2O_3	0.26	11.48	4.33	11.64	11.60
Cr_2O_3	30.68	33.88	27.75	34.48	34.16
FeOt	61.61	46.92	59.17	45.96	46.13
MnO	0.80	0.72	1.15	0.66	0.61
MgO	1.91	2.96	2.65	4.00	4.03
NiO	0.12	0.10	0.14	0.09	0.07
CaO	0.00	0.08	0.00	0.00	0.00
Na_2O	0.00	0.00	0.00	0.00	0.00
K_2O	0.01	0.01	0.02	0.02	0.02
Total	95.92	97.09	95.77	97.59	97.37
Formula based on 4 oxygens					
Si	0.00	0.00	0.00	0.00	0.00
Ti	0.01	0.02	0.02	0.02	0.02
Al	0.01	0.47	0.19	0.48	0.47
Cr	0.91	0.94	0.80	0.94	0.94
Fe^{3+}	1.05	0.54	0.98	0.54	0.55
Fe^{2+}	0.88	0.84	0.83	0.79	0.79
Mn	0.03	0.02	0.04	0.02	0.02
Mg	0.11	0.15	0.14	0.21	0.21
Ni	0.00	0.00	0.00	0.00	0.00
Ca	0.00	0.00	0.00	0.00	0.00
Na	0.00	0.00	0.00	0.00	0.00
K	0.00	0.00	0.00	0.00	0.00

7.4.3 Clinopyroxene

Clinopyroxenes from wehrlite, olivine-hornblende clinopyroxenite and hornblendite is Ca-rich and corresponds to diopside following Morimoto et al. (1988), with $Wo_{47.36-50.32}$ $En_{37.19-47.76}$ $Fe_{3.68-12.76}$ composition (Figure 7.4d). Diopside in wehrlite and olivine-hornblende

clinopyroxenite has higher Mg, Ca and Mg# than in hornblendite, with 0.91-0.94 apfu Mg, 0.93-0.99 apfu Ca and 0.94–0.97 Mg# contents in wehrlite and 0.82-0.93 apfu Mg, 0.94-1.00 apfu Ca and 0.88–0.95 Mg# contents in olivine-hornblende clinopyroxenite, while in hornblendite diopside has 0.71-0.83 apfu Mg, 0.95-0.98 apfu Ca and 0.84–0.89 Mg# contents. In all types of rock, diopside has low Al, Fe_{tot}, Ti and Na contents, though they are higher in hornblendites than in wehrlite and olivine-hornblende clinopyroxenite (Figure 7.4e-f; Table 7.3).

Table 7.3. Representative electron probe analyses of clinopyroxene from the Tampanchi ultramafic-mafic Complex.

Sample	AR-65		AR-14	AR-31B			AR-14b	AR-10	
Lithology	Wehrlite		Ol-Hbl pyroxenite				Hornblendite		
Major elements (wt.%)									
SiO_2	52.70	53.43	53.15	52.66	52.08	52.66	50.80	50.56	53.04
TiO_2	0.17	0.09	0.16	0.20	0.27	0.16	0.32	0.48	0.08
Al_2O_3	1.59	0.89	1.35	1.51	2.12	1.70	3.05	3.54	1.07
Cr_2O_3	0.49	0.17	0.12	0.14	0.04	0.01	0.06	0.00	0.00
FeO_t	2.93	2.53	3.78	3.72	4.73	5.18	6.15	6.65	6.34
MnO	0.11	0.10	0.12	0.13	0.15	0.17	0.24	0.18	0.21
MgO	16.88	17.30	16.79	16.31	15.25	15.74	14.51	13.76	14.26
NiO	0.01	0.03	0.00	0.00	0.01	0.00	0.00	0.00	0.00
CaO	24.20	24.76	24.10	24.53	24.96	24.10	23.82	24.32	24.56
Na_2O	0.11	0.04	0.07	0.06	0.07	0.09	0.17	0.22	0.33
K_2O	0.02	0.01	0.01	0.01	0.02	0.02	0.02	0.01	0.01
Total	99.21	99.34	99.65	99.27	99.69	99.82	99.15	99.73	99.90
Formula based on 6 oxygens									
Si	1.93	1.96	1.95	1.94	1.92	1.94	1.89	1.88	1.96
Ti	0.00	0.00	0.00	0.01	0.01	0.00	0.01	0.01	0.00
Al	0.07	0.04	0.06	0.07	0.09	0.07	0.13	0.15	0.05
Cr	0.01	0.00	0.00	0.00	0.00	0.00	0.00	0.00	0.00
Fe^{3+}	0.05	0.04	0.04	0.05	0.06	0.05	0.08	0.08	0.05
Fe^{2+}	0.04	0.03	0.07	0.07	0.09	0.11	0.11	0.12	0.15
Mn	0.00	0.00	0.00	0.00	0.00	0.01	0.01	0.01	0.01
Mg	0.92	0.94	0.92	0.89	0.84	0.86	0.80	0.76	0.79
Ni	0.00	0.00	0.00	0.00	0.00	0.00	0.00	0.00	0.00
Ca	0.95	0.97	0.95	0.97	0.99	0.95	0.95	0.97	0.97
Na	0.01	0.00	0.00	0.00	0.00	0.01	0.01	0.02	0.02
K	0.00	0.00	0.00	0.00	0.00	0.00	0.00	0.00	0.00
En%	47.00	47.38	46.34	45.27	42.55	43.76	41.36	39.36	40.21
Fs%	4.57	3.88	5.85	5.79	7.41	8.08	9.84	10.67	10.03
Wo%	48.43	48.73	47.81	48.95	50.04	48.16	48.80	49.98	49.76
Mg#	0.96	0.97	0.93	0.93	0.91	0.89	0.88	0.86	0.84

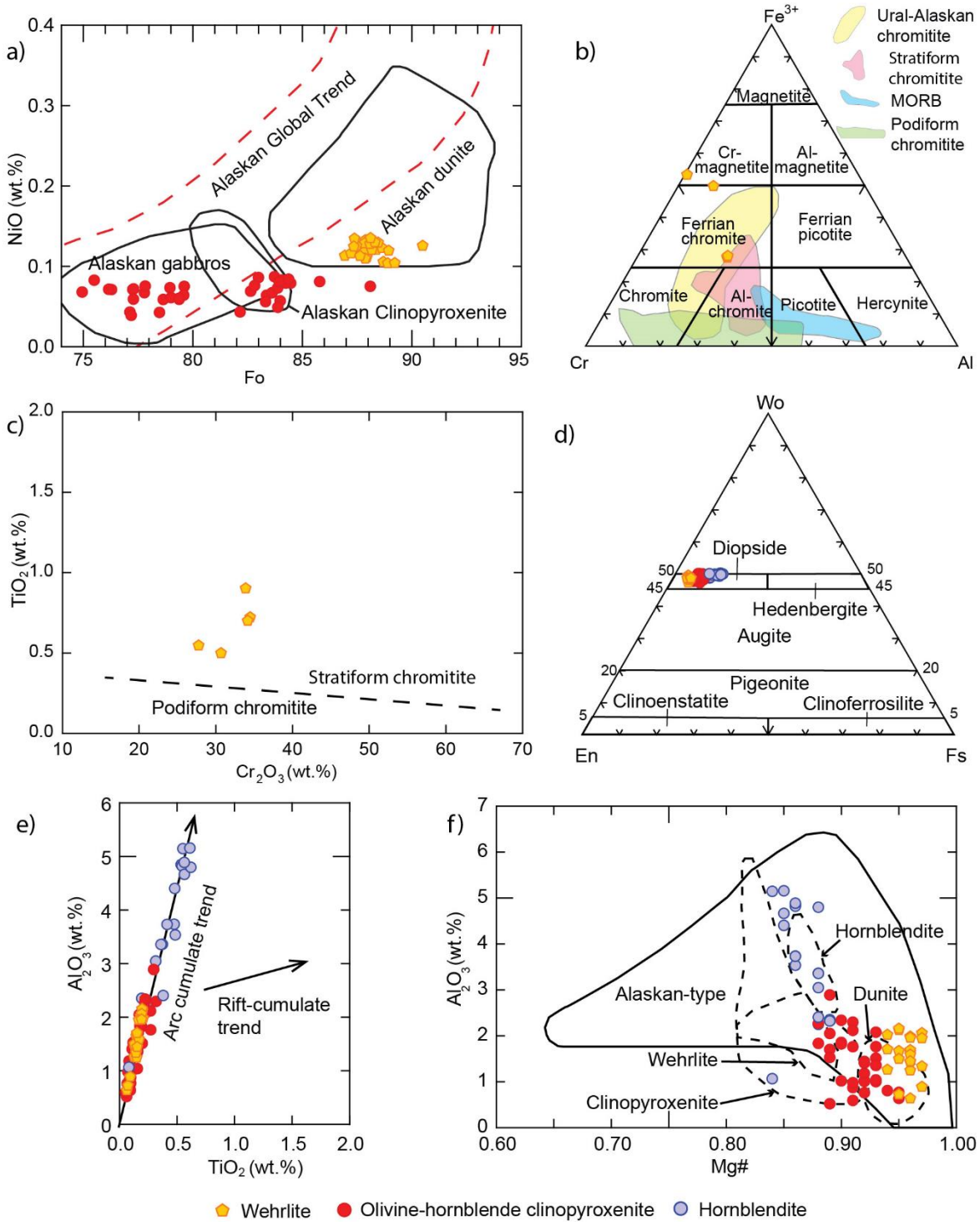

Figure 7.4. a) Composition of olivine from olivine-hornblende clinopyroxenite in terms of NiO (wt%) and forsterite (Fo) contents compared with Alaskan-type olivines (Himmelberg and Loney, 1995; Krause et al., 2007). b) and c) Composition of chromium spinel in terms of Al-Cr-Fe^{3+} and TiO_2 (wt%) vs Cr_2O_3 (wt%) (fields after Arai, 1992; Bonavia et al., 1993; Barnes and Roeder, 2001; Arai et al., 2004). d) - f) Clinopyroxene composition in terms of En-Wo-Fs (diagram after Morimoto et al., 1988), Al_2O_3 (wt.%) vs TiO_2 (wt.%) and Al_2O_3 (wt.%) vs. Mg#; field of Alaskan-type intrusions is from Himmelberg and Loney (1995) and fields of lithologies are from Krause et al. (2007).

7.4.4 Amphibole

Amphibole is the most common mineral in the complex, showing calcic composition in all lithological groups (Ca^B=1.82-1.99 apfu; Figure 7.5a) but with a wide compositional variation. As a whole, it has strong variation in Si (5.85-7.84 apfu), Al_{tot} (0.24-2.76 apfu), Mg (2.11-4.60 apfu), Fe_{tot} (0.36-2.09 apfu), Ca (1.67-2.02 apfu) and Na (0.05-0.58 apfu), and low contents in Ti (<0.20 apfu), Mn (<0.05 apfu), K (<0.30 apfu) and Cl (<0.02 apfu) (Figure 7.5; Table 7.4). Primary (i.e., magmatic) amphibole from olivine-hornblende clinopyroxenite is dominantly magnesio-ferri-hornblende and locally magnesio-hastingsite and pargasite (classification scheme after Hawthorne et al., 2012). Hornblendites are constituted mainly by pargasite and magnesio-hastingsite, and locally by magnesio-hornblende and magnesio-ferri-hornblende. In hornblende gabbros, amphibole is mainly pargasite and magnesio-hornblende, with local magnesio-ferri-hornblende. Coarse crystals are zoned, with pargasite cores and magnesio-hornblende rims. Amphibole from leucodiorite is mainly magnesio-ferri-hornblende and locally magnesio-hornblende. Amphiboles are magnesian (Mg# = 0.56–0.96), with the highest Mg# in olivine-hornblende clinopyroxenite, followed by amphibole rims of coarse-grained hornblende gabbros and amphiboles from leucodiorite, amphibole of fine-grained hornblende gabbros and amphibole cores of coarse-grained hornblende gabbros. In hornblendite, Mg# is in the range of hornblende gabbros. Local secondary (subsolidus) amphibole is tremolite and actinolite (Figure 7.5).

7.4.5 Feldspar

Feldspars are absent in wehrlite and olivine-hornblende clinopyroxenite groups. Plagioclase occurs in all other lithologies, and granites also bear alkali feldspar (Figure 7.6a, Table 7.5). The Ca-richest plagioclase is found in fine-grained hornblende gabbros and corresponds to bytownite (An_{71-89}). Plagioclase in coarse-grained hornblende gabbros is zoned, with Ca-rich cores of bytownite (An_{74-83}), locally labradorite (An_{63-66}) and rims and individual crystals of andesine (An_{38-44}). In leucodiorite, plagioclase is dominantly andesine (An_{34-50}) with local labradorite (An_{51-52}) and rims of oligoclase and albite (An_{8-28}), while in granites it is zoned (An_{12-42}) from more calcic cores (andesine) to sodium-rich rims (oligoclase). Alkali feldspar corresponds to orthoclase (Or_{92-95}). The progressive decrease in Ca towards the rims of zoned plagioclase in all types of rock suggests normal magmatic fractionation. In hornblendite, plagioclase is of oligoclase and albite (An_{7-14}) composition, pointing to a late magmatic (near-solidus) or non-magmatic origin.

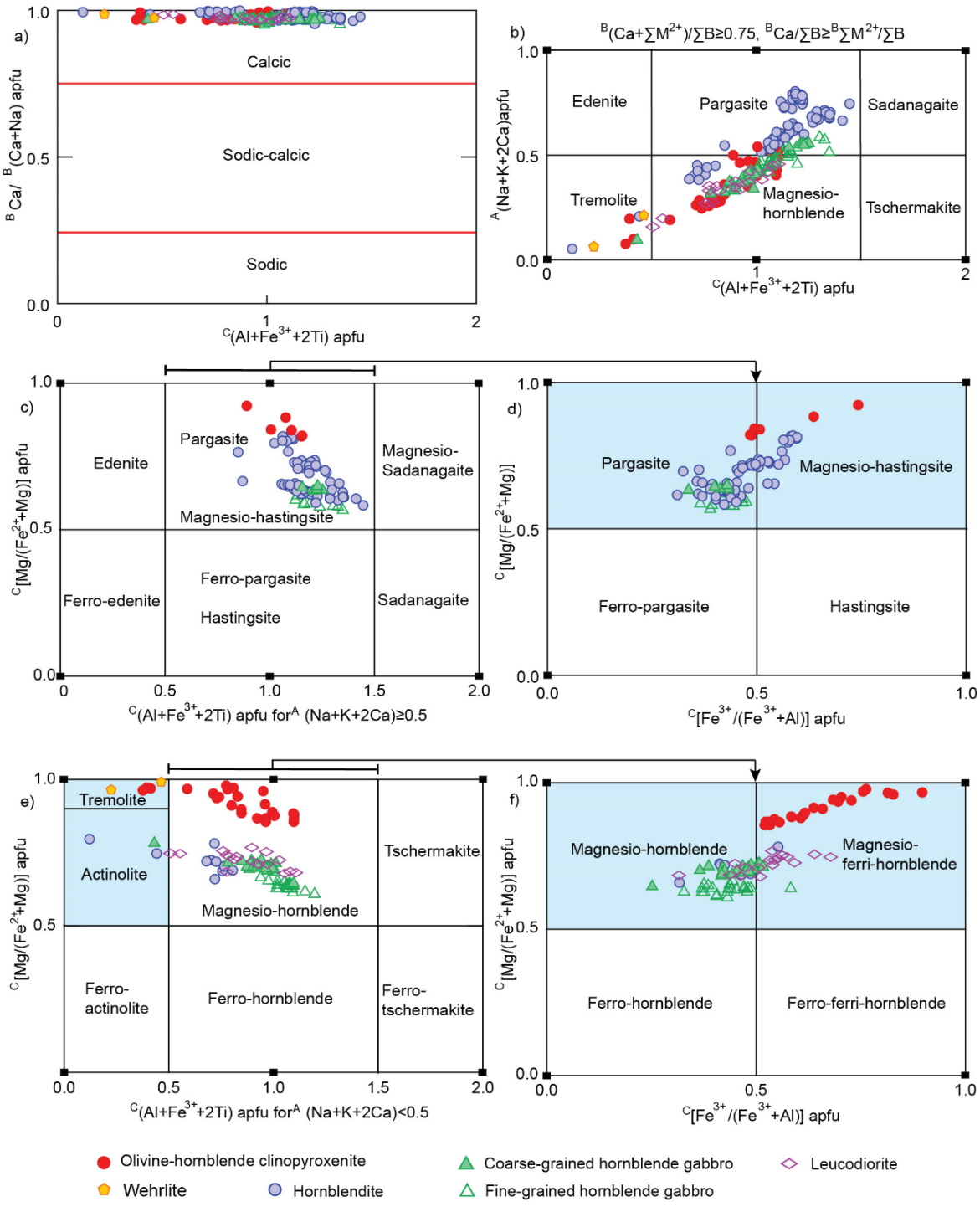

Figure 7.5. a) – f) Composition of calcic amphiboles from TUMC according to the classification scheme of Hawthorne et al. (2012).

Table 7.4. Representative electron probe analyses of amphiboles from the Tampanchi ultramafic-mafic Complex. Prg: Pargasite, Mhs: Magnesio-hastingsite; Mhb: Magnesio-hornblende, Mfhb: Magnesio-ferri-hornblende.

Sample	AR-31B			AR-14	AR-35		AR-10		
Lithology	Ol-Hbl pyroxenite				Hornblendite		Hornblendite		
Major elements (wt.%)									
SiO_2	42.46	43.87	50.05	46.02	42.43	43.11	41.07	46.55	46.81
TiO_2	1.19	0.80	0.32	0.65	1.34	1.19	1.36	0.33	0.67
Al_2O_3	12.98	12.06	6.74	9.22	11.95	11.18	13.01	8.76	8.26
Cr_2O_3	0.16	0.10	0.01	0.25	0.00	0.01	0.01	0.01	0.01
FeO_t	9.31	9.13	6.57	7.52	15.09	14.94	12.42	13.44	10.37
MnO	0.12	0.12	0.13	0.11	0.15	0.17	0.17	0.17	0.12
MgO	14.86	15.35	19.16	17.82	11.40	11.92	12.72	13.36	15.58
NiO	0.01	0.01	0.02	0.02	0.00	0.00	0.01	0.02	0.01
CaO	12.58	12.58	12.62	12.39	11.73	11.80	12.32	12.58	12.74
BaO	0.03	0.00	0.00		0.03	0.03	0.02	0.02	0.01
Na_2O	1.53	1.68	1.01	1.53	1.72	1.62	1.60	1.01	1.14
K_2O	1.07	0.33	0.09	0.65	0.80	0.75	1.46	0.68	0.71
Cl	0.04	0.03	0.02	0.03	0.03	0.02	0.04	0.00	0.00
Total	96.33	96.05	96.75	96.20	96.66	96.74	96.20	96.92	96.43
Formula based on 23 oxygens									
SiT	6.22	6.39	7.06	6.63	6.35	6.42	6.15	6.85	6.83
AlT	1.78	1.61	0.94	1.37	1.65	1.58	1.85	1.15	1.17
AlC	0.46	0.46	0.18	0.19	0.46	0.39	0.44	0.36	0.25
TiC	0.13	0.09	0.03	0.07	0.15	0.13	0.15	0.04	0.07
CrC	0.02	0.01	0.00	0.03	0.00	0.00	0.00	0.00	0.00
$Fe^{3+}C$	0.43	0.47	0.49	0.56	0.37	0.43	0.39	0.32	0.32
MgC	3.25	3.33	4.03	3.83	2.54	2.65	2.84	2.93	3.39
NiC	0.00	0.00	0.00	0.00	0.00	0.00	0.00	0.00	0.00
$Fe^{2+}C$	0.71	0.64	0.26	0.32	1.48	1.40	1.17	1.34	0.95
MnC	0.00						0.01	0.01	0.01
$Fe^{2+}B$	0.00	0.00	0.03	0.03	0.04	0.03	0.00	0.00	0.00
MnB	0.01	0.01	0.02	0.01	0.02	0.02	0.01	0.01	0.00
BaB	0.00	0.00	0.00		0.00	0.00	0.00	0.00	0.00
CaB	1.97	1.96	1.91	1.91	1.88	1.88	1.98	1.98	1.99
NaB	0.01	0.02	0.05	0.05	0.06	0.06	0.01	0.01	0.00
NaA	0.42	0.45	0.23	0.38	0.44	0.41	0.45	0.28	0.32
KA	0.20	0.06	0.02	0.12	0.15	0.14	0.28	0.13	0.13
Cl	0.01	0.01	0.00	0.01	0.01	0.01	0.01	0.00	0.00
Mg#	0.82	0.84	0.93	0.92	0.63	0.65	0.71	0.69	0.78
Subgroup	Calcic	Calcic	Calcic	Calcic	Calcic	Calcic	Calcic	Calcic	Calcic
Species	Prg	Mhs	Mfhb	Mhs	Prg	Mhs	Prg	Mhb	Mfhb

Table 7.4. (Continued). Representative electron probe analyses of amphiboles from the Tampanchi ultramafic-mafic Complex.

Sample	AR-07			AR-42B				AR-34	
Lithology	Fine Hbl-gabbro			Coarse Hbl-gabbro				Leucodiorite	
Major elements (wt.%)									
SiO_2	42.73	43.36	44.11	41.98	45.73	45.34	45.19	43.71	47.85
TiO_2	1.51	1.33	1.15	1.36	0.88	0.93	1.05	1.32	0.83
Al_2O_3	11.62	11.42	9.97	12.73	9.48	9.87	9.93	11.18	7.56
Cr_2O_3	0.10	0.05	0.01	0.07	0.02	0.03	0.01	0.02	0.01
FeO_t	15.28	15.25	15.67	14.35	13.09	13.32	13.12	13.39	11.97
MnO	0.28	0.25	0.29	0.27	0.28	0.29	0.31	0.38	0.37
MgO	11.10	11.16	11.68	11.37	13.38	13.11	13.32	12.43	14.53
NiO	0.01	0.01	0.00	0.02	0.00	0.01	0.02	0.00	0.00
CaO	11.83	11.95	11.76	11.71	11.97	11.92	11.69	12.01	12.19
BaO	0.03	0.02	0.03	0.03	0.03	0.01	0.03	0.02	0.00
Na_2O	1.54	1.44	1.35	1.50	1.23	1.28	1.33	1.28	0.85
K_2O	0.67	0.61	0.48	0.92	0.55	0.61	0.64	0.73	0.45
Cl	0.04	0.03	0.02	0.03	0.01	0.01	0.02	0.02	0.01
Total	96.74	96.88	96.52	96.34	96.67	96.72	96.64	96.50	96.63
Formula based on 23 oxygens									
SiT	6.39	6.47	6.58	6.28	6.73	6.68	6.65	6.48	6.98
AlT	1.61	1.53	1.42	1.72	1.27	1.32	1.35	1.52	1.02
AlC	0.44	0.47	0.33	0.53	0.37	0.39	0.38	0.44	0.28
TiC	0.17	0.15	0.13	0.15	0.10	0.10	0.12	0.15	0.09
CrC	0.01	0.01	0.00	0.01	0.00	0.00	0.00	0.00	0.00
$Fe^{3+}C$	0.35	0.32	0.47	0.40	0.37	0.37	0.40	0.37	0.32
MgC	2.48	2.48	2.60	2.54	2.93	2.88	2.92	2.75	3.16
NiC	0.00	0.00	0.00	0.00	0.00	0.00	0.00	0.00	0.00
$Fe^{2+}C$	1.55	1.57	1.47	1.38	1.22	1.26	1.18	1.29	1.14
MnC								0.01	0.00
$Fe^{2+}B$	0.01	0.01	0.02	0.02	0.02	0.02	0.03	0.00	0.00
MnB	0.04	0.03	0.04	0.03	0.04	0.04	0.04	0.04	0.04
BaB	0.00	0.00	0.00	0.00	0.00	0.00	0.00	0.00	0.00
CaB	1.90	1.91	1.88	1.88	1.89	1.88	1.84	1.91	1.91
NaB	0.05	0.05	0.06	0.06	0.06	0.06	0.08	0.05	0.05
NaA	0.39	0.37	0.33	0.37	0.29	0.30	0.30	0.32	0.19
KA	0.13	0.12	0.09	0.18	0.10	0.12	0.12	0.14	0.08
Cl	0.01	0.01	0.00	0.01	0.00	0.00	0.01	0.00	0.00
Mg#	0.61	0.61	0.64	0.64	0.70	0.69	0.71	0.68	0.74
Subgroup	Calcic	Calcic	Calcic	Calcic	Calcic	Calcic	Calcic	Calcic	Calcic
Species	Prg	Mhb	Mfhb	Prg	Mhb	Mhb	Mfhb	Mhb	Mfhb

Table 7.5. Representative electron probe analyses of feldspar from the Tampanchi ultramafi

Sample	AR-35	AR-07			AR-42B		AR-34		
Lithology	Hornblendite	Fine Hbl-gabbro			Coarse Hbl-gabbro		Leucodiorite		
Major elements (wt.%)									
SiO_2	64.61	45.12	45.62	48.52	46.51	56.59	53.85	54.96	57.70
TiO_2	0.00	0.00	0.00	0.00	0.00	0.00	0.00	0.00	0.00
Al_2O_3	21.76	34.19	33.78	31.75	33.19	26.75	28.19	27.48	26.03
FeO_t	0.16	0.22	0.20	0.17	0.05	0.10	0.09	0.05	0.08
MnO	0.00	0.00	0.00	0.00	0.01	0.00	0.01	0.02	0.00
MgO	0.00	0.01	0.01	0.01	0.01	0.00	0.00	0.00	0.01
CaO	2.99	18.07	17.53	15.26	16.68	8.80	10.62	9.67	7.88
BaO	0.01	0.00	0.00	0.00	0.01	0.02	0.01	0.03	0.05
Na_2O	10.25	1.31	1.61	2.92	2.04	6.83	5.55	6.08	7.14
K_2O	0.12	0.02	0.03	0.04	0.02	0.05	0.16	0.06	0.16
Total	99.88	98.95	98.78	98.67	98.52	99.14	98.48	98.34	99.04
Formula based on 8 oxygens									
Si	2.84	2.10	2.12	2.24	2.16	2.55	2.46	2.51	2.60
Ti	0.00	0.00	0.00	0.00	0.00	0.00	0.00	0.00	0.00
Al	1.13	1.87	1.85	1.73	1.82	1.42	1.52	1.48	1.38
Fe	0.01	0.01	0.01	0.01	0.00	0.00	0.00	0.00	0.00
Mn	0.00	0.00	0.00	0.00	0.00	0.00	0.00	0.00	0.00
Mg	0.00	0.00	0.00	0.00	0.00	0.00	0.00	0.00	0.00
Ca	0.14	0.90	0.87	0.76	0.83	0.42	0.52	0.47	0.38
Ba	0.00	0.00	0.00	0.00	0.00	0.00	0.00	0.00	0.00
Na	0.87	0.12	0.15	0.26	0.18	0.60	0.49	0.54	0.62
K	0.01	0.00	0.00	0.00	0.00	0.00	0.01	0.00	0.01
Or%	0.64	0.13	0.16	0.24	0.13	0.26	0.91	0.35	0.88
Ab%	85.57	11.55	14.26	25.62	18.07	58.29	48.16	53.03	61.57
An%	13.79	88.32	85.58	74.13	81.80	41.45	50.94	46.62	37.54

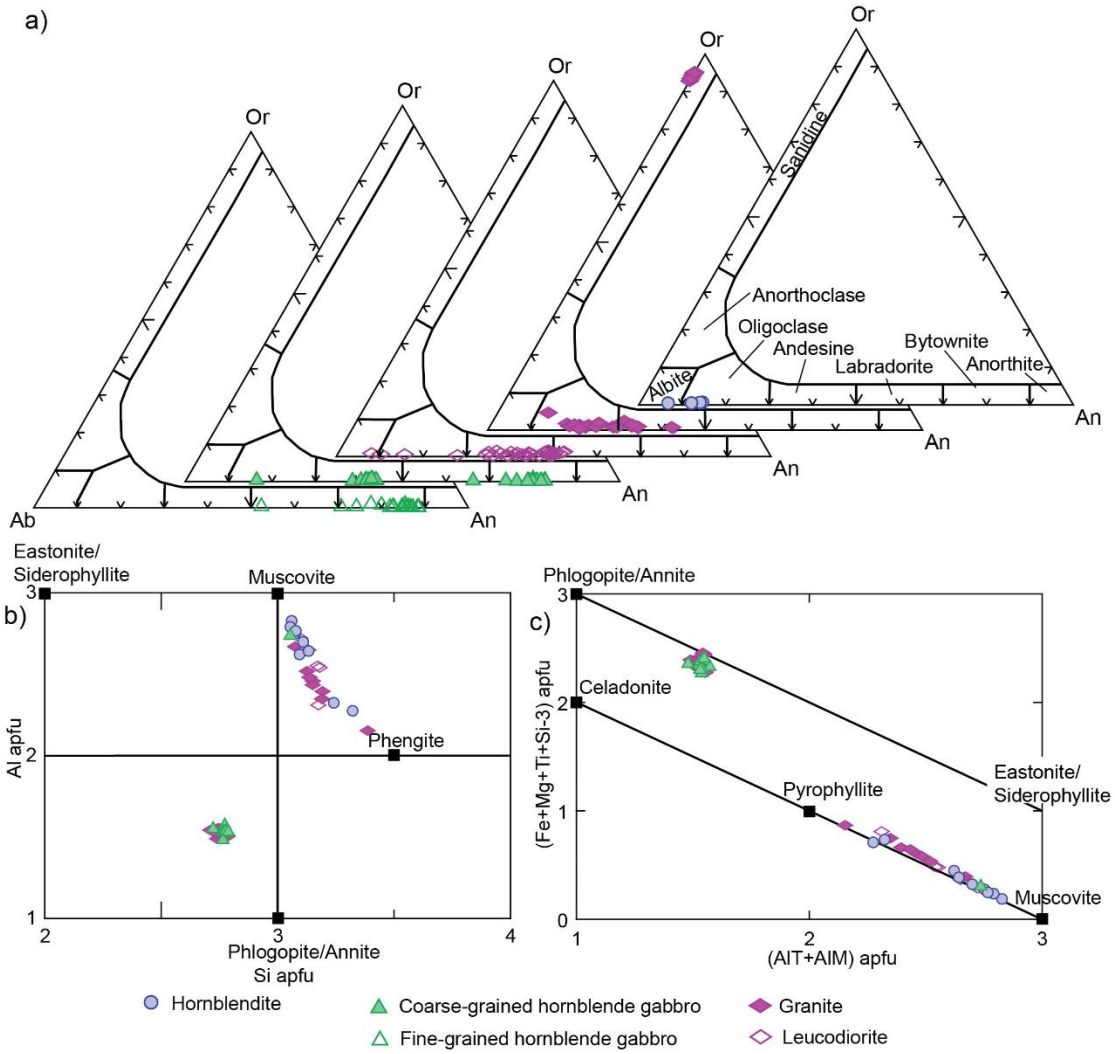

Figure 7.6. a) An-Ab-Or ternary diagram (Smith and Brown, 1988) showing the composition of plagioclase and alkali feldspar of studied samples. b) and c) Compositional variations of micas in terms of Al (apfu) vs Si (apfu) and Fe+Mg+Ti+Si-3 (apfu) vs AlT+AlM (apfu); also shown are relevant end-members.

7.4.6 Biotite

The composition of primary biotite of coarse-grained hornblende gabbro and granite indicates variation in the phlogopite/annite to siderophillite/eastonite series, with a slightly deviation towards dioctahedral end-members (i.e. Figure 7.6b-c; Table 7.6). Primary and secondary biotite replacing amphibole locally present in some samples are similar in composition, indicating a late growth of primary crystals. The content in Si ranges from 2.72 to 2.79 apfu, Mg from 1.29 to 1.73 apfu, Al_{tot} from 1.48 to 1.57 apfu, Fe from 0.80 to 1.16 apfu, K from 0.76 to 0.98 apfu and Mg# from 0.53 to 0.67. The Na and Cr contents are negligible. Biotite in coarse-grained hornblende gabbro has higher Mg (1.54-1.73 apfu) than in granite (1.29-1.46 apfu), while the reverse holds for MnO (0.12–0.15 vs. 0.88–1.07 wt.%).

Table 7.6. Representative electron probe analyses of micas from the Tampanchi ultramafic-mafic Complex. Bt: biotite; Ms: Muscovite.

Sample	AR-35		AR-42B		Ar-15				AR-34	
Lithology	Hornblendite		Coarse Hbl-gabbro		Granite				Leucodiorite	
Major elements (wt.%)										
SiO_2	45.47	47.14	36.46	36.68	35.04	35.61	44.85	44.26	45.29	46.62
TiO_2	0.02	0.10	1.72	2.66	1.94	1.93	0.66	0.04	0.00	0.01
Al_2O_3	33.48	28.69	17.13	16.67	16.17	16.74	29.69	32.61	33.78	31.82
Cr_2O_3	0.00	0.01	0.03	0.01	0.02	0.02	0.02	0.01	0.00	0.01
FeO_t	2.25	4.14	13.32	13.75	16.89	16.58	4.22	3.75	1.20	1.58
MnO	0.01	0.02	0.14	0.12	0.98	1.01	0.10	0.08	0.01	0.02
MgO	0.82	2.45	14.75	13.98	12.29	12.00	1.66	0.97	1.19	2.12
CaO	0.02	0.18	0.08	0.01	0.04	0.02	0.00	0.01	0.00	0.01
BaO	0.68	0.86	0.87	0.95	0.07	0.12	0.40	0.48	0.67	0.54
Na_2O	0.33	0.70	0.14	0.23	0.10	0.04	0.27	0.46	0.30	0.27
K_2O	10.85	10.22	8.41	9.45	8.83	9.43	10.71	10.65	11.28	11.24
Cl	0.00	0.00	0.03	0.02	0.03	0.02	0.02	0.00	0.00	0.00
Total	93.92	94.49	93.07	94.54	92.41	93.52	92.60	93.34	93.73	94.24
Formula based on 11 oxygens										
SiT	3.11	3.24	2.77	2.76	2.74	2.75	3.15	3.08	3.10	3.17
AlT	0.89	0.76	1.23	1.24	1.26	1.25	0.85	0.92	0.90	0.83
AlM	1.81	1.57	0.30	0.25	0.23	0.27	1.61	1.75	1.82	1.72
TiM	0.00	0.01	0.10	0.15	0.11	0.11	0.03	0.00	0.00	0.00
CrM	0.00	0.00	0.00	0.00	0.00	0.00	0.00	0.00	0.00	0.00
$Fe^{2+}M$	0.13	0.24	0.84	0.87	1.10	1.07	0.25	0.22	0.07	0.09
MnM	0.00	0.00	0.01	0.01	0.07	0.07	0.01	0.00	0.00	0.00
MgM	0.08	0.25	1.67	1.57	1.43	1.38	0.17	0.10	0.12	0.22
CaA	0.00	0.01	0.01	0.00	0.00	0.00	0.00	0.00	0.00	0.00
BaA	0.02	0.02	0.03	0.03	0.00	0.00	0.01	0.01	0.02	0.01
NaA	0.04	0.09	0.02	0.03	0.01	0.01	0.04	0.06	0.04	0.04
KA	0.95	0.90	0.81	0.91	0.88	0.93	0.96	0.94	0.98	0.98
Cl	0.00	0.00	0.00	0.00	0.00	0.00	0.00	0.00	0.00	0.00
Mg#	0.39	0.51	0.66	0.64	0.56	0.56	0.41	0.31	0.64	0.71
Species	Ms	Ms	Bt	Bt	Bt	Bt	Ms	Ms	Ms	Ms

7.4.7 White mica

White mica of muscovite-phengite composition (Figure 7.6b-c; Table 7.6) is common in felsic rocks, though they also appear in hornblendites and hornblende gabbros as a result of replacement of plagioclase. They are characterized by variable contents in Si (3.05-3.39 apfu), Al_{tot} (2.15-2.83 apfu) and K (0.81-0.98 apfu). The contents in Fe (0.07-0.28 apfu), Mg (0.04-0.40 apfu), Ti (<0.05 apfu) and Na (<0.2 apfu) are low. In granite, muscovite has

higher Ti (<0.05 apfu) and Fe (0.02-0.45 apfu) than in leucodiorite (Ti <0.01 apfu, Fe<0.22 apfu) and hornblendite (Ti <0.01 apfu, Fe<0.24 apfu). Some micas have less than 2.2 wt.% BaO. In general, they show a marked Tschermak Si(Mg,Fe)-$^{VI}Al_{-1}{}^{IV}Al_{-1}$ exchange along the dioctahedral mica series between muscovite and celadonite end-members that indicates its subsolidus origin (Figure 7.6c).

7.4.8 Fe-Ti oxides

The Fe-Ti oxides are magnetite and, locally, ilmenite (Figure 7.7a; Table 7.7). Magnetite in wehrlite has <10.99 wt.% Cr_2O_3, <0.99 wt.% TiO_2, <0.17 wt.% Al_2O_3 and <1.14 wt% MgO, while in the other lithologies is almost pure, with very low Cr_2O_3 (<0.77 wt.%), TiO_2 (<0.43 wt.%), Al_2O_3 (<0.89 wt.%) and MgO (<1.13%) contents. Ilmenite is almost pure.

Table 7.7. Representative electron probe analyses of Fe-Ti oxides from the Tampanchi ultramafic-mafic Complex.

Sample	AR-65		AR-14		AR-31B		AR-35	AR-10	
Lithology	Wehrlite		Ol-Hbl pyroxenite		Ol-Hbl pyroxenite		Hornblendite	Hornblendite	
Major elements (wt.%)									
SiO_2	0.03	0.05	0.07	0.02	0.04	0.04	0.04	0.03	0.03
TiO_2	0.52	0.99	0.12	0.02	0.21	0.11	0.04	0.20	0.09
Al_2O_3	0.04	0.17	0.00	0.02	0.05	0.00	0.08	0.02	0.00
Cr_2O_3	4.70	10.66	0.10	0.77	0.13	0.10	0.08	0.31	0.23
FeO_t	87.44	80.46	92.50	93.49	92.86	93.05	92.95	92.16	92.69
MnO	0.18	0.44	0.15	0.08	0.13	0.00	0.00	0.10	0.02
MgO	0.87	1.03	1.06	0.01	0.32	0.12	0.02	0.02	0.01
NiO	0.15	0.19	0.05	0.00	0.03	0.04	0.00	0.02	0.00
CaO	0.00	0.14	0.15	0.01	0.02	0.07	0.01	0.24	0.11
K_2O	0.02	0.02	0.00	0.00	0.01	0.02	0.02	0.01	0.02
Total	93.95	94.14	94.19	94.43	93.80	93.57	93.23	93.11	93.19
Formula based on 4 oxygens									
Si	0.00	0.00	0.00	0.00	0.00	0.00	0.00	0.00	0.00
Ti	0.01	0.03	0.00	0.00	0.01	0.00	0.00	0.01	0.00
Al	0.00	0.01	0.00	0.00	0.00	0.00	0.00	0.00	0.00
Cr	0.14	0.32	0.00	0.02	0.00	0.00	0.00	0.01	0.01
Fe^{3+}	1.83	1.61	1.99	1.97	1.98	1.99	1.99	1.98	1.99
Fe^{2+}	0.95	0.94	0.93	1.00	0.98	0.99	1.00	0.99	1.00
Mn	0.01	0.01	0.00	0.00	0.00	0.00	0.00	0.00	0.00
Mg	0.05	0.06	0.06	0.00	0.02	0.01	0.00	0.00	0.00
Ni	0.00	0.01	0.00	0.00	0.00	0.00	0.00	0.00	0.00
Ca	0.00	0.01	0.01	0.00	0.00	0.00	0.00	0.01	0.00
K	0.00	0.00	0.00	0.00	0.00	0.00	0.00	0.00	0.00

7.4.9 Titanite

Accessory titanite from hornblendite, hornblende gabbros and leucocratic rocks is homogeneous and almost pure in composition with very low Al (0.04-0.07 apfu) and Fe (0.02-0.04 apfu) contents (Table 7.8).

Table 7.8. Representative electron probe analyses of titanite from the Tampanchi ultramafic-mafic Complex.

Sample	AR-07		AR-35	AR-10		AR-42B
Lithology	Hbl-gabbro		Hornblendite			Coarse Hbl-gabbro
Major elements (wt.%)						
SiO_2	29.79	29.74	30.36	30.22	30.11	30.14
TiO_2	37.74	38.08	37.35	37.95	38.16	36.63
Al_2O_3	1.47	0.99	1.48	1.41	1.22	1.69
$Cr2O_3$	0.00	0.00	0.01	0.00	0.00	0.23
FeO_t	0.72	0.88	1.23	0.65	0.72	1.43
MnO	0.08	0.09	0.02	0.04	0.01	0.08
MgO	0.05	0.05	0.26	0.04	0.04	0.81
CaO	27.95	27.94	28.32	28.65	28.67	26.65
BaO	0.43	0.42	0.44	0.43	0.46	0.40
Na_2O	0.01	0.02	0.01	0.00	0.00	0.03
K_2O	0.02	0.02	0.03	0.01	0.01	0.06
Total	98.25	98.22	99.51	99.41	99.42	98.16
Formula based on 5 oxygens						
Si	0.98	0.98	0.99	0.99	0.98	0.99
Ti	0.94	0.95	0.91	0.93	0.94	0.91
Al	0.06	0.04	0.06	0.05	0.05	0.07
Cr	0.00	0.00	0.00	0.00	0.00	0.01
Fe	0.02	0.02	0.03	0.02	0.02	0.04
Mn	0.00	0.00	0.00	0.00	0.00	0.00
Mg	0.00	0.00	0.01	0.00	0.00	0.04
Ca	0.99	0.99	0.99	1.00	1.00	0.94
Ba	0.01	0.01	0.01	0.01	0.01	0.01
Na	0.00	0.00	0.00	0.00	0.00	0.00
K	0.00	0.00	0.00	0.00	0.00	0.00

7.4.10 Secondary minerals

7.4.10.1 Epidote.

Epidote has been characterized in hornblendites, where it its homogeneous in composition and with high Fe^{3+}(M3) content (0.62–0.85 apfu) as opposed to Al(M3) (0.12–0.33 apfu) and Mn (up to 0.02 apfu), indicating near-epidote composition, while in leucodiorite Al(M3) it is of intermediate composition (Figure 7.7b; Table 7.9).

Table 7.9. Representative electron probe analyses of epidote from the Tampanchi ultramafic-mafic Complex.

Sample	AR-35			AR-10			AR-34
Lithology	Hornblendite			Hornblendite			Leucodiorite
Major elements (wt.%)							
SiO_2	37.39	37.35	37.28	37.07	37.34	37.66	37.54
TiO_2	0.04	0.08	0.16	0.14	0.10	0.17	0.00
Al_2O_3	23.59	23.44	22.92	22.35	24.14	24.79	27.41
Cr_2O_3	0.03	0.03	0.00	0.02	0.01	0.00	0.00
FeO_t	11.34	11.47	11.97	12.63	10.63	9.86	6.80
MnO	0.05	0.08	0.07	0.15	0.09	0.16	0.17
MgO	0.04	0.05	0.05	0.04	0.04	0.05	0.03
CaO	23.41	23.30	23.20	23.04	23.45	23.23	23.32
Na_2O	0.00	0.00	0.01	0.00	0.01	0.00	0.00
K_2O	0.02	0.01	0.01	0.02	0.01	0.02	0.06
Cl	0.00	0.00	0.01	0.00	0.00	0.00	0.01
Total	95.91	95.83	95.69	95.47	95.84	95.95	95.34
Formula based on 12.5 oxygens							
SiT	2.99	2.99	3.00	3.00	2.99	3.00	2.98
AlT	0.01	0.01	0.00	0.00	0.01		0.02
AlM1	1.00	1.00	1.00	1.00	1.00	1.00	1.00
AlM2	1.00	1.00	1.00	1.00	1.00	1.00	1.00
AlM3	0.22	0.21	0.17	0.12	0.26	0.33	0.54
Fe^{3+}M3	0.76	0.77	0.80	0.85	0.71	0.66	0.45
MnM3	0.00	0.01	0.00	0.01	0.01	0.01	0.01
CrM3	0.00	0.00	0.00	0.00	0.00	0.00	0.00
MgM3	0.01	0.01	0.01	0.01	0.00	0.01	0.00
TiM3	0.00	0.00	0.01	0.01	0.01	0.01	0.00
CaA1	1.00	1.00	1.00	1.00	1.00	1.00	1.00
CaA2	1.01	1.00	1.00	0.99	1.01	0.98	0.98
NaA2	0.00	0.00	0.00	0.00	0.00	0.00	0.00
KA2	0.00	0.00	0.00	0.00	0.00	0.00	0.01
Xczo	0.23	0.22	0.18	0.13	0.28	0.33	0.55
Xep	0.77	0.78	0.82	0.86	0.72	0.66	0.44
Xpmt	0.00	0.01	0.00	0.01	0.01	0.01	0.01

7.4.10.2 Chlorite

Chlorite has higher Mg (5.60-6.71 apfu) than Fe (2.48-3.84 apfu) and Al^{VI} (2.30-2.65 apfu) contents. The Si content ranges from 5.46 to 6.00 apfu, Al^{IV} ranges from 2.00 to 2.54 apfu, while the calculated total vacancy is lower than 0.26 (Figure 7.7c-d; Table 7.10). These data indicate that chlorites are trioctahedral, belonging to the clinochlore-chamosite series (Wiewióra and Weiss, 1990). The Mg# is high (0.59-0.73), so the studied chlorites classify as clinochlore (Figure 7.7d).

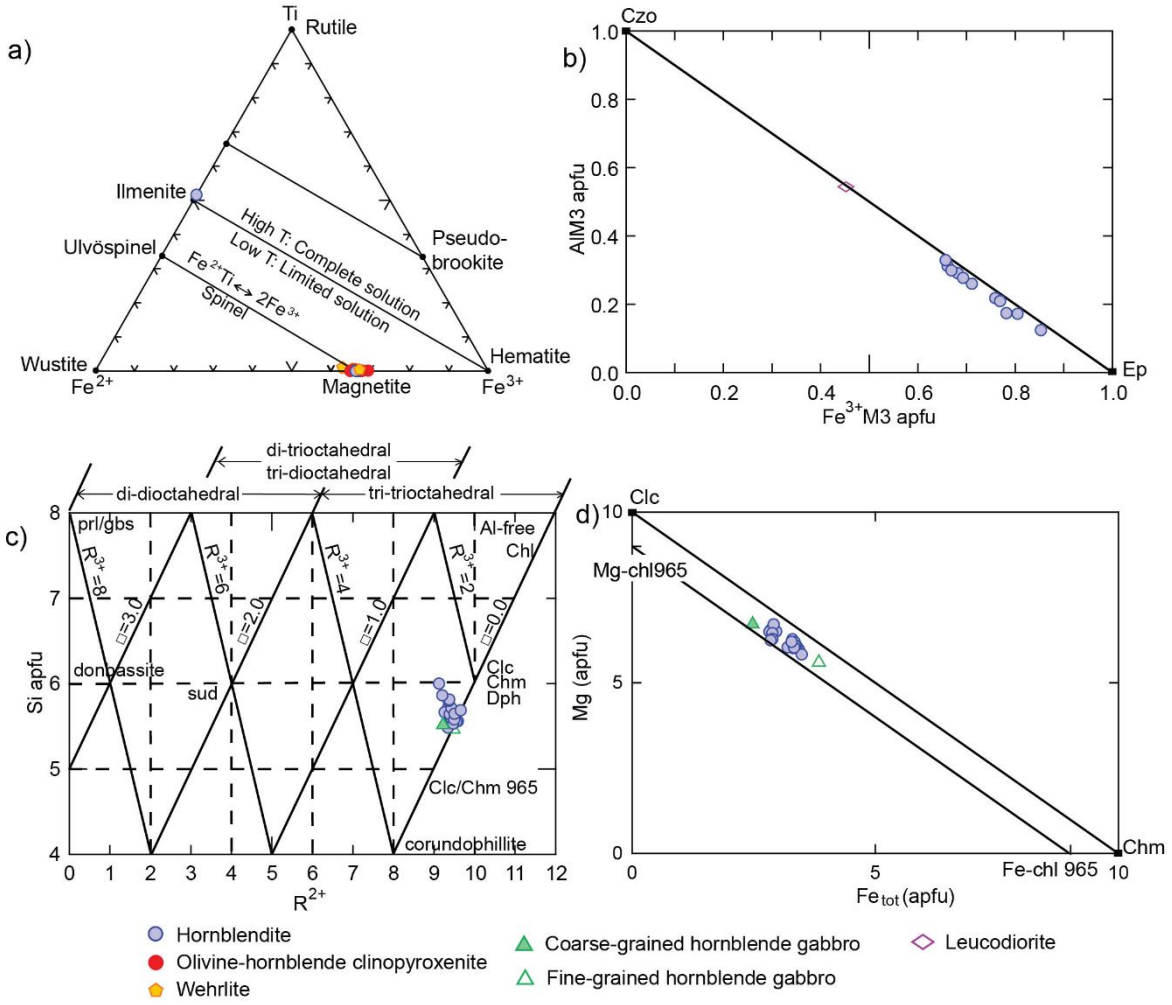

Figure 7.7. a) Fe-Ti oxides represented in the Fe^{3+}-Ti-Fe^{2+} ternary plot. b) Epidote group minerals classified according to M^{3+} cation substitution (Armbruster et al., 2006). c) Composition of chlorite in the multicationic diagram R^{2+} vs Si (end-members are after Wiewióra and Weiss, 1990; R^{2+} and R^{3+} include divalent and trivalent cations, respectively). d) Composition of chlorite in terms of Mg (apfu) vs. Fe_{tot} (apfu).

Table 7.10. Representative electron probe analyses of chlorite from the Tampanchi ultramafic-mafic Complex.

Sample	AR-07	AR-35		AR-10		AR-42B
Lithology	Fine Hbl-gabbro	Hornblendite		Hornblendite		Coarse Hbl-gabbro
Major elements (wt.%)						
SiO_2	26.10	27.48	26.47	28.31	28.79	27.33
TiO_2	0.09	0.02	0.05	0.03	0.04	0.06
Al_2O_3	20.38	20.25	20.87	19.85	19.50	21.59
Cr_2O_3	0.01	0.01	0.01	0.00	0.00	0.00
FeO_t	21.94	19.33	20.13	16.88	16.94	14.68
MnO	0.27	0.16	0.16	0.20	0.22	0.20
MgO	17.93	19.71	18.87	21.77	20.69	22.31
CaO	0.04	0.04	0.03	0.12	0.10	0.04
Na_2O	0.00	0.05	0.05	0.01	0.02	0.02
K_2O	0.01	0.03	0.05	0.09	0.09	0.02
Cl	0.00	0.01	0.02	0.00	0.00	0.00
Total	86.77	87.09	86.71	87.30	86.38	86.28
Formula based on 28 oxygens						
Si	5.46	5.63	5.48	5.71	5.86	5.52
Ti	0.01	0.00	0.01	0.00	0.01	0.01
Al	5.03	4.89	5.10	4.72	4.68	5.14
Cr	0.00	0.00	0.00	0.00	0.00	0.00
Fe^{2+}	3.84	3.31	3.49	2.85	2.89	2.48
Mn	0.05	0.03	0.03	0.03	0.04	0.03
Mg	5.60	6.02	5.83	6.55	6.28	6.71
Ca	0.01	0.01	0.01	0.03	0.02	0.01
Ba	0.00	0.00	0.00	0.00	0.00	0.00
K	0.00	0.01	0.01	0.02	0.02	0.01
Cl	0.00	0.00	0.01	0.00	0.00	0.00
Mg#	0.59	0.65	0.63	0.70	0.69	0.73

7.4.10.3 Serpentine

Serpentine is relatively constant in composition, with Si ranging from 1.93 to 2.08 apfu, Mg from 2.71 to 2.87 apfu and Fe_{tot} from 0.04-0.42 apfu contents (Table 7.11).

Table 7.11. Representative electron probe analyses of serpentine from the Tampanchi ultramafic-mafic Complex.

Sample	AR-65			AR-14	AR-31B	
Lithology	Wehrlite			Ol-Hbl pyroxenite		
Major elements (wt.%)						
SiO_2	40.77	39.85	41.40	40.74	44.83	45.19
TiO_2	0.00	0.00	0.01	0.01	0.00	0.01
Al_2O_3	0.00	0.00	0.24	0.00	0.00	0.11
Cr_2O_3	0.00	0.00	0.00	0.00	0.00	0.00
FeO_t	5.41	8.25	3.53	5.03	1.10	2.10
MnO	0.07	0.07	0.11	0.04	0.07	0.08
MgO	39.35	36.96	39.98	39.13	40.63	39.80
NiO	0.11	0.10	0.04	0.07	0.02	0.04
CaO	0.03	0.10	0.02	0.08	0.01	0.05
Na_2O	0.00	0.00	0.00	0.04	0.02	0.02
K_2O	0.02	0.01	0.01	0.05	0.02	0.02
Cl	0.06	0.06	0.08	0.03	0.01	0.00
Total	85.82	85.41	85.43	85.30	86.79	87.42
Formula based on 7 oxygens						
Si	1.97	1.96	1.99	1.98	2.07	2.08
Ti	0.00	0.00	0.00	0.00	0.00	0.00
Al	0.00	0.00	0.01	0.00	0.00	0.01
Cr	0.00	0.00	0.00	0.00	0.00	0.00
Fe^{2+}	0.22	0.34	0.14	0.20	0.04	0.08
Mn	0.00	0.00	0.00	0.00	0.00	0.00
Mg	2.83	2.72	2.86	2.83	2.80	2.73
Ni	0.00	0.00	0.00	0.00	0.00	0.00
Ca	0.00	0.01	0.00	0.00	0.00	0.00
Na	0.00	0.00	0.00	0.00	0.00	0.00
K	0.00	0.00	0.00	0.00	0.00	0.00
Cl	0.00	0.01	0.01	0.00	0.00	0.00

7.4.10.1 Iddingsite

Iddingsite, a common alteration product of olivine, is variable in composition, with SiO_2 ranging from 39.2 to 47.8 wt.%, MgO from 10.4 to 22.3 wt.%, FeO from 18.6 to 26.9 wt.% and CaO from 0.8 to 1.5 wt.%, and with FeO higher than in olivine pointing to the presence of Fe-oxhydroxides in the cryptocrystalline mixture (Table 7.12).

Table 7.12. Representative electron probe analyses of iddingsite from the Tampanchi ultramafic-mafic Complex.

Sample	AR-14				AR-31B		
Lithology	Ol-Hbl pyroxenite				Ol-Hbl pyroxenite		
Major elements (wt.%)							
SiO_2	47.84	45.34	42.98	39.53	42.26	42.63	42.41
TiO_2	0.01	0.00	0.00	0.00	0.00	0.00	0.00
Al_2O_3	0.01	0.19	0.25	0.00	0.00	0.00	0.00
Cr_2O_3	0.02	0.02	0.01	0.00	0.01	0.01	0.01
FeO_t	24.36	24.75	21.48	23.71	25.22	26.92	26.80
MnO	0.09	0.07	0.05	0.08	0.23	0.10	0.11
MgO	11.70	12.86	20.33	22.29	14.34	12.15	11.22
NiO	0.16	0.15	0.04	0.13	0.10	0.11	0.10
CaO	1.48	1.39	0.85	1.54	0.98	1.11	1.11
Na_2O	0.24	0.20	0.09	0.12	0.16	0.09	0.17
K_2O	0.53	0.47	0.28	0.29	0.69	0.64	0.82
Cl	0.05	0.02	0.02	0.02	0.30	0.54	0.33
Total	86.48	85.46	86.38	87.70	84.28	84.29	83.09

7.5 Whole rock composition and U-Th-Pb dating

7.5.1 Major and trace elements

The analyzed samples (Table 7.13) show variation from ultrabasic to acid composition, being dominant the basic compositions in the TAS diagram (Figure 7.8a). They are metaluminous with aluminum saturation index (ASI, $Al_2O_3/(CaO+K_2O+Na_2O)$, molar units) < 1.1 (Figure 7.8b).

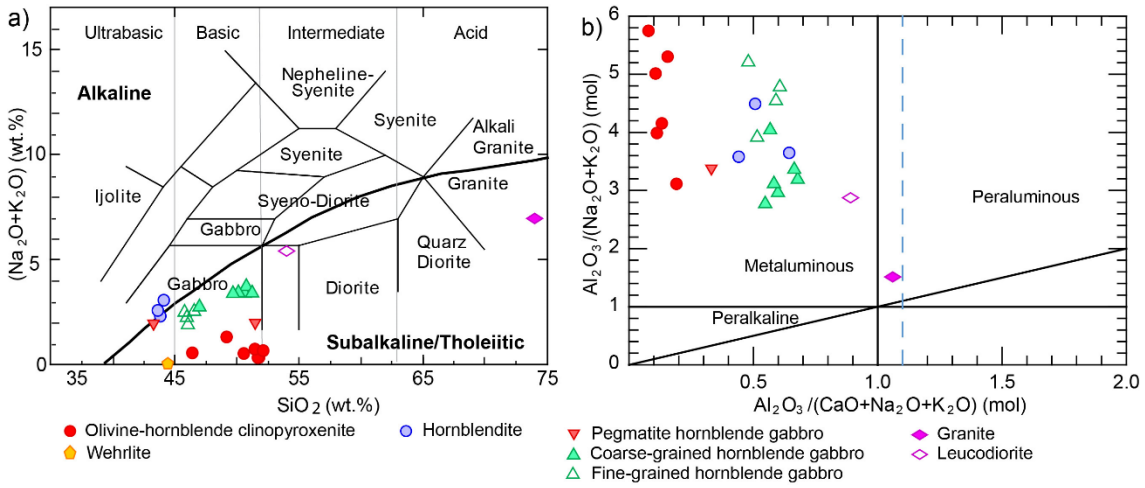

Figure 7.8. a) SiO_2 (wt.%) and Na_2O+K_2O (wt.%) (TAS) diagram showing the classification of plutonic rocks (after Cox et al., 1979). The TUMC are mostly basic in composition in this diagram, but note that clinopyroxenite cannot be properly classified as an ultramafic rock in this diagram. Note that leucodiorite plots in the intermediate field between gabbro and diorite. b) molar ratio of $Al_2O_3/(Na_2O+K_2O)$ vs $Al_2O_3/(CaO+K_2O+Na_2O)$ diagram (Shand, 1943); wehrlite with high $Al_2O_3/(Na_2O+K_2O)$ molar ratio plots outside the diagram.

Table 7.13. Major (wt.%) and trace element (ppm) chemistry of the lithologies from the Tampanchi ultramafic-mafic complex.

Sample	AR-065	AR-014	AR-019	AR-023	AR-027	AR-031B	AR-036
Litology	Wehrlite	Ol-Hbl pyroxenite	Ol-Hbl pyroxenite	Ol-Hbl pyroxenite	Ol-Hbl pyroxenite	Ol-Hbl pyroxenite	Ol-Hbl pyroxenite
Longitude	762137	761415	762179	762575	761559	761480	763604
Latitude	9707931	9707418	9709316	9707325	9707392	9707855	9710001
SiO_2	42.31	50.94	47.57	50.60	49.12	44.72	50.40
TiO_2	0.09	0.23	0.68	0.27	0.33	0.40	0.40
Al_2O_3	0.82	2.97	5.81	3.01	3.81	4.13	4.34
FeO*	11.22	5.51	10.17	6.15	8.13	11.53	6.35
MnO	0.20	0.13	0.19	0.13	0.14	0.21	0.14
MgO	34.85	17.74	15.23	17.20	15.92	20.56	14.89
CaO	4.99	20.46	15.71	20.18	19.15	14.21	20.66
Na_2O	<LLD	0.28	0.88	0.26	0.38	0.37	0.56
K_2O	0.01	0.06	0.39	0.06	0.13	0.16	0.16
P_2O_5	0.02	0.02	0.08	0.02	0.02	0.02	0.04
LOI	4.50	0.71	1.55	0.85	1.35	2.11	0.70
Total	99.01	99.05	98.26	98.73	98.48	98.42	98.64
Li	0.93	3.92	2.69	2.51	2.93	1.98	2.53
Rb	1.36	2.85	3.13	1.13	3.19	2.47	3.82
Cs	0.21	0.22	0.05	0.15	0.09	0.57	0.05
Be	0.10	0.12	0.22	0.10	0.08	0.08	0.17
Sr	14.64	82	113	60	72	60	100
Ba	33	27	70	27	45	47	38
Sc	22	125	95	94	133	98	126
V	39	242	387	186	224	287	306
Cr	3423	1542	560	1106	609	522	330
Co	130	83	103	64	61	123	55
Ni	718	190	284	156	287	206	107
Cu	5.66	22	654	8.15	3201	29	774
Zn	56	40	73	32	38	61	35
Ga	1.06	5.21	7.42	3.98	4.53	5.13	5.74
Y	0.86	8.69	15.33	6.67	6.58	8.16	9.36
Nb	0.23	0.32	1.16	0.27	0.33	0.33	0.41
Ta	0.24	0.37	0.26	0.49	0.21	0.28	0.24
Zr	0.86	9.70	18.10	10.10	10.20	10.50	12.90
Mo	2.24	2.25	1.25	2.38	1.68	3.22	2.62
Sn	0.19	0.73	1.79	0.70	0.90	0.90	0.87
Tl	0.05	0.03	0.13	0.03	0.04	0.07	0.03
Pb	0.51	1.23	1.49	1.14	3.20	1.27	1.90
U	0.25	0.06	0.07	0.07	0.18	0.04	0.10
Th	0.22	0.52	0.41	0.36	0.47	0.32	0.37
La	0.80	2.06	4.59	1.79	2.52	1.45	2.36
Ce	1.05	5.67	12.61	5.01	5.04	4.49	7.02
Pr	0.20	0.98	1.91	0.89	0.97	0.79	1.23
Nd	0.70	5.33	9.66	5.30	5.20	4.59	6.58
Sm	0.23	1.53	2.63	1.48	1.45	1.46	1.90
Eu	0.07	0.53	0.77	0.49	0.45	0.47	0.61
Gd	0.19	1.68	2.71	1.56	1.46	1.55	1.97
Tb	0.03	0.26	0.42	0.23	0.21	0.26	0.31
Dy	0.16	1.51	2.59	1.23	1.15	1.50	1.76
Ho	0.03	0.33	0.59	0.26	0.26	0.31	0.38
Er	0.08	0.93	1.52	0.69	0.70	0.89	0.92
Tm	0.01	0.14	0.25	0.11	0.11	0.13	0.15
Yb	0.08	0.89	1.49	0.68	0.69	0.85	0.97
Lu	0.01	0.13	0.22	0.09	0.09	0.11	0.13
Mg#	0.85	0.85	0.73	0.83	0.78	0.76	0.81
ASI	0.09	0.08	0.19	0.08	0.11	0.16	0.11
$(La/Yb)_n$	7.08	1.66	2.21	1.88	2.63	1.23	1.74
$(La/Sm)_n$	2.22	0.87	1.13	0.78	1.12	0.64	0.80
$(Sm/Yb)_n$	3.18	1.92	1.96	2.41	2.35	1.91	2.17
Eu/Eu*	0.98	1.00	0.88	0.99	0.95	0.95	0.96

Table 7.13. (Continued). Major (wt.%) and trace element (ppm) chemistry of the lithologies from the Tampanchi ultramafic-mafic complex.

Sample	AR-042A1	AR-009	AR-010-5	AR-035	AR-007	AR-012	AR-016
Litology	Ol-Hbl pyroxenite	Hornblendite	Hornblendite	Hornblendite	fine-grained hbl gabbro	fine-grained hbl gabbro	fine-grained hbl gabbro
Longitude	763543	762594	762412	762707	762684	762118	761471
Latitude	9708694	9707319	9707458	9708577	9707284	9707389	9707864
SiO_2	50.68	42.39	42.38	42.56	44.59	44.90	44.46
TiO_2	0.22	1.17	1.26	1.31	1.08	0.65	0.83
Al_2O_3	4.04	14.25	12.35	15.45	15.79	16.08	13.75
FeO*	6.62	11.61	11.96	12.40	11.71	9.00	10.75
MnO	0.17	0.20	0.16	0.13	0.21	0.21	0.23
MgO	18.47	10.70	12.88	10.65	8.49	9.74	11.61
CaO	16.27	13.70	13.50	10.86	12.51	13.02	12.74
Na_2O	0.50	1.36	1.33	1.85	1.72	1.62	1.61
K_2O	0.15	0.86	1.17	1.10	0.45	0.81	0.80
P_2O_5	0.09	0.44	0.11	0.13	0.41	0.39	0.29
LOI	1.50	1.35	0.97	1.63	1.15	1.87	1.14
Total	98.71	98.03	98.07	98.07	98.11	98.29	98.21
Li	1.41	4.23	2.94	4.31	2.49	7.05	6.85
Rb	2.29	7.82	11.17	25	6.36	16.28	11.91
Cs	0.06	0.15	0.17	0.39	0.42	0.78	0.21
Be	0.23	0.55	0.30	0.54	0.57	0.99	0.55
Sr	113	454	306	437	329	789	358
Ba	52	200	183	514	193	257	198
Sc	62	60	97	68	52	45	67
V	101	417	556	543	381	252	336
Cr	2373	263	93	46	176	501	501
Co	56	59	63	74	57	50	54
Ni	180	58	73	38	38	81	100
Cu	6.86	41	94	122	81	16.39	38
Zn	44	75	57	63	80	79	86
Ga	5.03	15.77	12.33	14.80	16.93	16.52	15.22
Y	8.04	22	16.40	15.90	27	19.62	21
Nb	1.12	3.81	1.28	3.17	2.28	4.19	3.05
Ta	0.23	0.44	0.24	0.38	0.87	0.44	0.37
Zr	15.60	50	32	41	45	47	49
Mo	1.72	2.05	1.11	1.80	2.79	2.15	1.69
Sn	1.40	1.82	1.53	1.56	1.76	1.37	1.36
Tl	0.04	0.09	0.08	0.24	0.06	0.19	0.08
Pb	0.77	2.56	2.39	3.70	2.26	6.66	2.77
U	0.18	0.26	0.09	0.52	0.42	0.83	0.27
Th	0.55	0.83	0.31	1.60	1.10	0.86	3.88
La	3.14	12.77	5.01	9.81	10.73	13.81	14.55
Ce	10.22	35	16.11	22	28	38	35
Pr	1.80	5.57	2.85	3.10	4.36	5.75	4.83
Nd	8.31	27	15.28	14.80	22	27	21
Sm	2.11	6.25	4.31	3.98	5.60	5.37	4.50
Eu	0.58	1.72	1.28	1.28	1.65	1.58	1.59
Gd	1.59	5.23	3.92	3.73	5.32	4.82	4.19
Tb	0.25	0.72	0.55	0.54	0.77	0.62	0.60
Dy	1.34	4.04	3.20	3.11	4.54	3.46	3.56
Ho	0.27	0.81	0.65	0.64	0.97	0.72	0.77
Er	0.68	2.00	1.59	1.50	2.49	1.83	2.08
Tm	0.12	0.31	0.23	0.23	0.38	0.29	0.33
Yb	0.67	1.83	1.42	1.32	2.26	1.83	2.14
Lu	0.10	0.28	0.20	0.19	0.33	0.28	0.33
Mg#	0.83	0.62	0.66	0.60	0.56	0.66	0.66
ASI	0.13	0.51	0.44	0.64	0.61	0.59	0.52
$(La/Yb)_n$	3.37	5.00	2.53	5.32	3.41	5.41	4.88
$(La/Sm)_n$	0.96	1.32	0.75	1.59	1.24	1.66	2.08
$(Sm/Yb)_n$	3.50	3.79	3.38	3.34	2.75	3.26	2.34
Eu/Eu*	0.97	0.92	0.95	1.01	0.92	0.95	1.12

Table 7.13. (Continued). Major (wt.%) and trace element (ppm) chemistry of the lithologies from the Tampanchi ultramafic-mafic complex.

Sample	AR-031A	AR-006	AR-020	AR-025	AR-033	AR-041	AR-042B
Litology	fine-grained hbl gabbro	Coarse grained hbl gabbro	Coarse-grained hbl gabbro	Coarse-grained hbl gabbro	Coarse-grained hbl gabbro	Coarse-grained hbl gabbro	Coarse-grained hbl gabbro
Longitude	761480	762684	763161	762010	762047	763193	763543
Latitude	9707855	9707284	9709502	9707379	9707476	9708214	9708694
SiO_2	44.45	49.40	49.42	49.80	48.69	45.38	48.39
TiO_2	0.78	0.98	0.67	0.85	0.84	1.04	0.79
Al_2O_3	13.61	16.72	14.95	14.57	15.04	15.21	16.88
FeO*	10.29	8.44	8.29	8.73	8.58	9.37	8.15
MnO	0.21	0.21	0.18	0.16	0.14	0.19	0.17
MgO	10.89	7.57	7.87	8.92	8.79	9.73	8.25
CaO	14.17	10.67	12.04	10.67	11.54	12.66	11.21
Na_2O	1.16	3.00	2.65	2.39	2.21	1.62	2.62
K_2O	0.66	0.28	0.96	0.91	1.10	1.01	0.66
P_2O_5	0.26	0.24	0.31	0.20	0.20	0.35	0.24
LOI	1.73	0.83	1.10	1.24	1.34	1.81	1.17
Total	98.21	98.34	98.44	98.44	98.47	98.37	98.53
Li	6.36	3.27	5.29	8.31	7.84	4.04	4.63
Rb	7.45	5.73	12.49	22	33	30	18.90
Cs	0.22	0.45	0.18	1.00	2.04	0.78	0.69
Be	0.53	0.65	1.07	1.07	0.81	0.86	1.15
Sr	430	405	633	643	702	533	751
Ba	170	206	673	450	1046	391	509
Sc	69	63	49	58	61	77	46
V	385	353	235	318	338	386	296
Cr	421	170	350	292	243	376	247
Co	61	46	44	61	53	54	56
Ni	73	51	44	57	52	57	62
Cu	91	47	23	31	72	6.04	28
Zn	78	70	65	64	63	74	70
Ga	14.57	16.23	14.83	15.15	15.21	17.37	17.56
Y	19.00	21	17.13	17.82	16.46	24	16.84
Nb	1.74	2.35	4.62	5.53	3.90	5.98	5.84
Ta	0.32	0.32	0.48	0.59	0.78	0.64	0.60
Zr	34	53	78	78	58	45	59
Mo	3.49	2.81	2.21	3.20	1.77	2.64	1.46
Sn	1.55	1.52	1.69	1.77	1.35	1.98	1.38
Tl	0.07	0.05	0.07	0.20	0.32	0.15	0.16
Pb	3.10	5.28	12.53	8.32	9.30	4.97	7.47
U	0.44	0.36	1.95	1.86	2.01	1.10	0.97
Th	0.77	0.80	4.52	3.37	2.11	1.98	3.13
La	10.57	9.77	19.78	14.58	10.77	14.77	16.28
Ce	26	26	40	34	26	37	36
Pr	3.73	3.84	5.02	4.73	3.94	5.42	4.88
Nd	17.39	18.49	22	22	18.65	25	19.10
Sm	4.28	4.30	4.49	5.10	4.63	6.16	4.05
Eu	1.23	1.69	1.26	1.46	1.24	1.80	1.17
Gd	3.91	4.06	4.06	4.50	4.05	5.62	3.32
Tb	0.53	0.59	0.54	0.61	0.57	0.78	0.52
Dy	3.31	3.61	3.02	3.36	3.11	4.41	2.85
Ho	0.69	0.77	0.61	0.66	0.61	0.90	0.59
Er	1.90	1.94	1.58	1.63	1.50	2.30	1.51
Tm	0.30	0.31	0.27	0.27	0.25	0.35	0.25
Yb	1.92	1.96	1.60	1.55	1.46	2.06	1.50
Lu	0.30	0.29	0.25	0.22	0.20	0.30	0.23
Mg#	0.65	0.62	0.63	0.65	0.65	0.65	0.64
ASI	0.48	0.68	0.55	0.60	0.58	0.57	0.66
$(La/Yb)_n$	3.95	3.57	8.87	6.75	5.30	5.14	7.81
$(La/Sm)_n$	1.59	1.47	2.84	1.85	1.50	1.55	2.59
$(Sm/Yb)_n$	2.48	2.44	3.12	3.65	3.52	3.32	3.01
Eu/Eu*	0.92	1.24	0.90	0.93	0.87	0.94	0.97

Table 7.13. (Continued). Major (wt.%) and trace element (ppm) chemistry of the lithologies from the Tampanchi ultramafic-mafic complex.

Sample	AR-013	AR-042A2	AR-034	AR-015
Litology	Pegmatite hbl gabbro	Pegmatite hbl gabbro	Leucodiorite	Granite
Longitude	762036	763543	762047	761638
Latitude	9707362	9708694	9707476	9707799
SiO_2	49.97	41.35	53.23	72.70
TiO_2	0.54	0.61	0.18	0.08
Al_2O_3	9.50	22.96	24.39	14.77
FeO*	7.67	6.64	2.11	0.94
MnO	0.14	0.14	0.06	0.05
MgO	12.94	5.59	2.51	0.57
CaO	14.23	15.32	10.39	2.29
Na_2O	1.28	1.40	4.85	4.22
K_2O	0.65	0.46	0.47	2.61
P_2O_5	0.15	1.01	0.37	0.06
LOI	1.31	3.21	0.92	0.97
Total	98.38	98.69	99.48	99.26
Li	7.34	6.59	2.66	11.56
Rb	16.30	16.21	12.76	85
Cs	0.67	0.37	0.41	3.90
Be	0.46	0.65	2.30	2.63
Sr	304	1323	2831	918
Ba	353	261	507	2247
Sc	76	17.38	9.65	4.10
V	240	151	46	10.10
Cr	1011	65	87	39
Co	54	31	51	42
Ni	106	51	19.28	5.32
Cu	43	8.68	8.16	13.79
Zn	46	48	25	22
Ga	9.16	19.81	22	16.58
Y	11.85	22	9.25	6.66
Nb	1.75	4.11	3.47	12.52
Ta	0.29	0.46	0.61	1.35
Zr	40	51	634	87
Mo	1.91	1.38	8.67	5.53
Sn	1.38	1.75	0.75	1.22
Tl	0.16	0.17	0.10	0.88
Pb	5.05	6.62	17.34	49
U	0.77	0.89	2.13	2.14
Th	1.65	7.67	3.53	7.87
La	6.70	14.12	28	20
Ce	16.26	37	48	36
Pr	2.43	5.91	5.21	3.63
Nd	11.79	27	19.79	12.44
Sm	2.99	5.96	3.08	2.16
Eu	0.86	16.07	4.08	0.26
Gd	2.89	4.43	2.76	1.98
Tb	0.40	0.67	0.31	0.22
Dy	2.22	3.68	1.46	1.04
Ho	0.45	0.76	0.31	0.20
Er	1.17	2.00	0.91	0.56
Tm	0.18	0.32	0.16	0.10
Yb	1.08	1.89	0.96	0.67
Lu	0.15	0.28	0.15	0.10
Mg#	0.75	0.60	0.68	0.52
ASI	0.33	0.75	0.89	1.06
$(La/Yb)_n$	4.46	5.36	20.99	21.78
$(La/Sm)_n$	1.45	1.53	5.86	6.07
$(Sm/Yb)_n$	3.08	3.50	3.58	3.59
Eu/Eu*	0.89	9.56	4.27	0.38

Table 7.13. (Continued).

FeO*: Total iron content
Mg#: molar ratio MgO/(MgO+FeO*)
ASI: aluminium saturation index; ASI = molar $Al_2O_3/(CaO + Na_2O + K_2O)$
$(La/Yb)_n$, $(La/Sm)_n$, $(Sm/Yb)_n$, ratios normalized to chondrite (Sun and McDonough, 1989)
$Eu/Eu^* = \frac{Eu(n)}{\sqrt{Sm(n)*Gd(n)}}$ (n) denotes chondrite-normalized values (Sun and McDonough, 1989)
LOI: loss on ignition; LLD: below lower limit of detection; Ol: olivine; Hbl: hornblende
Latitude and longitude in the coordinate system WGS84 UTM zone 17S

Wehrlite has the lowest SiO_2 (42.3 wt.%) and alkali (Na_2O+K_2O = 0.01 wt.%) contents and the highest MgO (34.9 wt.%), with Mg# = 0.85. It also has the highest Cr, Ni, and Co contents, with 3423, 718 and 130 ppm, respectively (Figure 7.9). Olivine-hornblende clinopyroxenite is characterized by variable SiO_2 (44.7–50.9 wt.%) and high MgO (14.9–20.6 wt.%) contents, with the highest CaO (14.2–20.7 wt.%) contents. This group has variably high Cr (330–2373 ppm), Ni (107–287 ppm), Sc (62-133 ppm) and Co (54.8–123.3 ppm) contents and Mg# ranges between 0.73 and 0.85 (Figure 7.9).

Hornblendite has low SiO_2 (42.4–42.6 wt.%) and the highest FeO*(FeO_{tot}, 11.6–12.4 wt.%) and TiO_2 (1.2–1.3 wt.%) contents. This type of rock has lower contents in MgO (10.7–12.9 wt.%), CaO (10.9–13.7 wt.%), Cr (46–263 ppm), Ni (38–73 ppm) and Co (59–74 ppm) than olivine-hornblende clinopyroxenites (Table 7.13; Figure 7.9). Mg# ranges from 0.60 to 0.66 and Sc content is high (60-97 ppm) but slightly lower than in olivine-hornblende clinopyroxenite.

Fine-grained hornblende gabbro has a slightly higher SiO_2 (44.5-45.0 wt.%) content than hornblendite and lower FeO* (9.0–11.7 wt.%), MgO (8.5–11.6 wt.%) and TiO_2 (0.7–1.1 wt.%). The contents in Al_2O_3 and CaO are in the ranges 13.6-16.1 wt.% and 12.5–14.2 wt.%, respectively. It has a high Cr (177–501 ppm) and low Ni (38–100 ppm) and Co (50–61 ppm) contents. Mg# ranges from 0.56 to 0.66. Coarse-grained hornblende gabbro is enriched in SiO_2 (45.4–49.8wt.%) and depleted in MgO (7.6–9.7 wt.%), FeO* (8.2–9.4 wt.%) and CaO (10.7–12.7 wt.%) as compared to fine-grained hornblende gabbro, with slightly lower Cr (170–376 ppm), Ni (44–62 ppm) and Co (44–61 ppm) contents (Figure 7.9). This type of rock has relatively high Na_2O (1.6–3.0 wt.%) content compared to wehrlite, clinopyroxenite and fine-grained hornblende gabbro, as is reflected by more abundant relatively sodic plagioclase. Mg# ranges from 0.62 to 0.65. Pegmatitic hornblende gabbro has variable composition, according to the relative abundance of amphibole and plagioclase. The contents in SiO_2 (41.4–50.00 wt.%), MgO (5.6–12.9 wt.%), Al_2O_3 (9.5–23.0 wt.%), Cr (65–1011 ppm) and Ni (51–107 ppm) display considerable variations (Table 7.13; Figure 7.9). Mg# ranges from 0.60 to 0.75.

The leucocratic rocks (leucodiorite and granite) have the highest SiO_2 (53.2 and 72.7 wt.%, respectively), Al_2O_3 (24.4 and 14.8 wt.%, respectively), Na_2O (4.9 and 4.2 wt.%, respectively) and K_2O (0.5 and 2.6 wt.%, respectively) and the lowest FeO* (2.1 and 0.9 wt.%, respectively), CaO (10.4 and 2.3 wt.%, respectively), MgO (2.5 and 0.6 wt.%, respectively) and TiO_2 (0.2 and 0.1 wt.%, respectively) contents (Table 7.13; Figure 7.9). The contents in Cr (87 and 39 ppm, respectively), Ni (19 and 5 ppm, respectively) and Co (51 and 42 ppm, respectively) are low and Mg# is 0.68 in leucodiorite and 0.52 in granite.

Using MgO as the differentiation index, the plot of the major oxides shows two clear trends (Figure 7.9). One defined by positive correlations of MgO with FeO, Cr, Ni and Co and negative correlations with Al_2O_3, SiO_2, TiO_2, CaO and Sc, which are consistent with olivine and clinopyroxene fractionation and are defined by rocks with cumulate characteristics, wehrlite and olivine-hornblende clinopyroxenite (T1). On the other hand, a second trend (T2) shows negative correlations of MgO with SiO_2, Al_2O_3, Na_2O and K_2O, while FeO, TiO_2, CaO, Cr, Ni and Sc correlate positively; this trend is formed by fine-grained hornblende gabbro (most primitive), coarse-grained hornblende gabbro and leucocratic rocks, which suggests magmatic fractionation. Hornblendites are in between both trends. The inflection of the two trends occurs at around MgO = 12 wt.%, corresponding to fine-grained hornblende gabbro composition.

In terms of trace elements and rare earth elements (REE), all types of rock show primitive mantle (PM)-normalized patterns enriched in large ion lithophile elements (LILE), depleted in high field strength elements (HFSE; Nb, Zr, Ti) and P, and with positive anomalies in Pb, Sr and Ba (Figure 7.10), while the REE chondrite-normalized patterns show variable trends but all show light rare earth elements (LREE) enrichment and heavy rare-earth elements (HREE) depletion (Figure 7.10). The value of ∑REE increases as MgO decreases in the sequence: wehrlite, olivine-hornblende clinopyroxenite, hornblendite, fine-grained hornblende gabbro, coarse-grained hornblende gabbro and leucocratic rocks.

Wehrlite bears the lowest REE content (<3.5 times chondrite). The pattern normalized to chondrite is characterized by $(La/Yb)_n$ = 7.08 (Figure 7.10a-b). Olivine-hornblende clinopyroxenite has REE concentrations that range 3 to 20 times chondrite and has open convex-upward patterns of LREE and middle rare-earth elements (MREE); HREE show a flat patterns of about 3 to 10 times chondrite; $(La/Yb)_n$ ranges from 1.22 to 3.40 and Th/La is low (0.09– 0.25) (Figure 7.10a-b). Horblendite presents slight or no negative anomaly in primitive mantle-normalized Ti and the ratio Th/La is less than 0.16. The REE patterns of hornblendite has similar shape than olivine-hornblende clinopyroxenite but with higher REE content and are slightly more fractionated ($(La/Yb)_n$ = 2.5–5.3) (Figure 7.10c-d).

Fine-grained hornblende gabbro, coarse-grained hornblende gabbro and pegmatitic hornblende gabbro show similar chondrite-normalized REE patterns. These types of rock are enriched in LREE and depleted in HREE ($(La/Yb)_n$ = 3.4 – 8.8) and do not show Eu anomaly (except a pegmatitic hornblende gabbro with Eu/Eu* = 9.5). The Th/La ratio is lower than 0.26 (Figure 7.10e-h).

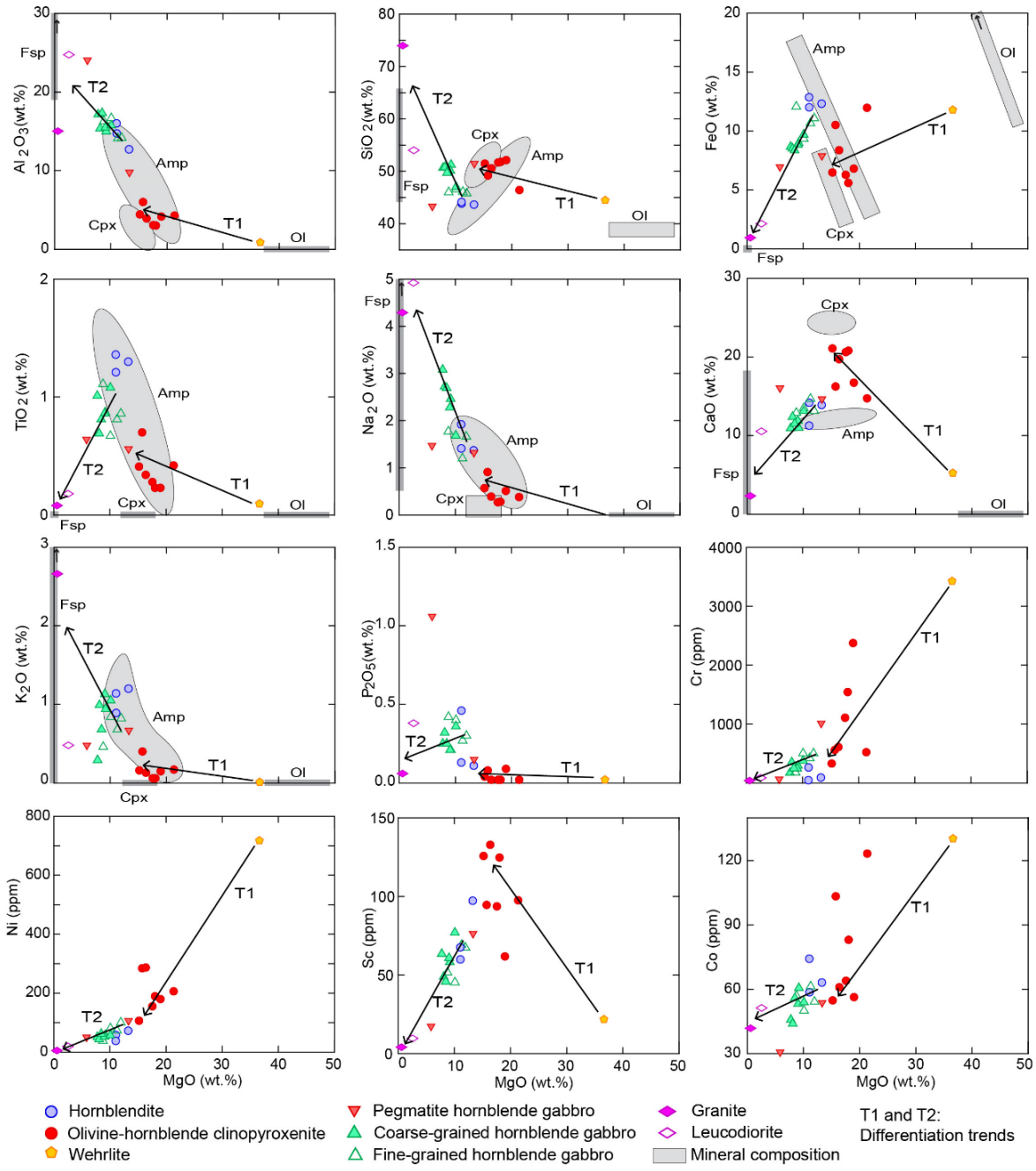

Figure 7.9. Harker diagrams showing main oxides (wt.%) and selected trace elements (ppm) vs MgO (wt.%). The fields of mineral composition are from this study; Ol (olivine), Cpx (clinopyroxene), Amp (amphibole) and Fsp (plagioclase and alkali feldspar).

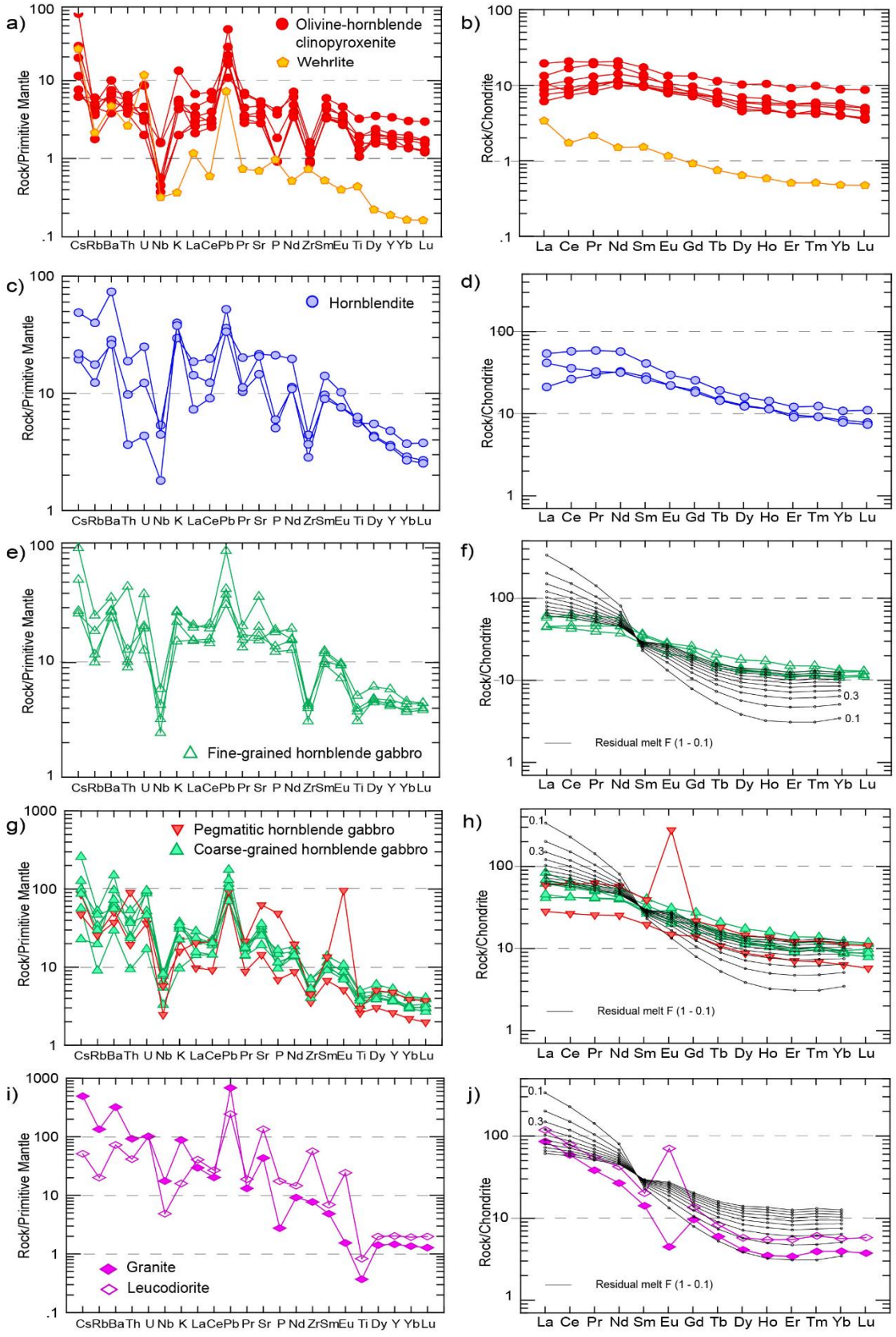

Figure 7.10. Multi-element diagrams normalized to primitive mantle (a, c, e, g, i) and chondrite–normalized REE patterns (b, d, f, h, j) of the TUMC lithologies; primitive mantle and chondrite after Sun and McDonough (1989). Also shown (f, h and j) are the results of the fractional crystallization model (Rayleigh fractionation, F = melt fraction).

The leucocratic rocks show the most fractionated patterns. They are enriched in LREE with respect to the MREE ($(La/Sm)_n$ = 5.8 – 6), HREE display flat patterns at about 4 times chondrite and the $(La/Yb)_n$ ratio ranges from 20.9 to 21.7. Granite has negative Eu anomaly (Eu/Eu* = 0.38), while leucodiorite has positive Eu anomaly (Eu/Eu* = 4.3), consistent with a cumulate plagioclase character. These lithologies do not show the negative primitive mantle-normalized Zr anomaly that characterizes other rock types, in agreement with more abundant zircon in these rocks. The Th/La ratio in this group ranges from 0.13 to 0.39 (Figure 7.10i-j).

7.5.2 U-Th-Pb zircon geochronology

For U-Th-Pb dating, zircon grains were separated from four samples. The zircons from olivine-hornblende clinopyroxenite (AR-31B) and fine-grained hornblende gabbro (AR-07) are small (150 µm x 70 µm) crystals, while in leucocratic rocks (leucodiorite AR-34 and granite AR-15) are bigger in size (< 250 µm). In all samples, zircons have euhedral shape, pyramidal terminations and well defined oscillatory magmatic zoning in cathodoluminescence images (Figure 7.11). The analyses of the reported ages were not corrected for common-lead and the discordant measures (>5% discordance as defined in Table 7.14) were excluded for the weighted mean age calculations.

Five spots (Figure 7.11a, Table 7.14) from 4 zircon grains of olivine-hornblende clinopyroxenite have U ranging from 453 to 2632 ppm, Th from 95 to 1695 ppm and Th/U between 0.21 and 0.66. Three concordant analyses (-0.8 to 2.8% discordance) yield a weighted mean $^{206}Pb/^{238}U$ age of 75.8 ± 0.7 Ma (MSWD=0.1). Two discordant analyses yield a $^{206}Pb/^{238}U$ apparent ages of 74.4 ± 2.3 Ma and 72.4 ± 2.2 Ma (6.4 and 6.6% of discordance, respectively). Three measurements from 3 inherited grains show U content ranging from 78 to 380 ppm and Th from 43 to 134 ppm, with Th/U in the range of 0.20-0.57. Two concordant analyses (1.0 to 1.8% discordance) show $^{206}Pb/^{238}U$ apparent ages of 507 ± 13 Ma and 539 ± 8 Ma, and one discordant measurement (5.4% discordance) has a $^{206}Pb/^{238}U$ apparent age of 116.2 ± 1.3 Ma.

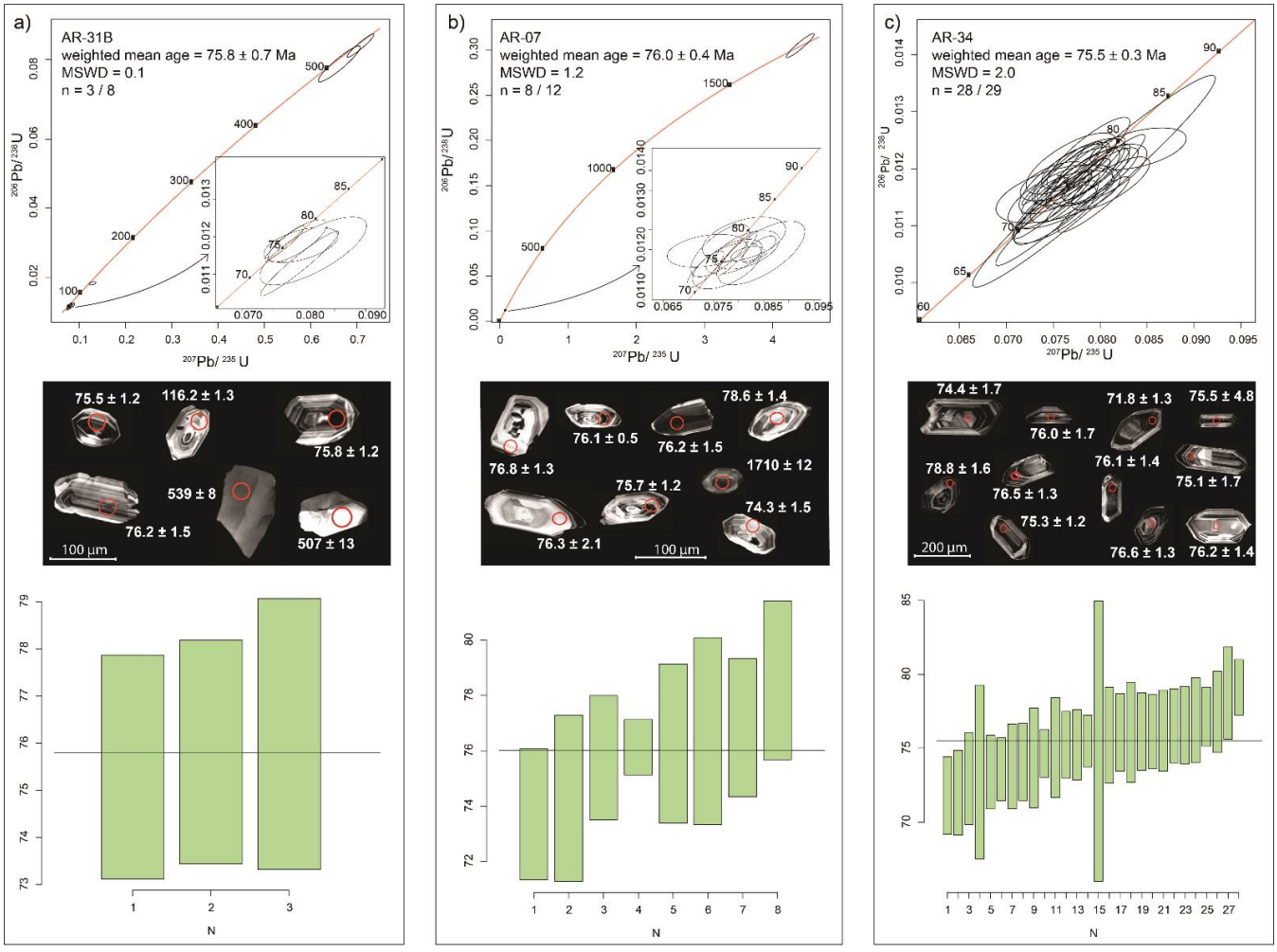

Figure 7.11. Zircon U-Pb data: a) olivine-hornblende clinopyroxenite (AR-31B); b) fine-grained hornblende
34); and d) granite (AR-15). The common lead-uncorrected concordia plot include inherited grain
cathodoluminescence images, with analytical spots and $^{206}Pb/^{238}U$ age in Ma, age bar charts and weighted
lead uncorrected data and errors/MSWD. MSWD: mean standard weighted deviation.

Eleven measurements on eleven zircons from fine-grained hornblende gabbro have variable contents of U ranging from 147 to 2176 ppm and Th from 38 to 1421 ppm, with Th/U = 0.26-0.88 (Table 7.14). Eight concordant determinations (-2.6 to 4.6% discordance) yielded a weighted mean $^{206}Pb/^{238}U$ age of 76.0 ± 0.4 Ma (MSWD=1.2) (Figure 7.11b). Three discordant analyses have $^{206}Pb/^{238}U$ apparent ages of 76.7 ± 1.1 Ma, 76.9 ± 0.9 Ma and 76.3 ± 2.1 Ma (-6.2, 6.2 and 7.4% discordance, respectively). One inherited zircon has a $^{207}Pb/^{206}Pb$ apparent age of 1710 ± 12 Ma.

Twenty-nine zircons from leucodiorite (29 spots; Table 7.14) show U = 439-2282 ppm, Th = 91-1315 ppm and Th/U = 0.21-0.59 contents. Twenty-eight concordant determinations (-3.6 to 5.0% discordance) yielded a weighted mean $^{206}Pb/^{238}U$ age of 75.5 ± 0.3 Ma (MSWD=2.0) (Figure 10c). One discordant analysis (6% discordance) has a $^{206}Pb/^{238}U$ apparent age of 72.9 ± 1.3 Ma. Inherited zircons were not identified.

In the granite sample, nineteen spots (Table 7.14) from 19 zircons show U variations from 388 to 3392 ppm, Th from 42 to 1404 ppm and Th/U from 0.08 to 0.64. Eighteen concordant determinations (-2.4 to 4.0% discordance) yielded a weighted mean $^{206}Pb/^{238}U$ age of 75.1 ± 0.2 Ma (MSWD=1.1) (Figure 10d). One discordant analysis (5.6% discordance) has a $^{206}Pb/^{238}U$ apparent age of 69.8 ± 1.4 Ma. No inherited zircons were identified.

The four weighted mean $^{206}Pb/^{238}U$ ages determined in samples of differentiation trends T1 and T2 are all essentially within error (75.8 ± 0.7 Ma, 76.0 ± 0.4 Ma, 75.5 ± 0.3 Ma and 75.1 ± 0.2 Ma), allowing considering the 57 concordant measurements of the four lithologies and a corresponding weighted mean $^{206}Pb/^{238}U$ age of 75.4 ± 0.2 Ma (MSWD=1.5), which is considered the generalized formation age of TUMC.

7.5.3 Nd-Sr isotopic systematics

Rb-Sr and Sm-Nd isotope systematics of 7 samples are listed in Table 7.15 and represented in Figure 7.12. The initial Nd and Sr ratios and the epsilon values ($\varepsilon Nd_{(t)}$, $\varepsilon Sr_{(t)}$; Table 7.15) were corrected to 75 Ma based on the formation age of the TUMC obtained in this study. All samples have very similar initial values of $(^{87}Sr/^{86}Sr)_i$ (0.703523-0.704481) and $(^{143}Nd/^{144}Nd)_i$ (0.512468-0.512559), clustering in a narrow range of composition evidencing a homogeneous source for all samples (Figure 7.12a). The data are proximal to the bulk silicate Earth composition (BSE). The $\varepsilon Nd_{(t)}$ from -1.28 to +0.49 and the $\varepsilon Sr_{(t)}$ from -12.62 to +0.98 are low (Table 7.15), while the $(La/Yb)_n$ ratio is variably greater than 1, indicating an enriched source (Figure 7.12b).

Table 7.14. Zircon SHRIMP U-Th-Pb data of the Tampanchi ultramafic-mafic complex. Data are unco

Spot	U	Th	206Pb	f206_4 %	f206_8%	Th/U	Isotope ratios									
							207/206	±err	206/238	±err	207/235	±err	208/232	±err	207/206	±err
Sample AR-31B (n=8) Olivine-hornblende pyroxenite																
zr 1 rim	453	94.7	4.6	0.0	0.2	0.21	0.05092	0.00149	0.01162	0.00037	0.08152	0.00352	0.00389	0.00016	237.3	66.4
zr 1 core	812	165	8.4	0.1	0.2	0.21	0.04820	0.00074	0.01189	0.00023	0.07902	0.00194	0.00401	0.00010	109.1	35.8
zr 2	725	207	7.4	0.1	0.2	0.29	0.04900	0.00130	0.01178	0.00019	0.07956	0.00245	0.00388	0.00007	147.9	60.8
zr 3	1297	456	12.7	0.0	0.0	0.36	0.05099	0.00048	0.01129	0.00035	0.07934	0.00257	0.00359	0.00022	240.3	21.4
zr 4	276	134	4.4	0.0	0.5	0.50	0.05130	0.00101	0.01820	0.00020	0.12865	0.00290	0.00613	0.00019	254.5	44.8
zr 5	77.5	43.1	5.5	0.1	0.4	0.57	0.05873	0.00061	0.08183	0.00213	0.66234	0.01858	0.02640	0.00081	557.3	22.6
zr 6	380	72.9	28.7	0.0	0.1	0.20	0.05897	0.00032	0.08714	0.00138	0.70824	0.01184	0.02747	0.00055	565.9	11.8
zr 7	2632	1695	27.0	0.0	0.1	0.66	0.04706	0.00027	0.01183	0.00019	0.07693	0.00132	0.00379	0.00006	0.0	0.0
Sample AR-07 (n=12) Fine-grained hornblende gabbro																
zr 1 rim	368	137	3.8	0.0	0.5	0.38	0.04471	0.00186	0.01197	0.00017	0.07375	0.00325	0.00411	0.00011	0.0	0.0
zr 1 core	514	195	5.1	0.0	0.1	0.39	0.04628	0.00053	0.01150	0.00019	0.07337	0.00150	0.00373	0.00010	0.0	0.0
zr 2	2176	1381	22.6	0.3	0.5	0.65	0.05085	0.00057	0.01200	0.00014	0.08409	0.00136	0.00398	0.00005	234.1	25.4
zr 3	309	225	81.5	0.0	0.0	0.75	0.10472	0.00068	0.30517	0.00545	4.40450	0.08360	0.08831	0.00170	1709.5	11.8
zr 4	280	74.5	2.9	0.1	0.3	0.27	0.04948	0.00135	0.01199	0.00020	0.08175	0.00262	0.00403	0.00008	170.7	62.4
zr 5	147	37.9	1.5	0.2	0.1	0.26	0.05150	0.00160	0.01191	0.00033	0.08455	0.00354	0.00387	0.00024	263.5	69.8
zr 6	432	122	4.5	0.0	0.3	0.29	0.04633	0.00105	0.01197	0.00027	0.07640	0.00242	0.00401	0.00015	0.0	0.0
zr 7	975	642	10.0	0.1	0.5	0.68	0.04999	0.00075	0.01188	0.00008	0.08182	0.00136	0.00395	0.00004	194.3	34.6
zr 8	1664	1421	17.1	0.0	0.4	0.88	0.04860	0.00038	0.01190	0.00023	0.07968	0.00165	0.00387	0.00008	128.7	18.4
zr 9	476	222	4.9	0.1	-0.2	0.48	0.04857	0.00119	0.01182	0.00018	0.07910	0.00229	0.00368	0.00015	126.9	56.6
zr 10	253	80.3	2.7	0.0	0.3	0.33	0.04799	0.00180	0.01226	0.00023	0.08111	0.00339	0.00415	0.00012	0.0	185.3
zr 11	208	61.9	2.1	0.1	0.3	0.30	0.04864	0.00145	0.01159	0.00024	0.07769	0.00280	0.00391	0.00013	130.5	68.8

207/206 = $^{207}Pb/^{206}Pb$; 206/238 = $^{206}Pb/^{238}U$; 207/235 = $^{207}Pb/^{235}U$; 208/232 = $^{208}Pb/^{232}Th$.

Errors are at one sigma level. The error in $^{206}Pb/^{238}U$ averaging the standard has been already propagated. Th/U ratio weight.

Point-to point errors, calculated on replicates of the TEMORA standard, are: 0.32 % for $^{206}Pb/^{238}U$, and 0.37 % for ^{207}

Discordance: d(%) = 100×(1–206/238 age /207/235 age).

Table 7.14. (Continued). Zircon SHRIMP U-Th-Pb data of the Tampanchi ultramafic-mafic complex. Data a

Spot	U	Th	206Pb	f206_4 %	f206_8%	Th/U	Isotope ratios										
							207/206	±err	206/238	±err	207/235	±err	208/232	±err	207/206	±err	
Sample AR-34 (n=29) Leucodiorite																	
zr 1	663	154	6.7	0.0	0.0	0.24	0.04713	0.00028	0.01160	0.00027	0.07537	0.00180	0.00369	0.00017	0.0	0.0	
zr 2	1112	474	11.9	0.1	0.4	0.44	0.04938	0.00107	0.01235	0.00015	0.08405	0.00209	0.00414	0.00007	165.9	49.8	
zr 3	439	90.5	4.3	0.0	0.5	0.21	0.04779	0.00036	0.01138	0.00025	0.07492	0.00172	0.00414	0.00013	0.0	106.5	
zr 4	2282	1315	23.8	0.0	0.4	0.59	0.04655	0.00062	0.01204	0.00016	0.07725	0.00143	0.00397	0.00005	0.0	0.0	
zr 5	650	158	6.4	0.1	0.1	0.25	0.04867	0.00053	0.01145	0.00047	0.07682	0.00325	0.00375	0.00030	132.1	25.4	
zr 6	992	431	9.9	0.1	-0.2	0.45	0.04871	0.00019	0.01148	0.00017	0.07707	0.00117	0.00355	0.00010	133.7	9.4	
zr 7	988	322	10.2	-0.2	0.1	0.33	0.04580	0.00018	0.01188	0.00021	0.07499	0.00136	0.00387	0.00011	0.0	0.0	
zr 8	755	189	7.8	0.1	0.0	0.26	0.04834	0.00043	0.01194	0.00020	0.07956	0.00149	0.00378	0.00012	115.7	21.0	
zr 9	768	215	7.7	0.0	0.2	0.29	0.04741	0.00145	0.01156	0.00021	0.07553	0.00270	0.00382	0.00008	0.0	141.5	
zr 10	674	154	6.6	0.1	0.1	0.23	0.04865	0.00062	0.01123	0.00023	0.07532	0.00182	0.00362	0.00012	130.9	29.8	
zr 11	757	202	7.7	0.0	0.1	0.27	0.04797	0.00045	0.01174	0.00018	0.07762	0.00141	0.00381	0.00007	0.0	120.1	
zr 12	793	204	8.1	0.1	0.3	0.26	0.05013	0.00068	0.01174	0.00019	0.08112	0.00170	0.00401	0.00008	201.1	31.4	
zr 13	630	148	6.4	0.1	0.1	0.24	0.04822	0.00076	0.01171	0.00027	0.07783	0.00215	0.00382	0.00012	110.1	36.6	
zr 14	858	238	8.9	0.0	0.2	0.28	0.04682	0.00050	0.01195	0.00021	0.07713	0.00157	0.00400	0.00010	0.0	0.0	
zr 15	1297	581	12.9	0.0	-0.3	0.46	0.04775	0.00045	0.01145	0.00020	0.07538	0.00152	0.00348	0.00016	0.0	109.5	
zr 16	845	243	8.7	0.2	0.2	0.30	0.04892	0.00056	0.01188	0.00020	0.08010	0.00161	0.00397	0.00009	144.1	26.4	
zr 17	678	190	6.7	0.2	0.3	0.29	0.05059	0.00039	0.01137	0.00020	0.07930	0.00155	0.00385	0.00008	222.3	18.0	
zr 18	602	145	6.1	0.0	0.2	0.25	0.04813	0.00093	0.01165	0.00013	0.07726	0.00173	0.00391	0.00007	105.7	45.2	
zr 19	1501	454	15.4	0.0	0.3	0.31	0.04733	0.00079	0.01187	0.00021	0.07742	0.00190	0.00396	0.00008	0.0	104.9	
zr 20	794	251	8.1	0.0	0.1	0.32	0.04628	0.00075	0.01178	0.00014	0.07515	0.00149	0.00385	0.00009	0.0	0.0	
zr 21	621	163	6.5	0.0	0.4	0.27	0.04616	0.00083	0.01209	0.00022	0.07693	0.00197	0.00424	0.00022	0.0	0.0	
zr 22	540	122	5.6	0.1	0.0	0.23	0.04876	0.00091	0.01189	0.00022	0.07989	0.00208	0.00379	0.00012	136.3	43.2	
zr 23	1750	883	18.6	0.0	-0.4	0.52	0.04648	0.00053	0.01229	0.00025	0.07874	0.00181	0.00371	0.00021	0.0	0.0	
zr 24	616	177	6.1	0.0	-0.1	0.29	0.04775	0.00109	0.01151	0.00023	0.07576	0.00227	0.00360	0.00011	0.0	139.7	
zr 25	856	243	8.8	0.0	0.0	0.29	0.04708	0.00090	0.01187	0.00027	0.07700	0.00230	0.00380	0.00010	0.0	0.0	
zr 26	1850	620	19.2	0.0	0.2	0.34	0.04742	0.00049	0.01200	0.00023	0.07843	0.00172	0.00396	0.00011	0.0	0.0	
zr 27	1576	670	16.1	0.0	0.2	0.44	0.04655	0.00039	0.01184	0.00026	0.07595	0.00176	0.00386	0.00008	0.0	0.0	
zr 28	1464	520	14.2	0.1	0.2	0.36	0.04869	0.00076	0.01120	0.00021	0.07514	0.00182	0.00369	0.00008	132.9	36.2	
zr 29	750	203	7.7	0.0	0.0	0.28	0.04885	0.00079	0.01178	0.00076	0.07933	0.00528	0.00373	0.00026	140.5	37.4	

Table 7.14. (Continued). Zircon SHRIMP U-Th-Pb data of the Tampanchi ultramafic-mafic complex. Data a

Spot	U	Th	206Pb	f206_4%	f206_8%	Th/U	Isotope ratios									
							207/206	±err	206/238	±err	207/235	±err	208/232	±err	207/206	±err
Sample AR-15 (n=19) Granite																
zr 1	2043	957	20.7	0.0	0.2	0.48	0.04734	0.00043	0.01172	0.00028	0.07650	0.00192	0.00383	0.00011	0.0	0.0
zr 2	1306	813	13.3	0.1	0.4	0.64	0.04829	0.00084	0.01176	0.00022	0.07830	0.00199	0.00387	0.00016	113.7	40.4
zr 3	2054	738	20.9	0.0	0.1	0.37	0.04649	0.00068	0.01177	0.00006	0.07541	0.00118	0.00379	0.00004	0.0	0.0
zr 4	704	97.8	6.7	0.1	0.0	0.14	0.04879	0.00105	0.01107	0.00027	0.07443	0.00242	0.00349	0.00015	137.5	49.8
zr 5	574	148	5.9	0.1	0.4	0.26	0.04859	0.00086	0.01178	0.00015	0.07889	0.00174	0.00409	0.00013	128.3	41.2
zr 6	3391	463	32.5	0.2	0.1	0.14	0.04943	0.00055	0.01089	0.00022	0.07551	0.00174	0.00364	0.00010	168.5	26.0
zr 7	1484	843	14.8	0.2	-0.3	0.58	0.04940	0.00072	0.01156	0.00017	0.07869	0.00161	0.00357	0.00008	166.9	33.6
zr 8	2006	255	20.5	0.0	0.1	0.13	0.04673	0.00035	0.01179	0.00020	0.07595	0.00142	0.00401	0.00008	0.0	0.0
zr 9	962	436	9.6	0.1	0.1	0.47	0.04831	0.00073	0.01157	0.00018	0.07705	0.00169	0.00372	0.00010	114.5	35.6
zr 10	497	179	4.9	0.0	0.3	0.37	0.04630	0.00130	0.01135	0.00021	0.07241	0.00243	0.00377	0.00008	0.0	0.0
zr 11	2249	1404	22.9	-0.1	0.3	0.64	0.04788	0.00016	0.01176	0.00022	0.07759	0.00149	0.00384	0.00008	0.0	101.1
zr 12	1200	363	12.6	0.0	0.2	0.31	0.04898	0.00081	0.01208	0.00023	0.08157	0.00205	0.00397	0.00011	146.9	38.4
zr 13	675	148	6.7	0.0	0.2	0.23	0.04730	0.00080	0.01151	0.00026	0.07503	0.00212	0.00384	0.00010	0.0	104.3
zr 14	1290	520	13.3	0.1	0.2	0.41	0.04911	0.00047	0.01189	0.00018	0.08050	0.00142	0.00391	0.00006	152.9	22.2
zr 15	1346	107	13.5	0.0	0.1	0.08	0.04639	0.00081	0.01155	0.00023	0.07384	0.00195	0.00403	0.00018	0.0	0.0
zr 16	650	166	6.6	0.0	0.2	0.26	0.04960	0.00191	0.01168	0.00034	0.07984	0.00385	0.00393	0.00021	176.1	87.6
zr 17	500	41.8	5.0	0.0	0.2	0.09	0.04798	0.00106	0.01153	0.00035	0.07626	0.00288	0.00422	0.00034	0.0	149.5
zr 18	2129	218	22.0	0.0	0.1	0.11	0.04760	0.00057	0.01195	0.00021	0.07841	0.00164	0.00404	0.00012	0.0	107.5
zr 19	388	80.4	3.9	0.0	0.5	0.21	0.04887	0.00096	0.01162	0.00013	0.07825	0.00176	0.00419	0.00028	141.9	45.2

Table 7.15. Rb-Sr and Sm-Nd isotopic data of representative samples from the Tampanchi ultra

Sample	Rb	Sr	$^{87}Rb/^{86}Sr$	$^{87}Sr/^{86}Sr$	Error Sr/Sr	$(^{87}Sr/^{86}Sr)_i$ (75 Ma)	εSr (75 Ma)	Sm	Nd	$^{147}Sm/^{144}Nd$	$^{143}Nd/^{144}N$
AR-031B	2.650	50.343	0.152242	0.704006	0.001	0.703844	-8.06	1.262	3.947	0.193312	0.51256
AR-010-5	10.482	282.652	0.107252	0.703637	0.002	0.703523	-12.62	4.225	14.941	0.170968	0.51258
AR-035	24.149	440.906	0.158410	0.704036	0.003	0.703867	-7.73	3.743	14.050	0.161069	0.51263
AR-007	5.787	308.488	0.054255	0.704025	0.001	0.703967	-6.31	5.489	21.193	0.156592	0.51260
AR-042B	17.142	739.401	0.067051	0.703896	0.003	0.703825	-8.34	3.675	17.269	0.128664	0.51262
AR-034	10.256	2307.497	0.012855	0.704145	0.001	0.704131	-3.98	2.822	17.752	0.096112	0.51252
AR-015	49.045	763.835	0.185717	0.704679	0.002	0.704481	0.98	1.760	9.850	0.108030	0.51256

Errors are instrumental measurements of $^{87}Sr/^{86}Sr$ and $^{143}Nd/^{144}Nd$ ratios, expressed as 2 sigma % rel.
Rb, Sr, Sm and Nd content are in ppm.

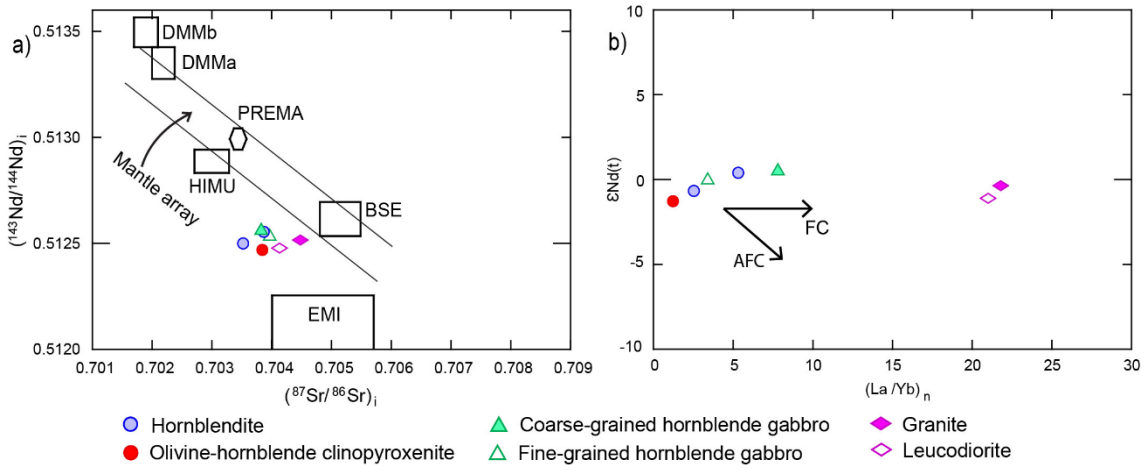

Figure 7.12. a) Nd – Sr isotope systematics of rocks from TUMC. The fields of main mantle reservoirs are from Zindler and Hart (1986); DMMa: depleted MORB-mantle with isotopic radiogenic enrichment; DMMb: depleted MORB-mantle; BSE, bulk silicate Earth; EMI, enriched mantle type I; HIMU, high U/Pb mantle; PREMA, frequently observed prevalent mantle composition. b) ℇNd(t) vs (La/Yb)n; ℇNd(t) were calculated using present-day values of $^{147}Sm/^{144}Nd$ = 0.1960 ± 4 and $^{143}Nd/^{144}Nd$ = 0.512630 ± 11 for CHUR (Bouvier et al., 2008); FC (fractional crystallization) and AFC (assimilation and fractional crystallization).

7.6 Discussion

7.6.1 Imprint of alteration process and crustal contamination

The rocks of the TUMC are undeformed and unmetamorphosed, but are locally affected by faults-shear zones where they show cataclastic-mylonitic fabric. The scarcity of secondary minerals and the good preservation of primary minerals in many samples evidence minor post-magmatic alteration and metasomatic processes. LILE are considered mobile elements (e.g. Winchester and Floyd, 1977), while Ce anomalies are indicative of REE mobility (Polat and Hofmann, 2003). The limited variation of LILE and the absence of Ce anomalies, besides the low loss on ignition (LOI) value in all samples, further indicate minor hydration and remobilization processes (Table 7.13). Hence, we consider that the geochemical composition of the analyzed samples is essentially the result of primary igneous processes.

On the other hand, the magmas involved could have been influenced by assimilation of continental crust, as well as being influenced by slab-components (aqueous fluids and/or melts). All types of rock from the TUMC show high Sr/Th at low Th/Ce, which denotes the presence of an aqueous fluid component in the magmas, as otherwise indicated by primary hydrous minerals (mainly hornblende) in the rocks (Figure 7.13a; Turner et al., 2012).

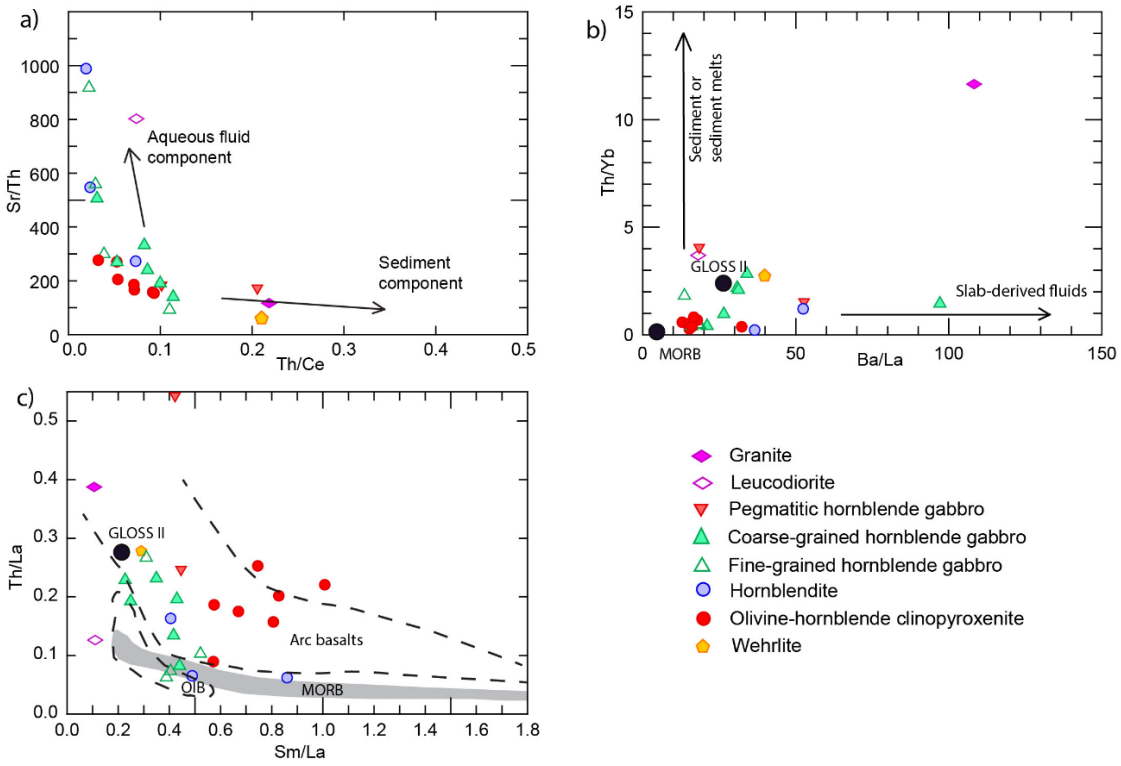

Figure 7.13. a) Sr/Th vs. Th/Ce diagram (Turner et al., 2012). b) Th/Yb vs. Ba/La diagram. c) Th/La vs Sm/La diagram (Plank, 2005), MORB data are from the Mid-Atlantic Ridge (Hannigan et al., 2001), OIB data from a compilation by T. Elliott cited by Plank (2005) and arc data from Elliott et al. (1997), Gust et al. (1995), Taylor and Nesbitt (1998), and Hochstaedter et al. (2000). GLOSS II is global subducting sediment (Plank, 2014).

The Th/Yb vs. Ba/La diagram show variable Ba/La at low Th/Yb (Figure 7.13; Turner et al., 1997; Class et al., 2000; Woodhead et al., 2001). Some samples of gabbros with moderate Th/Yb would suggest a crustal- (Class et al., 2000) or slab-derived (Davidson, 1987; Woodhead et al., 2001) sedimentary component (Figure 7.13b). Hornblende gabbros are aligned and trend toward the global subducting sediment composition (GLOSS II), indicating a sediment component input in addition to hydrous fluids in the magma-source (Figure 7.13b). The Th/La ratio in hornblende gabbros mainly ranges between 0.06 and 0.27. This ratio is high in the continents (bulk continental crust, >0,25) and varies in arc basalts and marine sediments (0,09–0,34) (Plank, 2005). In the Th/La vs Sm/La diagram (Figure 7.13c; Plank, 2005), hornblende gabbros and leucocratic rocks show variation between a MORB-OIB and a sedimentary composition (GLOSS II) denoting a subduction sediment input. This justifies the low $(^{143}Nd/^{144}Nd)_i$ at low $(^{87}Sr/^{86}Sr)_i$ (Figure 7.12). On the other hand, an important crustal assimilation process during differentiation is precluded by (i) the limited range in $\varepsilon Nd_{(t)}$ between basic and acid compositions (e.g. Figure 7.12b), (ii) the dominantly negative $\varepsilon Sr_{(t)}$ (Table 7.15), (iii) the negative Zr anomalies in PM-normalized trace elements patterns

(Figure 7.10), (iv) the scarcity of inherited zircons grains found in TUMC (Figure 7.11) and (v) the absence of crustal xenoliths. These data support an origin of the melt from a uniform mantle source influenced by slab-derived fluids and discards significant crustal assimilation.

7.6.2 Crystallization conditions

The temperature of amphibole crystallization was calculated using the calibration of Ridolfi et al. (2010), which works independently of pressure (Figure 7.14). Pargasite and magnesio-hastingsite formed at the highest calculated temperature (896-1025 °C) in the TUMC, ranging 899-985 °C in olivine–hornblende clinopyroxenite, 896-1025 °C in hornblendite, 904-958 °C in fine-grained hornblende gabbro and 928-952 °C in the cores in coarse-grained hornblende gabbro. On the other hand, the temperatures calculated for magnesio-hornblende and magnesio-ferri-hornblende crystallization range between 780 to 931 °C (780-931 °C in olivine-hornblende clinopyroxenite, 830-859 °C in hornblendite, 858-911 °C in fine-grained hornblende gabbro, 824-911 °C in the rims and single crystals of coarse-grained hornblende gabbro and 803-908 °C in leucodiorite). These values show that amphibole crystallized in a temperature range of ca. 800-1000ºC, with the lowest temperature (ca. 800 ºC) in the more evolved rock compositions, while the calculated temperature is highest in hornblendite. The temperature of clinopyroxene crystallization was estimated using equation 32d of Putirka (2008), considering a pressure of 3.6 kbar (see below). The results yield 1077-1177 °C in wehrlite, 980-1164 °C in olivine-hornblende clinopyroxenite (with predominant values over 1100 °C) and 935–1128 °C (with almost all values over 1070 °C) in hornblendites (Figure 7.14a).

The pressure was estimated according to the temperature-dependent calibration of plagioclase/amphibole Al-Si partitioning of Molina et al. (2015). The calculations were performed for fine-grained hornblende gabbro and coarse-grained hornblende gabbro, which contain the appropriate mineral paragenesis, using the temperature of amphibole crystallization calculated above with the calibration of Ridolfi et al. (2010). The plagioclase/amphibole pairs correspond to adjacent grains of magnesio-hornblende and plagioclase in apparent textural equilibrium. The calculated pressure ranges between 3.1 and 5.0 kbar in fine-grained hornblende gabbro and from 2.2 to 4.7 kbar in coarse-grained hornblende gabbro (Figure 7.14b), with a mean for both lithologies of around 3.6 kbar, which is considered the pressure of intrusion of the entire complex due to geochemical and geochronological evidences for co-genetic character of all types of rock. The pressure estimated suggests that the TUMC magma chamber was located at intermediate to shallow crustal levels (~12.5 km, using an average density the rock pile of 2.85 g/cm^3 corresponding to granodiorite-tonalite).

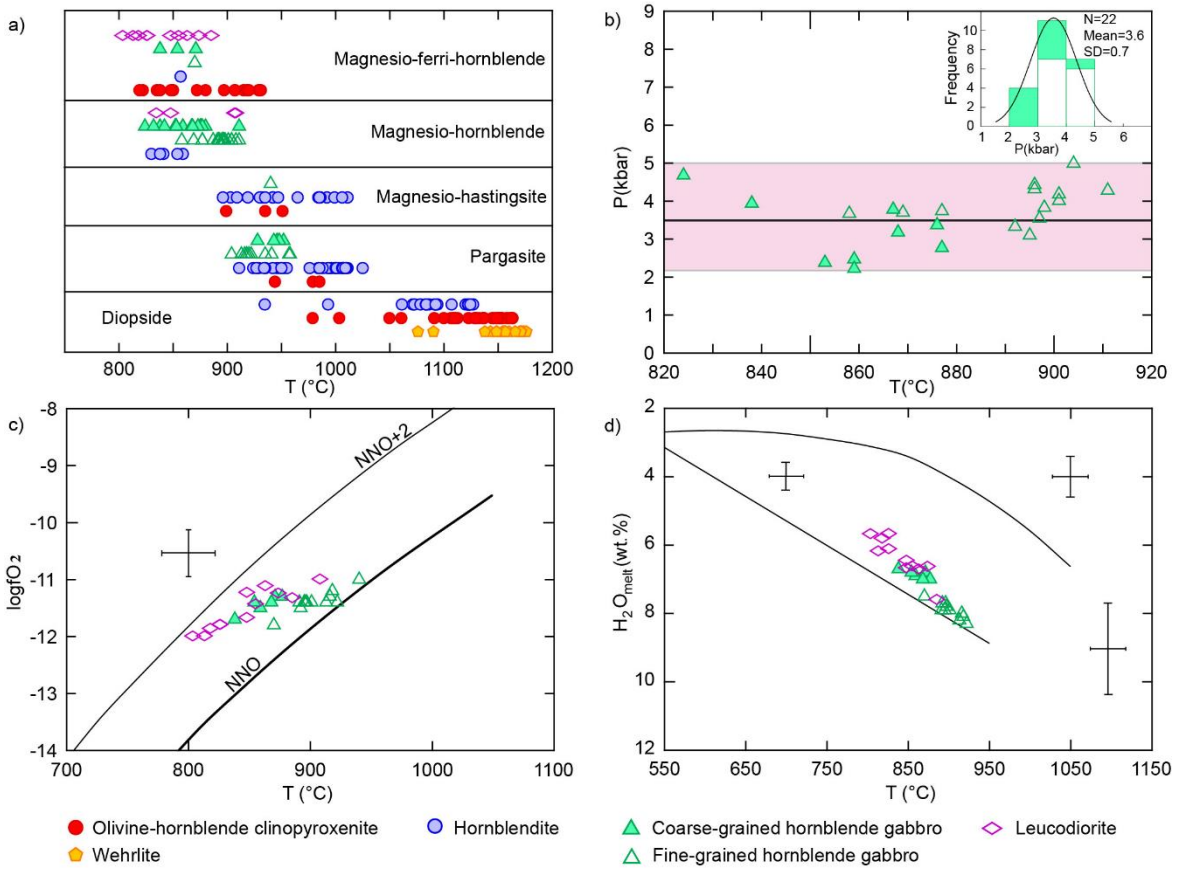

Figure 7.14. Thermobarometric conditions, oxygen fugacity and water content calculated for the TUMC. a) Temperature calculated for clinopyroxene and amphibole using equation 32d from Putirka (2008) and the calibrations of Ridolfi et al. (2010), respectively. b) P (kbar) vs. T (°C) diagram showing estimated conditions according to the barometer of Molina et al. (2015) (N= number of plagioclase/amphibole pairs; SD= standard deviation; the calculated pressure range is indicated in pink). c) Oxygen fugacity (fO_2) and d) H_2O content in the melt calculated for amphiboles using the calibrations of Ridolfi et al. (2010); the uncertainties are shown in each diagram. See text for details.

The oxygen fugacity (fO_2) and H_2O content in the melt were calculated in hornblende gabbros and leucodiorite using the calibrations of Ridolfi et al. (2010) for amphibole. The oxygen fugacities from the different lithologies show variations (Figure 7.14c), with -11.8 to -11.2 log units in fine-grained hornblende gabbro (ΔNNO (nickel-nickel oxide buffer) = 0-0.6), -13.4 to -11.3 log units in coarse-grained hornblende gabbro (ΔNNO = 1-1.4) and -12.0 to -11.0 log units in leucodiorite (ΔNNO = 0.7-1.8). These estimates indicate crystallization from an oxidized magma with around ΔNNO = 0-2. The estimations of melt H_2O contents from the different lithologies yielded 7.5-8.3 wt.% (fine-grained hornblende gabbro), 6.7-7 wt.% (coarse-grained hornblende gabbro) and 5.7-7.6 wt.% (leucodiorite) (Figure 7.14d). The relatively high H_2O_{melt} content agrees with the large amount of hornblende in all mafic lithologies.

7.6.3 Magmatic differentiation and petrogenetic model

The geochemical composition of rocks shows two trends of differentiation, one defined by cumulate ultramafic lithologies and other by mafic to leucocratic lithologies with the following crystallization sequences of the essential minerals in the different lithotypes: chromium spinel–olivine–clinopyroxene–amphibole in wehrlite and pyroxenite, amphibole and plagioclase (with later replacement of plagioclase by albite and mica) in hornblendites, clinopyroxene–amphibole–plagioclase–biotite in hornblende gabbros, and amphibole–plagioclase–alkali feldspar–mica–quartz in leucocratic rocks.

Amphibole is the dominant mineral in TUMC, being only absent in wehrlites and granites and scarce in leucodiorite, raising questions about how it formed. In olivine-hornblende clinopyroxenite amphibole replaces clinopyroxene rims and occur as generalized replacement lamellae within the grains yielding a pseudopoikilitic texture (Figure 7.2 and Figure 7.3). In hornblendite, relicts of clinopyroxene are enclosed by amphibole that mainly shows euhedral shape and granoblastic texture, implying subsolidus recrystallization at high temperature (Figure 7.3f-g). These observations, and the local relicts of clinopyroxene enclosed by amphibole in coarse-grained hornblende gabbro suggests generalized formation of amphibole by replacement of clinopyroxene. The field and textural relationships evidence that hornblende growth in clinopyroxenite and hornblendites is a consequence of a reaction-replacement process, as reported in other igneous complexes (e.g. Irvine, 1974; Smith, 2014; Cooper et al., 2016; Hayes et al., 2018, Chang and Audetat, 2018). The reaction-replacement mechanism is effective at generating amphibole in relatively immobile crystal mushes, and unlike true cumulates, hornblendite need not be the result of crystal phases nucleating and growing in the liquid melt (Smith, 2014). The location of hornblendites and the increasing amount of amphibole content in clinopyroxenite toward hornblende gabbros suggest their formation by the interaction of mafic hydrated magma (i.e., hornblende gabbros) ascending through the cumulate pile (clinopyroxenite) producing hornblendites in the contact (c.f., Figure 7.2b). The interstitial minerals between amphibole in hornblendites are a mass-balance result of clinopyroxene reaction with the liquid and associated amphibole growth (Figure 7.2f and Figure 7.2h).

The liquid that triggered the reaction-replacement process could either be the residual melt of the same magmatic phase that crystallized clinopyroxene + olivine and reacted with them during cooling of magmas in a crystal mush environment or a new unrelated liquid injected after olivine + clinopyroxene cristallization. A single magmatic pulse could produce both trends (cumulation and fractional crystallization), once olivine and pyroxene started crystallization and cumulation and the melt become rich in water. However, field and textural

relationships do not support this scenario (see discussion below) and reaction of cumulated rocks with a second magmatic phase is envisaged as a more likely scenario where the injected liquid corresponds to hornblende gabbros (e.g Figure 7.2b).

Wehrlite and olivine-hornblende clinopyroxenite show the highest Mg, Ni, Cr, and Co contents (Figure 7.9), evidencing fractionation from a primitive basaltic melt. The adcumulate texture indicate a general scarcity of trapped liquid due to continuous magma extraction. Hence, evolved liquids were expelled out of the growing chamber during olivine and diopside accumulation and compaction in the first stage of magmatism (phase I, Figure 7.15a). The key observation for this assertion is that hornblendite is a reaction product between a liquid and cumulate rocks. The composition of this liquid corresponds to fine-grained hornblende grabbro, which show non-cumulate texture, unzoned homogeneous relatively small mineral grains, primitive whole-rock chemical composition (Mg# > 65 and low SiO_2) and calcic plagioclase composition, precluding an origin of this type of rock after crystallization of the residual liquid extracted from wehrlite and pyroxenite. Instead, a second intrusive magmatic phase of primitive liquid is envisaged (Figure 7.15b). The second magmatic phase (phase II) is defined by the evolution from the more primitive fine-grained hornblende gabbro through coarse-grained hornblende gabbro to leucocratic rocks that represent residual melts after crystallization of the gabbros (Figure 7.15c). In fact, hornblende gabbros and leucocratic rocks define clear evolutionary trends in terms of major and trace elements, with patterns consistent with crystallization amphibole and plagioclase (Figure 7.9). This differentiation trend is also evidenced by the progressive enrichments in Sr, Zr, ∑REE and Pb while MgO decrease (Table 7.13) and by the chondrite-normalized REE patterns, which show a sub-parallel trend in the mafic rocks (Figure 7.10) and a more fractionated trend in the leucocratic rocks. Leucodiorite and granite are the last magmatic products, having similar REE patterns and $^{87}Sr/^{86}Sr$ and εNd(t) values. Locally, the thicker leucocratic dykes show a transition from leucodiorite in the rim of the dyke to granite in the core, involving the decrease (up to vanishing) of hornblende and the advent and increase of biotite, K-feldspar and quartz. These lithologies can hence be explained by fractional crystallization of liquids evolved from liquids that formed coarse-grained hornblende gabbros.

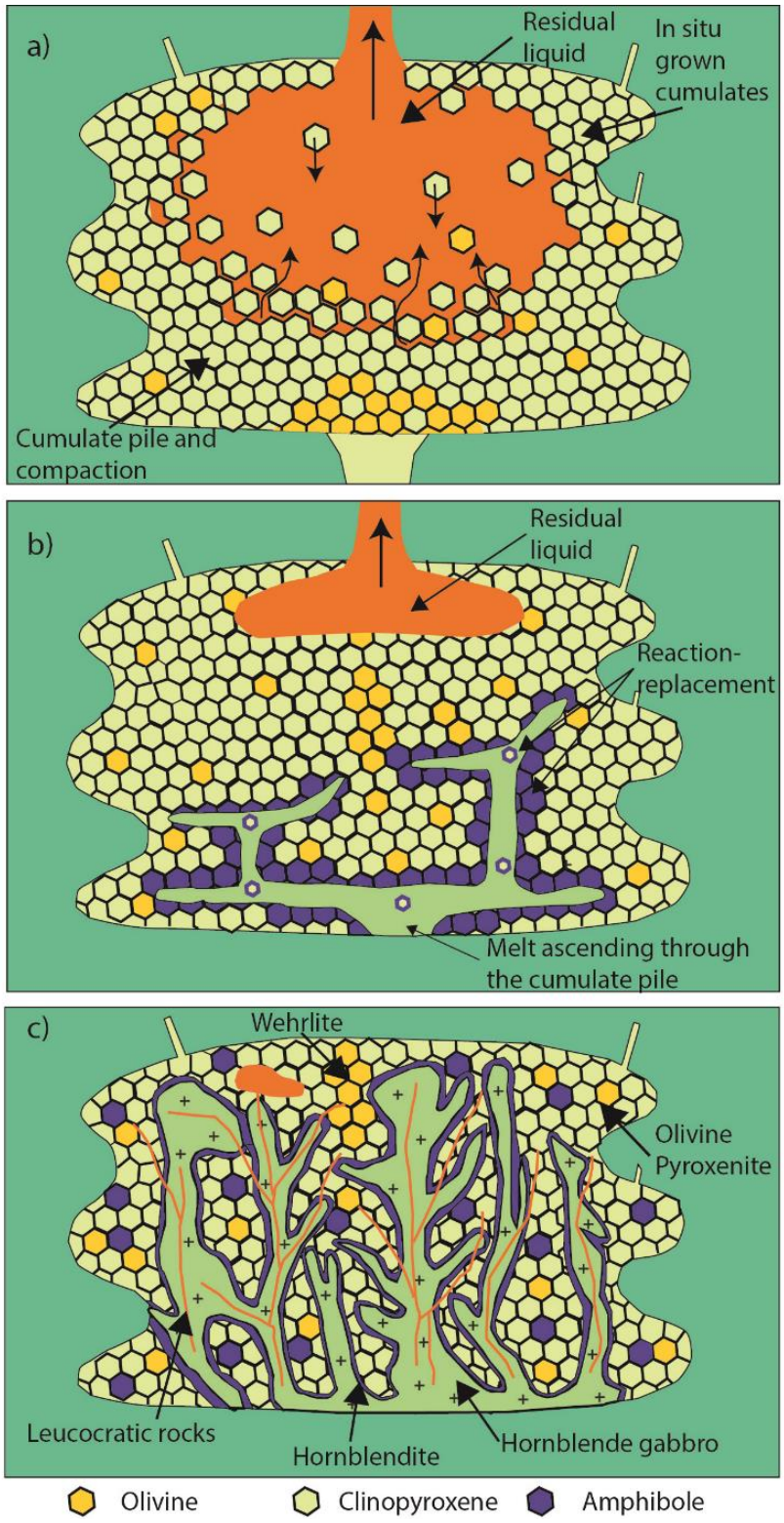

Figure 7.15. Schematic representation of the magmatic phases and evolution of TUMC. a) Initial magmatic phase, with crystallization and accumulation of olivine and clinopyroxene, compaction and melt extraction. b) and c) Second magmatic phase, with new-liquid invading the cumulate pile and generating amphibole by reaction replacement of clinopyroxene and olivine in the cumulate pile; differentiation of gabbroic magma yields acid compositions.

To reproduce the differentiation trend from fine-grained hornblende gabbros to leucocratic rocks, we modeled the REE evolution considering fractional crystallization using the composition of fine-grained hornblende gabbro (sample AR-16) as representative of the initial liquid. The mineral abundance considered were 30.8% plagioclase, 65% amphibole, 1% magnetite, 1% biotite, 1% titanite, 1% apatite, 0.2% zircon, and the melt fraction (F) from 1 to 0.1 (Figure 7.10; Appendix 7. 1). The modeled REE concentrations are in good agreement with the compositions of coarse-grained hornblende gabbro down to F = 0.6 ($(La/Sm)_n$ = 2.09–3.21, $(Sm/Yb)_n$=2.34-2.95, $(La/Yb)_n$ = 4.88–9.47); while at F = 0.3-0.1 the modeled MREE and HREE are similar to the observed composition of leucocratic rocks, though LREE are slightly enriched ($(La/Sm)_n$ = 5.8–14.58, $(Sm/Yb)_n$=4.04–6.66, $(La/Yb)_n$ = 23.3–97.00) as a likely consequence of the strong dependence of the model on the fractionation of accessory minerals at this stage of magmatic evolution. However, the calculations indicate that fractional crystallization of the basaltic liquid that produced fine-grained hornblende gabbro explains much of the magmatic evolution of mafic and leucocratic rocks from the TUMC.

7.6.4 Tectonic implications

Ultramafic cumulate- and mafic- rocks can form in different tectonic settings (e.g., Loucks, 1990; Himmelberg and Loney, 1995; Ao et al., 2010; Eyuboglu et al., 2010; Meng et al., 2015; Chang et al., 2018; Xu et al., 2019). Mineral composition, whole-rock major and trace elements and isotopic data provide a reliable base of information to decipher the tectonic setting of the lithologies of the TUMC. Considering the REE, all groups of the TUMC are enriched in LREE with respect to HREE (Figure 7.10), a feature which is common in rocks formed in subduction settings (e.g. Pearce, 1996). The trace elements normalized to PM are enriched in the most incompatible elements, with positive anomalies in Pb, Sr, and Ba and depletions in Nb, Zr, Ti, and P (Figure 7.10), which indicate magmas of arc-related origin (Hawkesworth et al., 1993; Pearce and Peate, 1995; Wallace, 2005; Pearce and Stern, 2006). This arc affinity is also supported by the low $\varepsilon Nd_{(t)}$ and $\varepsilon Sr_{(t)}$ values (Figure 7.12 and Table 7.15) and the arc-cumulate trend showed by clinopyroxene composition (Figure 7.4e). On the K_2O vs SiO_2 diagram hornblende gabbro and leucocratic rocks show a calc-alkaline signature (Figure 7.16a; Peccerillo and Taylor, 1976), while in the AFM diagram (Figure 7.16b), the lack of FeO enrichment during differentiation, which is a fundamental feature of the tholeiitic magmatic suite (e.g. Irvine and Baragar, 1971; Zimmer et al., 2010), is not appreciated while, in contrast, a relatively constant iron-magnesium ratio that define a trend indicative of the calc-alkaline series is observed.

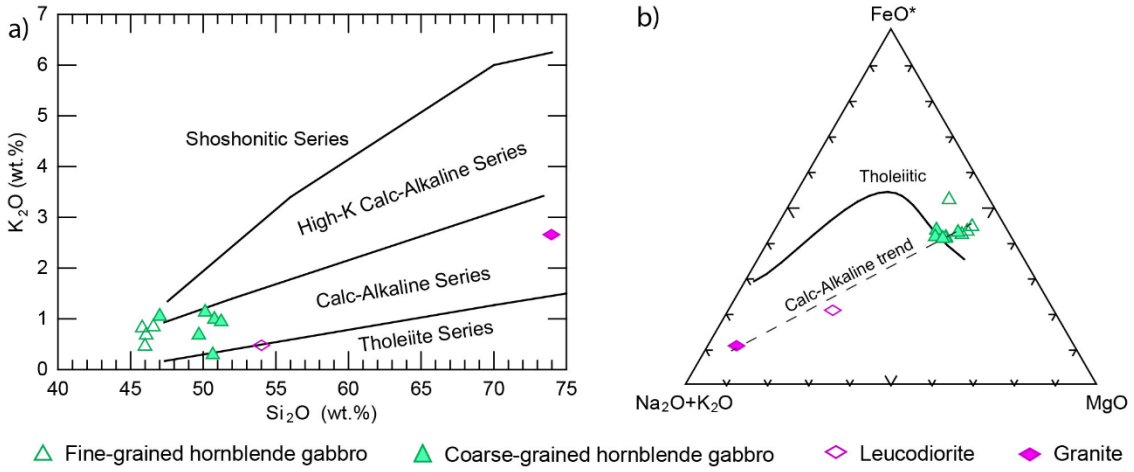

Figure 7.16. a) K_2O (wt%) vs. SiO_2 (wt%) diagram (Peccerillo and Taylor, 1976). b) AFM diagram showing the calc-alkaline trend of the TUMC (Irvine and Baragar, 1971).

The TUMC has been previously considered a Ural-Alaskan-type intrusion (Pozo, 1990; Litherland et al., 1994). The orthopyroxene-free mineral association and the composition of chromium spinel, olivine and clinopyroxene from TUMC do indeed agree with the characteristics of these complexes (Figure 7.4a-c, e-f; Himmelberg and Loney, 1995; Krause et al., 2007; Thakurta et al., 2008). Furthermore, the crystallization conditions estimated in this work fit the conditions of Alaskan-type complexes, in particular the highly hydrous nature of basaltic liquids, the shallow crustal depth of intrusion in the range of 6 to 18 km, the oxygen fugacity above the NNO buffer and below the HM buffer and crystallization temperatures from above 1025 °C to about 815 °C (Himmelberg and Loney, 1995). However, the internal structure, the calc-alkaline affinity and the lack of widespread dunite/wehrlite prevent classifying TUMC as a typical Alaskan-type complex even if it effectively likely corresponds to a storage reservoir of subduction zone-related volcanoes.

The TUMC, with a tight crystallization age of 75.1 - 76.0 Ma, intrudes the regional country-rock of the arc-related Alao-Paute Unit. The scarce inherited zircons found in TUMC rocks record recycling of the Cordillera Real basement, with the youngest inherited zircon ($^{206}Pb/^{238}U$ age of 116.2±1.3 Ma) recording the age of the country rock, as indicated by the K/Ar hornblende age of 115 ± 12 Ma of the Alao-Paute Unit (Litherland et al., 1994; also concordant with ages of the arc-related Quebradagrande complex in Colombia; Villagomez et al., 2011; Cochrane et al., 2014b; Zapata et al., 2019). The age of the TUMC, on the other hand, is consistent with other plutons along similar longitudinal position in the Cordillera Real of Ecuador and the Cordillera Central of Colombia, as for example the Pimanpiro (78 Ma) and Magtayán (75-80 Ma) plutons in Ecuador (Litherland et al., 1994,

Cochrane, 2013) and the Antioquia batholith in Colombia (95–75 Ma; Villagómez et al., 2011), as well as, with the Upper Cretaceous records of detrital zircons from sedimentary rocks of the Amazon basin (e.g., Vallejo et al., 2017; Gutierrez et al., 2019). Hence, the evidence provided by the TUMC for syn-subduction calc-alkaline igneous activity confirms the Late Cretaceous subduction-related magmatism in the Cordillera Real (Figure 7.17), and constitutes strong evidence for an east-dipping subduction in the western margin of northern South America until at least, 75 Ma (Figure 7.17), prior to the accretion of the Ecuadorian-Colombian-Caribbean oceanic plateau. This plateau complex contains associated Cretaceous oceanic volcanic arc rocks related to a coeval west-dipping subduction zone (e.g. Reynaud et al., 1999; Kerr et al., 2003; Vallejo et al., 2009). Our data hence support the existence of divergent double subduction zones, with simultaneous magmatic activity related to west-dipping (oceanic arc) and east-dipping (continental arc, Cordillera Real) subduction (Figure 7.17).

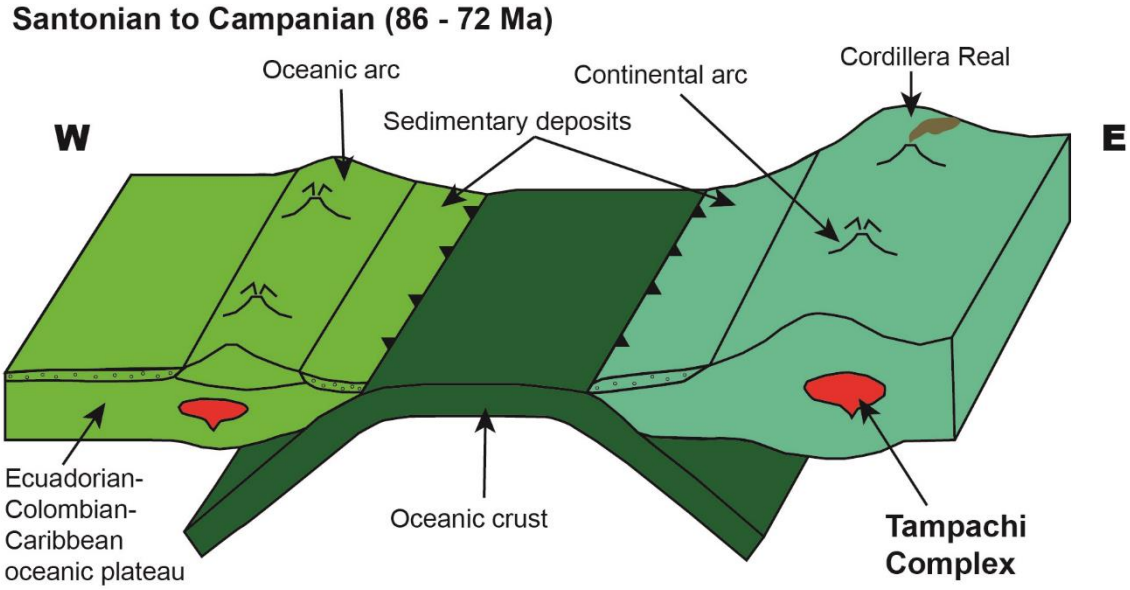

Figure 7.17. Schematic tectonic model for the eastern margin of South America during Santonian to Campanian times with simultaneous westward and eastward subduction and the corresponding magmatic-arcs (cf. Vallejo et al., 2019 and Cardona et al., 2020).

7.7 Conclusions

The Tampanchi ultramafic-mafic complex (Cordillera Real, Ecuador) is an oval-shaped intrusive body (6 km x 3 km) hosted in a Cretaceous metavolcanic and metavolcano-sedimentary sequence. It is constituted by cumulate wehrlite and olivine-hornblende clinopyroxenite, hornblendite product of reaction between hydrous basic liquid and

cumulate rocks, and hornblende gabbro, leucodiorite and granite as products of magmatic evolution. Whole rock major elements composition shows two trends of differentiation. The first stage generated the cumulate ultramafic lithologies such as wehrlite and olivine-hornblende clinopyroxenite with clinopyroxene and olivine as the dominant fractionated mineral phases. At this stage, the magmatic chamber which suffered compaction and melt extraction, while a subsequent second magmatic stage involved injection of primitive basaltic liquid that evolved upon fractional crystallizatiuon from primitive fine-grained hornblende gabbro through coarse grained and pegmatitic gabbro to intermediate-acid compositions (reaching granite) and with amphibole as the dominant phase of magmatic crystallization/fractionation. The second magmatic phase triggered a reaction-replacement process that formed amphibole after reacting clinopyroxene and olivine, producing hornblendites in the contact of hornblende gabbros with olivine clinopyroxenites, amphibole in the olivine clinopyroxenite and local lithological zonation. Estimations based on the chemical composition of rocks and minerals suggest hydrated basaltic parental magma produced from a uniform mantle source influenced by slab-derived fluids, which was emplaced at intermediate to shallow crustal levels (~3.6 kbar) with an oxygen fugacity above the NNO buffer indicating oxidized magmas. The mineral composition and whole-rock geochemistry point to calc-alkaline arc-related magmatism. Zircon SHRIMP U-Th-Pb dating constrains the crystallization of the TUMC to a tight time range between 75.1 ± 0.2 - 76.0 ± 0.4 Ma. These results confirm the existence of magmatic arc activity in the active margin of northern South America during the latest Cretaceous prior to the accretion of the Ecuadorian-Colombian-Caribbean oceanic plateau and support the existence of divergent double subduction zones with simultaneous magmatic activity related to west-dipping (oceanic arc) and east-dipping (continental arc, Cordillera Real) subduction.

Capítulo 8
Discusión general y conclusiones

8 Discusión general y conclusiones

El objetivo principal de esta tesis doctoral es la caracterización geoquímica, estructural y petrológica de dos complejos ultramáficos-máficos de la Cordillera Real (Ecuador), llamados Peltetec y Tampanchi, y sus implicaciones para la evolución geodinámica de los Andes del Norte. Estos complejos están localizados en el límite occidental e intruyendo a rocas relacionadas con el arco Alao respectivamente. Su estudio permite dilucidar la evolución tectónica del margen occidental de Gondwana/Sudamérica durante el Mesozoico. Este margen corresponde a los Andes del Norte y muestra una larga historia de subducción de litósfera oceánica Pacífica debajo de litosfera continental del occidente de Gondwana/Sudamérica. El sistema de subducción en el margen occidental ecuatoriano ha permanecido activo al menos desde el Triásico tardío hasta la actualidad, con períodos extensionales y compresivos y con la acreción/colisión de bloques/terrenos, dando lugar a productos magmáticos de variada edad, afinidad geoquímica y entorno tectónico. La discusión se realiza para cada uno de estos complejos por separado.

8.1 Complejo ofiolítico Peltetec

El cinturón ofiolítico Peltetec o Unidad Peltetec se localiza en la Cordillera Real de Ecuador a lo largo de la Zona de falla Peltetec, cuya expresión morfológica tiene una dirección NNE-SSW y es básicamente coincidente con el límite occidental de la Cordillera Real. Esta zona de falla se caracteriza por importante cizallamiento, deformación y mezcla de bloques. El cinturón ofiolítico de Peltetec corresponde a una zona estrecha y alargada menor a 2 km de ancho, con afloramientos discontinuos desde el sector de Río Zula en el Sur hasta el sector de Ambuquí en el Norte. Las zonas mejor expuestas corresponden a los sectores de Penipe, Quimiag, y los valles de los ríos Alao y Guarguallá (Figura 5.1). Estos afloramientos corresponden a escamas tectónicas de diferentes litologías con variable grado de deformación y metamorfismo, como son serpentinitas, metagabros, metabasaltos y metasedimentos. El límite oeste está marcado por la secuencia metasedimentaria Guamote de edad Jurásico tardío-Cretácico, a la cual localmente también se la identifica en el borde oriental y sobreyaciendo a la Unidad Peltetec, mientras que la Unidad Maguazo de edad Jurásico tardío-Cretácico constituye en gran parte el límite oriental. Desde el valle de Guaraguallá hacia el sur, en el borde occidental de la Unidad Peltetec afloran granitos de la Unidad Tres Lagunas de edad Triásica, incluidos en la zona de cizalla.

Las litologías dominantes son metabasaltos principalmente de grano fino, foliados y no foliados, constituidos por clinozoisita-epidota, clorita, actinolita, albita, titanita y localmente moscovita. Algunas variedades muestran textura porfirítica relicta (porfiroclastos de

piroxeno y plagioclasa alterada) y alteración variable con abundante clorita. Incluye diques y variedades brechificadas con similares características petrográficas. Estas rocas presentan un metamorfismo y alteración inicial de fondo oceánico evidenciado por la movilidad de los elementos LILE y metales de transición como Cu y Zn (análisis de isoconas, ver Capítulo 5), y por valores relativamente altos de la relación isotópica $(^{87}Sr/^{86}Sr)_i$ que revela un desacople en los sistemas isotópicos del Sr y Nd (Figura 5.11). Se identificaron tres grupos geoquímicos de rocas metabasálticas, todos con afinidad toleítica. Un grupo es distintivo por su bajo contenido de TiO_2 y Cr y enriquecimiento en LREE y Th, así como por una composición isotópica enriquecida ($\varepsilon Nd_{(t)}$= +1.75), indicativos de afinidad de arco. Los otros dos grupos, por el contrario, muestran un contenido moderado a alto de TiO_2 y bajo de Cr, además de empobrecimiento de LREE respecto al condrito, y patrones planos en torno a 1 al ser normalizados al NMORB, mientras que la composición isotópica muestra valores altos de $\varepsilon Nd_{(t)}$ (+6.61-+8.56 y +9.22-+10.48), todo ello consistente con un origen a partir de fusión de un reservorio de manto empobrecido (Figuras 5.6, 5.7, 5.11, 5.12). Todas las rocas presentan una variable influencia de fluidos de la zona de subducción y/o contaminación cortical, evidenciado por el enriquecimiento en Th y la anomalía negativa de Nb respecto al NMORB (Figura 5.7). Además, la composición de relictos de augita indica una afinidad tipo MORB (Figura 6.16), congruente con los datos de roca total. Todos estos datos confirman que las rocas basálticas de los grupos 2 y 3 corresponden a productos de tipo NMORB formados en una cuenca de tras-arco.

La datación radiométrica U-Pb en circones (magmáticos) de una diabasa (grupo 2 y afinidad NMORB) brindó una edad de 228 Ma (Triásico), permitiendo redefinir la edad de la unidad, que anteriormente era considerada Cretácica inferior en base a dataciones $^{40}Ar/^{39}Ar$ en plagioclasa (ca. 135 Ma, Spikings et al., 2015). Esta plagioclasa es supuestamente de composición albítica, por lo que la edad Ar-Ar debe reflejar procesos posteriores (ver más adelante).

Las serpentinitas son el único tipo de rocas ultramáficas identificadas en la unidad ofiolítica Peltetec, aunque trabajos previos han reportado también piroxenitas y hornblenditas (p.e. Litherland et al., 1994). Las serpentinitas estudiadas están constituidas principalmente por serpentina y clorita, con relictos mantélicos de espinela crómica que presentan una composición química indicativa de peridotitas de suprasubducción para los protolitos, concordante con las características observadas en las rocas basálticas.

Los metagabros corresponden a rocas cumulíticas y no cumulíticas (las últimas incluidas en los grupos 1, 2 y 3). Las rocas cumulíticas están constituidas principalmente por relictos

de augita y plagioclasa (alterada), con presencia local de pseudomorfos de olivino, y recristalización metamórfica de actinolita y clorita. Puntualmente presentan deformación dúctil. Estas rocas se caracterizan por un alto contenido de Cr y bajo de TiO_2 (wt%). Los patrones de elementos trazas inmóviles y tierras raras son empobrecidos con respecto al NMORB, pero enriquecidos en Th y con ligera anomalía negativa de Nb y Zr (Figura 5.7). Esto, así como composiciones isotópicas enriquecidas ($\varepsilon Nd_{(t)}$ de +0.07 y +1.65; Figura 5.11), se relaciona con la influencia de fluidos emanados de la zona de subducción en la fuente mantélica de los magmas. Las composiciones de la augita muestran una variación entre composiciones típicas de MORB y de arco, confirmando el ambiente de suprasubducción para su origen. Bloques con litologías con características similares a estos metagabros han sido recientemente datados en la zona de falla Peltetec como Neoproterozoico (566 – 586 Ma, $^{40}Ar/^{39}Ar$ en plagioclasa; Spikings et al., 2020). Sin embargo, la precisión de esta edad no es buena y los minerales datados están probablemente alterados, generando incertidumbre sobre su fiabilidad, por lo que es necesario datar los protolitos con métodos menos sensibles a la alteración y metamorfismo (p.e. U-Pb en circones) para confimar si estos bloques de gabros corresponden a la unidad Peltetec (Triásico tardío) o a bloques oceánicos Neoproterozoicos incorporados por la actividad de la zona de falla Peltetec.

Los granitos identificados al oeste y en la zona de falla Peltetec tienen una textura fanerítica ocasionalmente milonitizada. Están constituidos por cuarzo, feldespato potásico, plagioclasa, biotita, moscovita y trazas de monacita, rutilo, circón y apatito. Tienen afinidad peraluminosa, tipo-S, con una edad U-Pb en circones de 228 Ma, por lo que se asocian a la Unidad Tres Lagunas reportada por otros estudios hacia el este de la Unidad Alao-Paute. La Unidad Tres Lagunas es el resultado de anatexis de la corteza continental asociada al mismo evento extensional que abrió la cuenca tras-arco y originó la ofiolita (p.e. Litherland et al., 1994; Cochrane et al., 2014a; Spikings et al., 2015; Villares et al., 2020).

Las características geoquímicas de las rocas metabasálticas de la Unidad Peltetec indican un ambiente de suprasubducción de retro-arco a 228 Ma, con una fuente astenosférica del manto superior empobrecida para los grupos 2 y 3 y una fuente del manto más enriquecida para el grupo 1. Estas características son interpretadas como un cambio progresivo de un ambiente de arco (grupo 1) a NMORB (grupos 2 y 3), soportado además por la distribución de los HFSEs (p.e. Ti, Y, Yb), V y $\varepsilon Nd_{(t)}$, los cuales muestran un incremento progresivo del grupo 1 al grupo 2 y finalmente al grupo 3 mientras la relación $(Th/Nb)_{NMORB}$ disminuye. Esto es el resultado de una disminución progresiva de la influencia de la zona de

subducción y/o contaminación de componentes derivados de la corteza continental mientras se desarrolla la cuenca de retroarco por “rifting” y “drifting”.

Otros Complejos/Unidades máficos–ultramáficos con características geoquímicas similares a Peltetec y de edad Triásico tardío han sido reportados en los Andes del Norte, como son las Unidades Piedras y Monte Olivo en Ecuador y el Complejo Aburrá en Colombia (Noble et al., 1997; Correa-Martínez, 2007; Restrepo, 2008; Cochrane et al., 2014a; Spikings et al., 2015; Ibáñez-Mejía et al., 2020). Estas correlaciones indican un proceso regional extensional y de formación de corteza oceánica en el tras-arco de los Andes del Norte durante el Triásico tardío y, aunque no datada en el complejo Peltetec dada la aparente ausencia de una suela metamórfica, una obducción subsiguiente durante el Triásico tardío.

Asociado con el desarrollo de la cuenca de retro-arco e inmediatamente posterior a la extrusión de productos basálticos (228 Ma), se identifica un evento inicial de metamorfismo de fondo oceánico (M_0; alta temperatura y baja presión). Se caracteriza por la presencia de núcleos relictos de pargasita, magnesio-hornblenda y magnesio-ferri-hornblenda y localmente andesina y oligoclasa, si bien en determinadas zonas se caracteriza por alteración a clorita, albita y venas de calcita. No se identifica deformación asociada con este evento. Este metamorfismo es un proceso focalizado en zonas donde el agua marina penetra por sistemas de fracturas e interacciona con rocas relativamente calientes generando paragénesis secuencialmente retrógradas durante el enfriamiento de la litosfera oceánica recién creada.

A este evento se le superpone un metamorfismo (M_1) de facies de esquisto verde con la asociación de Act-Ab-Ep-Ttn-Chl±Ms. Las condiciones de P-T estimadas para este M_1 son de ~315°C y ~15 km de profundidad, que corresponde a un gradiente T/P intermedio (barroviano). Las características texturales y estructurales sugieren una recristalización syn-tectónica, con el alineamiento de los minerales siguiendo planos de esquistosidad (S_{1P}), los cuales presentan micro deformación entre planos de cizallamiento generando un pseudo clivaje de crenulación (S_{CP}). También se identifica zonas milonitizadas con minerales rotados y una matriz fina foliada o anastomosada formada por plagioclasa alterada. Todo esto indicativo de un régimen dinámico compresivo durante el metamorfismo.

En este trabajo no se ha podido datar el metamorfismo. No obstante, Spikings et al. (2015) presentaron dos edades $^{40}Ar/^{39}Ar$ en plagioclasas de 134.7 ± 0.9 y 134 ± 13 Ma en rocas metabasálticas de la Unidad Peltetec que podrían ser asociadas con la edad del evento

metamórfico M_1. Sin embargo, los datos presentados en este estudio evidencian un evento metamórfico compresivo, mientras que el régimen tectónico en los Andes del Norte durante el Jurásico – Cretácico temprano fue extensional, caracterizado por la apertura de cuencas marginales y sedimentación marina (Spikings et al., 2015; Zapata et al., 2018, Cardona et al., 2020). Esto hace difícil relacionar la edad Ar-Ar con el segundo evento metamórfico (M_1) de la Unidad de Peltetec. El evento (M_1) por lo tanto es atribuido al cierre de la cuenca de retro-arco y emplazamiento de la Unidad Peltetec, debido al cambio de régimen tectónico de extensivo a compresivo en el Triásico tardío. Este cambio en el régimen tectónico ha sido sugerido también en el Complejo Metamórfico El Oro (Sur de Ecuador) relacionado con la acreción tectónica de la losa oceánica (esquistos azules de la Unidad Arenillas-Panupalí) debajo de la unidad gabróica Piedras (anfibolitas) (226 Ma, Riel et al., 2014), y en el Norte en Colombia en la Ofiolita de Aburrá, con formación de una suela metamórfica y subsecuente obducción en la corteza continental (ca. 221 Ma; Ibañez-Mejia et al. in 2020). La edad $^{40}Ar/^{39}Ar$ en plagioclasas Cretácico temprano de rocas metabasálticas de la Unidad Peltetec puede por tanto corresponder al calentamiento regional reportado en este período, asociado con hundimiento de cuencas y aumento de flujo de calor durante un régimen extensivo (Paul et al., 2018). Con posterioridad al emplazamiento sobre el margen continental, los bloques tectónicos de la Unidad Peltetec han sufrido deformación cataclástica – milonítica asociada con el movimiento y actividad de la zona de falla Peltetec.

8.2 Complejo ultramáfico-máfico Tampanchi (TUMC)

El Complejo ultramáfico-máfico Tampanchi (TUMC, por sus siglas en inglés) corresponde a una intrusión localizada en la parte central de la Cordillera Real. El complejo no esta metamorfizado y presenta solo localmente deformación dúctil asociada a zonas de cizallamiento. En cambio, su encajante, la Unidad Alao-Paute está formada principalmente por esquistos verdes en la zona de estudio, sugiriendo que su metamorfismo es previo a la intrusión de TUMC. Más aún, las rocas adyacentes al cuerpo intrusivo son corneanas que desarrollan metamorfismo de contacto hasta, al menos, la facies de anfibolita.

El TUMC está constituido por varias litologías, cuyas relaciones de corte permiten establecer la siguiente cronología relativa: 1. wehrlita y clinopiroxenita (piroxenita, piroxenita con olivino y hornblenda, piroxenita olivínica, piroxenita hornbléndica), 2. gabros hornbléndicos y hornblendita y 3. leucodiorita y granito. El cuerpo no presenta una zonación litológica concéntrica; en cambio, se observa una compleja relación de corte entre las litologías que no obstante permiten definir el orden de cristalización. Los gabros hornbléndicos cortan a wehrlitas y piroxenitas, dando origen a hornblenditas en su contacto

debido a un proceso de reacción-reemplazamiento de olivino y clinopiroxeno por anfíbol, generando una zonación local, e indicativo de varios pulsos magmáticos.

Las características petrográficas, estructurales y geoquímicas permiten definir al menos dos patrones de diferenciación. El primero está conformado por wehrlitas y piroxenitas que definen un patrón de acumulación con fraccionamiento dominante de olivino, piroxeno y trazas de espinela crómica. El olivino se caracteriza por un contenido de forsterita (Fo) en la wehrlita de 87 a 91 % y en la piroxenita de 75 a 88 %, mientras que el piroxeno corresponde a diópsido (Mg# = 0.84-0.97). No se identificó la presencia ortopiroxeno en ninguna litología del complejo. Un segundo patrón de diferenciación está definido por gabros hornbléndicos variados, incluyendo variedades pegmatoides, donde el anfíbol es la fase dominante cristalizada. De ellos se diferencian magmas félsicos (líquido residual). Los anfíboles identificados son pargasita, magnesio-hastingsita, magnesio-ferri-hornblenda y magnesio-hornblenda. La plagioclasa es dominantemente bytownita, con zonación normal hasta andesina y oligoclasa. En los granitos se identifica además feldespato alcalino, biotita, moscovita y cuarzo.

Las estimaciones de las condiciones físico-químicas de los magmas basadas en la composición química mineral indican un magma parental basáltico hidratado, emplazado a niveles corticales intermedios a superficiales (~12.5 km) y con una fugacidad de oxígeno algo superior al tampón NNO que indica cristalización a partir de un magma oxidado (Figura 7.14).

La composición isotópica de todas las litologías es similar, con un $\varepsilon Nd_{(t)}$ entre -1.28 a 0.49 y $(^{87}Sr/^{86}Sr)_i$ entre 0.703523 a 0.704481, indicando una fuente mantélica uniforme (Figura 7.12).

La composición química de tierras raras normalizadas con respecto al condrito muestra patrones enriquecidos en LREE y empobrecidos en HREE (Figura 7.10). Los elementos en traza normalizados con respecto al manto primitivo muestran que todas las litologías tienen patrones enriquecidos en LILE, con anomalías negativas de HFSE y P y con anomalías positivas de Pb, Sr y Ba, lo que evidencia un ambiente de suprasubducción para la generación de los líquidos basálticos (Figura 7.10). Más aún, la composición química de elementos mayores de olivino, espinela crómica y diópsido también indica un ambiente de arco (Figura 7.4), y los análisis de elementos mayores y en trazas de roca total muestran una tendencia de diferenciación de afinidad calco-alcalina.

El TUMC fue considerado previamente como una intrusión de tipo Urales-Alaska (Pozo, 1990; Litherland et al., 1994). Las condiciones físico-químicas estimadas para los magmas,

así como la composición química del olivino, espinela crómica y diópsido, y una asociación mineral sin ortopiroxeno concuerdan con este tipo de intrusiones. Sin embargo, su estructura interna, la afinidad calco-alcalina y la escasa presencia de dunita/wehrlite, abundantes en los complejos alaskianos, no permiten clasificarlo como un típico complejo tipo Alaska. No obstante, se considera que el complejo corresponde a un reservorio magmático del volcanismo asociado a una zona de subducción bajo el margen continental de Sudamérica.

Edades U-Th-Pb en circones en la piroxenina, gabro hornbléndico, leucodiorita y granito, brindaron resultados similares (75.8 ± 0.7 Ma, 76.0 ± 0.4 Ma, 75.5 ± 0.3 Ma y 75.1 ± 0.2 Ma, respectivamente), indicando un origen común. En la Cordillera Real (Ecuador) y Central (Colombia), en equivalente posición estructural que el TUMC, se han identificado otras intrusiones de edad similar, como por ejemplo las intrusiones de Pimanpiro (78 Ma), Magtayán (75-80 Ma) (Litherland et al., 1994, Cochrane, 2013) y el batolito Antioqueño (95–75 Ma; e.g. Villagómez et al., 2011). Ello confirma un magmatismo activo en el Cretácico tardío en los Andes del Norte relacionado a una zona de subducción inclinada hacia el Este, previo a la acreción del plateau oceánico Ecuatoriano-Colombiano-Caribeño y su arco volcánico asociado, que habría sido formado por una subducción hacia el Oeste contemporánea con la del Este.

Capítulo 9
Referencias

9 Referencias

Allmendinger, R.W., Cardozo, N., and Fisher, D., 2012, Structural geology algorithms: Vectors and tensors in structural geology: Cambridge University Press, 302 p..

Anonymous, 1972, Penrose Field Conference on ophiolites: Geotimes, 17(12), p. 24–25.

Ao, S.J., Xiao, W.J., Han, C.M., Mao, Q.G., and Zhang, J.E., 2010, Geochronology and geochemistry of Early Permian mafic–ultramafic complexes in the Beishan area, Xinjiang, NW China: Implications for late Paleozoic tectonic evolution of the southern Altaids. Gondwana Research 18 (2–3), p. 466-478.

Arai, S., 1992, Chemistry of chromian spinel in volcanic rocks as a potential guide to magma chemistry: Mineralogical Magazine, 56, p. 173–184. doi.org/10.1180/minmag.1992.056.383.04

Arai, S., Uesugi, J., and Ahmed, A.H., 2004, Upper crustal podiform chromitite from the northern Oman ophiolite as the stratigraphically shallowest chromitite in ophiolite and its implication for Cr concentration: Contributions to Mineralogy and Petrology, 147, p. 145–154.

Armbruster, T., Bonazzi, P., Akasaka, M., Bermanec, V., Chopin, C., Gieré, R., Heuss-Assbichler, S., Liebscher, A., Menchetti, S., Pan, Y., and Pasero, M., 2006, Recommended nomenclature of epidote-group minerals: European Journal of Mineralogy, 18, p. 551-567, 10.1127/0935-1221/2006/0018-0551.

Arevalo, R., and McDonough, W., 2010, Chemical variations and regional diversity observed in MORB: Chemical Geology, v. 271, p. 70 – 85.

Aspden, J., Bonilla, W., and Duque, P., 1995, The El Oro Metamorphic Complex, Ecuador: Geology and Economic Mineral Deposits: Overseas Geology and Mineral Resources, British Geological Survey, Keyworth, Nottingham, England, v. 67, 63 p.

Aspden, J., Fortey, N., Litherland, M., Viteri, F., and Harrison, M., 1992, Regional S-type granites in the Ecuadorian Andes: Possible remnants of the breakup of western Gondwana: Journal of South American Earth Sciences, v. 6, no. 3, p. 123-132. doi.org/10.1016/0895-9811(92)90002-G

Aspden, J., and Litherland, M., 1992, The geology and Mesozoic collisional history of the Cordillera Real, Ecuador: Tectonophysics, v. 205, p. 187 - 204.

Barnes, S.J. and Roeder, P.L., 2001, The range of spinel compositions in terrestrial mafic and ultramafic rocks: Journal of Petrology, 42 , p. 2279-2302.

Bea, F., Bortnikov, N., Montero, P., Zinger, T., Sharkov, E., Silantyev, S., Skolotnev, S., Trukhalev, A., and Molina-Palma, J., 2020, Zircon xenocryst evidence for crustal recycling at the Mid-Atlantic Ridge: Lithos, v. 354–355, 105361. doi.org/10.1016/j.lithos.2019.105361

Beccaluva, L., Ohnenstetter, D., and Ohnenstetter, M., 1979, Geochemical discrimination between ocean floor and island arc tholeiites - Application to some ophiolites: Canadian Journal of Earth Sciences, 16, p. 1874-1882.

Black, L., Kamo, S., Allen, C., Aleinikoff, J., Davis, D., Korsch, J., and Foudolis, C., 2003, TEMORA 1: a new zircon standard for Phanerozoic U–Pb geochronology: Chemical Geology, v. 200, p. 155–170.

Blanco–Quintero, I.F., García–Casco, A., Toro, L.M., Moreno, M., Ruiz, E.C., Vinasco, C.J., Cardona, A., Lázaro, C., and Morata, D., 2014, Late Jurassic terrane collision in the northwestern margin of Gondwana (Cajamarca Complex, eastern fank of the Central Cordillera, Colombia): International Geology Review, 56(15), p. 1852–1872. doi.org/10.1080/00206814.2014.963710

Bonavia, F.F., Diella, V., and Ferrario, A., 1993, Precambrian podiform chromitites from Kenticha Hill, southern Ethiopia: Economic Geology, 88, p. 198–202.

Bosch, D., Gabriele, P., Lapierre, H., Malfere, J.L., and Jaillard, E., 2002, Geodynamic significance of the Raspas Metamorphic Complex (SW Ecuador): geochemical and isotopic constraints: Tectonophysics, v. 345, p. 83–102.

Bourgois, J., Toussaint, J.-F., Gonzales, H., Azema, J., Calle, B., Desmet, A., Murcia, L.A., Acevedo, A.P., Parra, E., Tournon, J., 1987, Geological history of the Cretaceous ophiolitic complexes of Northwestern South America (Colombian Andes): Tectonophysics 143, p. 307-327.

Bouvier, A., Vervoort, J., and Patchett, P., 2008, The Lu–Hf and Sm–Nd isotopic composition of CHUR: constraints from unequilibrated chondrites and implications for the bulk composition of terrestrial planets: Earth and Planetary Science Letters, v. 273, no. 1–2, p. 48-57. doi.org/10.1016/j.epsl.2008.06.010

Bristow, C.R., Longo, R. y Guevara, S., 1975, Mapa geológico del área de Cañar: Dirección General de Geología y Minas, Quito.

Bustamante, C., Archanjo, C.J., Cardona, A., Bustamante, A., and Valencia, V.A., 2017, U-Pb ages and Hf isotopes in zircons from parautochthonous Mesozoic terranes in the

western margin of Pangea: Implications for the terrane configurations in the northern Andes: The Journal of Geology, 125(5), p. 487–500. doi.org/10.1086/693014

Bustamante, C., Archanjo, C.J., Cardona, A., and Vervoort, J.D., 2016, Late Jurassic to Early Cretaceous plutonism in the Colombian Andes: A record of long-term arc maturity: Geological Society of America, Bulletin 128, p. 1762-1779.

Bustamante, C., Cardona, A., Bayona, G., Mora, A., Valencia, V., Gehrels, G., and Vervoort, J., 2010, U–Pb LA–ICP–MS geochronology and regional correlation of Middle Jurassic in trusive rocks from the Garzón Massif, Upper Magdalena Valley and Central Cordillera, southern Colombia: Boletín de Geología, 32(2), p. 93–109.

Bustamante, A., Juliani, C., Essene, E.J., Hall, C., and Hyppolito, T., 2012, Geochemical con straints on blueschist-facies rocks of the Central Cordillera of Colombia: the Andean Barragán region: International Geology Review, v. 54, p. 1013–1030.

Cabanis, B., and Lécolle, M., 1989, Le diagramme La/10, Y/15, Nb/8: un outil pour la discrimination des séries volcaniques et la mise en évidencedes processus de mélange et/ou contamination crustale: Comptes Rendus de l'Academie des Sciences Series II, v. 309, p. 2023-2029.

Cann, J., R., 1969, Spilites from the Carlsberg Ridge, Indian Ocean: Journal of Petrology, 10, p. 1-19.

Cardona, A., León, S., Jaramillo, J.S., Valencia, V., Zapata, S., Pardo–Trujillo, A., Schmitt, A.K., Mejía, D., and Arenas, J.C., 2020, Cretaceous record from a Mariana to an Andean–type margin in the Central Cordillera of the Colombian Andes. In: Gómez, J. & Pinilla–Pachon, A.O. (editors), The Geology of Colombia, v. 2 Mesozoic: Servicio Geológico Colombiano, Bogotá, Publicaciones Geológicas Especiales 36, p. 353–395. doi.org/10.32685/pub.esp.36.2019.10

Cardona, A., Valencia, V., Garzón, A., Montes, C., Ojeda, G., Ruiz, J., and Weber, M., 2010, Permian to Triassic I to S-type magmatic switch in the northeast Sierra Nevada de Santa Marta and adjacent regions, Colombian Caribbean: tectonic setting and implications within Pangea paleogeography: Journal of South American Earth Sciences, v. 29, p. 772–783.

Cardozo, N., and Allmendinger, R.W., 2013, Spherical projections with OSXStereonet: Computers & Geosciences, Volume 51, p. 193-205, doi.org/10.1016/j.cageo.2012.07.021.

Chang, J., and Audétat, A., 2018, Petrogenesis and Metal Content of Hornblende-Rich Xenoliths from Two Laramide-age Magma Systems in Southwestern USA: Insights into the Metal Budget of Arc Magmas: Journal of Petrology, 2018, Vol. 59, No. 10, p. 1869–1898, doi: 10.1093/petrology/egy083.

Chappell, B.W., and White, A.J.R., 2001, Two contrasting granite types: 25 years later: Australian Journal of Earth Sciences, v. 48, no. 4, p. 489–499.

Chew, D., Schaltegger, U., Košler, J., Whitehouse, M., Gutjahr, M., Spikings, R., and Miškovíc, A., 2007, U–Pb geochronologic evidence for the evolution of the Gondwanan margin of the north-central Andes: Geological Society of America Bulletin, v. 119, p. 697–711.

Chiaradia, M., Vallance, J., Fontboté, L., Stein, H., Schaltegger, U., Coder, J., Richards, J., Villeneuve, M., and Gendall, I., 2009, U-Pb, Re-Os and Ar/Ar geochronology of the Nambija Au-skarn and Pangui porphyry Cu deposits, Ecuador: implications for the Jurassic metallogenic belt of the northern Andes: Mineralium Deposita, v. 44, p. 371–387.

Chicangana, G., 2005, The Romeral Fault System: a shear and deformed extinct subduction zone between oceanic and continental lithospheres in northwestern South America: Earth Sciences Research Journal, 9(1), p. 50-64.

Class, C., Miller, D., Goldstein S., Langmuir, C., 2000, Distinguishing melt and fuid subduction components in Umnak Volcanics, Aleutian arc: Geochemistry, Geophysics, Geosystems, 1, doi.org/10.1029/1999GC000010.

Cochrane, R, 2013, U-Pb thermochronology, geochronology and geochemistry of NW South America: rift to drift transition, active margin dynamics and implications for the volume balance of continents, Thèse de doctorat: Univ. Genève, no. Sc. 4566.10.13097/archive-ouverte/unige:30029

Cochrane, R., Spikings, R., Gerdes, A., Ulianov, A., Mora, A., Villagómez, D., Putlitz, B., and Chiaradia, M., 2014a, Permo-Triassic anatexis, continental rifting and the disassembly of western Pangaea: Lithos, v. 190–191, p. 383–402.

Cochrane, R., Spikings, R., Gerdes, A., Winkler, W., Ulianov, A., Mora, A., and Chiaradia, M., 2014b, Distinguishing between in-situ and accretionary growth of continents along active margins: Lithos, v. 202–203, p. 382–395.

Connolly, J.A.D., 1990, Multivariable phase diagrams; an algorithm based on generalized thermodynamics: American Journal of Science, v. 290, p. 666–718.

Connolly, J.A.D., 2005, Computation of phase equilibria by linear programming: A tool for geodynamic modeling and its application to subduction zone decarbonation: Earth and Planetary Science Letters, v. 236, p. 524–541.

Cooper, G.F., Davidson, J.P., and Blundy, J.D., 2016, Plutonic xenoliths from Martinique, Lesser Antilles: evidence for open system processes and reactive melt flow in island arc crust: Contributions to Mineralogy and Petrology 171, 87.

Correa-Martínez, A., 2007, Petrogenesis and Evolution of Aburrá Ophiolite, Colombian Andes, Central Range. (Ph.D. thesis): University of Brasilia.

Correa-Martínez, A., Martens, U. and Rodríguez, G., 2020, Collage of tectonic slivers abutting the eastern Romeral Fault System in central Colombia: Journal of South American Earth Sciences, V. 104. doi.org/10.1016/j.jsames.2020.102794

Cox, K.G., Bell, B.G., and Pankhurst, R.J., 1979, The Interpretation of Igneous Rocks. George Allen and Unwin, London, p. 450.

Davidson, J.P., 1987, Crustal contamination versus subduction zone enrichment: examples from the Lesser Antilles and implications for the mantle source composition of island arc lavas: Geochimica et Cosmochimica Acta, 51, p. 2185 - 2198.

De Bari, S.M., and Coleman, R.G., 1986, Petrologic aspects of gabbros from the Tosnia complex, Chugach mountains, Alaska: evidence for deep magma chambers under an island arc: Geological Society of America (Abstracts and Programs), 18, 99.

DePaolo, D., 1988, Age dependence of the composition of continental crust: evidence from Nd isotopic variations in granitic rocks: Earth and Planetary Science Letters, v. 90, p. 263–271, doi:10.1016/0012- 821X(88)90130-6.

Dick, H.J.B., and Bullen, T., 1984, Chromium-spinel as a petrogenetic indicator in abyssal and alpine-type peridotites and spatially associated lavas: Contributions to Mineral Petrology 86, p. 54–76. doi.org/10.1007/BF00373711.

Diener, J.F.A., Powell, R., White, R.W., Holland, T.J.B., 2007, A new thermodynamic model for clino- and orthoamphiboles in the system Na2O-CaO-FeO-MgO-Al2O3-SiO2-H2O-O: Journal of Metamorphic Geology, 25, p. 631-56.

Dilek, Y., Furnes, H., and Shallo, M., 2008, Geochemistry of the Jurassic Mirdita ophiolite (Albania) and the MORB to SSZ evolution of a marginal basin oceanic crust: Lithos, v. 100, p. 174–209.

Dilek, Y., and Furnes, H., 2011, Ophiolite genesis and global tectonics: Geochemical and tectonic fingerprinting of ancient oceanic lithosphere: Geological Society of America Bulletin, v. 123, p. 387 – 411.

Dilek, Y., and Furnes, H., 2014, Ophiolites and their origins: Elements, v. 10, p. 93–100.

Drobe, J., Lindsay, D., Stein, H., and Gabites, J., 2013, Geology, Mineralization, and Geochronological Constraints of the Mirador Cu-Au Porphyry District, Southeast Ecuador: Economic Geology, v. 108, p. 11–35.

Eguez, A., 1986, Evolution Cenozoique de la Cordillere Occidentale septentrionale d'Equateur (0°15' S -01°10' S), les mineralisations associetees. Doc. Thesis: Université Pierre et Marie Curie, Paris, 116 pp. (unpublished).

Egüez, A., Gaona, M., and Albán, A., 2017, Mapa Geológico de la República del Ecuador: Instituto Nacional de Investigación Geológico Minero Metalúrgico, Quito – Ecuador, scale 1: 1 000 000.

Elliott, T., Plank, T., Zindler, A., White, W., and Bourdon, B., 1997, Element transport from subducted slab to volcanic front at the Mariana arc: Journal of Geophysical Research,102, p. 14,991–15,019.

Ersoy, Y., Helvaci, C., 2010, FC–AFC–FCA and mixing modeler: A Microsoft Excel spreadsheet program for modeling geochemical differentiation .of magma by crystal fractionation, crustal assimilation and mixing: Computers and Geosciences 36, p. 383–390, doi:10.1016/j.cageo.2009.06.007.

Eyuboglu, Y., Dilek, Y., Bozkurt, E., Bektas, O., Rojay, B., Sen, C., 2010, Structure and geochemistry of an Alaskan-type ultramaficemafic complex in the Eastern Pontides, NE Turkey: Gondwana Research, 18, p. 230-252.

Feininger, T., 1978, Geologic Map of Western El Oro Province: Escuela Politecnica Nacional, Quito, Ecuador, scale 1:50.000.

Feininger, T., 1980, Eclogite and related high-pressure regional metamorphic rocks from the Andes of Ecuador: Journal of Petrology, v 21, part 1, 107-140.

Fisher, G.W., 1989, Matrix analysis of metamorphic mineral assemblages and reactions: Contributions to Mineralogy and Petrology, 102,p. 69–77.

Fisher, G.W., 1993, An improved method for algebraic analysis of metamorphic mineral assemblages: American Mineralogist, 78, p. 1257–1261.

Floyd, P.A., and Winchester, J.A., 1978, Identification and discrimination of altered and metamorphosed volcanic rocks using immobile elements: Chemical Geology, v. 21, p. 291 – 306.

Fortey, N.J., 1990, Petrographic data and course notes for the Cordillera Real Project, Ecuador: British Geological Survey Technical Report WG/90/14/R, 67 pp.

Franz, G., and Liebscher, A., 2004, Physical and Chemical Properties of the Epidote Minerals: An introduction: Reviews in Mineralogy and Geochemistry, 56, p. 1–81. doi.org/10.2138/gsrmg.56.1.1

Frost, B.R., Barnes, C.G., Collins, W.J., Arculus, R.J., Ellis D.J., and Frost, C.D., 2001, A Geochemical Classification for Granitic Rocks: Journal of Petrology, 42, no. 11, p. 2033 – 2048.

Fuhrman, M.L., and Lindsley, D.H., 1988, Ternary-Feldspar Modeling and Thermometry: American Mineralogist, 73, p. 201-15.

Fujimaki, H., 1986, Partition coefficients of Hf, Zr, and REE between zircon, apatite, and liquid: Contributions to Mineral Petrology, 94, p. 42-45.

Furnes, H., and Dilek, Y., 2017, Geochemical characterization and petrogenesis of intermediate to silicic rocks in ophiolites: A global synthesis: Earth-Science Reviews, v. 166, p. 1–37.

Gabriele, P., 2002, HP terranes exhumation in an active margin setting: Geology, petrology and geochemistry of the Raspas Complex in SW Ecuador. Unpublished PhD Thesis: University of Lausanne, Switzerland.

Gale, A., Dalton, C.A., Langmuir, C.H., Su, Y. and Schilling J.G., 2013, The mean composition of ocean ridge basalts: Geochemistry, Geophysics, Geosystems, v. 14, p. 489–518, 10.1029/2012GC004334.

Garcia-Casco, A., 2007, Magmatic paragonite in trondhjemites from the Sierra del Convento mélange, Cuba: American Mineralogist, 92, p. 1232–1237.

Garcia-Casco, A., Restrepo, J.J., Correa-Martínez, A.M., Blanco-Quintero, I.F., Proenza, J.A., Weber, M., and Butjosa. L., 2020, The petrologic nature of the “Medellin Dunite” revisited. An algebraic approach and proposal of a new definition of the geological body. In Jorge Gomez Tapias (Ed.). The Geology of Colombia: Servicio Geológico Colombiano, v. 2 (Chapter 2), 33-51. doi.org/10.32685/pub.esp.36.2019.02

García-Ramírez, C.A., Ríos-Reyes, C.A., Castellanos-Alarcón, O.M., and Mantilla-Figueroa, L.C., 2017, Petrology, geochemistry and geochronology of the Arquía

Complex´ s metabasites at the Pijao-Génova sector, Central Cordillera, Colombian Andes: Boletín de Geología, v. 39, no. 1, p. 105-126.

Gilbert, M.C., 1982. Chapter 2, Experimental studies of amphibole stability; Introduction: Reviews in Mineralogy and Geochemistry, 9B (1), p. 229–231.

Govindaraju, K., 1994, Compilation of working values and sample description for 383 geostandards: Geostandards and Geoanalytical Research, v. 18, p. 1–158.

Grant, J.A., 1986, The isocon diagrama simple solution to Gresens equation for metasomatic alteration: Economic Geology, v. 81, p. 1976 – 1982.

Grant, J.A., 2005, Isocon analysis: A brief review of the method and applications: Physics and Chemistry of the Earth, v. 30, p. 997–1004

Green, E., Holland, T., and Powell, R., 2007, An order-disorder model for omphacitic pyroxenes in the system jadeite-diopside-hedenbergite-acmite, with applications to eclogitic rocks: American Mineralogist, 92, p. 1181-1189. doi.org/10.2138/am.2007.2401

Gresens, R.L., 1967, Composition–volume relationships of metasomatism: Chemical Geology, v. 2, p. 47–55.

Guerrero, E., 2020, Geocronología y geoquímica de los intrusivos de Pungalá, Amaluza, San Lucas e intrusión porfídica vía Alao, Tesis de Grado (No publicado): Escuela Politécnica Nacional, Quito, Ecuador, 90 p.

Gust, D.A., Arculus, R.J., and Kersting, A.B., 1995, Aspects of magma sources and processes in the Honshu arc, Canadian Mineralogist, 35, p. 347–365.

Gutiérrez, G., Horton, B., Vallejo, C., Jackson, L., and George, S., 2019, Chapter 9 - Provenance and geochronological insights into Late Cretaceous-Cenozoic foreland basin development in the Subandean Zone and Oriente Basin of Ecuador, in: Brian K. Horton, Andrés Folguera, Andean Tectonics. Elsevier, p. 237-268, ISBN 9780128160091, doi.org/10.1016/B978-0-12-816009-1.00011-3.

Hannigan, R.E., Basu, A.R, and Teichmann, F., 2001, Mantle reservoirgeochemistry from statistical analysis of ICP-MS trace element data of equatorial mid-Atlantic MORB glasses: Chemical Geology,175, p. 397–428.

Hawthorne, F.C., Oberti, R., Harlow, G.E., Maresch, W.V., Martin, R.F., Schumacher, J.C., and Welch, M.D., 2012, IMA report: nomenclature of the amphibole supergroup: American Mineralogist, 97, p. 2031–2048.

Hawkesworth, C.J., Gallagher, K., Hergt, J.M., and McDermott, F., 1993, Mantle and slab contributions in arc magmas: Annual Reviews in Earth and Planetary Science, 21, p. 175 – 204.

Hayes, B., Bybee, G., Mawela, M., Nex, P., and Niekerk, D., 2018, Residual melt extraction and out-of-sequence differentiation in the Bushveld Complex, South Africa: Journal of Petrology, egy101, doi.org/10.1093/petrology/egy101.

Herron, M., 1988, Geochemical classification of terrigenous sands and shales from core or log data: Journal of Sedimentary Research, v. 58, no. 5, p. 820–829. doi.org/10.1306/212F8E77-2B24-11D7-8648000102C1865D

Himmelberg, G., and Loney, R., 1995, Characteristics and petrogenesis of Alaskan-type ultramafic-mafic intrusions, Southeastern Alaska: U. S. Geological Survey Professional Paper 1564, 47.

Hochstaedter, A.G., Gill, J.B., Taylor, B., Ishizuka, O., Yuasa, M., and Morita, S., 2000, Across-arc geochemical trends in the Izu Bonin arc: Constraints on source composition and mantle melting, Journal of Geophysical Research,105, p. 495–512.

Hoernle, K., Hauff, F., and Van den Bogaard, P., 2004, 70 m.y. history (139-69 Ma) for the Caribbean large igneous province: Geology, 32, p. 697-700.

Hofmann, A., and Wilson, A.H., 2007, Silicified basalts, bedded cherts and other sea floor alteration phenomena of the 3.4 Ga Nondweni greenstone belt, South Africa. In: Van Kranendonk, M.J., Smithies, R.H., Bennett, V.C. (Eds.), Earth's Oldest Rocks. Developments in Precambrian Geology v. 15. Elsevier, Amsterdam, p. 571 – 605.

Holland, T.J.B., Powell, R., 1998, An internally consistent thermodynamic data set for phases of petrological interest: Journal of Metamorphic Geology, 16, p. 309-343.

Holland, T., and Powell R., 2011. An improved and extended internally consistent thermodynamic dataset for phases of petrological interest, involving a new equation of state for solids: Journal of Metamorphic Geology, 29, p. 333–383. 10.1111/j.1525-1314.2010.00923.x

Hughes, R.A., Pilatasig, L.F., 2002, Cretaceous and tertiary block accretion in the Cordillera Occidental of the Andes of Ecuador: Tectonophysics, 345, p. 29–48.

Humphris, S.E., and Thompson, G., 1978, Hydrothermal alteration of oceanic basalts by seawater: Geochimica et Cosmochimica Acta, 42, p. 107-125.

Ibañez–Mejia, M., 2020, The Putumayo Orogen of Amazonia: A synthesis. In: Gómez, J., & Mateus–Zabala, D., (editors), The Geology of Colombia, Volume 1 Proterozoic –

Paleozoic, Servicio Geológico Colombiano, Publicaciones Geológicas Especiales 35, p. 101–131. doi.org/10.32685/pub.esp.35.2019.06

Ibañez-Mejia, M., Restrepo, J.J., and Garcia-Casco, A., 2020, Tectonic juxtaposition of Triassic and Cretaceous meta-(ultra)mafic complexes in the Central Cordillera of Colombia (Medellin area) revealed by zircon U-Pb geochronology and Lu-Hf isotopes. In: "Geocronologia e tectônica do continente Sul Americano: a contribuição de Umberto Giuseppe Cordani". Sociedade Brasileira de Geologia. Eds: Andrea Bartorelli, Wilson Teixeira and Benjamim de Brito Neves, Solaris Edições Culturais e Multimídia Ltda. Sao Paulo, Brazil, p. 418-443.

Ibañez-Mejia, M., Tassinari, C.C.G., and Jaramillo-Mejia, J.M., 2007, U–Pb Zircon Ages of the "Antioquian Batholith": Geochronological Constraints of Late Cretaceous Magmatism in the Central Andes of Colombia: 11th Colombian Geological Congress, extended abstracts.

Irvine, T., 1974, Petrology of the Duke Island Ultramafic Complex Southeastern Alaska: Geological Society of America, v. 138, doi.org/10.1130/MEM138.

Irvine, T., and Baragar, W., 1971, A guide to the chemical classification of the common volcanic rocks: Canadian Journal of Earth Science, v. 8, p. 523 – 548.

Ishii, T., Robinson, P.T., Maekawa, H., and Fiske, R., 1992, Geochemistry of peridotites from ODP Leg 125 diapiric serpentinites: PANGAEA, doi.org/10.1594/PANGAEA.770907

Ishikawa, Y., Sawaguchi, T., Iwaya, S., and Horiuchi, M., 1976, Delineation of prospecting targets for Kuroko deposits based on modes of volcanism of underlying dacite and alteration halos: Mining Geology, v. 26, p. 105–117 (in Japanese with English abs.).

Ishizuka, O., Tani, K., Reagan, M.K., Kanayama, K., Umino, S., Harigane, Y., Sakamoto, I., Miyajima, Y., Yuasa, M., and Dunkley, D.J., 2011, The timescales of subduction initiation and subsequent evolution of an oceanic island arc: Earth and Planetary Science Letters, v. 306, p. 229–240.

Jaillard, E., Ordoñez, M., Bengtson, P., Berrones, G., Bonhomme, M., Jiménez, N., and Zambrano I., 1996, Sedimentary and tectonic evolution of the arc zone of southwestern Ecuador during Late Cretaceous and Early Tertiary times: Journal of South American Earth Science, v. 9, p. 131–140.

Jaramillo, J.S., Cardona, A., León, S., Valencia, V., and Vinasco, C., 2017, Geochemistry and geochronology from Cretaceous magmatic and sedimentary rocks at 6°35' N,

western flank of the Central cordillera (Colombian Andes): Magmatic record of arc growth and collision: Journal of South American Earth Sciences, 76, 460–481.

John, T., Scherer, E.E., Schenk, V., Herms, P., Halama, R., and Garbe-Schönberg, D., 2010, Subducted seamounts in an eclogite-facies ophiolite sequence: the Andean Raspas Complex, SW Ecuador: Contributions to Mineralogy and Petrology, v. 159, p. 265 – 284.

Kamenetsky, V.S., Crawford, A.J., and Meffre, S., 2001, Factors controlling chemistry of magmatic spinel: and empirical study of associated olivine, Cr-spinel, and melt inclusions from primitive rocks: Journal of Petrology, 42, p. 655–671.

Kelemen, P., Hanghøj, K., and. Greene, A., 2014, One view of the geochemistry of subduction-related magmatic arcs, with an emphasison primitive andesite and lower crust. The Crust, Treatise on Geochemistry, edited by Holland, H., and. Turekian, K., Elsevier-Pergamon, Oxford, U. K., p. 669–701.

Kennerley, J., 1980, Outline of the geology of Ecuador: Overseas Geology and Mineral Resources, No. 58.

Kerr, A.C., Aspden, J.A., Tarney, J., and Pilatasig, L.F., 2002, The nature and provenance of accreted oceanic blocks in western Ecuador: Geochemical and tectonic constraints: Journal of the Geological Society of London, v. 159, p. 577–594, doi: 10.1144/0016-764901-151.

Kerr, A., Tarney, J., Marriner, G., Nivia, A., Klaver, G., and Saunders, A., 1996, The geochemistry and tectonic setting of late Cretaceous Caribbean and Colombian: Journal of South American Earth Sciences, v. 9, p. 111–120.

Kerr, A.C., White, R.V., Thompson, P.M., Tarnez, J., and Saunders, A.D., 2003, No oceanic plateau–no Caribbean plate? The seminal role of an oceanic plateau in Caribbean plate evolution, in Bartolini, C., Buffl er, R.T., and Blickwede, J., eds., The Circum-Gulf of Mexico and the Caribbean: Hydrocarbon Habitats, Basin Formation, and Plate Tectonics: American Association of Petroleum Geologists (AAPG) Memoir, v. 79, p. 126–168.

Krause, J., Brügmann, G.E., Pushkarev, E.V., 2007, Accessory and rock forming minerals monitoring the evolution of zoned mafic–ultramafic complexes in the Central Ural Mountains: Lithos, 95, p. 19-42.

Kroonenberg, S.B., 1982, A Grenvillian granulite belt in the Colombian Andes and its relation to the Guiana Shield: Geologie en Mijnbouw, 61(4): 325–333.

Large, R.R., Gemmell, J.B., Paulick, H., and Huston, D.L., 2001, The alteration box plot – A simple approach to understanding the relationship between alteration mineralogy and lithogeochemistry associated with volcanic-hosted massive sulfide deposits: Economic Geology, v. 96, p. 957–971.

Leal–Mejía, H., 2011, Phanerozoic gold metallogeny in the Colombian Andes: A tectono–magmatic approach. Doctorade thesis, Universitat de Barcelona, Barcelona, 989 p.

Le Maitre, R.W., Streckeisen, A., Zanettin, B., Le Bas, M.J., Bonin, B., and Bateman, P., 2002, Igneous Rocks, a Classification and Glossary of Terms: Recommendation of the International Union of Geological Sciences Subcommission on the Systematics of Igneous Rocks, University Press, 236 pp.

Leterrier, J., Maury, R.C., Thonon, P., Girard, D., and Marchal, M., 1982, Clinopyroxene composition as a method of identification of the magmatic affinities of paleo-volcanic series, Earth and Planetary Science Letters, 59, p. 139-154.

Li, C., Ripley, E.M., and Naldrett, A.J., 2003, Compositional variations of olivine and sulfur isotopes in the Noril'sk and Talnakh intrusions, Siberia: implications for ore formingprocesses in dynamic magma conduits: Economic Geology, 98, p. 69-86.

Litherland, M., and Aspden, J., A., 1992, Terrene-boundary reactivation: A control on the evolution of the Northern Andes: Journal of South America Earth Sciences, v5, No 1, p. 71-76.

Litherland, M., Aspden, J., and Jemielita, R., 1994, The metamorphic belts of Ecuador: Overseas Memoir of the British Geological Survey, (Nottingham, England), v. 11, p. 147.

López-Males, G.G., Aiglsperger, T., Pujol-Solà, N., and Proenza, J.A., 2020, New mineralogical data on platinum-group minerals from the Río Santiago alluvial placer, Esmeraldas province, Ecuador: Boletín de la Sociedad Geológica Mexicana. dx.doi.org/10.18268/BSGM2020v72n3a090720

Loucks, R., 1990, Discrimination of ophiolitic from nonophiolitic ultramafic–mafic allochthons in orogenic belts by the AIFI ratio in clinopyroxene: Geology 18, p. 346–349.

Luzieux, L.D.A., Heller, F., Spikings, F., Vallejo, C.F., and Winkler, W., 2006, Origin and Cretaceous tectonic history of the coastal Ecuadorian forearc between 1°N and 3°S: Paleomagnetic, radiometric and fossil evidence: Earth and Planetary Science Letters, v. 249, p. 400–414, 10.1016/j.epsl.2006.07.008.

Macías-Mosquera, K., S., and Rojas-Agramonte, Y., 2019, Age, geochemistry and emplacement of the Pascuales plutons in western Ecuador and their geodynamic implications: 8th International Symposium on Andean Geodynamics (ISAG), Quito – Ecuador.

Mantilla–Figueroa, L.C., Bissig, T., Cottle, J.M., and Hart, C.J.R., 2012, Remains of early Ordovician mantle–derived magmatism in the Santander Massif (Colombian Eastern Cordillera): Journal of South American Earth Sciences, 38: p. 1–12. doi.org/10.1016/j.jsames.2012.03.001

Mantilla–Figueroa, L.C., Bissig, T., VAlencia, V., and Hart, C.J.R., 2013, The magmatic history of the Vetas-California mining district, Santander Massif, Eastern Cordillera, Colombi: Journal of South American Earth Sciences, 45, 235-249. 10.1016/j.jsames.2013.03.006

Martens, U., Restrepo, J.J., Ordóñez–Carmona, O., and Correa–Martínez, A.M., 2014, The Tahamí and Anacona Terranes of the Colombian Andes: Missing links between South American and Mexican Gondwana margins: The Journal of Geology, 122(5): 507–530. doi.org/10.1086/677177

Massonne, H.J., and Toulkeridis, T., 2012, Widespread relics of high-pressure metamorphism confirm major terrane accretion in Ecuador: a new example from the Northern Andes: International Geology Review, v. 54, Issue 1. doi.org/10.1080/00206814.2010.498907

Maya, M., and González, H., 1995, Unidades litodémicas en la Cordillera Central de Colombia: Boletín Geológico, INEGEOMINAS, v. 35, p. 43-57.

McCulloch, M., Gregory, R., Wasserburg, G., and Taylor, H., 1979, A Neodymiun, Strontium, and oxygen isotopic study of the Cretaceous Samail ophiolite and implications for the petrogenesis ans seawater-hydrothermal alteration of oceanic crust: Earth and Planetary Science Letters, v. 46, p. 201-211.

Meng, F., Cui, M., Wu, X., Ren, Y., 2015, Heishan mafic–ultramafic rocks in the Qimantag area of Eastern Kunlun, NW China: Remnants of an early Paleozoic incipient island arc. Gondwana Research 27, p. 745-759.

Menuge, J., Pedersen, R.B., and Furnes, H., 1989, Seawater alteration of the Karmøy Ophiolite Complex, SW Norway: Nd and Sr isotopic evidence. Norsk Geologisk Tidsskrift, v. 69, p. 191-200. ISSN 0029-196X.

Miyashiro, A., 1973, The Troodos ophiolitic complex was probably formed in an island arc: Earth and Planetary Science Letters, v. 19, p. 218-224.

Molina, J.F., Moreno, J.A., Castro, A., Rodriguez, C., and Fershtater, G.B., 2015, Calcic amphibole thermobarometry in metamorphic and igneous rocks: new calibrations based on plagioclase/amphibole Al-Si partitioning and amphibole-liquid Mg partitioning: Lithos, 232, p. 286–305.

Montes, C., Bayona, G., Cardona, A., Buchs, D., Silva, C., Morón, S., Hoyos, N., Ramírez, D., Jaramillo, C., and Valencia, V., 2012, Arc-continent collision and orocline formation: closing of the Central American seaway: Journal of Geophysical Research, 117, B04105. dx.doi.org/10.1029/2011JB008959.

Montes, C., Guzmán, G., Bayona, G., Cardona, A., Valencia, V., and Jaramillo, C., 2010, Clockwise rotation of the Santa Marta Massif and simultaneous Paleogene to Neogene deformation of the Plato–San Jorge and Cesar–Ranchería Basins: Journal of South American Earth Sciences, 29(4): p. 832–848. doi.org/10.1016/j.jsames.2009.07.010

Montero, P., and Bea, F., 1998, Accurate determination of $^{87}Rb/^{86}Sr$ and $^{147}Sm/^{144}Nd$ ratios by inductively-coupled-plasma mass spectrometry in isotope geoscience: an alternative to isotope dilution analysis: Analytica Chimica Acta, v. 358, p. 227–233.

Morimoto N., and Kitamura M., 1983, Q–J diagram for classification of pyroxens: Journal of the Japanese Association of Mineralogy, Petrology, and Economic Geology, 78 , p. 141.

Morimoto, N., Fabries, J., Ferguson, A.K., Ginzburg, I.V., Ross, M., Seifert, F.A., Zussman, J., Aoki, K., and Gottardi, G., 1988, Nomenclature of pyroxenes: Mineralogical Magazine, 52, p. 535-550.

Morris, R.A., DeBari, S.M., Busby, C., Medynski, S., and Jicha, B.R., 2019, Building Arc Crust: Plutonic to Volcanic Connections in an Extensional Oceanic Arc, the Southern Alisitos Arc, Baja California: Journal of Petrology, Volume 60, Issue 6, p. 1195–1228, doi.org/10.1093/petrology/egz029

Mullen, E.D., 1983, MnO/TiO2/P205: a minor element discriminant for basaltic rocks of oceanic environments and its implications for petrogenesis: Earth and Planetary Sciences Letters, 62, p. 53-62.

Murray, C.G., 1972, Zoned ultramafic complexes of the Alaskan type: Feeder pipes of andesitic volcanoes, in Studies in Earth and Space Sciences (Hess Volume), edited by R. E. Shagam et al.: Memoirs - Geological Society of America, 132, p. 313-335.

Naldrett, J., 1999, World-class Ni-Cu-PGE deposits: Key factors in their genesis: Mineralium Deposita, 34, p. 227–240, 10.1007/s001260050200.

Naldrett, J., 2005, A history of our understanding of magmatic Ni–Cu sulfide deposits: The Canadian Mineralogist; 43(6), p. 2069–2098. doi.org/10.2113/gscanmin.43.6.2069

Nandedkar, R.H., Hürlimann, N., Ulmer, P., and Müntener, O., 2016, Amphibole–melt trace element partitioning of fractionating calc-alkaline magmas in the lower crust: an experimental study: Contribution to Mineralogy and Petrology, 171:71, 10.1007/s00410-016-1278-0.

Noble, R., Aspden, J., and Jemielita, R., 1997, Northern Andean crustal evolution: New U–Pb geochronological constraints from Ecuador: Geologial Society of American Bulletin, v. 109, p. 789–798.

Ordóñez–Carmona, O., and Pimentel, M.M., 2002, Rb–Sr and Sm–Nd isotopic study of the Puquí Complex, Colombian Andes: Journal of South American Earth Sciences, 15(2), p. 173–182. doi.org/10.1016/S0895-9811(02)00017-2

Paster, T.P., Schauwecker, D.S., and Haskin, L.A., 1974, The behavior of some trace elements during solidification of the Skaergaard layered series: Geochimica et Cosmochimica Acta, V. 38, p. 1549-1577.

Paul, A.N., Spikings, R.A., Ulianov, A., and Ovtcharova, M., 2018, High temperature (>350°C) thermal histories of the long lived (>500Ma) active margin of Ecuador and Colombia: apatite, titanite and rutile U- Pb thermochronology: Geochimica et Cosmochimica Acta, v. 228, p. 275-300.

Pearce, J.A., 1982, Trace element characteristics of lavas from destructive plate boundaries. In: Thorpe, R.S. (Ed.), Orogenic Andesites: Wiley, Chichester, U.K., p. 528 – 548.

Pearce, J.A., 1996, A user's guide to basalt discrimination diagrams: Geological Association of Canada Special Publication, v. 12, p. 79 – 113.

Pearce, J.A., and Peate, D.W., 1995, Tectonic implications of the composition of volcanic arc magmas: Annual Review of Earth Planetary Sciences, V. 23, p. 251 – 285.

Pearce, J.A., 2003, Supra-subduction zone ophiolites: The search for modern analogues, in Dilek, Y., and Newcomb, S., eds., Ophiolite concept and the evolution of geological thought: Boulder, Colorado: Geological Society of America Special Paper, v. 373, p. 269 – 293.

Pearce, J.A., and Stern, D.W., 2006, Origin of back arc basin margins: trace element and isotope perspectives: Geophysical Monograph Series, 166, p. 63–86. doi.org/10.2138/am.2005.1498.

Pearce, J.A., 2008, Geochemical fingerprinting of oceanic basalts with applications to ophiolite classification and the search for Archean oceanic crust: Lithos, v. 100, p. 14-48.

Pearce, J.A., 2014, Ophiolites: immobile elements fingerprinting of ophiolites: Elements, v. 10, no. 2, p. 101–108.

Peccerillo, A., Taylor, S.R., 1976, Geochemistry of Eocene calcalkaline volcanic rocks from the Kastamonu area, Northern Turkey: Contributions to Mineralogy and Petrology, 58, p. 63–81.

Pepper, M., Gehrels, G., Pullen, A., Ibanez-Mejia, M., Ward, K.M., and Kapp, P., 2016, Magmatic history and crustal genesis of western South America: constraints from U-Pb ages and Hf isotopes of detrital zircons in modern rivers: Geosphere, 12, p. 1532–1555.

Piraquive, A., 2017, Structural framework, deformation and exhumation of the Santa Marta Schists: Accretion and deformational history of a Caribbean Terrane at the north of the Sierra Nevada de Santa Marta. Doctorade thesis, Université Grenoble Alpes and Universidad Nacional de Colombia, Grenoble–Bogotá, 393 p.

Plank, T., 2005, Constraints from thorium/lanthanum on sediment recycling at subduction zones and the evolution of the continents: Journal of Petrology, 46 (3), p. 921–944.

Plank, T., 2014, The Chemical Composition of Subducting Sediments. In: Treatise on Geochemistry 2nd Edition, ed. by Keeling, Ralph F., Elsevier, Amsterdam, p. 607-629, dx.doi.org/10.1016/B978-0-08-095975-7.00319-3.

Plank, T., and Langmuir, Ch., 1998, The chemical composition of subducting sediment and its consequences for the crust and mantle: Chemical Geology, v. 145, p. 325–394.

Polat, A., and Hofmann, A.W., 2003, Alteration and geochemical patterns in the 3.7–3.8 Ga Isua greenstone belt, West Greenland : Precambrian Research 126, p. 197–218.

Powell, R., and Holland, T.J.B., 1994, Optimal geothermometry and geobarometry: American Mineralogist, 79, p. 120–133.

Pozo, M., 1990, Complejo ultramáfico Tampanchi: Minería Ecuatoriana, No, 2, p. 35-37.

Pratt, W.T., Duque, P., and Ponce, M., 2005, An autochthonous geological model for the eastern Andes of Ecuador: Tectonophysics, v. 399, p. 251–278.

PRODEMINCA, 2000, Depositos porfídicos y epi-mesotermales relacionados con intrusiones de la Cordillera del Cóndor: Evaluacion de distritos mineros del Ecuador: UCP Prodeminca Proyecto MEM BIRF 36-55 EC 5, 223p.

Putirka, K.D., 2008, Thermometers and barometers for volcanic systems: Reviews in Mineralogy and Geochemistry, 69, p. 61–120.

Ramos, V.A., 1999, Plate tectonic setting of the Andean Cordillera: Episodes, v. 22, p. 183–190.

Ramos, V.A., 2009, Anatomy and global context of the Andes: Main geologic features and the Andean orogenic cycle. In Kay SM, Ramos VA, Dickinson W (eds.) Backbone of the Americas: Shallow Subduction, Plateau Uplift, and Ridge and Terrane Collision: Geological Society of America, Memoir 204, p. 31–65.

Reagan, M.K., Ishizuka, O., Tsukuaba, H., Stern, R.J., Kelley, K.A., Ohara, Y., Blichert-Toft, J., Bloomer, S.H., Cash, J., Fryer, P., Hanan, B.B., Hickey Vargas, R., Ishii, T., Kimura, J.I., Peate, D.W., Rowe, M.C., and Woods, M., 2010, Forearc basalts and subduction initiation in the Izu-Bonin-Mariana system: Geochemistry, Geophysics, Geosystems, v. 11. dx.doi.org/10.1029/2009GC002871

Reitsma, M.J., 2012, Reconstructing the Late Paleozoic–Early Mesozoic Plutonic and Sedimentary Record of South-East Peru: Orphaned Back-Arcs Along the Western Margin of Gondwana (PhD thesis), University of Geneva, Switzerland, 226 p.

Restrepo, J.J., 2008, Obducción y metamorfismo de ofiolitas triásicas en el flanco occidental del Terreno Tahamí, cordillera Central de Colombia: Boletín de Ciencias de la Tierra, v. 22, p. 49–100.

Restrepo, J.J., Ordóñez–Carmona, O., Armstrong, R., and Pimentel, M.M., 2011, Triassic metamorphism in the northern part of the Tahamí Terrane of the Central Cordillera of Colombia: Journal of South American Earth Sciences, 32(4), p. 497–507. doi.org/10.1016/j.jsames.2011.04.009

Restrepo, J.J., and Toussaint, J., 1988, Terranes and continental accretion in the Colombian Andes: Episodes, v. 11, no. 3, p. 189–193.

Restrepo, J.J., Toussaint, J.F., González, H., Cordani, U., Kawashita, K., Linares, E., and Parica, C., 1991, Precisiones geocronológicas sobre el occidente colombiano: Simposio sobre Magmatismo Andino y su Marco Tectónico, Manizales, Memoirs, I, 21 p.

Reyes, P., 2006, El complejo ofiolítico Peltetec y su relación con las unidades metamórficas jurásicas de la Cordillera Real. Tesis de Grado (No publicado): Escuela Politécnica Nacional, Quito, Ecuador, 180 p.

Reynaud, C., Jaillard, E., Lapierre, H., Mamberti, M., and Mascle, G., 1999, Oceanic Plateau Island arcs of southwestern Ecuador: their place in the geodynamic evolution of northwestern South America: Tectonophysics, v. 307, p. 235–254.

Riding, J., 1989, A palynological investigation of nine rock samples from Ecuador (Maguazo Unit): British Geological Survey Technical Report, WH/89/361/R, 4.

Ridolfi, F., Renzulli, A., and Puerini, M., 2010, Stability and chemical equilibrium of amphibole in calc-alkaline magmas: an overview, new thermobarometric formulations and application to subduction-related volcanoes: Contribution to Mineralogy and Petrology, 160, p. 45–66. 10.1007/s00410-009-0465-7.

Riel, N., Guillot, S., Jaillard, E., Martelat, J.E., Paquette, J.L., Schwartz, S., Goncalves, P., Duclaux, G., Thebaud, N., and Lanari, P., 2013, Metamorphic and geochronogical study of the Triassic El Oro metamorphic complex, Ecuador: Implications for high-temperature metamorphism in a forearc zone: Lithos, v. 156, p. 41-68.

Riel, N., Martelat, J.E., Guillot, S., Jaillard, E., Monié, P., Yuquilema, J., Duclaux, G., and Mercier J., 2014, Fore arc tectonothermal evolution of the El Oro metamorphic province (Ecuador) during the Mesozoic: Tectonics, v. 33, doi:10.1002/2014TC003618.

Rodríguez–García, G., Correa–Martínez, A.M., Zapata–García, G., Arango–Mejía, M.I., Obando–Erazo, G., Zapata–Villada, J.P., and Bermúdez, J.G., 2020, Diverse Jurassic magmatic arcs of the Colombian Andes: Constraints from petrography, geochronology, and geochemistry. In: Gómez, J. & Pinilla–Pachon, A.O. (editors), The Geology of Colombia, Volume 2 Mesozoic. Servicio Geológico Colombiano, Publicaciones Geológicas Especiales 36, 54 p. doi.org/10.32685/pub.esp.36.2019.04

Rodríguez–García, G., Correa–Martínez, A.M., Zapata–Villada, J.P., and Obando–Erazo, G., 2019, Fragments of a Permian arc on the western margin of the Neoproterozoic basement of Colombia. In: Gómez, J. & Mateus–Zabala, D. (editors), The Geology of Colombia, Volume 1 Proterozoic – Paleozoic: Servicio Geológico Colombiano, Publicaciones Geológicas Especiales 35, 34 p. doi.org/10.32685/pub.esp.35.2019.10

Rojas-Agramonte, Y., Garcia-Casco, A., Kemp, A., Kröner, A., Proenza, J.A., Lázaro, C., and Liu, D., 2016, Recycling and transport of continental material through the mantle

wedge above subduction zones: A Caribbean example: Earth and Planetary Science Letters, v. 436, p. 93–107. 10.1016/j.epsl.2015.11.040

Romeuf, N., Aguirre, L., Soler, P., Féraud, G., Jaillard, E., Ruffet, G., 1995, Middle Jurassic volcanism in the Northern and Central Andes: Revista Geológica de Chile, 22, p. 245–259.

Ross, P.S., and Bédard, J.H., 2009, Magmatic affinity of modern and ancient subalkaline volcanic rocks determined from trace-element discriminant diagrams: Canadian Journal of Earth Sciences, v. 46, p. 823–839,:10.1139/E09-054.

Ruiz, G., Seward, D., and Winkler, W., 2004, Detrital thermochronology. A new perspective on hinterland tectonics; an example from the Andean Amazon Basin, Ecuador: Basin Research, v. 16, p. 413–430, 10.1111/j.1365-2117.2004.00239.x.

Ruiz-Jimenez, E., Blanco, I., Toro, L., Moreno, M., Vinasco, C., García, A., Morata, D., and Gómez, A., 2012, Geoquímica y petrología de las metabasitas del Complejo Arquía (Municipio de Santafé de Antioquia y Río Arquía, Colombia): Implicaciones geodinámicas: Boletín Ciencias de la Tierra, v. 32, 65 – 80.

Rundle, C., 1988, Potassium-argon ages for minerals from the Cordillera Real, Ecuador: Natural Environment Research Council Isotope Geology Centre Report, No. NIGC/88/7.20.

Scott, R.B., and Hajash Jr., A., 1976, Initial submarine alteration of basaltic pillow lavas: a microprobe study: American Journal of Science, v. 276, p. 480 – 501.

Seyfried, W.E., Berndt, M.E., and Seewald, J.S., 1988, Hydrothermal alteration processes at mid ocean ridges: constraints from diabase alteration experiments, hot-spring fluids and composition of the oceanic crust: Canadian Mineralogist, v. 26, p. 787 – 804.

Shand, S. J., 1943, Eruptive Rocks. Their Genesis, Composition, Classification, and their Relation to Ore-Deposits with a Chapter on Meteorite: New York: John Wiley & Sons.

Shervais, J.W., 1982, Ti – V plots and the petrogenesis of modern and ophiolitic lavas: Earth and Planetary Science Letters, v. 59, p. 101 – 118.

Smith, D., 2014, Clinopyroxene precursors to amphibole sponge in arc crust: Nature Communications, 5, 4329, 10.1038/ncomms5329.

Smith, J.V., and Brown, W.L, 1988, Feldspar Minerals: Second Revised and Extended Edition. Springer Verlag, Berlin Heidelberg, New York, London, Paris, Tokyo.

Song, X., Wang, Y., and Chen, L., 2011, Magmatic Ni-Cu-(PGE) deposits in magma plumbing systems: Features, formation and exploration: Geoscience Frontiers,2(3), p. 375–384.

Spear, F.S., 1993, Metamorphic Phase Equilibria and Pressure–Temperature–Time Paths: Mineralogical Society of America Monographs, Washington.

Spikings, R., Cochrane, R., Villagomez, D., Van der Lelij, R., Vallejo, C., Winkler, W., and Beate, B., 2015, The geological history of northwestern South America: from Pangea collision of the Caribbean Large Igneous Province (290 – 75 Ma): Gondwana Research, GR-01278, 45, dx.doi.org/10.1016/j.gr.2014.06.004

Spikings, R., and Crowhurst, P., 2004, (U-Th)/He thermochronometric constraints on the late Miocene-Pliocene tectonic development of the northern Cordillera Real and the Interandean Depression, Ecuador: Journal of South American Earth Sciences 17, p. 239–251.

Spikings, R., and Paul, A., 2019, The Permian – Triassic history of magmatic rocks of the northern Andes (Colombia and Ecuador): Supercontinent assembly and disassembly. In: Gómez, J. & Pinilla–Pachon, A.O. (editors), The Geology of Colombia, Volume 2 Mesozoic: Servicio Geológico Colombiano, Publicaciones Geológicas Especiales 36, 42 p. doi. org/10.32685/pub.esp.36.2019.01

Spikings, R., Paul, A., Vallejo, C., and Reyes, P., 2021, Constraints on the ages of the crystalline basement and Palaeozoic cover exposed in the Cordillera real, Ecuador: $^{40}Ar/^{39}Ar$ analyses and detrital zircon U/Pb geochronology: Gondwana Research, 90, 77-201. doi.org/10.1016/j.gr.2020.10.009

Spikings, R., Winkler, W., Seward, D., and Handler, R., 2001, Along-strike variations in the thermal and tectonic response of the continental Ecuadorian Andes to the collision with heterogeneous oceanic crust: Earth and Planetary Science Letters 186, p. 57–73.

Starr, P., and Pattison, D., 2019, Metamorphic devolatilization of basalts across the greenschist-amphibolite facies transition zone: insights from isograd mapping, petrography and thermodynamic modelling: Lithos, Volumes 342–343, p. 295-314, doi.org/10.1016/j.lithos.2019.05.020.

Staudigel, H., and Hart, R., 1983, Alteration of basaltic glass: mechanism and significance for the oceanic crust-seawater budget: Geochimica et Cosmochimica Acta, v. 47, p. 37 – 50.

Suhr, N., Rojas-Agramonte, Y., Chew, D.M., Pinto, A.J., Villagómez, D., Toulkeridis, T., and Mertz-Kraus, R., 2019, Detrital-zircon geochronology and provenance of the El Oro Metamorphic Complex, Ecuador: Geodynamic implications for the evolution of the western Gondwana margin: Journal of South American Earth Sciences, v. 90, p. 520-539.

Sun, S.S., and McDonough, W.F., 1989, Chemical and isotopic systematics of oceanic basalts; implications for mantle composition and processes: Geological Society of London Special Publication, v. 42, p. 313 – 345.

Thakurta, J., Ripley, E.M., and Li, C., 2008, Geochemical constraints on the origin of sulfide mineralization in the Duke Island Complex, southeastern Alaska. Geochemistry, Geophysics and Geosystems, 9, 34 p., Q07003, 10.1029/2008GC001982.

Taylor, B., and Martinez, F., 2003, Back-arc basin basalt systematics: Earth and Planetary Science Letters, v. 210, no. 3–4, p. 481-497.

Taylor, S., and McLennan, S., 1985, The Continental Crust: Its Composition and Evolution: Oxford, London, Edinburgh, Boston, Palo Alto, Melbourne: Blackwell Scientific. pp. xvi, 312.

Taylor, R.N., and. Nesbitt, R.W, 1998, Isotopic characteris-tics of subduction fluids in an intra-oceanic setting, Izu-Bonin arc, Japan, Earth and Planetary Science Letters, 164, 79–98.

Tistl, M., 1994, Geochemistry of platinum-group elements of the zoned ultramafic Alto Condoto complex, northwest Colombia: Economic Geology, 89, 158-167.

Tiepolo, M., Oberti, R., and Vannucci, R., 2002, Trace-element incorporation in titanite: constraints from experimentally determined solid/liquid partition coefficients: Chemical Geology, 191, p. 105–119.

Torres-Roldán, R.L., and Garcia-Casco, A., DWImager: una implementación para el procesamiento de matrices de intensidades de Rayos X (no publicado).

Torres-Roldán, R.L., Garcia-Casco, A., and García-Sánchez, P.A., 2000, CSpace: an integrated workplace for the graphical and algebraic analysis of phase assemblages on 32-bit Wintel platforms: Computers and Geosciences, 26, p. 779–793.

Torró, L., Proenza, J.A., Rojas-Agramonte, Y., Garcia-Casco, A., Yang, J., and Yang, Y., 2018, Recycling in the subduction factory: Archaean to Permian zircons in the oceanic Cretaceous Caribbean island-arc (Hispaniola): Gondwana Research, v. 54, p. 23-37. 10.1016/j.gr.2017.09.010

Tschopp, H.J., 1953, Oil explorations in the Oriente of Ecuador: American Association of Petroleum Geologist, Bulletin 37 (10), p. 2303–2347.

Turner, S., Hawkesworth, C., Rogers, N., Bartlett, J., Worthington, T., Hergt, J., Pearce, J., Smith, I., 1997, U-Th disequilibria, magma petrogenesis and fux rates beneath the depleted Tonga-Kermadec island arc: Geochimica et Cosmochimica Acta, 61, p. 4855-4884.

Turner, S., Caulfield, J., Turner, M., Van Keken, P., Maury, R., Sandiford, M., and Prouteau, G., 2012, Recent contribution of sediments and fluids to the mantle's volatile budget: Nature Geoscience, 5(1), p. 50-54. 10.1038/ngeo1325.

Vallejo, C., Spikings, R., Horton, B., Luzieux, L., Romero, C., Winkler, W., Thomsen, T., 2019, Chapter-8, Late Cretaceous to Miocene stratigraphy and provenance of the coastal forearc and Western Cordillera of Ecuador: Evidence for accretion of a single oceanic plateau fragment, in: Brian K. Horton, Andrés Folguera, Andean Tectonics, Elsevier, p. 237-268, ISBN 9780128160091, doi.org/10.1016/B978-0-12-816009-1.00010-1.

Vallejo, C., Spikings, R.A., Winkler, W., Luzieux, L., Chew, D., and Page, L., 2006, The early interaction between the Caribbean Plateau and the NW South American plate: Terra Nova, v. 18, p. 264–269.

Vallejo, C., Tapia, D., Gaibor, J., Steel, R., Cardenas, M., Winkler, W., Valdez, A., Esteban, J., Figuera, M., Leal, J., Cuenca, D., 2017, Geology of the Campanian M1 sandstone oil reservoir of eastern Ecuador: a delta system sourced from the Amazon Craton: Marine and Petroleum Geology, 86, p. 1207–1223, doi.org/10.1016/j.marpetgeo.2017.07.022.

Vallejo, C., Winkler, W., Spikings, R.A., Luzieux, L., Heller, F., and Bussy, F., 2009, Mode and timing of terrane accretion in the forearc of the Andes in Ecuador. In: Kay, S.M., Ramos, V.A., Dickinson, W.R. (Eds.), Backbone of the Americas: Shallow Subduction, Plateau Uplift, and Ridge and Terrane Collision. v. 204: Geological Society of America Memoirs, p. 197–216.

Van der Lelij, R., 2013, Reconstructing North-Western Gondwana with Implications for the Evolution of the Iapetus and Rheic Oceans: A Geochronological, Thermochronological and Geochemical study (PhD thesis): University of Geneva, Switzerland, 221 p.

Van der Lelij, R., Spikings, R.A., and Mora, A., 2016, Thermochronology and tectonics of the Mérida Andes and the Santander Massif, NW South America: Lithos, 248–251, p. 220–239. doi.org/10.1016/j.lithos.2016.01.006

Vermeesch, P., 2018, IsoplotR: a free and open toolbox for geochronology: Geoscience Frontiers, v.9, p.1479-1493.

Villagómez, D., Spikings, R., Magna, T., Kammer, A., Winkler, W., and Beltrán, A., 2011, Geochronology, geochemistry and tectonic evolution of the Western and Central cordilleras of Colombia: Lithos, v. 125, p. 875 – 896.

Villagómez, D., and Spikings, R., 2013, Thermochronology and tectonics of the Central and Western Cordilleras of Colombia: Early Cretaceous–Tertiary evolution of the Northern Andes: Lithos, v. 168, p. 228–249.

Villares, F., Egüez, A., and Yánez, E., 2014, Petrographic and geochemical characterization of the Triassic and Jurassic magmatic and volcanic rocks of southeastern Ecuador: European Geosciences Union (EGU general assembly), Austria/Viena.

Villares, F., Garcia-Casco, A., Blanco-Quintero, I.F., Montes, C., Reyes, P., and Cardona, C., 2020, The Peltetec ophiolitic belt (Ecuador): A window to the tectonic evolution of the Triassic margin of western Gondwana: International Geology Review. dx.doi.org/10.1080/00206814.2020.1830313.

Vinasco, C, 2019, The Romeral Shear Zone in: F. Cediel, R.P. Shaw (Eds.), Geology and Tectonics of Northwestern South America: the Pacific-Caribbean-Andean Junction, Springer International Publishing, Cham, p. 833-876, 10.1007/978-3-319-76132-9_12

Vinasco, C., Cordani, U., González, H., Weber, M., and Pelaez, C., 2006, Geochronological, isotopic, and geochemical data from Permo-Triassic granitic gneisses and granitoids of the Colombian Central Andes: Journal South American Earth Science, v. 21, p. 355–371.

Wakabayashi, J., and Dilek, Y., 2003, What constitutes “emplacement” of an ophiolite? Mechanisms and relationship to subduction initiation and formation of metamorphic soles. In: Dilek, Y., and Robinson, P.T., (eds.), Ophiolites and Earth history: Geological Society of London, Special Publication, p. 427–448. doi.org/10.1144/GSL.SP.2003.218.01.22.

Wallace, P.J., 2005, Volatiles in subduction zone magmas: concentrations and fluxes based on melt inclusion and volcanic gas data: Journal of Volcanology and Geothermal Research 140, p. 217-240.

Wang, J., Wang, Q., Dan, W., Yang, J.H., Yang, Z.Y., Sun, P., Qi, P., Hu, W.L., 2019, The role of clinopyroxene in amphibole fractionation of arc magmas: Evidence from mafic intrusive rocks within the Gangdese arc, southern Tibet: Lithos, v. 338–339, p. 174-188, doi.org/10.1016/j.lithos.2019.04.013.

Wang, C.Y., Zhou, M.F., Qi, L., 2011, Chalcophile element geochemistry and petrogenesis of high-Ti and low-Ti magmas in the Permian Emeishan large igneous province, SW China: Contributions to Mineralogy and Petrology, 161, p. 237-254.

Weber, M., Cardona, A., Valencia, V., García–Casco, A., Tobón, M., and Zapata, S., 2010, U/Pb detrital zircon provenance from Late Cretaceous metamorphic units of the Guajira Peninsula, Colombia: Tectonic implications on the collision between the Caribbean Arc and the South American margin: Journal of South American Earth Sciences, 29(4), p. 805–816. doi.org/10.1016/j.jsames.2009.10.004

Weiser, T., and Schmidt-Thomé, M., 1993, Platinum-group minerals from the Santiago River, Esmeraldas Province, Ecuador: Canadian Mineralogist, 31, p. 61-73.

Whattam, S.A., and Stern, R.J., 2011, The “subduction initiation rule”: a key for linking ophiolites, intra-oceanic forearcs, and subduction initiation: Contributions to Mineralogy and Petrology, v. 162, p. 1031–1045.

Whattam, S.A., Stern, R.J., 2015, Late Cretaceous plume-induced subduction initiation along the southern margin of the Caribbean and NW South America: the first documented example with implications for the onset of plate tectonics: Gondwana Research, 27, p. 38–63.

White, R.W., Powell, R., Holland, T.J.B., and Worley, B.A., 2000, The effect of TiO2 and Fe2O3 on metapelitic assemblages at greenschist and amphibolite facies conditions: mineral equilibria calculations in the system K2O-FeO-MgO-Al2O3-SiO2-H2O-TiO2-Fe2O3: Journal of Metamorphic Geology, 18, p. 497– 511.

White, R.W., Powell, R., and Clarke, G.L., 2002, The interpretation of reaction textures in Fe-rich metapelitic granulites of the Musgrave Block, central Australia; constraints from mineral equilibria calculations in the system K2O-FeO-MgO-Al2O3-SiO2-H2O-TiO2-Fe2O3: Journal of Metamorphic Geology, 20 (1), p. 41-55.

White, R.W., Powell, R., Holland, T.J.B., Johnson, T.E., and Green, E.C.R., 2014, New mineral activity–composition relations for thermodynamic calculations in metapelitic systems: Journal of Metamorphic Geology, 32, p. 261-286. doi.org/10.1111/jmg.12071

Whitney, D., and Evans, B., 2010, Abbreviations for names of rock-forming minerals: American Mineralogist, v. 95, p. 185–187.

Widmer, T., Ganguin, J., Thompson A.B., 2000, Ocean floor hydrothermal veins in eclogite facies rocks of the Zermatt-Saas Zone: Switzerland Schweizerische mineralogische und petrographische Mitteilungen, 80, p. 63-73.

Wiewióra, A., Weiss, Z., 1990, Crystallochemical classifications of phyllosilicates based on the unified system of projection of chemical composition: II. The chlorite group: Clay Minerals, 25, p. 83–92.

Williams, I., and Claesson, S., 1987, Isotopic evidence for the Precambrian provenance and Caledonian metamorphism of high grade paragneisses from the Seve Nappes, Scandinavian Caledonides. II: ion microprobe zircon U–Th–Pb: Contribution to Mineralogy and Petrology, v. 97, p. 205–217.

Winter, L.S., Tosdal, R.M., Mortensen, J.K., and Franklin, J.M., 2010, Volcanic Stratigraphy and Geochronology of the Cretaceous Lancones Basin, Northwestern Peru: Position and Timing of Giant VMS Deposits: Bulletin of the Society of Economic Geologist, v. 105, p. 713–742.

Winchester, J.A., Floyd, P.A., 1977, Geochemical discrimination of different magma series and their differentiation products using immobile elements. Chemical Geology 20, p. 325–343.

Woodhead, J.D., Hergt, J.M., Davidson, J.P., and Eggins, S.M., 2001, Hafnium isotope evidence for conservative element mobility during subduction zone processes: Earth and Planetary Science Letters, v. 192, p. 331–346. doi:10.1016/S0012-821X(01)00453-8.

Xu, W., Zhu, D., Wang, Q., Weinberg, R., Wang, R., Li, S., Zhang, L., and Zhao, Z., 2019, Constructing the Early Mesozoic Gangdese Crust in Southern Tibet by Hornblende-dominated Magmatic Differentiation: Journal of Petrology, Volume 60, Issue 3, p. 515–552, doi.org/10.1093/petrology/egz005.

Yánez, E., Quilachamín, V., and Reyes, P., 2017, Estudio petrográfico y geoquímico del Arco Alao (Cretácico Inferior) al este de Chambo, provincia de Chimborazo: implicaciones geodinámicas: VIII Jornadas en Ciencias de la Tierra, EPN-Quito, 5p.

Zapata, S., Cardona, A., Jaramillo, J., Patiño, A., Valencia, V., León, S., Mejía, D., Pardo-Trujillo, A., and Castañeda, J., 2019, Cretaceous extensional and compressional

tectonics in the Northwestern Andes, prior to the collision with the Caribbean oceanic plateau: Gondwana Research, v. 66, p. 207-226.

Zimmer, M.M., Plank, T., Hauri, E.H., Yogodzinski, G.M., Stelling, P., Larsen, J., Singer, B., Jicha, B., Mandeville, C., Nye, C.J., 2010, The Role of Water in Generating the Calc-alkaline Trend: New Volatile Data for Aleutian Magmas and a New Tholeiitic Index: Journal of Petrology, Volume 51, Issue 12, p. 2411–2444. doi.org/10.1093/petrology/egq062

Zindler, A., and Hart, S., 1986, Chemical geodynamics: Annual Review of Earth Planetary Sciences, v. 14, p. 493–571.

Apéndices

Apéndice

Appendix 5.1. Data scaled for portrayal in the isocon diagram of Figure 5.5 for group 3 basaltic rocks.

	Major (wt.%) and trace elements (ppm)														
Element	PIMI-43	P-08	P-30	P-33	P-35	P-36	P-40	P-42	P-44	P-46	P-47	P-52	PIMI-6	PIMI-22	PIMI-81A
SiO_2	48.3	50.7	46.2	47.9	48.6	42.7	49.1	48.9	50.0	49.7	49.7	49.0	47.8	48.6	48.4
Al_2O_3	14.0	12.9	13.9	13.5	12.8	16.7	13.7	14.6	18.1	14.5	15.2	15.7	13.6	14.3	14.5
CaO	9.53	8.96	9.77	9.68	10.3	8.96	7.85	9.11	6.48	10.7	9.77	10.5	8.99	10.6	10.4
$FeO_{(t)}$	9.41	11.1	12.4	10.8	12.1	13.4	10.9	10.5	8.75	8.66	8.68	7.84	11.4	9.66	9.39
MgO	8.05	6.97	6.61	7.27	6.02	6.87	6.85	6.98	6.06	7.34	7.94	8.34	7.58	7.32	7.99
Na_2O	3.22	3.14	2.03	3.74	2.93	2.73	3.69	3.21	3.26	3.39	3.67	2.72	3.05	3.42	3.14
TiO_2	1.31	1.73	1.99	1.60	2.16	1.81	1.73	1.36	0.82	1.18	1.14	1.08	1.78	1.34	1.34
MnO	0.19	0.21	0.21	0.17	0.19	0.18	0.20	0.15	0.10	0.16	0.15	0.14	0.22	0.18	0.16
P_2O_5	0.12	0.17	0.17	0.14	0.20	0.17	0.16	0.14	0.07	0.10	0.09	0.09	0.16	0.11	0.13
K_2O	0.08	0.03	0.06	0.09	0.04	0.29	0.01	0.15	0.54	0.02	0.12	0.53	0.02	0.06	0.08
Cr	318	163	128	169	140	342	277	257	34	373	347	364	208	215	266
V	310	366	464	355	430	386	350	317	291	284	276	233	374	321	291
Cu	192	64	43	102	86	50	64	46	20	12.32	23	86	112	72	77
Zn	133	110	67	116	85	117	87	101	77	56	57	489	152	71	53
Sr	87	122	31	60	334	46	80	146	87	36	150	129	137	90	147
Ni	85	61	53	59	53	78	99	77	7	88	98	95	67	73	84
Zr	70	95	101	91	124	95	95	75	57	62	59	63	97	70	74
Co	58	39	48	55	46	48	44	41	25	51	42	43	45	46	43
Sc	43	41	48	44	43	50	38	43	35	43	42	37	44	45	41
Y	31	39	47	39	51	44	38	36	14	28	28	24	40	31	31
Ga	15.72	16.5	21.3	16.9	19.2	19.6	16.2	16.8	19.1	14.6	15.9	14.7	17.8	16.1	15.2
Ba	8.97	11.8	23	18.1	16.6	30	22	28	202	10.75	25	50	9.26	18.6	18.6
Ce	8.67	13.1	12.0	10.4	14.6	13.3	12.2	10.6	10.2	7.71	6.47	7.27	12.60	8.92	7.95
Nd	8.44	11.7	12.1	9.99	14.1	12.7	11.4	10.1	7.30	7.65	6.89	7.15	11.69	8.58	8.26
Li	6.66	4.29	12.9	9.52	4.25	11.2	9.25	9.41	19.6	6.17	10.9	11.1	8.12	9.86	10.7
Dy	5.12	6.42	7.62	6.29	8.32	7.21	6.29	5.74	2.49	4.55	4.43	3.99	6.79	5.02	4.89
Gd	3.97	5.03	5.90	4.77	6.32	5.67	5.03	4.53	2.27	3.67	3.50	3.24	5.28	3.92	3.74
Er	3.03	3.75	4.47	3.84	4.93	4.06	3.65	3.29	1.37	2.60	2.68	2.30	3.83	3.02	3.01
Sm	2.99	3.94	4.56	3.79	5.06	4.43	4.02	3.47	2.14	2.72	2.58	2.51	4.24	2.95	2.90
Yb	2.96	3.32	4.20	3.75	4.77	3.50	3.25	3.03	1.47	2.54	2.53	2.13	3.30	2.91	2.87
La	2.92	4.76	3.84	3.45	4.90	4.98	4.30	4.08	3.95	2.57	2.03	2.39	4.48	3.07	2.52
Mo	2.81	1.63	1.31	1.85	1.74	1.68	1.67	1.37	0.95	2.51	1.36	1.77	1.55	1.37	1.07
Nb	1.83	4.11	2.52	2.18	3.44	2.53	3.45	1.95	1.90	1.64	1.23	1.44	3.50	2.13	1.68
Pr	1.47	2.13	2.07	1.78	2.47	2.25	2.03	1.77	1.51	1.32	1.16	1.27	2.11	1.49	1.40
Pb	1.26	1.54	1.29	5.01	6.17	4.69	1.57	2.00	5.44	1.20	1.33	1.69	1.47	1.48	1.42
Eu	1.17	1.76	1.67	2.13	2.19	1.71	1.33	1.50	1.26	1.12	1.15	1.10	1.53	1.66	2.09
Ho	1.14	1.44	1.72	1.43	1.84	1.57	1.40	1.29	0.50	1.01	1.00	0.84	1.48	1.13	1.13
Sn	1.11	1.71	2.23	1.47	2.09	1.59	1.57	1.39	0.97	1.35	1.08	1.07	1.47	1.11	1.19
Rb	0.99	1.06	1.30	2.70	1.10	4.99	0.52	2.23	15.24	0.97	1.51	6.70	0.92	1.34	1.17
Tb	0.73	0.92	1.07	0.88	1.16	1.01	0.91	0.81	0.39	0.66	0.64	0.58	0.94	0.71	0.71
Tm	0.50	0.58	0.70	0.60	0.77	0.63	0.56	0.51	0.24	0.42	0.42	0.36	0.56	0.49	0.47
Lu	0.47	0.48	0.64	0.59	0.74	0.50	0.50	0.46	0.22	0.37	0.38	0.31	0.45	0.46	0.42
Be	0.41	0.53	0.48	0.44	0.52	0.46	0.47	0.32	0.59	0.47	0.38	0.36	0.52	0.39	0.37
Ta	0.33	0.51	0.34	0.41	0.48	0.35	0.37	0.29	0.27	0.44	0.25	0.28	0.37	0.29	0.25
Th	0.21	0.85	0.37	0.34	0.39	0.32	0.29	0.27	0.80	0.23	0.22	0.22	0.28	0.23	0.22
Cs	0.11	0.05	1.95	0.44	0.06	0.12	0.06	0.31	0.60	0.06	0.11	0.48	0.03	0.05	0.10
U	0.05	0.13	0.05	0.07	0.08	0.05	0.06	0.07	0.50	0.04	0.05	0.04	0.06	0.04	0.07
Tl	0.01	0.01	0.02	0.02	0.03	0.06	0.00	0.03	0.08	0.02	0.01	0.06	0.01	0.01	0.01

Appendix 5.1. (Continued). Data scaled for portrayal in the isocon diagram of Figure 5.5 for group 3 basaltic rocks.

			C^{A_i}												
Element	Scale	C^{0_i}	**P-08**	**P-30**	**P-33**	**P-35**	**P-36**	**P-40**	**P-42**	**P-46**	**P-47**	**P-52**	**PIMI-6**	**PIMI-22**	**PIMI-81A**
SiO_2	1.99	96	101	91.8	95.1	96.5	84.8	97.6	97.1	99	99	97.3	95.0	96.5	96.2
Al_2O_3	6.70	94	86.2	93.0	90.4	86.0	112	92.1	98	97.2	102	106	91.0	96.1	97.1
CaO	9.65	92	86.5	94.3	93.4	100	86.5	75.8	87.9	103	94.3	101	86.8	103	100
$FeO_{(t)}$	9.56	90	106	119	103	116	128	104	101	82.8	83.0	74.9	109	92.3	89.8
MgO	10.9	88	76.2	72.3	79.5	65.8	75.1	74.9	76.3	80.2	86.8	91.2	82.9	80.0	87.3
Na_2O	26.7	86	83.9	54.2	100	78.3	72.9	99	85.7	90.5	98	72.6	81.5	91.3	83.9
TiO_2	64.1	84	111	128	103	139	116	111	87.2	75.7	73.1	69.3	114	85.9	85.9
MnO	432	82	90.6	90.6	73.4	82.0	77.7	86.3	64.7	69.1	64.7	60.4	94.9	77.7	69.1
P_2O_5	667	80	113	113	93.3	133	113	107	93.3	66.7	60.0	60.0	107	73.3	86.7
K_2O	975	78	29.3	58.5	87.8	39.0	283	9.8	146	19.5	117	517	19.5	58.5	78.0
Cr	0.24	76	39.1	30.7	40.3	33.5	81.7	66.2	61.5	89.2	83.1	86.9	49.8	51.5	63.7
V	0.24	74	87.5	111	84.6	103	92.2	83.6	75.6	67.8	66.0	55.6	89.4	76.7	69.5
Cu	0.38	72	24.0	16.1	38.4	32.4	18.9	23.9	17.2	4.6	8.5	32.4	42.2	27.2	29.1
Zn	0.53	70	58.3	35.1	61.3	44.6	61.9	46.0	53.4	29.4	30.0	258	80.4	37.4	27.7
Sr	0.78	68	95.1	24.1	46.9	261	35.8	62.9	114	28.3	118	101	107	70.2	115
Ni	0.77	66	47.3	40.7	45.4	41.2	60.0	76.3	59.5	67.9	75.6	73.4	52.2	56.4	64.7
Zr	0.91	64	86.6	91.5	83.1	113	86.7	86.4	67.8	56.5	53.9	57.4	87.8	63.3	67.3
Co	1.08	62	42.6	52.0	59.3	49.6	51.9	47.4	44.4	54.9	45.5	46.8	48.7	49.3	45.8
Sc	1.40	60	56.7	66.4	60.9	60.5	70.1	52.8	59.8	59.6	57.9	51.5	60.8	62.8	57.4
Y	1.86	58	73.3	88.1	72.4	95.4	82.0	71.1	67.4	51.3	51.5	44.1	75.2	58.1	57.3
Ga	3.56	56	58.8	76.0	60.3	68.2	69.8	57.6	59.9	52.2	56.6	52.4	63.3	57.2	54.2
Ba	6.02	54	71.0	138	109	100	179	131	169	64.7	152	300	55.8	112	112
Ce	6.00	52	78.7	71.7	62.5	87.4	79.6	73.1	63.7	46.2	38.8	43.6	75.5	53.5	47.6
Nd	5.92	50	69.2	71.7	59.2	83.5	75.4	67.3	59.9	45.3	40.8	42.4	69.2	50.8	48.9
Li	7.20	48	30.9	92.7	68.5	30.6	80.7	66.6	67.8	44.4	78.9	80.0	58.5	71.0	77.0
Dy	8.98	46	57.7	68.4	56.5	74.6	64.7	56.5	51.5	40.9	39.7	35.8	61.0	45.1	43.9
Gd	11.1	44	55.7	65.4	52.9	70.0	62.8	55.7	50.1	40.7	38.7	35.8	58.5	43.4	41.4
Er	13.8	42	51.9	61.9	53.2	68.2	56.2	50.5	45.6	36.0	37.2	31.9	53.0	41.8	41.7
Sm	13.4	40	52.7	60.9	50.7	67.7	59.2	53.8	46.4	36.4	34.6	33.6	56.7	39.5	38.7
Yb	12.8	38	42.6	53.9	48.2	61.3	44.9	41.7	38.9	32.6	32.5	27.4	42.3	37.3	36.9
La	12.3	36	58.7	47.3	42.5	60.5	61.5	53.0	50.3	31.7	25.1	29.5	55.3	37.9	31.1
Mo	12.1	34	19.7	15.9	22.3	21.0	20.4	20.2	16.6	30.3	16.4	21.4	18.8	16.6	13.0
Nb	17.5	32	71.9	44.1	38.1	60.2	44.3	60.4	34.2	28.7	21.6	25.2	61.3	37.2	29.3
Pr	20.4	30	43.4	42.3	36.4	50.4	45.8	41.4	36.1	27.0	23.7	25.9	43.1	30.4	28.5
Pb	22.3	28	34.3	28.7	112	137	104	35.0	44.5	26.6	29.6	37.6	32.7	33.0	31.6
Eu	22.3	26	39.1	37.1	47.4	48.7	38.0	29.7	33.5	25.0	25.6	24.6	34.0	36.9	46.6
Ho	21.1	24	30.3	36.2	30.2	38.8	33.2	29.6	27.1	21.4	21.1	17.7	31.3	23.8	23.8
Sn	19.8	22	33.8	44.2	29.1	41.4	31.5	31.0	27.6	26.6	21.3	21.2	29.1	22.0	23.5
Rb	20.2	20	21.5	26.2	54.6	22.2	101	10.6	45.1	19.5	30.5	135.4	18.5	27.1	23.6
Tb	24.7	18	22.8	26.4	21.6	28.7	25.0	22.5	20.1	16.2	15.7	14.4	23.1	17.6	17.5
Tm	32.3	16	18.7	22.7	19.5	24.8	20.2	18.0	16.4	13.4	13.5	11.5	18.1	15.6	15.0
Lu	30.0	14	14.4	19.1	17.6	22.1	15.1	15.0	13.6	11.2	11.4	9.2	13.4	13.8	12.7
Be	29.5	12	15.5	14.2	12.9	15.4	13.6	13.9	9.52	13.9	11.1	10.5	15.3	11.6	11.0
Ta	30.8	10	15.8	10.5	12.5	14.7	10.9	11.4	9.05	13.4	7.63	8.49	11.3	8.80	7.82
Th	38.3	8	32.5	14.2	12.9	14.7	12.4	11.1	10.3	8.80	8.50	8.23	10.7	8.61	8.27
Cs	57.1	6	2.57	111	25.3	3.54	6.74	3.66	17.8	3.26	6.00	27.4	1.77	3.03	5.66
U	78.4	4	10.1	3.76	5.49	6.43	4.16	4.39	5.73	3.22	4.16	2.75	4.86	3.45	5.25
Tl	182	2	0.91	2.73	4.00	4.55	10.0	0.73	5.09	3.09	1.64	11.09	0.91	1.45	1.82

C^{0_i} : scaled unaltered (reference) composition C^{A_i} scaled altered composition

Appendix 6.1. Major (wt.%) element composition of serpentinites from the Peltetec Unit.

Sample	P-007	P-024
Lithology	Serpentinite	Serpentinite
Longitude	774779	770950
Latitude	9824878	9791747
SiO_2	48.0	37.3
TiO_2	0.09	0.13
Al_2O_3	3.08	1.84
Cr_2O_3	0.31	0.43
FeO*	6.21	13.71
MnO	0.08	0.14
MgO	26.9	33.8
NiO	0.20	0.23
CaO	2.79	0.07
Na_2O	0.20	
K_2O	0.22	0.01
P_2O_5	0.03	0.02
LOI	10.9	10.9
Total	99.0	98.5

Appendix 7. 1 Rare-earth elements (REEs) fractional crystallization model (TU

			Partition coefficients								
Reference	Mineral	Content (%)	La	Ce	Pr	Nd	Sm	Eu	Gd	Tb	D
Fujimaki et al. (1984)	Biotite	1	0.029	0.037	0.0405	0.044	0.058	0.145	0.082	0.0895	0.0
Nandedkar et al. (2016)	Amphibole	65	0.129	0.237	0.4	0.628	1.125	1.221	1.617	1.708	1.1
Paster et al. (1974)	Plagioclase	30.8	0.069	0.062	0.035	0.028	0.017	0.68	0.014	0.013	0.0
Paster et al. (1974)	Apatite	1	8.6	11.2	12.6	14	14.6	9.6	15.8	14.4	13
Paster et al. (1974)	Magnetite	1	0.015	0.016	0.021	0.026	0.024	0.025	0.018	0.019	0.0
Tiepolo et al. (2002)	Titanite	1	6.43	11.1	14.85	18.6	21.4	20.4	18.3	15.3	1
Fujimaki (1986)	Zircon	0.2	3.11	3.49	3.65	3.8	4.72	4.23	6.77	35.1	6
		F (fraction of melt remaining)	Fractional crystallization (liquid pha								
		1	14.55	35.22	4.83	21.18	4.50	1.59	4.19	0.60	3.
		0.9	15.72	37.50	5.06	21.74	4.45	1.54	4.01	0.57	3.
		0.8	17.15	40.23	5.33	22.39	4.40	1.48	3.82	0.54	3.
		0.7	18.93	43.57	5.66	23.14	4.34	1.42	3.62	0.50	2.
		0.6	21.21	47.76	6.06	24.05	4.26	1.35	3.40	0.47	2.
		0.5	24.26	53.25	6.58	25.17	4.18	1.28	3.15	0.43	2.
		0.4	28.60	60.83	7.27	26.60	4.08	1.19	2.88	0.38	2.
		0.3	35.37	72.21	8.26	28.58	3.96	1.09	2.55	0.33	1.
		0.2	47.70	91.96	9.91	31.61	3.79	0.96	2.16	0.27	1.
		0.1	79.56	139.04	13.50	37.56	3.52	0.77	1.63	0.20	0.

DOCTORAL THESIS

2021

UNIVERSIDAD DE GRANADA

Departamento de
Mineralogía y Petrología

Programa Doctorado
Ciencias de la Tierra